TRANSFERT DE CHARGE ET D'ÉNERGIE DANS LES DYADES ET OLIGOMÈRES DE PORPHYRINE

Par

Mohammed Abdelhameed

Mémoire présenté au Département de Chimie en vue
de l'obtention du grade de maître ès sciences (M. Sc.)

FACULTÉ DES SCIENCES
UNIVERSITÉ DE SHERBROOKE

Sherbrooke, Québec, Canada, Juin 2014

Le 25 juin

Le jury a accepté le dépôt du mémoire de monsieur Mohammed Abdelhameed
Dans sa version finale

Membres du jury

Professeur Pierre Harvey
Directeur de recherche
Département de chimie

Professeur Patrick Ayotte
Membre interne
Département de chimie

Professeur Gessie Brisard
Président-rapporteur
Département de chimie

CHARGE AND ENERGY TRANSFER IN PORPHYRIN DYADS AND OLIGOMERS

By

Mohammed Abdelhameed

Thesis submitted to the Chemistry department as part of the fulfillment required to the Master degree (M. Sc.).

FACULTÉ DES SCIENCES
UNIVERSITÉ DE SHERBROOKE

Sherbrooke, Québec, Canada, June 2014

RESUMÉ

Le travail de recherche présenté dans ce mémoire fut inspiré par le processus de la photosynthèse qui se produit chez les plantes. Au cours de ce processus l'énergie solaire est convertie en énergie chimique via différentes étapes de transferts d'électrons et d'énergie. En maîtrisant bien ces concepts, de nombreuses applications, telles que les cellules photovoltaïques ou les DEL (Diodes électro-luminescentes) peuvent être améliorées. Pour se faire, il est important d'optimiser les propriétés des matériaux existants (oligomères, polymères, etc…) en préparant des systèmes conjugués plus efficaces, mais aussi de pleinement comprendre les processus qui s'y produisent (processus de transferts d'électrons et d'énergie photo-induist). La série d'oligomères et de polymères présentée dans ce mémoire le sont pour leurs applications dans des systèmes photoniques.

Dans cette optique, ce mémoire a été divisé en cinq grands chapitres. Le premier présente les principes théoriques de la photophysique. Le second présente le suivi du transfert d'énergie T_1 dans les états triplets, $T_{1,}$ une dyade constituée de la tétraphénylporphyrine de zinc(II), **[ZnTPP]**, et de la bis(phénylpyridinato)(bipyridine) d'iridium(III), **[Ir]**, chromophores liés avec un pont *trans*-diéthynylbis(phosphine)-platine(II). Malgré que cette dyade soit entièrement conjuguée et qu'elle soit constituée d'un donneur (**[ZnTPP])** et d'un accepteur (**[Ir]**), aucun transfert d'énergie T_1 **[Ir]** → S_1/T_1 **[ZnTTP]** n'a été observé. Ce résultat fut attribué à l'absence de recouvrement des orbitales moléculaires entre la HSOMO(donneur*) et la HSOMO(accepteur), LSOMO(accepteur) and LSOMO (donneur*) (mécanisme de Dexter). Ainsi, l'échange d'électrons est impossible. Ce chapitre suggère que l'équation de Dexter, $k_{Dexter} = KJ_{exp}(-2r_{DA}/L)$ ne reste qu'une approximation. Ce travail a été publié dans *ChemComm* (**2013**, 49, 5544-5546).

Le troisième chapitre présente le transfert d'énergie singulet beaucoup lent qu'attendu se produisant dans une dyade constituée d'une porphyrine de zinc(II) avec une porphyrine base libre liées par un pont palladium(II) (*trans*-PdI_2). Sachant que cette dyade est entièrement conjuguée et que la distance entre les deux centres de masse des porphyrines est relativement courte, ce système aurait dû présenter un transfert d'énergie très rapide, d'après la théorie de Förster. Dans ce cas, ce comportement a été expliqué par le faible recouvrement des orbitales frontières (OM) du donneur et de l'accepteur. Ce travail a été accepté le 2014-05-26 dans *Chemistry – A European Journal* (chem.201403146).

Le quatrième chapitre rapporte une étude du transfert d'énergie ultra-rapide (650 fs) entre des états singulets dans une dyade composé d'une porphyrine de zinc(II) (le donneur) et une porphyrine base libre (l'accepteur) liées à l'aide d'un pont de palladium (β,β–*trans*-$Pd(NH)_2(CO)_2$). Ces résultats ont été attribués à la présence d'un couplage fort entre les OM du donneur et de l'accepteur et de la très faible contribution (atomique) du Pd(II) vers ces OM. Cette dyade montre la plus rapide constante de transfert d'énergie k_{ET} que nous connaissons pour des dyades similaires contenant un fragment métallique. Les résultats du troisième et quatrième chapitre montrent que la théorie de Förster tel quel ne suffit pas pour prédire les vitesses de transferts d'énergie dans certains systèmes : d'autres facteurs doivent être pris en compte. Ce travail a été soumis dans *JACS* (ja-2014-061774, 19-6-2014).

Dans le cinquième chapitre de ce mémoire, la synthèse du bis(-α-(amino(4-éthynylbenzene (triméthylsilane)(R))))bis(4-éthynylbenzene-(triméthylsilane))quinone diimine (R= H, Boc) comme modèle pour des polymères conjugués et non-conjugués contenant le colorant porphyrine a été proposée. Le corps du composé désiré (tétrakis(4-éthynlyphenyl)quinone-1,4-diimine-2,5-diamine) a montré un transfert de charge partant des groupes terminaux riches en électrons une la benzoquinone centrale plus pauvre. La nature de l'émission fut observée uniquement à 77K pour le cas où R = H et fut attribuée à de la fluorescence. À température ambiante, l'intensité était trop faible pour être observée. Dans le cas où R = Boc, aucune emission n'a été détectée. Malheureusement, le composé espéré ne fut pas obtenu, le procédé de synthèse employé engendra uniquement la forme réduite. Cette forme fut malgré tous analysé, et ne présenta pas de transfert de charge ni de communication entre les différents chromophores. Ceci a été expliqué simplement par le fait que la conjugaison est brisée quand ce composé est sous sa forme réduite. Ce travail sera soumis au *Journal of Inorganic and Organometallic Polymers and Materials*.

Mots clés:

porphyrine - Transfert d'énergie - Dexter - Förster - DFT.

SUMMARY

The research work presented in this master thesis is inspired by the photosynthetic process occurring in plants where solar energy is converted into chemical energy via several energy and electron transfer processes. In the light of these concepts, several applications such as solar cells and light emitting diodes can be improved. To do so, we need to optimize the properties of polyads, oligomers and polymers to device more efFficient conjugated materials as well as developing a full understanding of the photo-induced energy and electron transfer processes that occur. Several organometallic oligomers and polymers are presented in this thesis due to their potential photonic applications.

In this respect, this master thesis has five chapters. The first one introduces some theoritical principles of photophysics. The second one presents the monitoring of triplet state (T_1) energy transfer in a dyad that consists of zinc(II)tetraphenylporphyrin, [**ZnTPP]**, and bis(phenylpyridinato)-(bipyridine)iridium(III), **[Ir]**, chromophores linked by a platinum(II) containing bridge. Despite the conjugation in this dyad and the presence of the [**ZnTPP]** energy donor and the **[Ir]** energy acceptor species, no T_1 **[Ir]** → S_1/T_1 **[ZnTTP]** energy transfer occurs. This result was explained by the absence of MO overlap between HSOMO(donor*) and HSOMO(acceptor), LSOMO(donor*) and LSOMO(acceptor) , and hence no efficient double electron transfer exchange (i.e. Dexter mechanism) is likely to occur. This chapter suggested that Dexter formulation, $k_{Dexter} = KJ\exp(-2r_{DA}/L)$, appears as an approximation. This work has been published in *ChemComm* (**2013**, 49, 5544-5546).

The third chapter shows an unexpected slow singlet energy transfer in a dyad built upon a zinc(II)porphyrin and the corresponding free base chromophores linked by a palladium(II)-containing bridge (*trans*-PdI_2), despite the presence of conjugation and the relative short center-to-center distance. This behavior was explained by two factors, the first is the lack of large molecular orbitals (MOs) overlaps between the frontier MOs of the donor and acceptor, and thus preventing a double electron exchange to occur through the *trans*-PdI_2 bridge. The second factor affected the energy transfer is the electronic shielding induced by the presence of this same linker, namely the electron rich iodides, preventing the two

chromophores to fully interact via their transition dipoles. This work has been accepted on 2014-05-26 in *Chemistry-A European Journal* (chem.201403146).

The fourth chapter reports an ultrafast singlet energy transfer (650 fs) in a dyad composed of a zinc(II)porphyrin (donor) and a free base porphyrin (acceptor) β,β-linked via *trans*-$Pd(NH)_2(C=O)_2$. These results were explained by the presence of strong MO couplings of the donor and acceptor and the very weak atomic contribution of the Pd(II) atom to this MO. This dyad shows the fastest energy transfer rate k_{ET} among other similar dyad systems incorporating a bridge either in the form of a metal fragment or carbon-based. The results of these third and fourth chapters showed that the Förster mechanism is not enough to account for the energy transfer in some systems and other factors affect that transfer. This work has been submitted in *JACS* (ja-2014-061774, 19-6-2014).

In chapter 5, the synthesis of bis-α-(amino(4-ethynylbenzene (trimethylsilane)(R))bis(4-ethynylbenzene-(trimethylsilane))quinone diimine (R = H, Boc) as a model for conjugated and unconjugated porphyrin dye polymers was proposed. The central core of the desired compound, tetrakis(4-ethynlypenyl)quinone-1,4-diimine-2,5-diamine, provided evidence for a charge transfer interaction from the electron richer terminal groups to be more electron poorer benzoquinone ring. The nature of the emission of the core compound was found to be fluorescence at 77K for the case R = H but was too weak to be observed at 298K. No emission was detected for the case R = Boc. Unfortunately, the synthetic route of the desired compound gave the reduced form. The analyses of the reduced compound showed the complete absence of the charge transfer or any communication between the different chromophores due to the broken conjugation between the porphyrin units in the reduced product. This work will be submitted to *Journal of Inorganic and Organometallic Polymers and Materials*.

Keywords:

Porphyrin - Energy transfer - Dexter - Förster - lifetime - DFT.

ACKNOWLEDGEMENT

I would like to thank Professor Pierre D. Harvey for giving me the opportunity to pursue my master's studies in his laboratory. I especially thank him for his guidance and support. His advices given to me were greatly appreciated.

I would like to thank all of my colleagues, who all significantly contributed to my training and understanding of chemical research: Adam Langlois, Antoine Bonnot, Antony Lapprand, Ahmed Soliman，Peng Luo, Xiaorong Wang, Hu Lei, Lounès Haroune and Di Gao.

Many thanks to Dr. René Gagnon, Dr. Daniel Fortin, Dr. Jean Marc Chapuzet and Dr. Shawkat Aly for their help and advices. Special thanks to Dr. Paul-Ludovic Karsenti for all the measurements that he has done for me.

I would like to thank my family for their support during all of my studies.

Finally, thanks to the Université de Sherbrooke for having admitted me to the M.Sc. program and to the CQMF (centre québécois sur les materiaux fonctionnels), FQRNT (fonds de recherche sur la nature et les technologies) and the CEMOPUS (Centre d'Excellence sur les Matériaux Optiques et Photoniques de l'Université de Sherbrooke) for their financial support which is absolutely essential for such research.

TABLE OF CONTENT

LIST OF ABBREVIATIONS

DFT	Density functional theory
TDDFT	Time-dependent density functional theory (TDDFT)
MLCT	Metal to ligand charge transfer
LLCT	ligand to ligand charge transfer
[ZnTPP]	zinc(II) tetraphenylporphyrin
S_0	singlet ground state
S_1	first singlet excited state
T_1	first triplet excited state
λ	wavelength
A	absorption
UV	ultraviolet
Φ	quantum yield
τ	lifetime
HOMO	Highest Occupied Molecular Orbital
LUMO	Lowest Unoccupied Molecular Orbital
HSOMO	Highest Singly Occupied Molecular Orbital
LSOMO	Lowest Singly Occupied Molecular Orbital
μs	microsecond
ns	nanosecond
ps	picosecond
K	Kelvin
k_{ET}	rate of energy transfer
τ_p	phosphorescence lifetime
τ_F	fluorescence lifetime
2-MeTHF	2-methyltetrahydrofuran
MO	molecular orbitals

LIST OF TABLES

CHAPTER 2: Monitoring the on/off switching of the electronic communication in diethynylplatinum(II)-bridged dyads using triplet energy transfer.

CHAPTER 3. Unexpected drastic decrease in the excited state electronic communication between porphyrin chromophores covalently linked by a palladium(II) bridge.

CHAPTER 4. Ultrafast energy transfer in a Pd(II)-bridged bisporphyrin dyad.

CHAPTER 5. Bis-α-(amino(4-ethynylbenzene(trimethylsilane)(R))bis(4-ethynyl-benzene(trimethylsilane))quinone diimine (R = H, Boc) as potential building blocks for conjugated porphyrin dye-containing polymers exhibiting low-energy band gaps.

LIST OF FIGURES

Introduction

CHAPTER 1. Theory

CHAPTER 2. Monitoring the on/off switching of the electronic communication in diethynylplatinum(II)-bridged dyads using triplet energy transfer.

CHAPTER 3. Unexpected drastic decrease in the excited state electronic communication between porphyrin chromophores covalently linked by a palladium(II) bridge.

CHAPTER 4. Ultrafast energy transfer in a Pd(II)-bridged bisporphyrin dyad

CHAPTER 5. Bis-α-(amino(4-ethynylbenzene(trimethylsilane)(R))bis(4-ethynylbenzene(trimethylsilane)) quinone diimine (R = H, Boc) as potential building blocks for conjugated porphyrin dye-containing polymers exhibiting low-energy band gaps.

LIST OF SCHEMES

CHAPTER 2. Monitoring the on/off switching of the electronic communication in diethynylplatinum(II)-bridged dyads using triplet energy transfer.

CHAPTER 3. Unexpected drastic decrease in the excited state electronic communication between porphyrin chromophores covalently linked by a palladium(II) bridge.

CHAPTER 4. Ultrafast energy transfer in a Pd(II)-bridged bisporphyrin dyad.

CHAPTER 5.

LIST OF CHARTS

Introduction

Chapter 5. Bis-α-(amino(4-ethynylbenzene(trimethylsilane)(R))bis(4-ethynyl benzene (trimethyl -silane)) quinone diimine (R = H, Boc) as potential building blocks for conjugated porphyrin dye-containing polymers exhibiting low-energy band gaps.

5.2. Supporting Infornation

General Discussion

INTRODUCTION

Nowadays, one of the biggest challenges the world faces is the rising global consumption of energy. The U.S. Energy Information Administration (EIA) predicted that the world energy consumption will increase from 524 quadrillion British thermal units, Btu, in 2010 to 630 quadrillion Btu in 2020 and 820 quadrillion Btu in 2040, a 30-year increase of 56 percent.[1] Currently most of the world's energy supply comes from the fossil fuels, such as coal, gas and oil which leads to several environmental problems generated by burning fossil fuels. Using sunlight to produce energy is one of the most sustainable energy solutions to overcome many of these problems. One hour of the whole sun illumination is equivalent to the yearly energy consumption of our world today[2]. what happens in nature is that sunlight is dispersed hence the light needs to be captured, stored and converted to other forms of energy such as electrical or chemical to be useful. In a similar manner, the green plant absorbs the sunlight and the absorbed energy is converted into chemical energy via a complex series of electron and energy transfer processes.

Photosystems are functional and structural units of protein complexes involved in photosynthesis that carry out the primary photochemistry of photosynthesis which includes the absorption of light and the transfer of energy and electrons. There are two types of photosystems, PSII and PSI. At the heart of the photosystem lies the reaction center protein, which is a complex supramolecular device that uses light to reduce molecules. This reaction center is surrounded by light-harvesting complexes that enhance the absorption of light and transfer the energy to the reaction centers. Light-harvesting and reaction center complexes are membrane protein complexes that are made of several protein-subunits and contain numerous cofactors. There are two families of reaction centers, type I and II reaction centers (absorb light at 700 and 680 nanometers, for **PSI** and **PSII** in the chloroplasts, respectively). This overall series of processes are represented in Figure 1. Understanding the mechanism of this process may lead to efficient artificial photosynthetic systems.

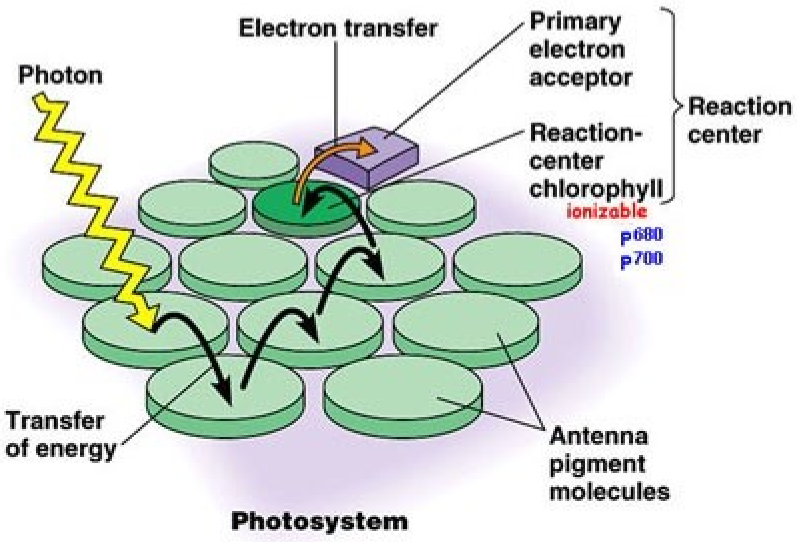

Figure 1. Light is absorbed by the antenna and the energy is transferred to the reaction centrer.[3]

Photosynthesis includes two processes,[4] the light and dark reactions respectively. The **light reaction** occurs in the thylakoid membrane and converts light energy to chemical energy. This chemical reaction must, therefore, take place in the light. Chlorophyll and several other pigments such as β-carotene are organized in clusters in the thylakoid membrane and are involved in the light reaction. Each of these differently colored pigments can absorb different color of light and pass its energy to the central slipped chlorphyll dimer molecule (called the special pair) to perform the photosynthetic process (photo-induced electron transfer). The central part of the chlorophyll structure is similar to that of porphyrin which consists of several fused rings of carbon and nitrogen with a magnesium ion in the center.

Porphyrins and their metal derivatives have been the subject of spectroscopic, photophysical, and photochemical study for several decades.[5] The importance of these compounds is due to their applications such as in photodynamic therapy,[6] as chemical and biological sensors,[7] as molecular logic [8] and optoelectronic devices,[9] and in artificial solar energy harvesting and storage schemes,[10] which has prompted a widespread renewal of interest among both experimentalists and theorists.

Electronic absorption properties of porphyrins

The delocalised aromatic character of porphyrins, which results from extensive conjugation (Figure 2), accounts for the one of the most striking features of these chromophores. The UV-visible absorption spectrum of porphyrins consists of two distinct regions. In the ultra violet region, an extremely intense absorption known as the ($\pi \rightarrow \pi^*$) Soret or B bands and in the visible region, a number of absorptions known as the ($\pi \rightarrow \pi^*$) Q bands are present.

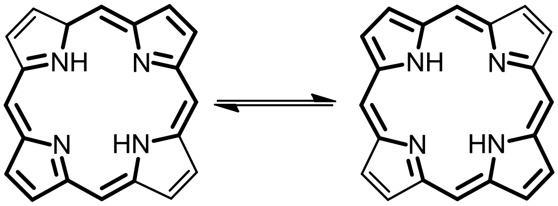

Figure 2. Delocalized 18 π -electron conjugation pathway and tautomerism of the 16 membered ring of the porphyrin.

The UV-visible spectrum of Zn(II)tetraphenylporphyrin, **[ZnTPP]**, showed significant absorption bands (Figure 3) in the visible and near UV regions which is assigned to the Soret band and Q-band in the visible region. The first one corresponds to a strongly allowed transition from the ground state to the second exited state ($S_0 \rightarrow S_2$). The latter corresponds to a transition from the ground to the first excited state ($S_0 \rightarrow S_1$).

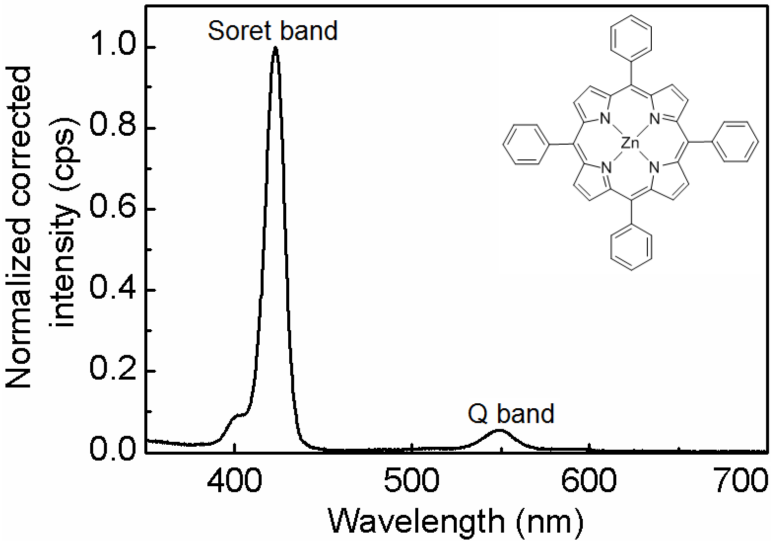

Figure 3. UV-visible spectrum of **[ZnTPP]** showing the Soret band and Q-band.

For a free-base tetraphenylporphyrin, **[H_2TPP]**, which possesses a D_2h symmetry across the plane of the ring, the opposing protons stabilize an 18-membered cyclic polyene, with each proton causing a one electron perturbation of the macrocycle. This perturbation causes the split in the absorption bands in the visible region but not in the ultraviolet (Figure 4).The splitting about the origin of transitions for porphyrins of lower symmetry arise from the mixing of anti-symmetrised products which are nearly or accidentally degenerate, and is known as inter-configurational interaction.

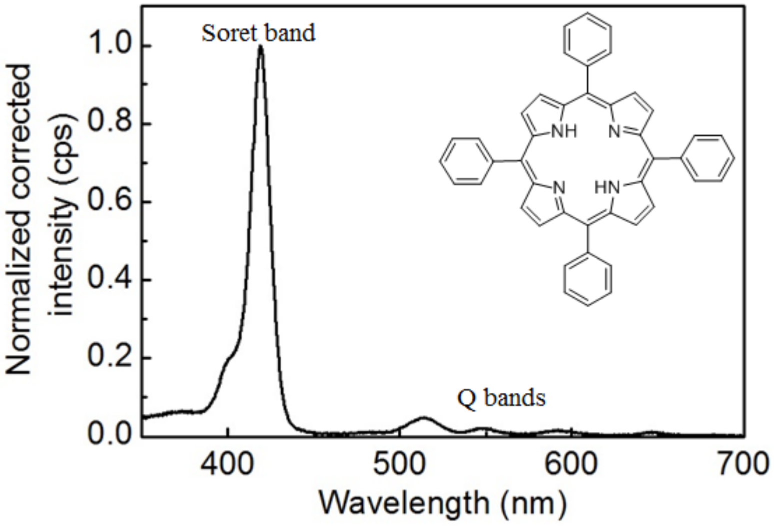

Figure 4. UV-visible spectrum of **[H_2TPP]** showing the Soret band and Q-bands.

Several dyads that incorporate porphyrin chromophores were synthesized, studied and analyzed photophysically revealing results that vary from absent to slow to ultra-fast energy transfer. This master thesis reports an example of a dyad that showed an unexpected absence of energy transfer: **[Ir]-Pt-[Zntpp]** (Chapter 2).[11] An example for a slow energy transfer is compound **[2Zn-Fb]** when compared to other dyads having similar structural features (Chapter 3). Conversely, compound **[3Zn-Fb]** (Chart 1; Chapter 4) shows an ultra-fast energy transfer from the zinc(II)porphyrin to the free base porphyrin. The overlap extent of the frontier molecular orbitals, MOs, between the donor and acceptor is one of the key factors which determine how efficient the energy transfer in the molecule is.

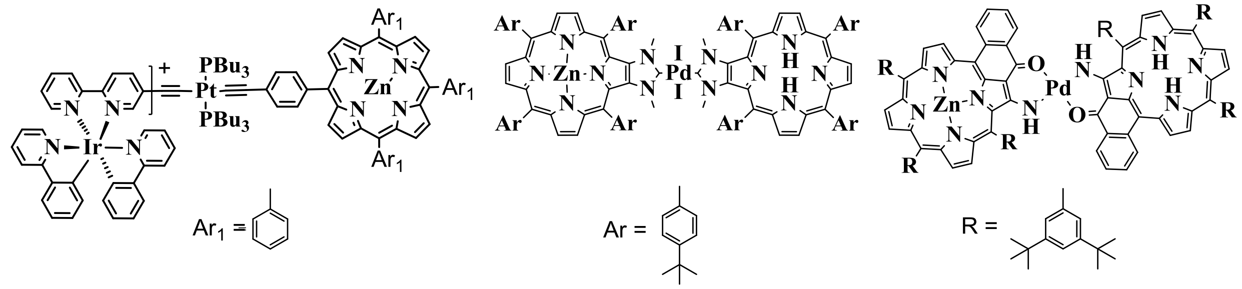

[Ir]-Pt-[ZnTPP] **[2Zn-Fb]** **[3Zn-Fb]**

Chart 1. Structures of the compounds **[Ir]-Pt-[ZnTpp], [2Zn-Fb]** and **[3Zn-Fb].**

The incorporation of porphyrins in the backbone of polyanilines in its different forms (the reduced, oxidized and mixed valence forms) models in a way the natural photosynthetic proteins **PSII**. These "bio-inspired" polymers shows a charge transfer from the terminal porphyrins to the central benzoquinone ring. Two bioinspired polymers of this type were reported. The first one, **P1**,[12] (Chart 2) was built on an electron rich (zinc(II)porphyrin) unit and an electron poor (quinone diimine) center, which are similar structually to chlorophyll *a* and plastoquinone, respectively, involved in the photosynthetic process. An example for the unconjugated polymer that shows low band gap (i.e. here a charge transfer absorption) is composed of an electron rich zinc(II)porphyrin unit that is incorporated in the backbone of a quinone-containing polymer (at the α-position), **P2**, (Chart 2; work performed by Mrs. Xiaorong Wang; Ph.D. candidate in our laboratory; unpublished results). To further understand the charge transfer processes occurring in polymers **P1** and **P2**, the synthesis of

TAI-Znpor as a model compound that combines both the conjugated and unconjugated motifs within the same assembly is necessary.

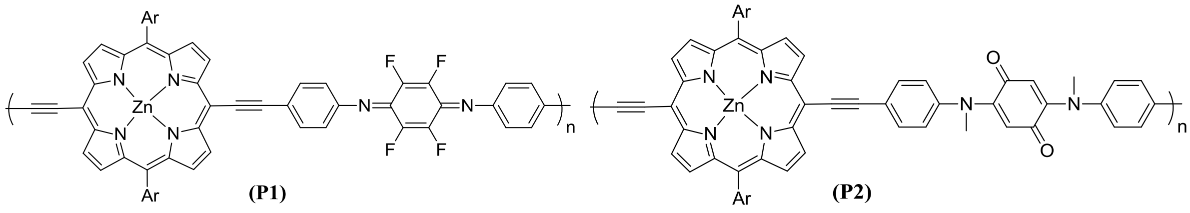

Chart 2. Structure of the polymers **P1** and **P2.**

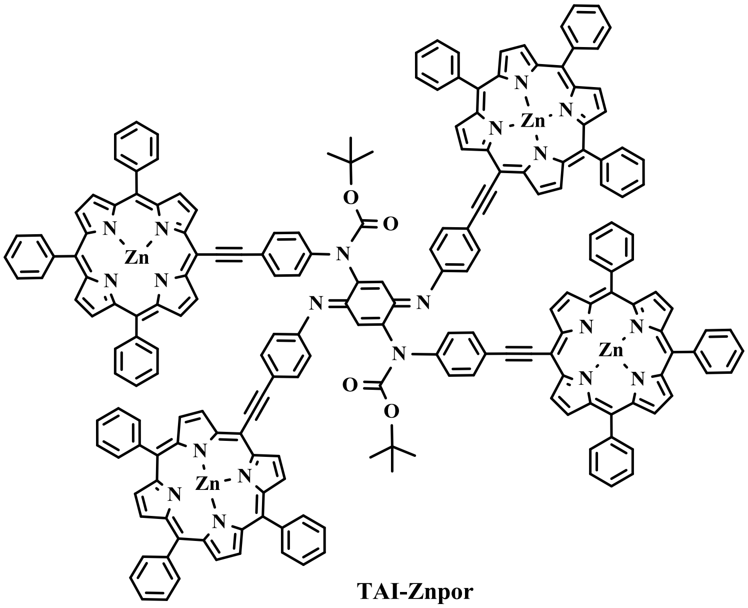

Chart 3. Structure of TAI-Znpor

Objectives of this thesis

This research project focused on the photophysics of bisporphyrin dyad systems and oligomers where the donors and acceptors are linked together by a conjugated metal-containing fragment of a benzoquinone. This aim is motivated by the high possibility of photo-induced electron and energy transfer properties of these chromophores and their potential applications in the field of optoelectronic devices, sensors, luminescent markers, and solar energy conversion.

Again, the specific interest is focused on compounds designed for the study of photo-induced singlet (S_1) and triplet (T_1) energy transfers and a large emphasis was given to the study of bisporphyrin dyads linked by metallo-bridges (specifically Pt(II) and Pd(II) ions) and metalloporphyrin-containing oligomers with potential photonic applications.

CHAPTER 1

Theory

This chapter outlines the theory, the physical basis and the different techniques that are used to characterize photoactive systems including absorption, energy and electron transfer, excitation energy migration and emission without a chemical reaction which is called photophysical studies of the matter.

1.1. Electronic absorption and emission spectroscopy

When a molecule (M) absorbs light, the resulting molecule will have an excess energy. It is then an excited molecule (M^*)(Equation 1.1). This molecule can simply re-emit the excess energy as the form of light to go back to its ground state (Equation 1.2).

$$M + h\upsilon \rightarrow M^* \qquad [1.1]$$

$$M^* \rightarrow M + h\upsilon \qquad [1.2]$$

The excited molecule (M^*) can transfer its excess energy to another acceptor molecule, A. This process is also called quenching (Equation 1.3).

$$M^* + A \rightarrow M + A^* \qquad [1.3]$$

1.2. Excitation energy migration

If there are two molecules in close proximity, one with an absorption band at a wavelength shifted to the longer wavelengths than the other, light energy absorbed by the one absorbing at the shorter wavelength (i.e. higher energy) is often transferred to the one that absorbs at the longer wavelength. One molecule acts as a donor, D, of excitation energy, and the other as an acceptor, A, of this energy. This transfer probably takes place by a resonance mechanism which is described in terms of quantum mechanics. Remotely placed chromophore molecules do not participate directly in the primary photochemical process in photosynthesis, but transfer their excitation energy to the chromophore molecules directly associated with the reaction centers that lead to the primary charge separation (formation of high energy anion and cation).

Excitation energy is in the form of an electron placed in the LUMO and a hole in the HOMO in the S_1 excited state of the molecule. Then this energy is transfered from one chromophore to another. This process is called excitation energy migration. What are transferred are the excited electron and the hole from one molecule to the neighbour. (Figure 5). The mechanism for this process arises from dipole-dipole interactions.

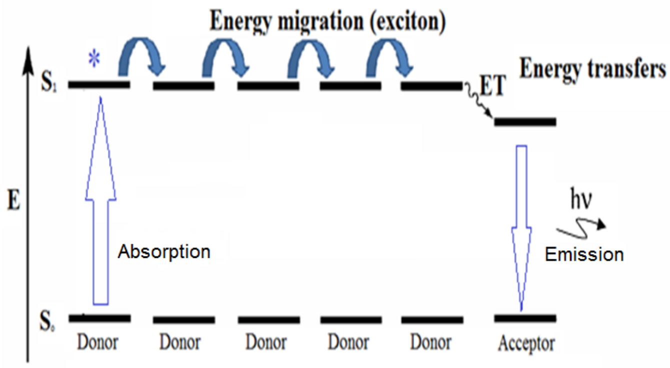

Figure 5. The exciton and energy transfer process (Modified from Ref. 13).

Energy transfer between different chromophore molecules is known as heterogeneous transfer, unlike the homogeneous transfer that occurs between identical molecules. The energy transfer can be repeated many times, giving rise to energy migration. Direct evidence of energy transfer between different chromophores is provided by sensitized fluorescence. Light quanta absorbed by molecules of one chromophore are transferred to molecules of another chromophore. When the first chromophore is excited, only fluorescence of the second is observed. This phenomenon of sensitized fluorescence is well known from studies on gases and solutions. The two possible mechanisms (Dexter and Förster) for this process are decribed below.

1.3. Electron transfer

The process of photoinduced electron transfer (PET) is considered one of the most basic photochemical reactions and at the same time it is the most favourable way to convert light energy or to store it for further applications. The process is taking place between a donor and an acceptor of electron after excitation resulting in the formation of a charge-separated state which relaxes to the ground state via an electron-hole recombination. The process (PET) involves an electron transfer within an electron donor-acceptor pair as shown in Figure 6.

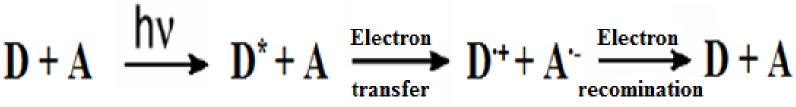

Figure 6. Photoinduced electron transfer process.

Marcus theory was used to interpret the photoinduced electron transfer in solution by which the electron transfer reaction can be treated using transition state theory where the reactant state representing the excited donor/acceptor while the product state is the charge-separated state of donor cation and acceptor anion (D^+-A^-), as shown in Figure 7. [14-20]

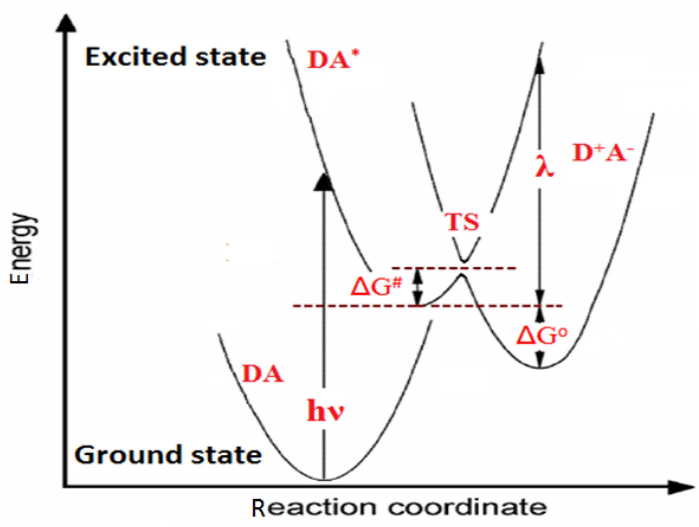

Figure 7. Schematic representation of potential energy surfaces for the ground state(DA), the excited state (DA^*, reactant state), and the charge-separated state (D^+-A^-,product state), as proposed by Marcus theory. λ = total reorganization energy, and TS = transition state (modified from ref. 21).

According to the Franck-Condon principle, the photoexcitation induces a vertical transition to the excited state which proceeds to a rapid nuclear equilibration. After exciting the donor, electron transfer occurs at the crossing of the equilibrated excited state surface and the product state. The change in Gibbs free energy associated with the electron transfer event is given by the following Equation (Equation 1.4) :

$$\Delta G^{\#} = \frac{(\lambda + \Delta G°)^2}{4\lambda} \qquad [1.4]$$

The total reorganization energy (λ), which is required to distort the reactant structure to the product structure without electron transfer, is composed of a solvent (λ_S) and internal (λ_i) components ($\lambda = \lambda_S + \lambda_i$). The reaction free energy (ΔG^o), is the difference in free energy between the equilibrium configuration of the reactant (DA^*) and product states (D^+A^-). The internal reorganization energy represents the energy change that occurs in bond lengths and bond angles distortion during the electron transfer step and is usually represented by a sum of harmonic potential energies. In the classical Marcus theory, the rate for electron transfer is given by:[17-18]

$$k_{ET} = \kappa_{ET} \nu_n exp(\frac{-\Delta G^{\#}}{k_B T}) \qquad [1.5]$$

where ν_n is the effective frequency of motion along the reaction coordinate and κ_{ET} is the electronic transmission factor. The transmission factor is related to the transition probability (P_o) at the intersection of two potential energy surfaces, as given by the Landau-Zener theory:[19]

$$\kappa_{ET} = \frac{2P_o}{1 + P_o} \qquad [1.6]$$

1.4. Light absorption

Light is generally considered an electromagnetic radiation that can be viewed as waves or particles.

In the wave model, the electromagnetic radiation is treated as a wave emitted from a source and is characterised by (Equation 1.7):

$$\lambda = c/\nu \qquad [1.7]$$

where λ is the wavelength, c is the velocity of light (2.998×10^8 m/s) and ν is the frequency.

In the particles model, light is composed of particles which are called photons (particles having no mass but only energy). Each photon has an energy of Plank's quantum, h c/ λ, where h is Plank's constant ($h = 6.62 \times 10^{-34}$ Js), c is the light velocity and λ is the wavelength of the radiation.

The photon absorption by a system (M) leads to photophysical or / and photochemical processes as it was stated by the Grotthus-Draper law.

Indeed, the optical transmittance, T, is a measure for how much light enters a sample and that is then absorbed (Equation 1.8).

$$T = I/I_o \qquad [1.8]$$

where I is the intensity of the transmitted light and I_o is the intensity of the incident light. Absorbance, A, is the logarithm of the ratio of the intensity of the transmitted light to the intensity of the incident light (Equation 1.9).

$$A = \log (I/I_o) \qquad [1.9]$$

and hence

$$A = \log (1/T) = -\log T \qquad [1.10]$$

Beer's law states that, the absorbance of a chromophore increases in proportion to the concentration of the latter (Equation 1.11).

$$A \propto c \qquad [1.11]$$

$$A = k\,c \qquad [1.12]$$

where k is a constant.

Lambert's law stated that the absorbance is directly proportional to the path length (Equation 1.13).

$$A \, \alpha \, l \qquad [1.13]$$

$$A = k' \, l \qquad [1.14]$$

where l is the path length and k′ is a constant.

The Beer-Lambert law combines the two laws giving

$$A = \varepsilon \, l \, c \qquad [1.15]$$

where ε is the molar absorption coefficient.

The absorption of a photon by a molecule at a certain wavelength leads to an excited molecule where the absorbed energy can be translated into rotational, vibrational and electronic modes. The quantized internal energy, E_{int}, of the molecule in both its ground and excited stated can be approximated by (Equation 1.16).

$$E_{\text{int}} = E_{\text{el}} + E_{\text{vib}} + E_{\text{rot}} \qquad [1.16]$$

where E_{el} , E_{vib}, E_{rot} are the electronic, vibrational and rotational energies respectively.

According to the Born-Oppenheimer approximation, as the electronic transitions are very fast and occur in about 10^{-15}s compared to the characteristic time scale for molecular vibrations that occur in 10^{-12} s, the influence of the vibrational and the rotational motions are almost negligible.

The Frank-Condon principle states that the electronic transition occurs mostly without change in the position of the nuclei in the molecular entity and its environment and hence, it is possible to describe the molecular energy by a potential energy diagram (Figure 8).

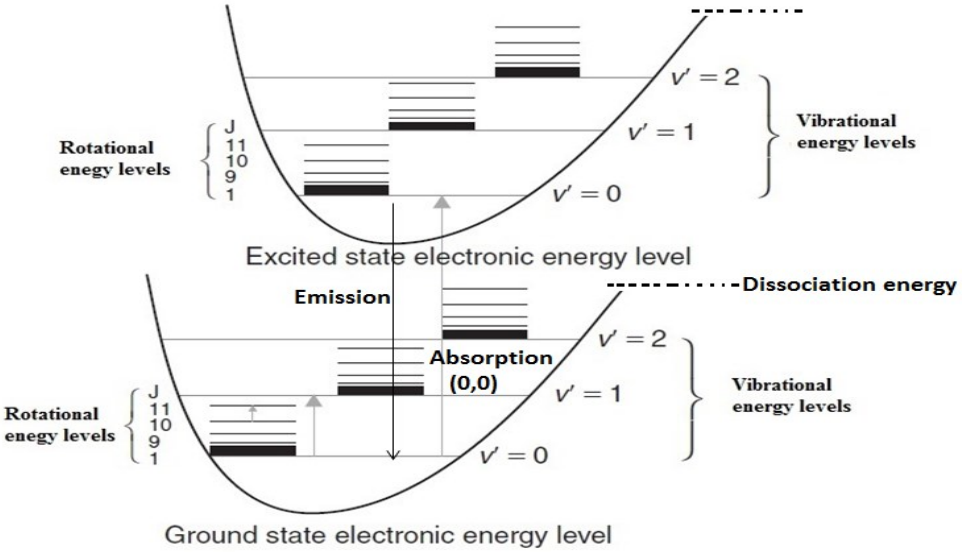

Figure 8. The relative order of electronic, vibrational and rotational energy levels (modified from Ref. 15).

However the UV-Vis spectrum for most molecules is expected to be simple as only one or two lower energy electronic transitions are normally postulated, but it is usually more complicated .

The Frank-Condon principle indicates that both the vibrational and electronic transitions will be observed in the spectrum. According to this concept for a diatomic molecule, let's consider the example in Figure 9. According to the Boltzman distribution, at room temperature, most of the molecules are in the lowest vibrational level (ν) of the ground state (i.e., ν = 0). The absorption in the spectrum (Figure 5b) exhibits a combination of both the pure electronic transitions (i.e., from ν = 0 to $\nu^{\backslash}$ = 0) and several vibronic peaks for which intensities depend on the relative position and shape of the potential curves of the ground and excited atates.

In the example provided in Figure 9, the 0-2 peak has the highest intensity as going from ν = 0 in the ground state to ν = 2 in the excited sate is the most probable for vertical transitions as it falls on the highest point in the vibrational probability curve in the excited state.

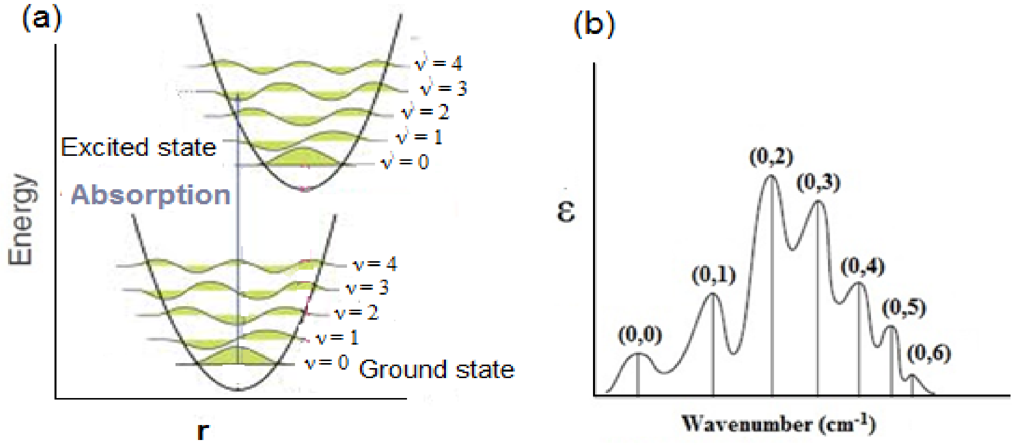

Figure 9. (a) Potential energy diagram for a diatomic molecule, illustrating the Frank-Condon excitation and, r is the nuclear coordinate. (b) Intensity distribution among vibronic bands as determined by the Frank-Condon principle. (Modified from Ref. 22).

The emission and excitation spectra are two types of distinct spectra but they usually overlap. The excitation spectrum is normally known as the spectrum of light emitted by the material as a function of the excitation wavelength while the absorption spectrum is known as the spectrum of light absorbed by the material as a function of the wavelength. Usually, these two spectra, absorption and excitation, should overlap perfectly. The absorption of a photon by a molecule can lead to electron migration from the highest occupied molecular orbital, HOMO, to the lowest unoccupied molecular orbital, LUMO.

1.5. Luminescence

Luminescence is the emission of light by a substance not resulting from heat. It is thus a form of cold body radiation. It can be caused by chemical reactions, electrical energy, subatomic motions or stress on a crystal.

Types of Luminescence

1.5.1. Chemiluminescence is an emission of light as a result of a chemical reaction. There are two types of chemiluminescence. The first type is bioluminescence which is an emission as a result of biochemical reaction by a living organism. The second type is electrochemiluminescence which is an emission as result of an electrochemical reaction.

1.5.2. Crystalloluminescence is produced during crystallization. There are two types of crystalloluminescence. The first type is the electroluminescence which is a result of an electric current passed through a substance. An example of devices using this process is the light emitting diode (LED). The second type is the cathodoluminescence which is a result of a luminescent material being struck by the electrons. Examples for this process involve the well-known neon tube light.

1.5.3. Mechanoluminescence is a result of a mechanical action on a solid. There are four types of mechanoluminescence. The first type is the triboluminescence which is generated when bonds in a material are broken when that material is scratched, crushed, or rubbed. The second type is the fractoluminescence which is generated when bonds in certain crystals are broken by fractures. The third type is piezoluminescence which is produced by the action of pressure on certain solids. The fourth type is the sonoluminescence which is a result of imploding bubbles in a liquid when excited by sound.

1.5.4. Photoluminescence is a result of absorption of photons. There are two types of photoluminescence. The first type is fluorescence which shows photoluminescence as a result of singlet–singlet electronic relaxation . The typical lifetime of fluorescence is the nanoseconds range. The second type is phosphorescence which shows photoluminescence as a result of triplet–singlet electronic relaxation. The typical lifetime of phosphorescence ranges from milliseconds to hours.

1.5.5. Radioluminescence is a result of bombardment by ionizing radiation.

1.5.6. Thermoluminescence is the re-emission of absorbed light when a substance is heated.

Generally when a molecule absorbs a photon, it is described as an excited molecule (i.e. a molecule lying in an upper electronic excited state) and after a certain time, the excited state molecule can relax by a number of different pathways. One of these pathways is conversion to a triplet state that can then relax towards lower lying states through phosphorescence and some nonradiative steps including chemical reactions and isomerization.

The Molecular Orbital theory (MO) is a method for determining molecular structure in which electrons are treated as moving under the influence of the nuclei in the whole molecule. In Molecular Orbital theory, the bonding between atoms is described as a combination of their atomic orbitals. It allows to predict the distribution of electrons in a molecule which in turn can help predict molecular properties such as shape, magnetism, and bond order.

The Frontier Molecular Orbital theory (FMO) is an application of MO theory in which a good approximation for reactivity could be found by looking at the frontier orbitals (HOMO/LUMO). The HOMO is the orbital of highest energy that is still occupied, so energetically it is easy to remove electrons from this orbital. This could be simply donating electron density to form a bond. The LUMO is the lowest lying orbital that is empty, so energetically it is the easiest to add more electrons into this orbital.

1.6. Jablonski diagram

It is an energy diagram that represents the different electronic states and transitions in molecules (Figure 10). S_0 represents the electronic ground state and S_1, S_2 represent the first and second singlet excited states respectively. T_1 and T_2 represent the first and second triplet excited states respectively. In the singlet states, all electrons spin are paired and the multiplicity of this state is 1 while in the triplet state, the electrons are no longer antiparallel and the electronic spin multiplicity is 3 as the total spin states can take values of -1, 0 and 1. The triplet state is more stable than the singlet state because of the Coulomb repulsion energy between the two electrons and the increase in degree of freedom of the magnetic spins.

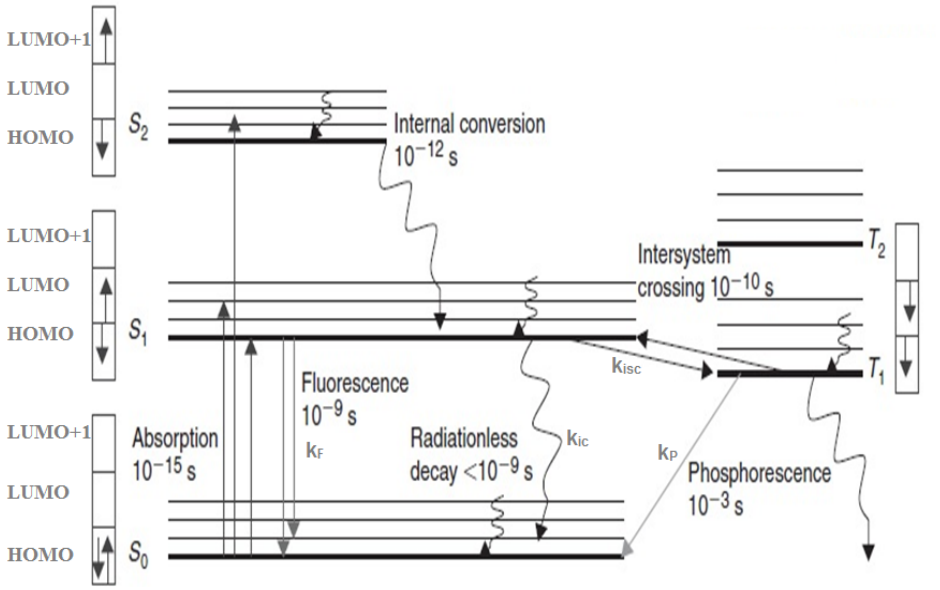

Figure 10. Jablonski diagram showing different states and transitions (Modified from Ref. 22).

In Figure 6, the arrows in the boxes represent the electron spins when they are paired in the singlet states and in the triplet states where electrons are no longer antiparallel. The subscript indicates the relative energetic position compared to other states of the same multiplicity. The symbols $k_{F,}$ k_{isc}, $k_{ic,}$ k_P represent the fluorescence, intersystem crossing, internal conversion and phosphorescence rate constant respectively. Different processes in Jablonski diagram include the absorption, vibrational relaxation and internal conversion, fluorescence, intersystem crossing and phosphorescence.

1.6.1. Absorption

The first transition in the Jablonski diagram is the absorption of a photon of a particular energy by the molecule (the characterization of this process has already been provided in section 1.3). This process is indicated in the diagram by a straight arrow pointing up. The absorbance is a very fast transition which occurs on the order of 10^{-15} second.

1.6.2. Vibrational relaxation and internal conversion

Once the electron is excited, hence generating a molecule in its excited state (S_1,S_2,..,T_1,T_2,..etc), there are several pathways by which the energy may be dissipated.

First is through vibrational relaxation, a nonradiative process which is represented in the Jablonski diagram as curved arrows between vibrational levels. The vibrational relaxation is where the accumulated energy is released as kinetic energy (i.e. heat) and the molecule relaxes to a lower vibrational level of the same electronic state. The kinetic energy may stay within the same molecule or it could be transfered to other molecules around the excited molecule (i.e. the solvent for example). This process is very fast occuring on the order of 10^{-11}-10^{-14} second.

The internal conversion is another nonrdiative process which is observed when the excited molecule relaxes to a lower excited state of the same multiplicity (i.e. $S_2 \rightarrow S_1$; $S_1 \rightarrow S_0$). It is mechanistically identical to the vibrational relaxation except it occurs between two different electronic states. It is indicated in the Jablonski diagram as a curved line between two vibrational levels in two different electronic states. This process occurs in the time scale of 10^{-12} second.

1.6.3. Fluorescence

This is a radiative process taking place between two electronic states (excited and ground states) of the same multiplicity (e.g., $S_1 \rightarrow S_0$ and $S_2 \rightarrow S_0$). The lifetime of the fluorescence is typically on the order of (10^{-8}-10^{-9} second for $S_1 \rightarrow S_0$). It is indicated in Jablonski diagram as a straight line going down on the energy axis between two different electronic states.

Generally, the fluorescence band is a mirror image of the absorption band ($S_0 \rightarrow S_1$) (Figure 11). This is particularly true for rigid molecules (such as aromatics) as the Frank-Condon principle is applicable. The vibronic peaks are also expected to be present in both directions ($S_1 \rightarrow S_0$ and $S_0 \rightarrow S_1$) in the fluorescence band. There are some exceptions to this rule, when the molecule changes geometry very much in its excited state. The difference in the wavelength between the (0,0) absorption and emission peaks is known as the **Stokes shift**.

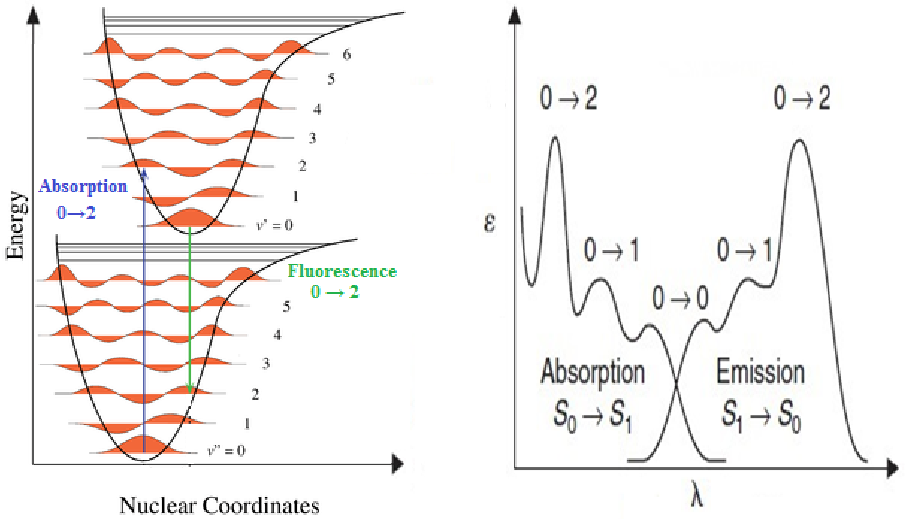

Figure 11. Potential energy curves and vibronic structures of fluorescence spectra (Modified from Ref. 23).

1.6.4. Intersystem crossing (ISC)

It is another nonradiative process which occurs when an electronically excited molecule changes spin multiplicity from an excited singlet state to an excited triplet state or the inverse. This process occurs on a time scale of (10^{-6}-10^{-8} second) for organic molecules and 10^{-11} second for organometallics. This rate enhancement is due to spin-orbit coupling that is induced by the presence of heavy atoms such as metal containing systems. This is an interaction between the spin angular momentum and the orbital angular momentum of S_n and T_n states and thus, singlet and triplet states are no longer "pure" as singlet or triplet.

The presence of a heavy atom in the system leads to decreasing the phosphorescence lifetime because of increasing the rate of the nonradiative process, decreasing the fluorescence lifetime and increasing of the phosphorescence quantum yield because the triplet state population has increased.

1.6.5. Phosphorescence

This process is a radiative process which includes relaxation of the molecule from the triplet state to the ground state. It exhibits longer lifetimes than fluorescence on time scale of 10^{-3} second for organic samples and (10^{-5}-10^{-7} second) for metal containing samples. The difference between the fluorescence and phosphorescence is due to the fact that it involves a spin-forbidden electronic transitions.

The phosphorescence bands are always more red shifted than those for fluorescence due to the relative stability of the triplet state compared to the singlet state (Figure 12).

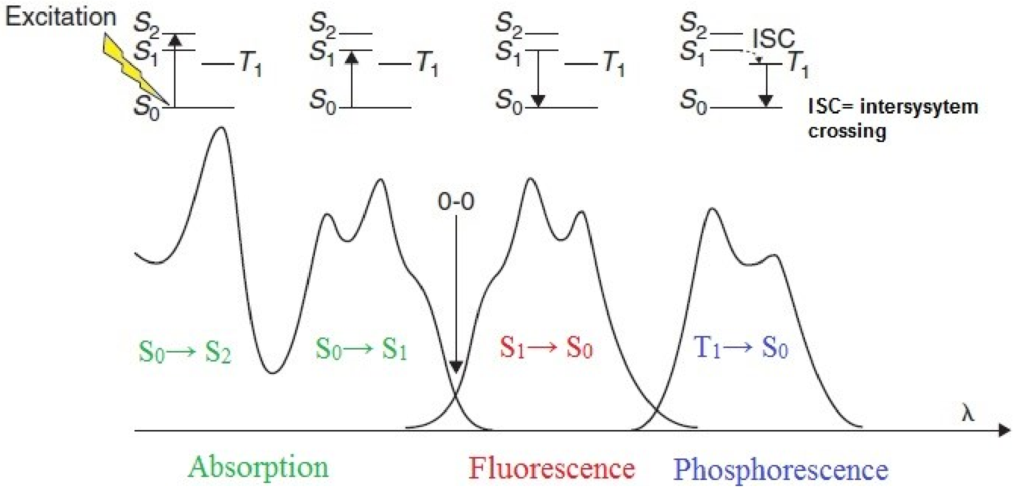

Figure 12. Relative positions of absorption, fluorescence and phosphorescence (Modified from Ref. 23).

1.7. Emission lifetime

The emission lifetime is the average time that the molecules remain in its excited state before the photon is emitted. According to the viewpoint of the kinetics, the lifetime is the rate of depopulation of the excited state (singlet or triplet) states following an optical excitation from the ground state.

Luminescence generally follows first order kinetics as in Equation 1.17.

$$[S_1] = [S_1]_o\ e^{-k_F t} \qquad [1.17]$$

where $[S_1]$ is the concentration of the excited state molecules at time t, $[S_1]_o$ is the initial concentration and k_F is the decay rate.

The various radiative and nonradiative processes can decrease the excited state population, and so the overall decay rate is given as the sum of the radiative and nonradiative decay rates (Equation 1.18).

$$k_{total} = k_{radiative} + k_{nonradiative} \qquad [1.18]$$

Again when a molecule, *A*, is excited, it is promoted from the ground state to the excited state (Equation 1.19).

$$A + h\upsilon \rightarrow A^{*} \quad [1.19]$$

The excited molecule can relax to its ground state after losing its extra energy via radiative (Equation 1.20) and non-radiative processes (Equation 1.21).

$$A^{*} \rightarrow A + h\upsilon \text{ (radiative process, } k_r) \quad [1.20]$$

$$A^{*} \rightarrow A \text{ +heat (nonradiative process, } k_{nr}) \quad [1.21]$$

where k_r and k_{non} are the rate constants for the radiative and the nonradiative processes.

$$-\frac{d[A^*]}{dt} = (k_r + k_{nr})\,[A^*] = \frac{1}{\tau}[A^*] \quad [1.22]$$

where $[A^*]$ is the concentration of the species *A* in its excited state at a given time t.

$$\ln\frac{[A^*]_t}{[A^*]_{t=0}} = -\,(k_r + k_{nr})\,t = -\,\frac{t}{\tau} \quad [1.23]$$

Hence the mean emission lifetime (τ) of $[A^*]$ is given by

$$\tau = \frac{1}{(k_r + k_{nr})} \quad [1.24]$$

The emission lifetime can be measured using a time-resolved experiment at which very short pulses excitation is made and followed and measurement of the time-dependent intensity.

From a kinetic standpoint, the fluorescence and phosphorescence lifetimes τ_F and τ_P can be expressed respectively as the following (Equations 1.25,1.26).

$$\tau_F = \frac{1}{k_F + k_{IC} + k_{ISC}} \quad [1.25]$$

$$\tau_P = \frac{1}{k_P + k_{IC}} \quad [1.26]$$

Thus, the measured unimolecular radiative lifetime is the reciprocal of the sum of the unimolecular rate constants for all the deactivation processes. The general form of the equation is given by:

$$\tau = \frac{1}{\sum_i \mathrm{k}_i} \qquad [1.27]$$

where τ is the observed radiative lifetime and the rate constant k_i represents the unimolecular or pseudo-unimolecular processes that deactivate A^*.

1.8. Quantum yield (Φ)

Quantum yield represents the ratio of the number of the molecules of the reactant consumed to the number of absorbed photons consumed. It's useful as it provides information about the electronic excited state relaxation process (such as the rates of the radiative and non-radiative process) .

The emission quantum yield is defined as ratio of the number of photons emitted to the number of photons absorbed. The measurements of quantum yields were performed by preparing three different solutions of the same concentration of the sample and the standard for each photophysical datum quantum yields. The sample and standard concentrations are adjusted to obtain an absorbance of 0.05 or less. This absorbance is adjusted to be the same as much as possible for the standard and the sample. Each absorbance value is measured five times for better accuracy in the measurements of the quantum yields (Equation 1.28).

$$\Phi_u = \left[\frac{(A_s F_u n^2)}{(A_u F_s n_o^2)}\right] \Phi_s \qquad [1.28]$$

where, the subscript u refers to "unknown", and it refers to a comparative standard, Φ is the emission quantum yield, A is the absorbance at a certain excitation wavelength, *F* is the integrated emission area across the band of a spectrum plotted in a linear scale of energy (i.e. cm^{-1}), n and n_o are the refractive indices of the solvent containing the unknown and the standard , respectively. From a kinetic standpoint, the fluorescence and phosphorescence quantum yield Φ_F and Φ_P can be expressed respectively as the following (Equations 1.29, 1.30).

$$\Phi_F = \frac{k_F}{k_F + k_{iC} + k_{ISC}} \qquad [1.29]$$

$$\Phi_P = \frac{k_p}{k_P + k_{ISC}} \quad [1.30]$$

So,

$$k_F = \frac{\Phi_F}{\tau_F} \quad [1.31]$$

$$k_P = \frac{\Phi_P}{\tau_P} \quad [1.32]$$

1.9. Energy transfer

In the presence of an energy acceptor molecule of a lower energy, A, the excited donor, D^*, can be deactivated by a process called energy transfer which can be represented as in (Equations 1.33,1.34).

$$D + h\upsilon \rightarrow D^* \quad [1.33]$$

$$D^* + A \rightarrow D + A^* \quad [1.34]$$

For the energy transfer to occur, the energy level of the excited state of the donor, D^*, has to be higher than that of the acceptor, A^*,and the time scale of the energy transfer process should be faster than the lifetime of the D^*.

There are two possible types of the energy transfer:

1.9.1. Radiative energy transfer which occurs when the extra energy in $D^*$is emitted in the form of luminescence and this radiation is absorbed by the acceptor, A, as in (Equations 1.35,1.36).

$$D + h\upsilon \rightarrow D^* \quad [1.35]$$

$$A + h\upsilon \rightarrow A^* \quad [1.36]$$

This interaction operates even when the distance between the donor and the acceptor is large (100Å). However, this process is not efficient since only a very small fraction of the emitted light is absorbed by the acceptor because the emission occurs in all directions.

1.9.2. <u>Radiationless energy transfer</u> can be described according to Förster and Dexter mechanisms and both are very efficient, even occasionnally reaching close to 100% efficiency.

1.9.2.1. Förster mechanism (FRET)

Förster resonance energy transfer, FRET, involves the migration of energy by the resonant coupling of electrical dipoles from the donor molecule to the acceptor molecule. This process can occur over a long distance (30-100Å). As shown in Figure 13, the Förster mechanism involves the migration (i.e. relaxation) of an electron from the excited donor that is placed in the LUMO to the HOMO and the released energy is transferred to the acceptor via Coulombic interactions and an electron in the HOMO of the acceptor is promoted to the LUMO. This mechanism operates mostly in the singlet states of both the donor and the acceptor.

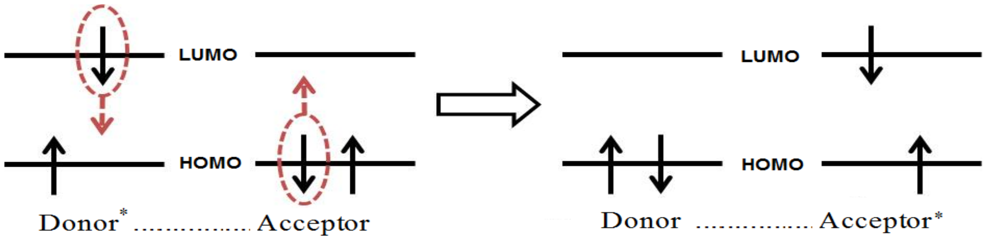

Figure 13. Mechanism of the energy transfer according to Förster.

The rate of the energy transfer (k_{ET}) can be determined as in Equation 1.37.

$$k_{ET} = k_D R_F^6 (1/R)^6 \qquad [1.37]$$

where k_D is the emission rate constant of the donor in the absence of the acceptor, R is the center-to-center inter chromophore separation and R_F is the Förster radius. The Förster radius is defined as the distance between the donor and the acceptor at which 50% of the excited state decays by energy transfer. R_F is calculated by the overlap of the emission spectrum of the donor excited state (D^*) and the absorption spectrum of the acceptor (*A*).

$$R_F^6 = \frac{9000\,\Phi_F\,(\ln 10)\kappa^2 J}{128\,\pi^5 n^4 N_A} \qquad [1.38]$$

where Φ_F is the fluorescence quantum yield of the donor in the absence of the acceptor, κ^2 is the dipole orientation factor, n is the refractive index of the medium, N_A is Avogadro's number, and *J* is the spectral overlap integral which can be calculated as in Equation 1.39.

$$J = \int f_D\,(\lambda)\varepsilon_A\,(\lambda)\lambda^4\,d\lambda \qquad [1.39]$$

where f_D is the normalized donor emission spectrum, and ε_A is the acceptor molar extinction coefficient.

Applications and limitations of FRET

FRET provides an efficient way to measure the distance between a donor and an acceptor chromophore. The energy transfer efficiency is highly influenced by the ratio of R and R_F because of the exponent 6. Thus, by measuring the FRET efficiency, one can easily get the precise distance between the donor and the acceptor. If choosing the donor and acceptor properly, this experiment can also be carried out *in vivo*. However, the FRET only gives the information about distances. If a dramatic conformational change happens, such as lengthening or kink, it is unable to know the exact movement of donor and the acceptor. Besides, attaching the chromophores to precise sites of a macromolecule is also important, both in quantity of chromophores and in position of a macromolecule, or the FRET might produce noise signals.

1.9.2.2. Dexter mechanism

This mechanism involves a double electron exchange between the donor and the acceptor (Figure 14). The Dexter mechanism involves the migration of one electron from the LUMO of the donor to the LUMO of the acceptor and at the same time, an electron from the HOMO of the acceptor moves to the HOMO of the donor. Both singlet-singlet and triplet-

triplet transfers are possible, but the mechanism requires a close contact between the MO involved, either from the resonance structures (if any) of very close proximity in order to promote orbitals overlap favouring electron transfers.

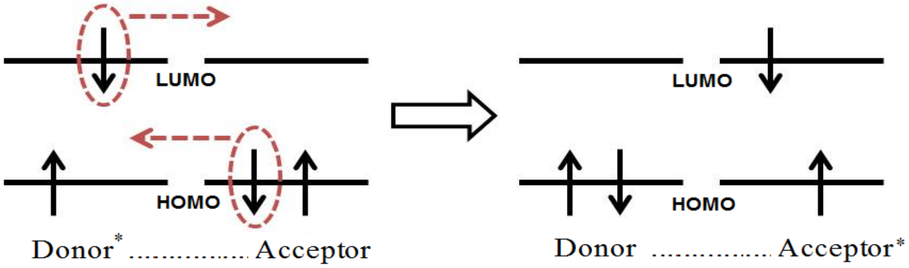

Figure 14. Mechanism of the energy transfer according to Dexter.

The rate of the energy transfer (k_{ET}) can be expressed as in Equation 1.26.

$$k_{ET} = \frac{2\pi}{h} V_0^2 J \exp\left(-\frac{2 R_{DA}}{L}\right) \qquad [1.40]$$

where R_{DA} is the distance between the donor and acceptor, J is the internal spectral overlap between the donor and acceptor, L is the effective Bohr radius of the orbitals between which the electron is transferred, h is plank's constant, V_o is the electronic coupling matrix element between the donor and the acceptor at the contact distance.

The rate of the energy transfer can be determined experimentally using Equation 1.41.

$$k_{ET} = \frac{1}{\tau_F} - \frac{1}{\tau_F^0} \qquad [1.41]$$

where τ_F is the emission lifetime of the donor in the absence of the acceptor and τ_F^0 is the emission lifetime of the donor in the presence of the acceptor.

1.10. Transient absorption spectroscopy (Flash photolysis)

The phosphorescence or emission arising from the triplet states is often difficult to be observed in fluid solution at room temperature due to the high efficiency of the nonradiative processes from long lived triplet states such as intermolecular collisional processes with the solvent .

This was an obstacle for the development of triplet-state theory untill 1949 when two scientists, Porter and Norris, introduced the flash photolysis technique.[24] This technique allows the observation of the triplet states in fluid solution by direct measurement of their absorption spectra . The long-lived nature of the triplet-states allow the build up of the concentration of species residing in the T_1 state and the fact that $T_1 \rightarrow T_n$ is a spin allowed transition making these transitions as intense as the $S_0 \rightarrow S_n$. The basic principle of this concept is shown in Figure 15.

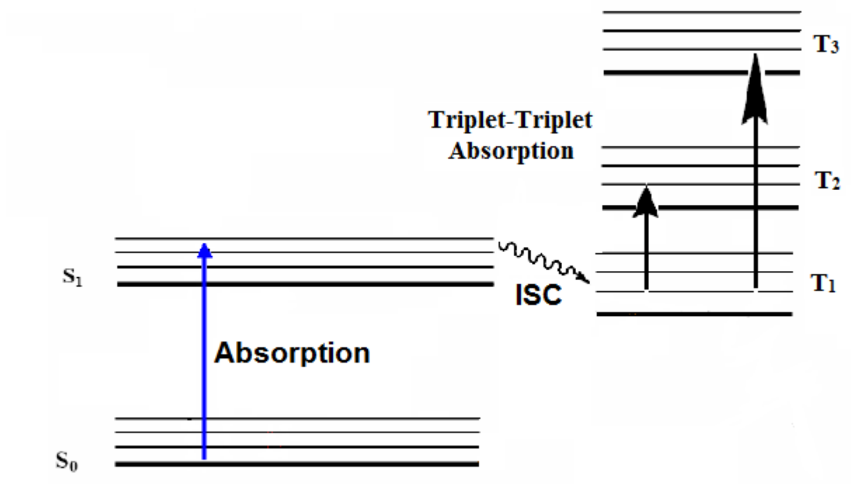

Figure 15. State diagram showing the pathway leading to T_1-T_n absorption.

The basic principles of this technique involve the excitation of the molecule by the application of an intense flash (pump) which creates a high concentration of the singlet excited molecules, first in the S_1 state. Then two scenarios can occur depending on the width of the laser pulse (pump). If the laser pulse is very narrow (i.e. fs or ps) and that a second excitation (probe) is performed almost right away (delay time between the first and second pulse of fs or ps), then $S_0 \rightarrow S_n$ absorption is possible. At this time scale, the concentration of species lying on the S_1 state is still large since the time scale for the usually very fast inter-system crossing process is about 10^{-11} s. However for larger excitation pulse width (ns for example), then species lying on the S_1 state have the time to relax to the T_1 state. At this point, the concentration of these species is the highest. Hence, with an appropriate delay time after the pump and probe excitation (Figure 15) observation of $T_1 \rightarrow T_n$ absorption bands is possible.

CHAPTER 2

MONITORING THE ON/OFF SWITCHING OF THE ELECTRONIC COMMUNICATION IN DIETHYNYLPLATINUM(II)-BRIDGED DYADS USING TRIPLET ENERGY TRANSFER

This chapter reports the synthesis of a dyad, **[Ir-Pt-Zn]**, which incorporates two chromophores, **[Ir]** = bis(phenylpyridinato)(bipyridine)iridium(III) and **[ZnTPP]** = (tetraphenylporphyrin)zinc(II), linked by a metallo-bridge, **[Pt]**= *trans*-C≡CPt$(PBu_3)_2$-$(C≡C)_2$. The photophysical as well as the computational analyses of this dyad revealed unexpected absence of T_1**[Ir]**→S_1/T_1**[ZnTTP]** energy transfer.

This work has been published in *Chem. comm.*, 2013, **49**, 5544-5546 by Ahmed M. Soliman, Mohammed Abdelhameed, Eli Zysman-Colman and Pierre D. Harvey.

The synthesis part has been carried out by Ahmed Soliman. The electrochemical measurements were measured by Ahmed Soliman. The rest of the work was carried out by myself. This part involves spectroscopic and photophysical measurements including the absorption and emission spectra, emission quantum yields and lifetimes as well as the DFT (density functional theory) and TDDFT (time-dependent density functional theory) computations. I did all the measurements, analyses and discussion of the photophysical parameters under the supervision of Dr. Pierre D. Harvey and Dr. Eli Zysman-Colman.

2.1. Manuscript

Monitoring The On/Off Switching Of The Electronic Communication In Diethynylplatinum(II)-Bridged Dyads Using Triplet Energy Transfer.

Ahmed M. Soliman, Mohammed Abdelhameed, Eli Zysman-Colman,* and Pierre D. Harvey*, *Chem. comm.*, 2013, **49**, 5544-5546.

Département de Chimie, Université de Sherbrooke, 2550 Boulevard de l'Université, Sherbrooke, Québec, Canada J1K 2R1, Fax: Tel: E-mail:

2.1.1. Abstract

Despite conjugation and downhill manifolds in **[Ir]-[Pt]-[ZnTPP]** (**[ZnTPP]** = (tetraphenylporphyrin)zinc(II), **[Ir]** = bis(phenylpyridinato)(bipyridine)iridium(III), [**Pt**] = *trans*-C≡CPt(PBu_3)$_2$-C≡C), essentially no T_1**[Ir]**→S_1/T_1**[ZnTTP]** energy transfer occurs.

2.1.2. Introduction

The *trans*-C≡CPt(PR_3)$_2$C≡C (R = aryl, alkyl) bridge, **[Pt]**, is a commonly used building block in conjugated materials for photonic applications such as bulk hetero-junction photocells, dye sensitized solar cells (DSSCs)[1] and organic light emitting diodes (OLEDs).[2] Additionally these materials can show non-linear optical[3] and multiple photon absorption properties[4] and electron transfer processes.[4] These properties rely on a good electronic communication across **[Pt]**. The degree of ground and excited state communication can be assessed by electrochemical and triplet state (T_1) energy transfer studies, respectively.[5] This latter process proceeds via Dexter mechanism[6] and depends on molecular orbital overlaps between the donor and the acceptor. We recently explored the excited state communication across **[Pt]** using this method for **[Pt]**-bridged polymers such as **1** (Fig. 1).[7]

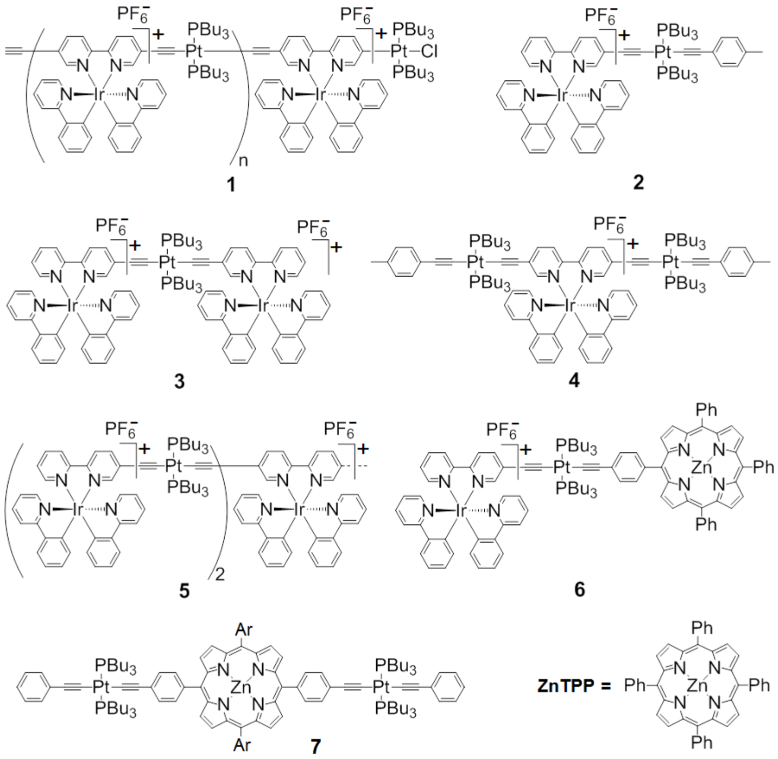

Figure 1. Structures of **1** – **6** and **ZnTPP**. (Ar = Mes)

Using model complexes **2-4** and oligomer **5**,[7,8] it was shown that these polymers act as dyads where the terminal and internal **[Ir]** units are, respectively, the T_1 energy donor and acceptor.[7,8j] This conclusion is consistent with that brought by Schanze *et al.* who showed that the T_1 excitons are rather localized in **[Pt]**-bridged polymers, implying that any energy migration is a rather local photophysical event.[9] Despite an identical **[Pt]** bridge and quasi-identical terminal chromophores, the rates for T_1 energy transfer, $k_{ET}(T_1)$, for polymer **1** (0.9×10^5 s^{-1}) and triad **5** (3.1×10^5 s^{-1}) differed by ~3 folds. The only apparent difference is the slight red shift of the 0-0 peak of the **[Ir]** donor emission for the polymer (554 (**1**) vs 550 nm (**5**)). In an attempt to rationalize this curious behavior, we now report dyad **6** where surprisingly no T_1 **[Ir]*→[ZnTPP]** energy transfer occurs despite conjugation. Knowing that $k_{ET}(T_1) = 0.5 \times 10^5$ s^{-1} for **[Pt]*→[ZnTPP]** in **7**,[10] the **[Pt]-[ZnTPP]** frame is not a structural limiting factor.

2.1.3. Results and Discussion

Synthesis: Compound **6** is prepared according to Scheme 1 (ESI), whereby **8** and **9** are coupled under Hagihara conditions to afford **10** in 48% yield. The target complex **6** is then obtained in 93% yield by reacting **10** with $[(ppy)_2IrCl]_2$ (ppyH = 2-phenylpyridine). Both **6** and **10** were characterized by ^1H, ^{13}C and ^{31}P NMR and ESI-TOF HRMS (ESI).

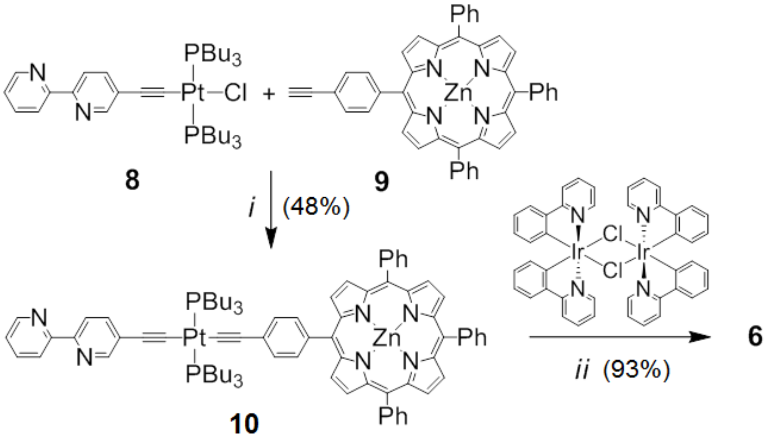

Scheme 1. Synthesis of **6** and **10**. *i)* CuI, CH_2Cl_2, *i*-Pr_2NH. *ii)* CH_2Cl_2.

The ground state electronic communication is addressed by means of electrochemistry paying attention to the redox wave splitting and large shifting in the cyclic voltamogram (CV), if any.[5] The electrochemical response for **[Ir]** is evidenced by chemically quasi-reversible reduction and oxidation processes at -1.36 and 1.31 V vs SCE, respectively, using **3** as a reference (Fig. 2). By contrast, **10** exhibits redox signals at -1.58, -1.37, 0.78 and 1.31 V (centre of waves) vs SCE and are reminiscent of **[ZnTPP]** in CH_2Cl_2 (reference Ag/AgCl).[11] The irreversible signal at -0.91V is assigned to the reduction of the bipyridine unit. Compound **6** exhibits the characteristic **[ZnTPP]** signals at 0.75 and 1.24 V but the latter signal is presumably broadened by the presence of the strongly overlapping Ir^{III}/Ir^{IV} oxidation couple. In addition, the reduction waves at -1.36 and -1.43 V also overlap, which is consistent with the superposition of the redox waves of **[Ir]** and **[ZnTPP]**. No obvious splitting or large shift of the redox waves is observed for compound **6** in comparison with those for **10** and **3**. Thus, the ground state electronic communication between **[Ir]** and **[ZnP]** is modest, which is consistent with the large dihedral angle formed by the average planes of **[ZnTPP]** and the CC_6H_4 bridge (86.7° for **7**, X-ray,[8] and 61° for **6**; DFT, B3LYP, ESI), hence preventing efficient conjugation.

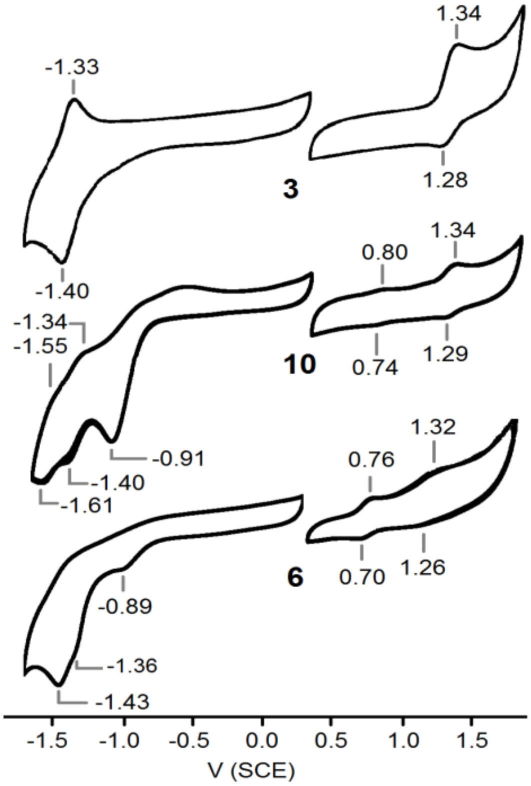

Figure 2. CV traces of **3**, **6** and **10** in degassed ACN at 298 K. Scan rate = 50 mV s^{-1}, with 0.1 M *n*-Bu_4NPF_6 as the supporting electrolyte. The peak data are placed in the ESI. Data for **3** from ref. 7a.

The energy diagram is built upon the position of the 0-0 peaks from the absorption and emission spectra of **2**, **6** and **10** (Figure 3). The 572 nm phosphorescence 0-0 peak for the known compound **2**,[8] in comparison with the 605 nm fluorescence for **10** (assigned on the basis of the ns lifetime and small Stokes shift; 220 cm^{-1}), establishes that the **[Ir]** chromophore is the T_1 energy donor to **[ZnTPP]** in both its S_1 and T_1 states. The phosphorescence peak of **[ZnTPP]** is not observed here but it is generally found above 750 nm.[12] The 572 nm emission peak for **[Ir]** appears only as a shoulder in the spectrum of **6**. This signal as such cannot address the efficiency of the energy transfer as $k_{ET}(T_1)$ cannot be reliably measured on a basis of the relative intensity. First, the emission intensity is a function of the chromophore absorptivity at a given wavelength, which is rarely accurately known in dyads. Second, the absorptivity in the region of the porphyrin Soret band is on the order of 10^5 $M^{-1}cm^{-1}$, hence dominating the spectrum.

Accurate measurements of $k_{ET}(T_1)$ are extracted from $k_{ET} = (1/\tau_e)-(1/\tau_e^o)$, where τ_e and τ_e^o are the emission lifetimes of the donor in the presence and absence of an energy acceptor.[12] This method is favored over monitoring the rise time in the transient absorption spectra because of the relative uncertainty of the exact nature of the probed excited states in the latter. Conversely, the emission is the unambiguous fingerprint of the studied species. At first glance, **2** appears to be an adequate comparison complex for τ_e^o but the absence of a second chromophore makes it not ideal because of likely unequal non-radiative rate constants of the donor. So **3** is also used for comparison and the presence of two donors secures absence of energy transfer. Hence, the combination of both **2** and **3** as comparison compounds make the analysis more reliable.

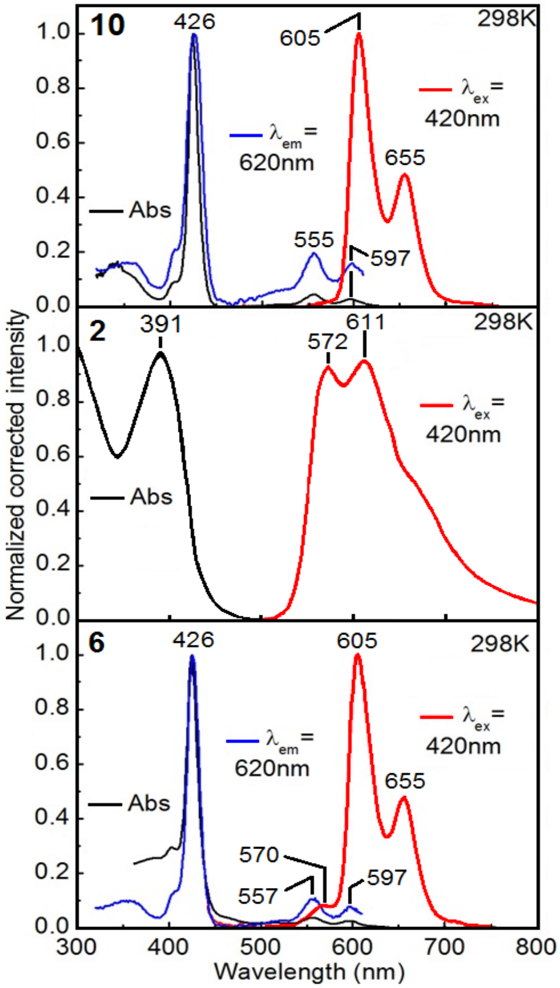

Figure 3. Absorption (black), excitation (blue) and emission (red) spectra of **2**, **6** and **10** in 2MeTHF at 298 K (see ESI for the 77K spectra).

Table 1. Emission lifetimes of **2**, **3**, **6** and **10** (2-MeTHF).[a]

Compound	**298**	**77**
2	$\boldsymbol{\tau_P}$=0.72 μs (8.5 %)[8]	$\boldsymbol{\tau_p}$=3.44 μs[8]
3	$\boldsymbol{\tau_p}$=2.90 μs (31.5 %)[8]	$\boldsymbol{\tau_p}$=11.0 μs[8]
6	$\boldsymbol{\tau_p}$=3.79 ± 0.52 μs ([b])	$\boldsymbol{\tau_p}$=10.0 ± 0.6 μs
	$\boldsymbol{\tau_F}$=0.70 ± 0.03 ns (6.3 %)	$\boldsymbol{\tau_F}$=1.23 ± 0.04 ns
10	$\boldsymbol{\tau_F}$=0.99 ± 0.02 ns (2.5 %)	$\boldsymbol{\tau_F}$=1.99 ± 0.02 ns

[a] Quantum yields values in brackets, $\boldsymbol{\tau_p}$ and $\boldsymbol{\tau_F}$ = phosphorescence and fluorescence lifetimes of the **[Ir]** and **[ZnTPP]** units, respectively. [b] Included with the total quantum yield of **6**.

The fluorescence lifetime, τ_F, in the 1 ns time scale for **6** and **10** is typical for the **[ZnTPP]** chromophore (Table 1).[12] Introducing **[Ir]** in **10**, yielding **6**, slightly decreases τ_F, due to the heavy atom effect. The **[Ir]** phosphorescence lifetimes for **6**, τ_p, are in the μs range, which is typical for this lumophore.[7] In comparison with **2** and **3**, the absence of emission quenching or decrease in τ_p of the **[Ir]** luminophore upon introducing a S_1/T_1 acceptor, i.e. **[ZnTPP]**, in **6** is totally unexpected. This result indicates absence of electronic communication in the T_1 excited state. The presence of T_1 energy transfer in **1** and **5**, and none in **6**, also illustrates the large sensitivity of the structure on $k_{ET}(T_1)$ where a subtle change leads to a completely different set of the energy transfer properties.

Triplet energy transfer generally occurs via a double electron exchange (Dexter). The rate is given by $k_{Dexter} = KJ\exp(-2r_{DA}/L)$, where $\boldsymbol{J}$ is the normalized spectral overlap integral of the absorption spectrum of the acceptor and emission spectrum of the donor, K is an experimental factor, r_{DA} is the center-to-center distance between the donor and acceptor, and L is the sum of van der Waals radii (r_{vdW}) of both chromophores (ESI). In the absence of X-ray structures, r_{DA} for **3** (model for **1** and **5**; 16.81 Å; *anti*-conformation) and **6** (21.97 Å) and r_{vdW} for **[Ir]** (13.16 Å) and **[ZnTPP]** (10.32 Å) have been evaluated from optimized geometries of **3**[9] and **6** (DFT; ESI). These structural parameters indicate that $\exp(-2r_{DA}/L)$ is 0.28 for **1** and **5** and 0.15 for **6**. Assuming that K is the same for **1**, **5** and **6**, these structural parameters alone do not account for the complete shut off of the T_1 energy transfer in **6**. In fact a lowering of 99% of τ_P was expected but not observed. Finally, the $\boldsymbol{J}$ value should be much larger for **6** in a $T_1 \rightarrow S_1$ transfer since the absorptivity values for the Q bands of the **[ZnTPP]** acceptor in **6** (typically on the order of 20 000 M^{-1} cm^{-1})[13] are much larger than those for the S_0-T_1 absorption of the **[Ir]** acceptor (< 1000 M^{-1} cm^{-1}) for **1** and **5**.

A complete shut off the T_1 process upon a small structural change in not unprecedented. Indeed, a series of three cofacial dyads, **11-13**, was reported several years ago in which a rigid spacer separates the donor from the acceptor by 3.8, 4.3 and 6.3 Å (X-ray $C_{meso}\cdots C_{meso}$ distances, Fig. 4).[13] The introduction of a Pt atom secures T_1 population of the donor, hence permitting the measurements of $k_{ET}(T_1)$. Surprisingly, a complete shut off was noted going from **12** to **13** (4.3 to 6.3 Å). Again, it is easy to demonstrate that $\exp(-2r_{DA}/L)$ cannot account for this shut off.

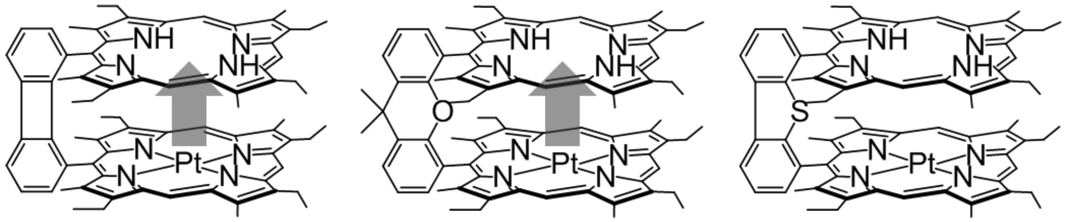

11 (3.8 Å)   **12** (4.3 Å)   **13** (6.3 Å)

$k_{ET}(T_1) = 0.84 \times 10^3\ s^{-1}$ $2.22 \times 10^3\ s^{-1}$ no transfer

Figure 4. Structures and $k_{ET}(T_1)$ for **11-13** (with d(C_{meso}-C_{meso})).[13] The arrows indicate the direction of the T_1 energy transfer.

Noteworthy, the size of $k_{ET}(T_1)$ in **1**, **5** and **6** are in complete contrast with those reported for other **[Ir]**-dyads for which the bridge is not or only poorly conjugated: **[Ir]**-bridge-**[Os]** (**[Os]** = $Os(bpy)_3^{2+}$, bridge = spirobifluorene, r_{DA} = 17.5 Å; $k_{ET}(T_1) = 4.1 \times 10^8\ s^{-1}$),[14a] **[Ir]**-bridge-**[Ru]** (**[Ru]** = $Ru(bpy)_3^{2+}$, bridge = 7,7-diphenylnorbonane, r_{DA} = 29.7 Å, $k_{ET}(T_1) = 3.2 \times 10^{10}\ s^{-1}$),[14b] and **[Ir]**-bridge-C_{60} (bridge= CH_2O-1,3,5-$C_6H_2(CH_2O(CO)$-$CMe_2R)_2$, $k_{ET}(T_1) = 8.0 \times 10^8\ s^{-1}$),[14c] but other examples exit.[14d] In the first two cases, it was proposed that the bridge is mediating the energy transfer. However, examples with very weak T_1 energy transfer using Ir(III) species also exit: $[(ppy)_2Ir(LOC(O)L)Re(CO)_3Br]^+$ (L = 6'-phenyl-2,2'-bipyridyl-4'-yl); $[(terpy)Ir(L)Ru(L)Ru(L)Ir$-$(terpy)]^{10+}$ (terpy = terpyridyl, L = 1,3-(m-C_6H_4)-5-$CH_3C_6H_3$).[15]

2.1.4. Conclusion

The monitoring of the T_1 energy transfer, which is a function of orbital overlap between the acceptor and donor, provides important information on the extent of electronic communication in the dyad excited states. However, the numerous conflicting data in the literature suggest that the Dexter formulation, $k_{Dexter} = KJ\exp(-2r_{DA}/L)$, appears as an approximation. This remark is new simply because dyads exhibiting no transfer attract little attention. Conversely, the Förster theory has long been defined as an approximation.[16] This work points the same way for Dexter.

Acknowledgments

This is work was supported by the Natural Sciences and Engineering Research Council of Canada (NSERC), the Centre Québécois des Matériaux Fonctionnels (CQMF) and the fonds québecois sur la recherch en nature et technologie (FQRNT).

References

[1] (a) F.-R. Dai, H.-M. Zhan, Q. Liu, Y.-Y. Fu, J.-H. Li, Q.-W. Wang, Z. Xie, L. Wang, F. Yan, and W.-Y. Wong, *Chem Eur. J.,* (2012), **18**, 1502-1511. (b) W. Wu, X. Xu, H. Yang, J. Hua, X. Zhang, L. Zhang, Y. Long, and H. Tian, *J. Mat. Chem.,* (2011), **21**, 10666-10671. (c) Q. Wang, Z. He, A. Wild, H. Wu, Y. Cao, U. S. Schubert, C.-H. Chui, and W.-Y. Wong, *Chem. Asian J.*, (2011), **6**, 1766-1777.

[2] (a) C.-L. Ho; C.-H. Chui, W.-Y. Wong, S. M. Aly, D. Fortin, P. D. Harvey, B. Yao, Z. Xie, and L. Wang, *Macromol. Chem. Phys.,* (2009), **210**, 1786-1798. (b) T. Goudreault, Z. He, Y. Guo, C.-L. Ho, H. Zhan, Q. Wang, K. Y.-F. Ho, K.-L. Wong, D. Fortin, B. Yao, Z. Xie, L. Wang, W.-M. Kwok, P. D. Harvey, and W.-Y. Wong, *Macromolecules,* (2010), **43**, 7936-7949.

[3] (a) C. K. M. Chan, C.-H. Tao, K.-F. Li, K. M.-C. Wong, N. Zhu, K.-W. Cheah, and V. W.-W. Yam, *Dalton Trans.,* (2011), **40**, 10670-10685. (b) C. K.-M. Chan, C.-H. Tao, K.-F. Li, K. M.-C. Wong, N.-Y. Zhu, K.-W. Cheah, and V. W.-W. Yam, *J. Organomet. Chem.,* (2011), **696**, 1163-1173.

[4] (a) M. G.Vivas, E. Piovesan, D. L. Silva, T. M. Cooper, L. De Boni, and C. R. Mendonca, *Opt. Mat. Express,* (2011), **1**, 700-710. (b) E. Glimsdal, M. Carlsson, T. Kindahl, M. Lindgren, C. Lopes, B. and Eliasson, *J. Phys. Chem. A,* (2010), **114**, 3431-3440. (c) C. Liao, A. H. Shelton, K.-Y. Kim, and K. S. Schanze, *ACS Appl. Mater. Interfaces*, (2011), **3**, 3225-3238. (d) J. E. Rogers, J. E. Slagle, D. M. Krein, A. R. Burke, B. C. Hall, A. Fratini, D. G. McLean, P. A. Fleitz, T. M. Cooper, M. Drobizhev, N. S. Makarov, A. Rebane, K.-Y. Kim, R. Farley, and K. S. Schanze, *Inorg. Chem*., (2007), **46**, 6483-6494. (e) J. M. Keller, K. D. Glusac, E. O. Danilov, S. McIlroy, P. Sreearuothai, A. R. Cook, H. Jiang, J. R. Miller, and K. S. Schanze, *J. Am. Chem. Soc.,* (2011), **133**, 11289-11298. (f) G. B. Cunningham, Y. Li, S. Liu, and K. S. Schanze, *J. Phys. Chem. B,* (2003), **107**, 12569-12572. (g) E. Göransson, J. Boixel, C. Monnereau, E. Blart, Y. Pellegrin, H.-C. Becker, L. Hammarström, and F. Odobel, *Inorg. Chem*., (2010), **49**, 9823-9832.

[5] (a) P. J. Ball, T. R. Shtoyko, J. A. Krause Bauer and W. B. Connick, *Inorg. Chem.,* (2004), **43**, 622-632. (b) J. H. K. Yip, J. Wu, K.-Y. Wong, K. P. Ho, C. S.-N. Pun, J. J. Vittal, *Organometallics,* (2002), **21**, 5292-5300. (c) A. M. Soliman, D. Fortin, P. D. Harvey and E. Zysman-Colman, *Dalton.,* (2012), 9382-9393. (d) S. Clément, T. Goudreault, D. Bellows, D. Fortin, L. Guyard, M. Knorr and P. D. Harvey, *Chem. Comm.*, (2012), **48**, 8640-8642.

[6] D. L. Dexter, *J. Chem. Phys.,* (1953), **21**, 836-850.

[7] (a) A. M. Soliman, D. Fortin, E. Zysman-Colman, and P. D. Harvey, *Chem. Comm.*, (2012), **48**, 6271-6273. (b) A. M. Soliman, D. Fortin, E. Zysman-Colman, and P. D. Harvey, *Macromol. Rapid Comm.,* (2012), **33**, 522-527.

[8] A. M. Soliman, D. Fortin, P. D. Harvey, and E. Zysman-Colman, *Chem.Comm.,* (2012), **48**, 1120-1122.

[9] K. Glusac, M. E. Koese, H. Jiang, and K. S Schanze, *J. Phys. Chem. B*, (2007), **111**, 929-940.

[10] L. Liu, D. Fortin, and P. D. Harvey, *Inorg. Chem.*, (2009), **48**, 5891-5900.

[11] C.-Y. Huang and Y. O. Su., *Dalton Trans.*, (2010), **39**, 8306-8312.

[12] P. D. Harvey. In *The Porphyrin Handbook*; Kadish, K. M., Smith, K. M., Guilard, R., Eds.; Academic Press, San Diego, (2003), **18**, Chapter 113.

[13] S. Faure, C. Stern, E. Espinosa, R. Guilard, and P. D. Harvey, *Chem. Eur. J.*, (2005)**,** **11**, 3469-3481.

[14] (a) B. Ventura, A. Barbieri, A. Degli Esposti, J. B. Seneclauze, and R. Ziessel, *Inorg. Chem.,* (2012), **51**, 2832. (b) J. Osio Barcina, N. Herrero-Garcia, F. Cucinotta, L. De Cola, P. Contreras-Carballada, R. M. Williams, and A. Guerrero-Martinez, *Chem. Eur. J.,* (2010), **16**, 6033-6040. (c) F. Nastasi, F. Puntoriero, S. Campagna, S. Schergna, S. M. Maggini, F. Cardinali, B. Delavaux-Nicot, J.-F. Nierengarten, *Chem. Commun.,* (2007), 3556-3558. (d) V. L. Whittle and J. A. G. Williams., *Dalton Trans.*, (2009), 3929-3940.

[15] (a) F. Neve, A. Crispini, S. Serroni, F. Loiseau, and S. Campagna. *Inorg. Chem.*, (2001), **40**, 1093-1101 (b) M. Cavazzinia P. Pastorelli,a S. Quici, F. Loiseau and S Campagna., *ChemComm*, (2005), 5266-5268.

[16] (a) Y. R. Khan, T. E. Dykstra and G. D. Scholes*, Chem. Phys. Let.*, (2008), **461**, 305-309. (b) G. D. Scholes, *Annu. Rev. Phys. Chem.*, (2003), **54**, 57-87 (c) C. Curutchet, B. Mennucci, G. D. Scholes and D. Beljonne, *J. Phys. Chem. B,* (2008), **112***,* 3759-3766.

2.2. SUPPORTING INFORMATION

Monitoring the On/Off Switching of the Electronic Communication in Diethynylplatinum(II)-bridged Dyads Using Triplet Energy Transfer

Ahmed M. Soliman, Mohammed Abdelhameed, Eli Zysman-Colman,* and Pierre D. Harvey*

Département de chimie, Université de Sherbrooke,
2500 Boul. Université, Sherbrooke, QC, J1K 2R1

Table of Contents:

Experimental Section.

Experimental section

Synthesis: General Procedures

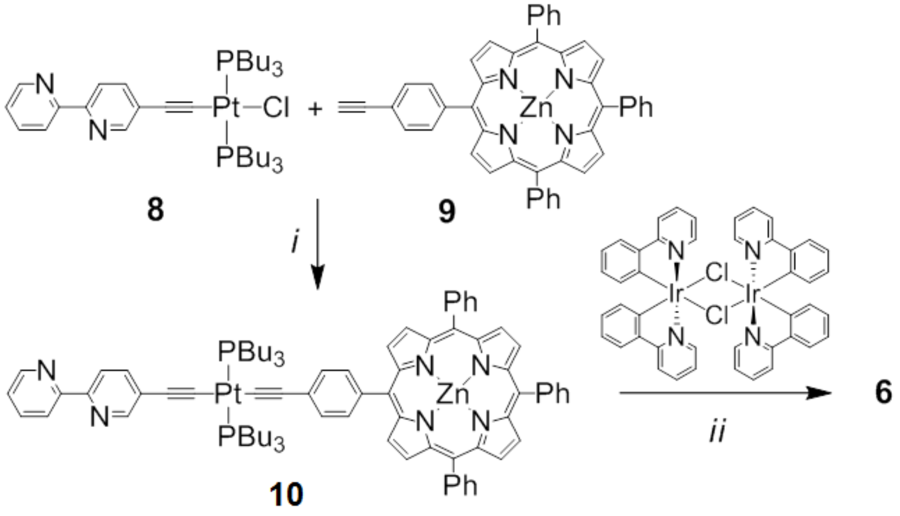

Commercial chemicals were used as supplied. All experiments were carried out with freshly distilled anhydrous solvents obtained from a Pure Solv^{TM} solvent purification system from Innovative Technologies except where specifically mentioned. *N,N,N*-Triethylamine (Et_3N), *N,N*-di*iso*propylamine (*i*-Pr_2NH) were distilled over CaH_2 under a nitrogen atmosphere. $PtCl_2(PBu_3)_2$ was obtainedfollowing standard literature protocol[1] and heated to 165 ^{o}C to obtain the *trans* form. CuI,[2] $[(ppy)_2Ir\text{-}\mu\text{-}Cl]_2$dimer,[3] *trans*-(5-ethynyl-2,2'-bipyridine)-chloro-bis(tri-*n*-butylphosphine)platinum (**8**)[4] and 5(4-ethynylphenyl)-10,15,20-trisphenylporphyrin-zinc(II)(**9**)[5] were prepared following literature procedures. All reagents wherein the synthesis is not explicitly described in the SI were purchased and used without further purification. Flash column chromatography was performed using silica gel (Silia-P from Silicycle, 60 Å, 40-63 μm). Analytical thin layer chromatography (TLC) was performed with silica plates with aluminum backings (250 μm with indicator F-254). Compounds were visualized under UV light. ^{1}H and ^{13}C NMR spectra were recorded on a BruckerAvance spectrometer at 400 MHz and 100 MHz, respectively or a BruckerAvance spectrometer at 300 MHz and 75MHz, respectively. ^{31}P NMR spectra were recorded on a BruckerAvance spectrometer at 121 MHz and 162 MHz, respectively. The following abbreviations have been used for multiplicity assignments: "s" for singlet, "d" for doublet, "t" for triplet and "m" for multiplet. Deuteratedcholorform ($CDCl_3$) and deuteratedacétonitrile (CD_3CN) were used as the solvent of record. Melting points (Mp's) were recorded using open end capillaries on a Meltemp melting point apparatus and are uncorrected. High resolution mass spectra were recorded on a Waters Synapt MS G1 (ES-Q-TOF) at the Université de Sherbrooke.

Compound 10:

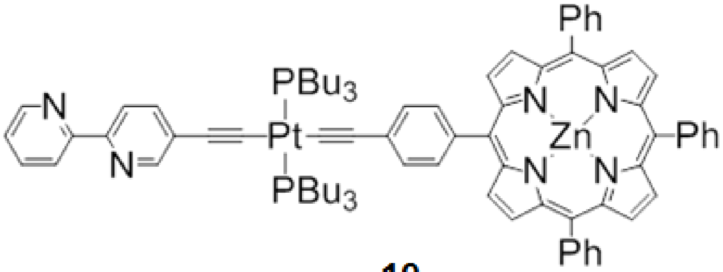

10

A dry flask charged with **8** (38 mg, 0.05 mmol, 1.1 equiv.) and CuI (2.0 mg, 0.01, 0.25 equiv.) in DCM (15 mL) and *i*-Pr_2NH (7.0 mL) was purged with N_2 for 30 min. Compound **9** (30 mg, 0.04mmol, 1.0 equiv.), dissolved in DCM (7.0 mL), was then added. The mixture was stirred at room temperature for 20 h. The solvent was removed under reduced pressure and the residue was redissolved in DCM (30 ml). The organic phase was washed with H_2O twice then dried over $MgSO_4$ and concentrated under reduced pressure. The residue was purified by flash chromatography (10% EtOAc/Hexanes on silica gel) to yield 33 mg of violet solid (**Yield**: 48%). **^{1}H NMR (400 MHz, CD_3CN) δ (ppm):** 9.02 (d, *J* = 4.5 Hz, 2H), 8.95 (d, *J* = 5.4 Hz, 4H), 8.66 (d, *J* = 4.4 Hz, 1H), 8.63 (s, 1H), 8.36 (d, *J* = 7.9 Hz, 1H), 8.26 (d, *J* = 8.3 Hz, 2H), 8.22 (d, *J* = 6.6 Hz, 5H), 8.07 (d, *J* = 7.9 Hz, 2H), 7.84 – 7.72 (m, 8H), 7.72 – 7.63 (m, 4H), 7.31 – 7.23 (m, 4H), 2.35 – 2.21 (m, 12H), 1.79 – 1.65 (m, 12H), 1.62 – 1.52 (m, 12H), 1.01 (t, *J* = 7.3 Hz, 18H). **^{13}C NMR (75 MHz, CD_3CN) δ(ppm):** 156.3, 151.5, 151.2, 150.2, 150.1, 149.1, 142.8, 139.4, 138.2, 136.8, 134.4, 134.3, 132.0, 131.9, 127.4, 126.5, 125.9, 123.1, 121.0, 121.0, 120.8, 120.2, 110.1, 109.7, 109.3, 26.45, 24.50, 24.02, 13.90. **^{31}P NMR (162 MHz, CD_3CN) δ(ppm):** δ 3.58 (d, *J* = 2345.3 Hz). **LR-MS (**ES-Q-TOF**) (*m/z*):** 1497.6 (MH^+), 751.3. **HR-MS (**ES-Q-TOF**): Calculated** ($C_{82}H_{88}N_6P_2PtZn$)**:** 1479.5587 (MH^+), **Found**: 1479.5545 (MH^+).

Compound 6:

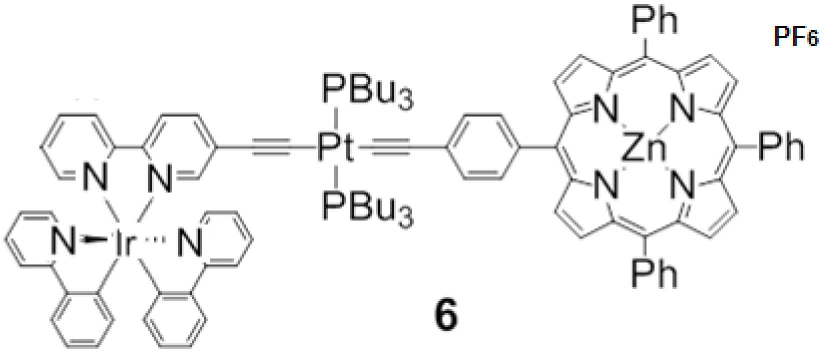

6

Iridium dimer $[(ppy)_2Ir\text{-}\mu\text{-}Cl]_2$ (7.0 mg, 0.01mmol, 0.50 equiv.) was dissolved in DCM (4.0 mL) and methanol (4.0 mL) and compound **10** (18 mg, 0.01 mmol, 1.0 equiv.) was added as a solid. The mixture was heated to 60 °C for 18 h at room temperature. The solution was cooled to RT and extracted with water (3 x 50 mL), then washed with ether (3 x 50 mL) to remove unreacted **10**. To the aqueous solution was slowly added a solution of NH_4PF_6 (10 mL, 10 % w/w in H_2O) under gentle stirring. The first drop caused the precipitation of an orange solid. The suspension was conserved at 0 °C for 2 h and then filtered and the resulting solid was washed with cold water to yield 12 mg of a violet solid (**Yield**: 93%).**^{1}H NMR (400 MHz, CD_3CN) δ (ppm):** 9.00 (d, *J* = 3.5 Hz, 2H), 8.94 (s, 4H), 8.64 (d, *J* = 8.0 Hz, 1H), 8.50 (d, *J* = 8.3 Hz, 1H), 8.22 (d, *J* = 6.6 Hz, 4H), 8.15 (t, *J* = 7.8 Hz, 2H), 8.07 (d, *J* = 7.3 Hz, 2H), 7.95 – 7.86 (m, 4H), 7.84 – 7.72 (m, 8H), 7.69 (d, *J* = 7.2 Hz, 2H), 7.62 (d, *J* = 7.4 Hz, 2H), 7.56 (dd, *J* = 8.6, 6.5 Hz, 2H), 7.35 (t, 2H), 7.26 (s, 4H), 7.12 – 6.97 (m, 4H), 6.98 (s, 1H), 6.92 (dd, *J* = 13.4, 6.7 Hz, 2H), 6.39 – 6.22 (m, 2H), 2.24 – 1.95 (m, 9H), 1.68 – 1.36 (m, 24H), 1.01 – 0.79 (m, 22H).**^{13}C NMR (75 MHz, CD_3CN) δ (ppm):** 167.9, 167.7, 156.0, 152.0, 150.8, 150.1, 149.9, 148.8, 148.5, 143.6, 143.4, 142.8, 140.2, 139.9, 139.7, 138.0, 137.9, 134.4, 134.3, 132.0, 131.7, 130.9, 130.6, 129.0, 127.5, 127.5, 126.5, 125.0, 124.7, 124.7, 124.6, 123.4, 123.1, 122.6, 122.3, 121.2, 121.1, 119.6, 119.4, 110.3, 110.0, 29.32, 26.37, 24.46, 23.91, 13.63. **^{31}P NMR(162 MHz, CD_3CN) δ (ppm):**4.46 (d, *J* = 2315.8 Hz). **LR-MS (**ES-Q-TOF) **(*m/z*):** 1979.6(M^+), 1314.4, 1001.3. **HR-MS** (ES-Q-TOF) **Calculated** ($C_{104}H_{104}IrN_8P_2PtZn$)**:** 1979.6426; **Found**: 1979.6416.Warning: During the course of this investigation, degradation of this compound was noticed yielding to modifications of the absorption and mass spectra. The latter exhibited a growing band at 620 nm upon prolonged time (months). This product could not be separated by column chromatography. All analyses were performed with freshly synthesized samples.

Photophysical characterization: All samples were prepared in 2-methyltetrahydrofuran (2-MeTHF), which was distilled over CaH_2 under nitrogen or HPLC grade acetonitrile (ACN) for the external reference. Absorption spectra were recorded at 298 K using a Shimadzu UV-1800 double beam spectrophotometer, or a HP-8453 diode array spectrophotometer or a Varian Cary 300 spectrophotometer. Molar absorptivity determination was verified by linear least squares fit of values obtained from at least three independent solutions at varying concentrations with absorbances ranging from 0.01-2.6. Steady-state emission and excitation spectra were recorded at 298 K and at 77 K in a 1.0 cm capped quartz cuvette and an NMR tube inserted into a liquid nitrogen filled quartz dewar, respectively. Emission spectra were obtained by exciting at the lowest energy absorption maxima using a Horiba JobinYvon Fluorolog-3 spectrofluorometer equipped with double monochromators and a photomultiplier tube detector (Hamamatsu model R955). Photon Technology International (PTI) and Fluorescence QuantaMaster Series QM1 spectrophotometer have been also used to confirm the emission results.Emission quantum yields were determined using the optically dilute method.[6-7] A stock solution with absorbance of ca. 0.5 was prepared and then four dilutions were prepared with dilution factors of 40, 20, 13.3 and 10 to obtain solutions with absorbances of ca. 0.013, 0.025, 0.038 and 0.05, respectively. The Beer-Lambert law was found to be linear at the concentrations of the solutions. The emission spectra were then measured after the solutions were rigorously degassed with solvent-saturated nitrogen gas (N_2) for 20 minutes prior to spectrum acquisition using septa-sealed quartz cells from Starna. For each sample, linearity between absorption and emission intensity was verified through linear regression analysis and additional measurements were acquired until the Pearson regression factor (R^2) for the linear fit of the data set surpassed 0.9. Individual relative quantum yield values were calculated for each solution and the values reported represent the slope value. The equation $\Phi_s = \Phi_r(A_r/A_s)(I_s/I_r)(n_s/n_r)^2$ was used to calculate the relative quantum yield of each of the sample, where Φ_r is the absolute quantum yield of the reference, n is the refractive index of the solvent, A is the absorbance at the excitation wavelength, and *I* is the integrated area under the corrected emission curve. The subscripts s and r refer to the sample and reference, respectively. A solution of $[Ru(bpy)_3](PF_6)_2$ in ACN (Φ_r = 0.095 %) was used as the external reference.[8] The experimental uncertainty in the emission quantum yields is conservatively estimated to be 10%, though we have found that statistically we can reproduce PLQYs to 3% relative error. The emission lifetimes were measured on a TimeMaster model TM-3/2003 apparatus from PTI. The source was a nitrogen laser with high-resolution dye laser (fwhm∼1400 ps), and the excited state lifetimes were obtained from deconvolution or distribution lifetimes analysis. Some samples were also measured using a time-correlated single photon counting (TCSPC) option of the JobinYvon Fluorolog-3 spectrofluorometer, a pulsed NanoLED at 341 nm (pulse duration < 1 ns; fwhm = 14 nm), mounted directly on the sample chamber at 90° to the emission monochromator, was used to excite the samples and emitted light was collected using a FluoroHub from Horiba JobinYvon single-photon-counting detector. . The luminescence lifetimes were obtained using the commercially available Horiba JobinYvon Decay Analysis Software version 6.4.1, software included within the spectrofluorimeter.

Computational Methodology. All density functional theory (DFT) calculations were performed with Gaussian 09[9] at the Université de Sherbrooke with the MP2 supercomputer supported by *Le Réseau Québécois De CalculsHautes Performances*. The DFT geometry optimisations as well as TD-DFT calculations[10-12] were carried out using the B3LYP method. 6-31g*[13-19] basis sets were used for the porphyrin, Acetylene group, bipyridine and phenyl pyridine. 3-21g* basis sets[20-23] were used for the Solubilizing groups (Phenyl groups of the porphyrin and(PBu_3) that are attached to the Pt. VDZ (valence double ζ) with SBKJC effective core potentials were used for Zn, Pt and Ir. The calculated absorption spectra,were obtained from GaussSum 2.1.[24-25]

Electrochemical Characterization. Cyclic voltammetry were performed on an Electrochemical Analyzer potentiostat model 600D from CH Instruments. Solutions for cyclic voltammetry were prepared in ACN and degassed with ACN-saturated nitrogen bubbling for ca. 15 min prior to scanning. Tetra(n-butyl)ammonium hexafluorophosphate ($TBAPF_6$; ca. 0.1 M in ACN) was used as the supporting electrolyte. It was recrystallized twice from EtOH and dried under vacuum prior to use. A non-aqueous Ag/Ag^+ electrode (silver wire in a solution of 0.1 M $AgNO_3$ in ACN) was used as the pseudo-reference electrode; a glassy-carbon electrode was used for the working electrode and a Pt electrode was used as the counter electrode. The redox potentials are reported relative to a saturated calomel (SCE) electrode with a ferrocenium/ferrocene (Fc^+/Fc) redox couple as an internal reference (0.40 V vs SCE).[26]

Table S1. Electrochemical data for **10** and **6**

	E_{ox}/V		E_{red}/V			E_{redox}/V
	E_{pa}^{1}/E_{pc}^{1}	E_{pa}^{2}/E_{pc}^{2}	E_{pa}^{1}/E_{pc}^{1}	E_{pa}^{2}/E_{pc}^{2}	E_{pa}^{3}/E_{pc}^{3}	
10	0.80/0.74	1.34/1.29	-/-0.91	-1.34/-1.40	-1.55/-1.61	1.71
6	0.76/0.70	1.32/1.26	-/-0.89	-/-1.36	-/-1.43	1.65

[a] Conditions: CVs recorded in N_2-saturated ACN at 298 K at a 200 mV/s scan rate with 0.1 M $(nBu_4N)PF_6$ as the supporting electrolyte. A non-aqueous Ag/Ag^+ electrode (silver wire in a solution of 0.1 M $AgNO_3$ in ACN) was used as the pseudoreference electrode; a glassy-carbon electrode was used for the working electrode, and a Pt electrode was used as the counter electrode. Waves are referenced vs Fc/Fc^+ as an internal standard and reported in V vs SCE (Fc/Fc^+ vs SCE = 0.40V);[26b] Epa and Epc stand for anodic and cathodic peak potentials, respectively , with all waves found to be irreversible; [c] Δ Eredox = $Epa^{1,ox}$-$Epc^{1,red}$.

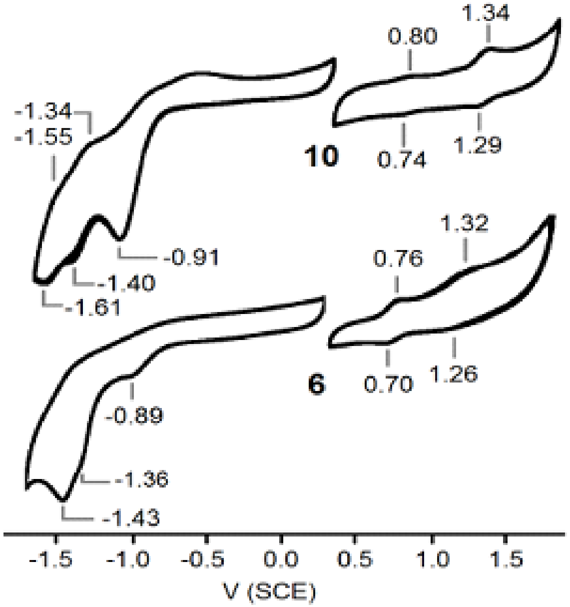

Figure S1. CV traces of **10** and **6** in degassed ACN at 298 K. Scan rate = 200 mV s^{-1}, with 0.1 M n-Bu_4NPF_6 as the supporting electrolyte.

Note on the Dexter mechanism. The Dexter energy transfer (introduced by David L Dexter) is sometimes called short-range energy transfer. It is a process that the donor and the acceptor exchange their electron. Hence, besides the overlap of emission spectra of donor and absorption spectra of acceptor, the exchange energy transfer needs the overlap of wavefunctions,meaning it needs the overlap of the electron cloud. The overlap of wavefunctions also implies that the excited donor and ground-state acceptor should be close enough so the exchange could occur. The rate constant of exchange energy transfer is given by $k_{Dexter} = K\boldsymbol{J}\exp(-2r_{DA}/L)$ where K is an experimental factor, r_{DA} is the center-to-center distance between the donor and acceptor, and L is the sum of van der Waals radius (r_{vdW}) of both chromophoresand, $\boldsymbol{J}$ is the spectral overlap integral calculated as:

$$J = \int f_{\mathrm{D}}(\lambda)\, \epsilon_{\mathrm{A}}(\lambda)\, \lambda^4\, d\lambda$$

where f_{D} is the normalized donor emission spectrum, and ϵ_{A} is the acceptor molar extinction coefficient.

For **1**, **5** and **6**, the structural parameters have been extracted from the optimized geometry of **3** (model complex) and **6** (DFT; B3LYP) below.

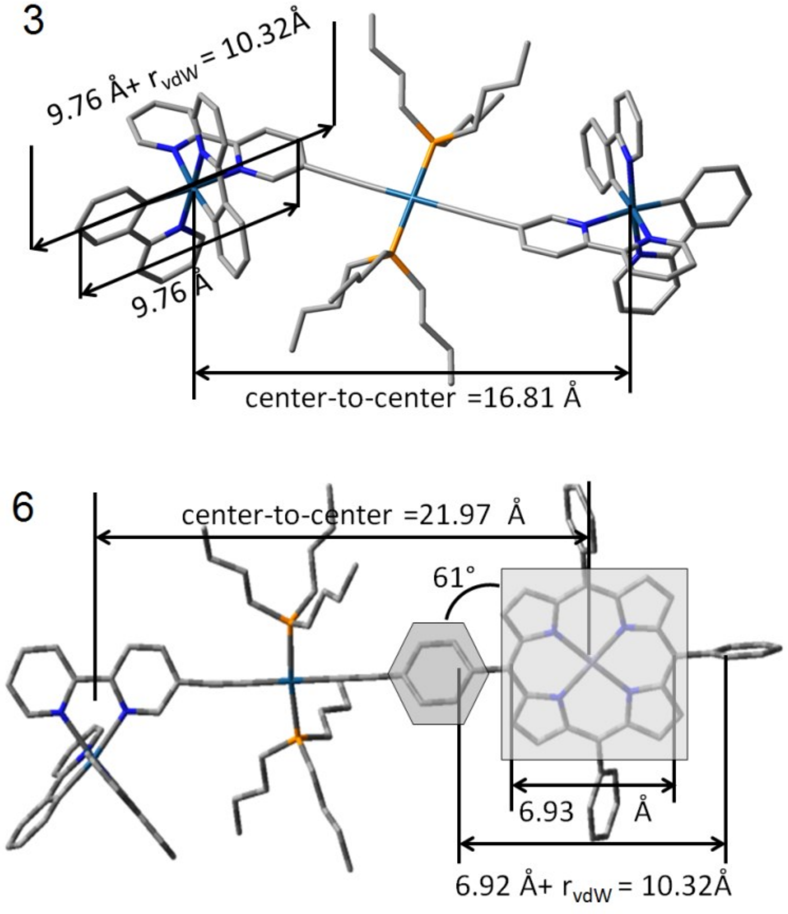

Figure S2. Optimized geometry of **3** and **6** (DFT; B3LYP) stressing on the r_{DA} and r_{vdW} data.

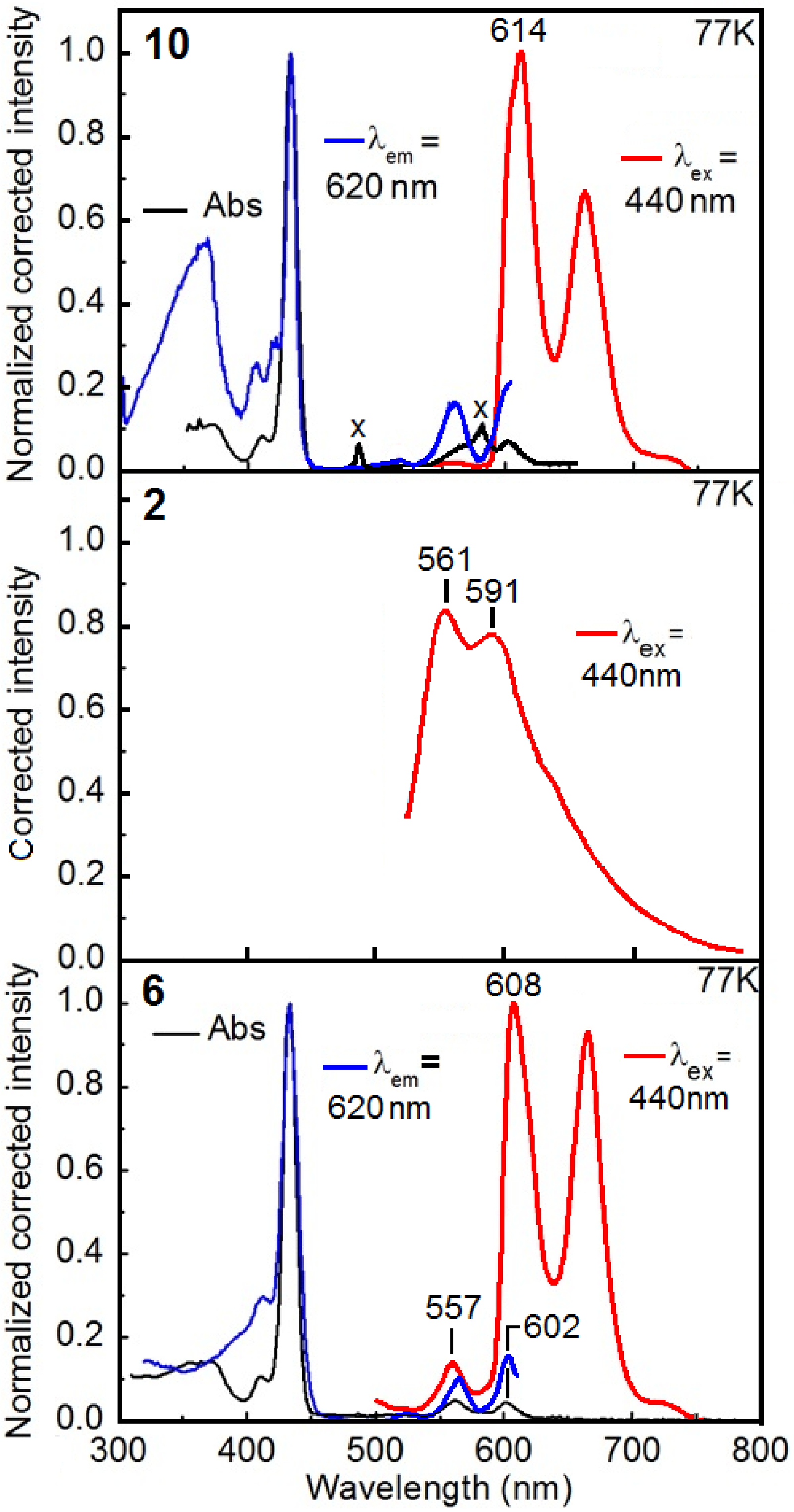

Figure S3. Absorption (black), emission (red) and excitation (blue) spectra of **10, 2** (from ref. 4) and **6** in 2MeTHF at 77 K. The signals marked with an X are instrumental artifacts.

Compound 10

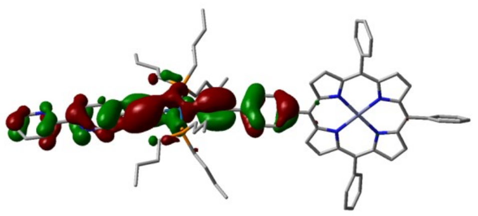

HOMO -4 (- 0.219)

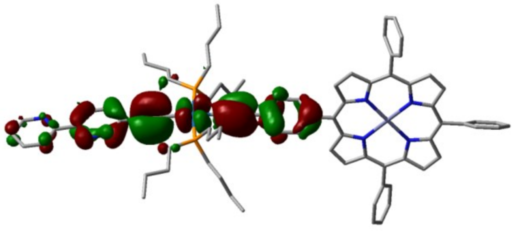

HOMO -3 (- 0.214)

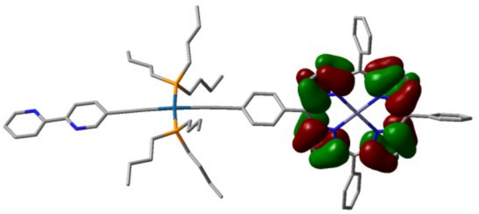

HOMO -2 (- 0.196)

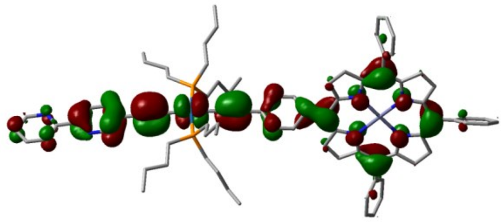

HOMO -1 (- 0.193)

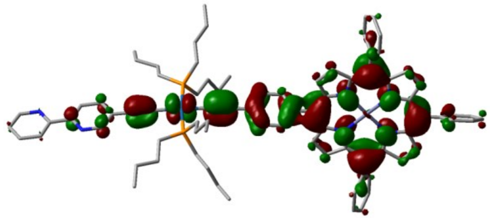

HOMO (- 0.185)

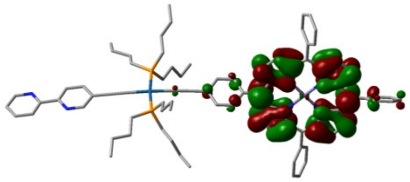

LUMO (- 0.085)

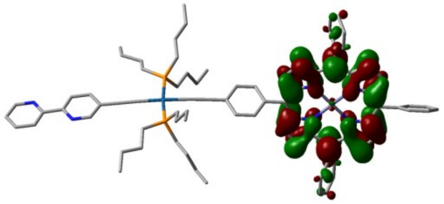

LUMO +1 (- 0.084)

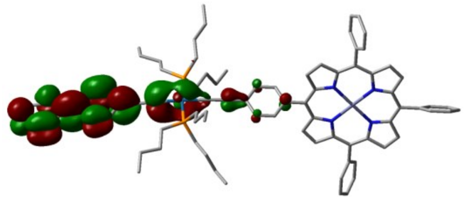

LUMO +2 (- 0.059)

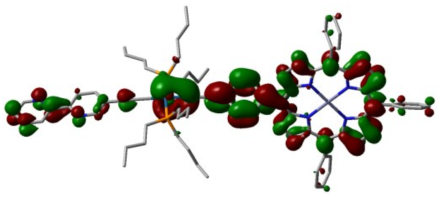

LUMO +3 (- 0.032)

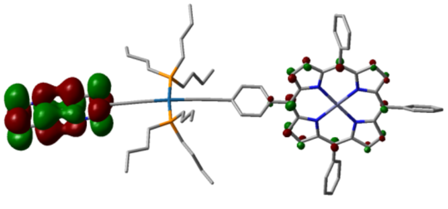

LUMO +4 (- 0.025)

Figure S4. Representations of the frontier MOs for compound **10** (the energy is in a.u.).

Compound 6

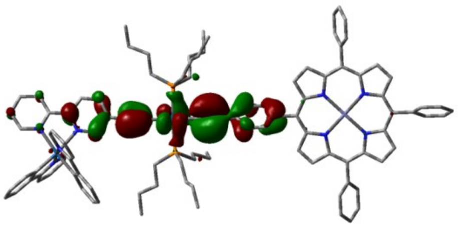

HOMO -4 (- 0.221)

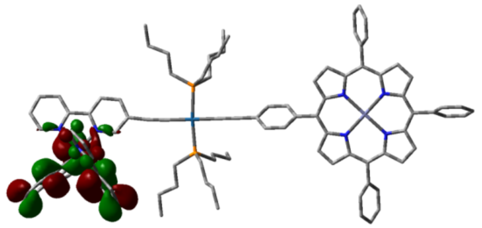

HOMO -3 (- 0.214)

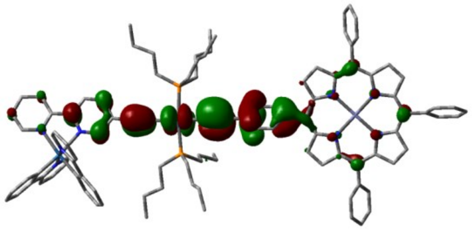

HOMO -2 (- 0.208)

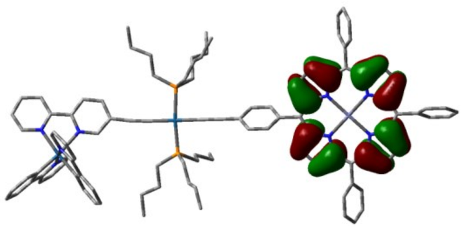

HOMO -1 (- 0.199)

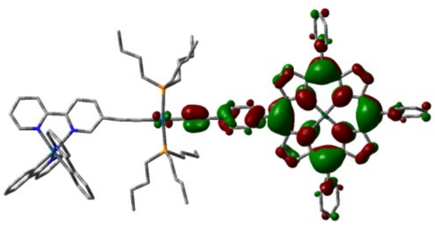

HOMO (- 0.19)

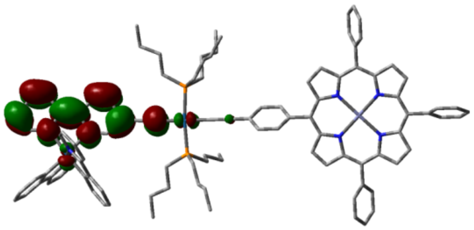

LUMO (- 0.0978)

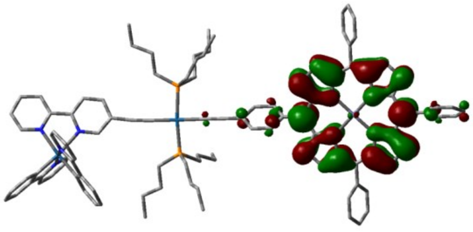

LUMO +1 (- 0.088)

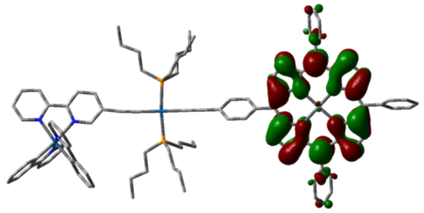

LUMO +2 (- 0.088)

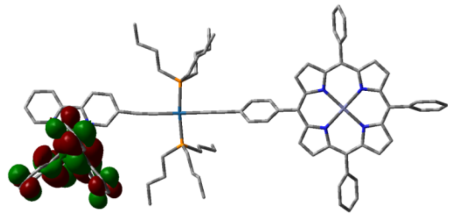

LUMO +3 (-0.072)

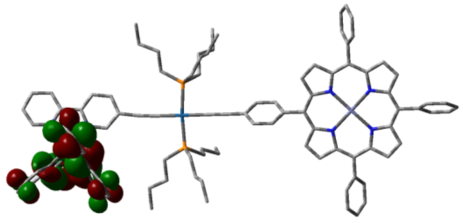

LUMO +4 (- 0.068)

Figure S5. Representations of the frontier MOs for compound **6** (the energy is in a.u.).

Table S2. Atomic Contributions to the MOs of **6** and **10**.

The table below shows the % electronic contributions over given molecular fragments from HOMO-4 to LUMO+4. The fragments listed on the left of the table. The fragment exhibiting the largest atomic contributions is highlighted.

Compound 10

	H-4	H-3	H-2	H-1	HOMO	LUMO	L+1	L+2	L+3	L+4
Zinc- Porphyrin	16.0	15.1	97.2	36.0	66.1	91.2	87.4	3.6	62.4	7.7
Acetylene groups	38.7	46.6	0.01	24.5	11.6	0.4	0.0	7.8	6.6	0.4
Pt	10.3	18.6	0.00	17.6	7.4	0.1	0.00	5.0	5.7	0.6
Bipyridine	24.7	14.7	0.0	15.7	3.8	0.1	0.00	78.4	10.3	89.0
Solubilizing groups	10.3	5.0	2.8	6.3	11.1	8.2	12.58	5.3	15.1	2.3

Compound 6

	H-4	H-3	H-2	H-1	HOMO	LUMO	L+1	L+2	L+3	L+4
Zinc Porphyrin	17.4	0.0	30.1	97.2	81.0	0.6	91.0	87.5	0.0	0.0
Acetylene groups	43.8	0.5	35.7	0.0	2.8	5.1	0.4	0.0	0.0	0.1
Pt	23.1	0.2	21.3	0.0	0.9	2.0	0.1	0.0	0.0	0.0
Bipyridine	8.9	4.5	8.5	0.00	0.2	86.5	0.3	0.0	2.6	2.8
Phenylpyridine	0.3	49.5	0.1	0.0	0.0	2.5	0.0	0.0	92.9	92.3
Ir	0.4	45.2	0.2	0.0	0.0	2.1	0.0	0.0	4.2	4.6
Solubilizing groups	6.1	0.1	4.0	2.8	15.1	1.2	8.2	12.5	0.3	0.3

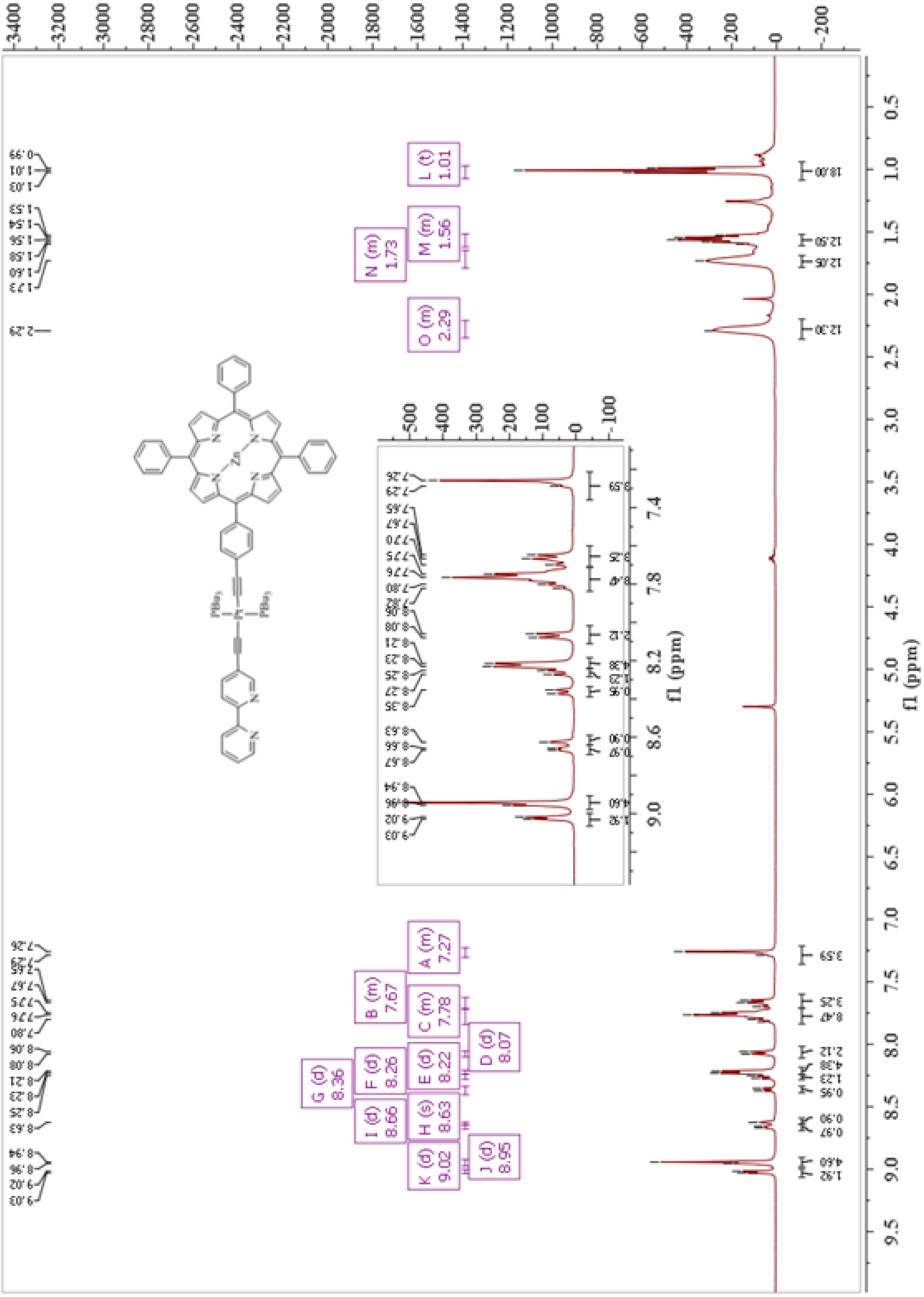

Figure S6. ^{1}H NMR spectrum for **(10).**

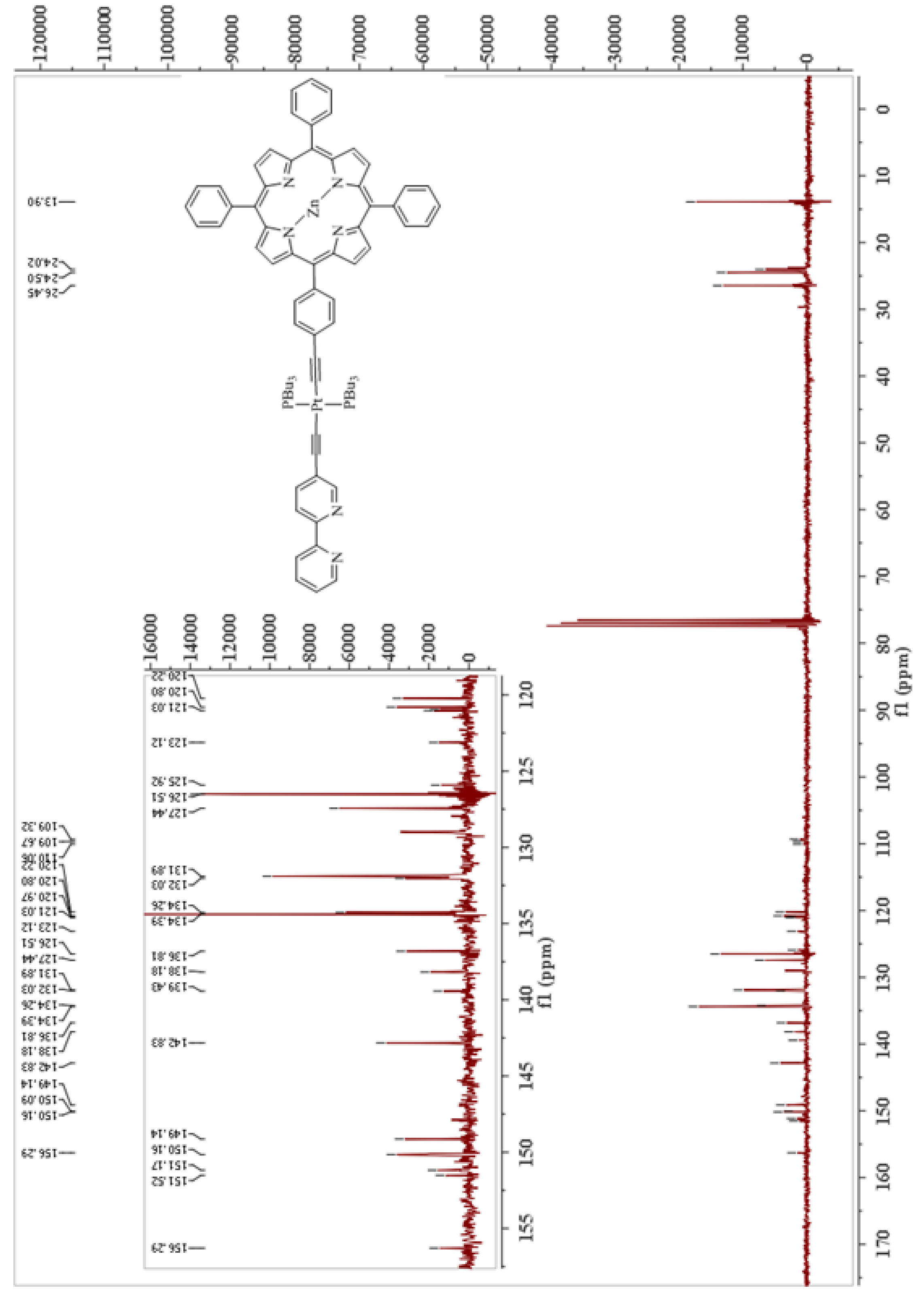

Figure S7. ^{13}C NMR spectrum for **(10).**

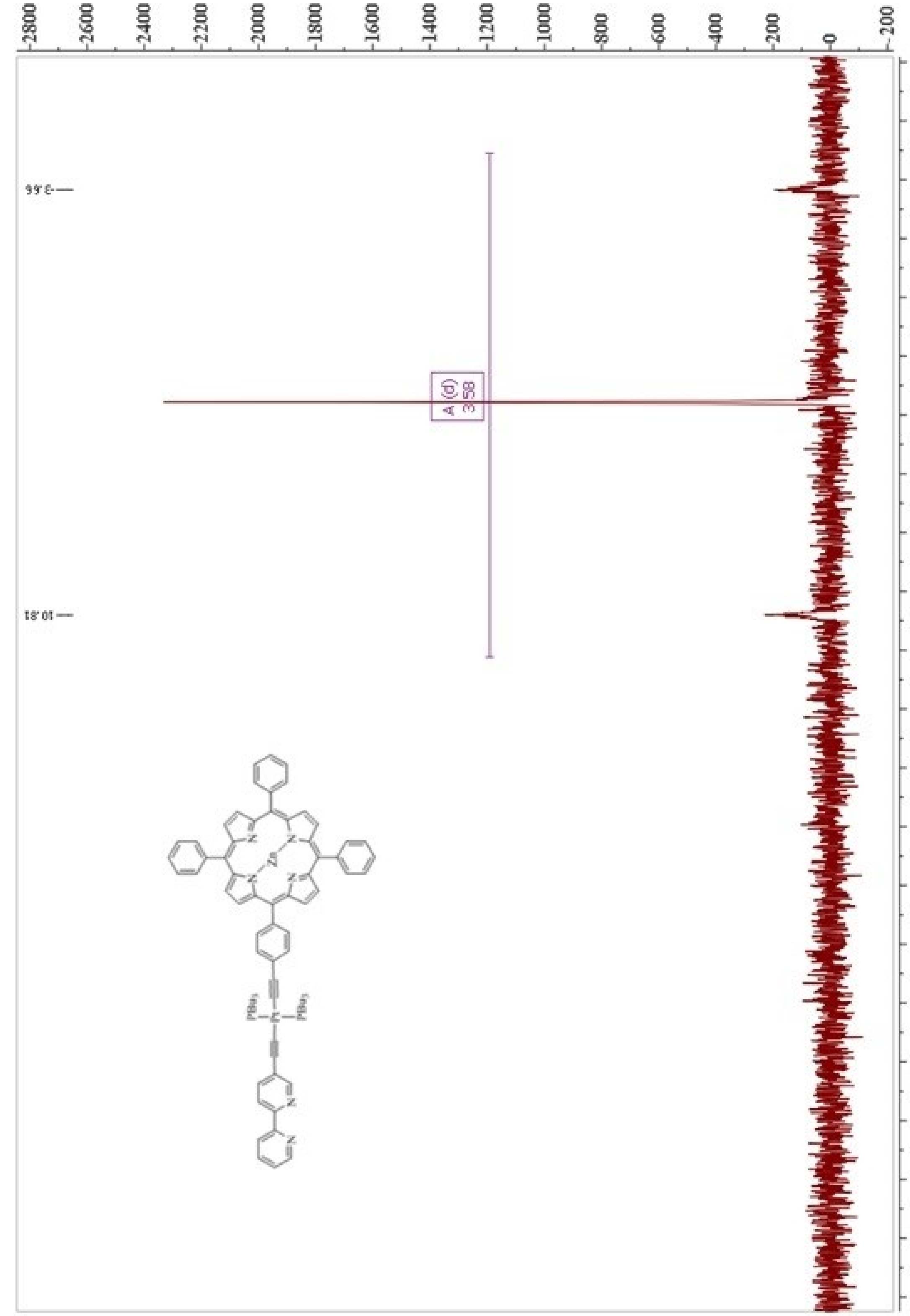

Figure S8. ^{31}P NMR spectrum for**(10).**

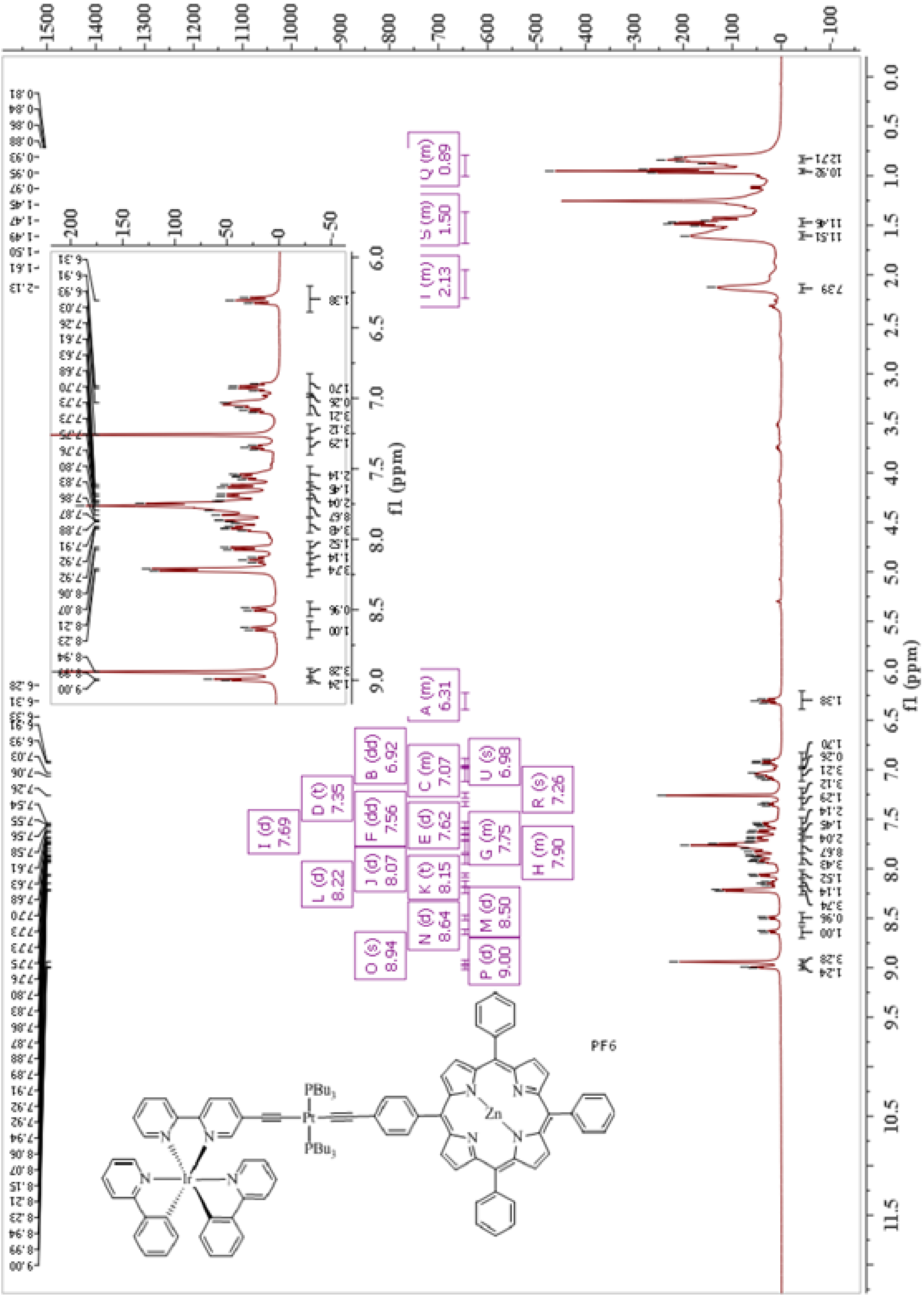

Figure S9. ^{1}H NMR spectrum for **(6).**

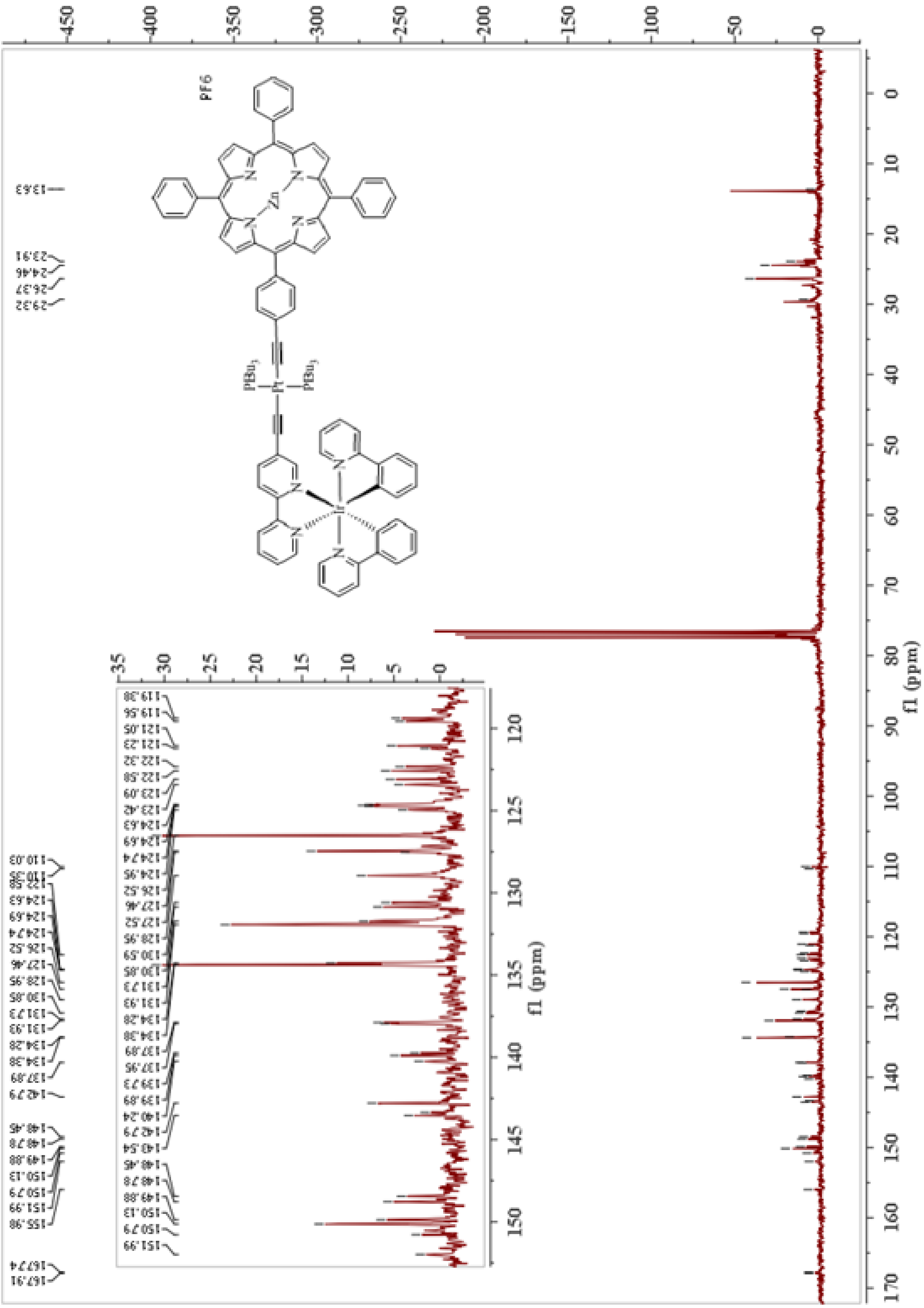

Figure S10. ^{13}C NMR spectrum for **(6).**

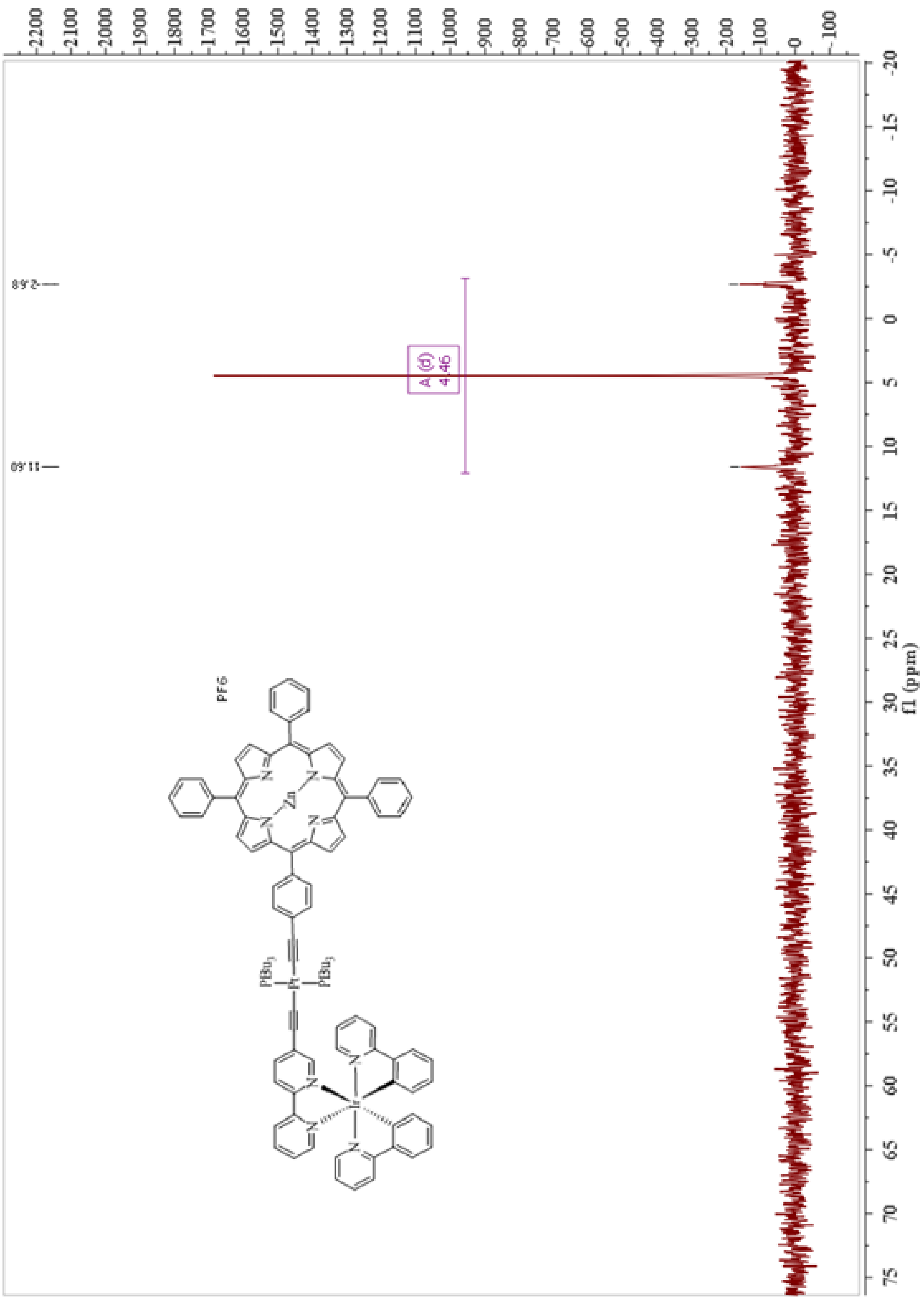

Figure S11. ^{31}P NMR spectrum for **(6).**

References

(1) G. B. Kauffman, L. A. Teter and J. E. Huheey, *Inorg. Synth.*, John Wiley & Sons, Inc., (2007), pp. 245-249.

(2) W. L. F. Armarego and D. D. Perrin, *Purification of Laboratory Chemicals, 3rd edition*, Pergamon Press, Oxford, (1988).

(3) M. Nonoyama, *Bull. Chem. Soc. Japan*, (1974), **47**, 767-768.

(4) A. M. Soliman, D. Fortin, P. D. Harvey, and E. Zysman-Colman, *Chem. Comm.*, (2012), **48**, 1120-1122.

(5) A. R. McDonald, N. Franssen, G. P. van Klink, G. van Koten, *J. Organomet. Chem.*, (2009), **694**, 2153–2162.

(6) G. A. Crosby and J. N. Demas, *J. Phys. Chem.*, (1971), **75**, 991-1024.

(7) S. Fery-Forgues and D. Lavabre, *J. Chem. Educ.*, (1999), **76**, 1260-1264.

(8) H. Ishida, S. Tobita, Y. Hasegawa, R. Katoh and K. Nozaki, *Coord. Chem. Rev.*, (2010), **254**, 2449-2458.

(9) M. J. Frisch *et al. Gaussian Inc., Wallingford CT*, (2004).

(10) P. Hohenberg and W. Kohn, *Phys. Rev.,* (1964); **136**, B864–871.

(11) P. Hohenberg and W. Kohn, *J. Phys. Rev.,* (1965), **140**, A1133–1138.

(12) R. G. Parr and W. Yang, *Density-functional theory of atoms and molecules,* Oxford Univ. Press: Oxford, (1989).

(13) D. R. Salahub and M. C. Zerner. *The Challenge of d and f Electrons, Amer. Chem. Soc. Washington, D.C.* (1989).

(14) R. Bauernschmitt and R. Ahlrichs, *Chem. Phys. Lett.*, (1996), **256**, 454–464.

(15) M. E. Casida, C. Jamorski, K. C. Casida and D. R. Salahub, *J. Chem. Phys., (*1998), **108**, 4439–4449.

(16) R. E. Stratmann, G. E. Scuseria and M. J. Frisch, *J. Chem. Phys., (*1998), **109**, 8218–8224.

(17) C. Lee, W. Yang and R. G. Parr, *Phys. Rev. B, (*1988), **37**, 785–789.

(18) B. Miehlich, A. Savin, H. Stoll and H Preuss, *Chem. Phys. Lett.,*(1989),**157**, 200–206.

(19) A. D. Becke, *J. Chem. Phys, (*1993), **98**, 5648–5652.

(20) J. S. Binkley, J. A. Pople and W. J. Hehre, *J. Am. Chem. Soc.,* (1980), **102**, 939-947.

(21) M. S. Gordon, J. S. Binkley, J. A. Pople, W. J. Pietro and W. J. Hehre, *J. Am. Chem. Soc.*, (1982), **104**, 2797-2803.

(22) W. J. Pietro, M. M. Francl, W. J. Hehre, D. J. Defrees, J. A. Pople and J. S. Binkley, *J. Am. Chem. Soc.*, (1982), **104**, 5039-5048.

(23) K. D. Dobbs and W. J. Hehre, *J. Comput. Chem.,* (1986), **7**, 359-378.

(24) K. D. Dobbs and W. J. Hehre, *J. Comput. Chem.,* (1987), **8**, 861-879.

(25) K. D. Dobbs and W. J. Hehre, *J. Comput. Chem*., (1987), **8**, 880-893.

(26) N. G. Connelly and W. E. Geiger, *Chem. Rev*., (1996), **96**, 877-910.

CHAPTER 3

UNEXPECTED DRASTIC DECREASE IN THE EXCITED STATE ELECTRONIC COMMUNICATION BETWEEN PORPHYRIN CHROMOPHORES COVALENTLY LINKED BY A PALLADIUM(II) BRIDGE.

This chapter reports the energy transfer in a bisporphyrin dyad linked by a metallo-bridge. The dyad was built on a zinc(II)porphyrin and the corresponding free base and bound together by *trans*-PdI_2 bridge. The photophysical and computational analyses of this dyad revealed unexpected slow singlet energy transfer.

This work has been accepted in *Chemistry - A European Journal.* The authors are Mohammed Abdelhameed, Paul-Ludovic Karsenti, Adam Langlois, Jean-François Lefebvre, Sébastien Richeter,* Romain Ruppert* and Pierre D. Harvey* (Manuscript number: chem.201403146 on 26 th of May 2014).

The synthesis part has been carried out at the Université de Strasbourg and Université Montpellier by Dr. Jean-François Lefebvre, Dr. Sébastien Richeter and Dr. Romain Ruppert. The second part of the work was carried out by me. This part involves spectroscopic and photophysical measurements including the absorption and emission spectra, emission quantum yields and lifetimes as well as the DFT (density functional theory) and TDDFT (time-dependent density functional theory) computations. Adam Langlois calculated the values of the J-integrals. The lifetime measurements using transient absorption spectroscopy and Streak camera were done by Paul-Ludovic Karsenti. I did the measurements, analyses and discussion of the photophysical parameters under the supervision of Dr. Pierre D. Harvey, Dr. Sébastien Richeter and Dr. Romain Ruppert. I wrote the first draft of the manuscript and Prof. Harvey, finalized the manuscript.

3.1. Manuscript

Unexpected Drastic Decrease In The Excited State Electronic Communication Between Porphyrin Chromophores Covalently Linked By A Palladium(II) Bridge.

Mohammed Abdelhameed,[a] Paul-Ludovic Karsenti,[a] Adam Langlois,[a] Jean-François Lefebvre,[b] Sébastien Richeter,*[b] Romain Ruppert*[c] and Pierre D. Harvey*[a]

[a] Département de Chimie, Université de Sherbrooke, 2550 Boulevard de l'Université, Sherbrooke, Québec, Canada J1K 2R1, Fax: Tel: E-mail:

[b] Institut Charles Gerhardt de Montpellier, UMR CNRS 5253, Université Montpellier 2, CC 1701, Place E. Bataillon, 34095 Montpellier Cedex 05 (France). E-mail:

[c] Institut de Chimie, UMR CNRS 7177, Université de Strasbourg 1 rue Blaise Pascal,
67000, Strasbourg.
E-mail:

3.1.1. Abstract

A dyad built upon a zinc(II)porphyrin and the corresponding free base, **[Zn-Fb]**, fused to N-heterocyclic carbene (NHCs) ligands, respectively acting as singlet energy donor and acceptor, and a bridging *trans*-PdI_2 unit, along with the corresponding **[Zn-Zn]** and **[Fb-Fb]** dimers were prepared and investigated by means of steady state absorption and fluorescence and time-resolved ps emission, (77 and 298 K), fs transient absorption spectroscopy (298 K), and DFT (density functional theory) and time-dependent DFT (TDDFT) computations. Despite favourable structural (π-conjugation, relatively short center-to-center distance, non-nil orientation factor of the transition moments, κ^2), and spectroscopic parameters (i.e. large J-integral), unexpectedly slow singlet energy transfer rates are measured (i.e. $k_{ET}(S_1) = (3 \text{ to } 11) \times 10^9\ s^{-1}$) in comparison with the predicted values by the Förster theory ($\sim 4 \times 10^{12} < k_{ET}(S_1) < \sim 7 \times 10^{12}\ s^{-1}$) and those observed for other structurally related dyads ($3 \times 10^{11} < k_{ET}(S_1) < 11 \times 10^{11}\ s^{-1}$). This observation is rationalized by the lack of large molecular orbitals (MOs) overlaps between the frontier MOs of the donor and acceptor thus preventing a double electron exchange through the

trans-PdI_2 bridge (*i.e.* based on a Dexter mechanism), and by an electronic shielding induced by the presence of this same linker preventing the two chromophores to fully interact via their transition dipoles (i.e. expected by the Förster mechanism).

3.1.2. Introduction

Singlet energy transfer and excitation energy migration are very important photophysical processes in plants and photosynthetic bacteria where the light energy absorbed by a chromophore (*i.e.* chlorophyll or bacteriochlorophyll antennas) is transported to the central special pair in the reaction center protein prior to the primary electron transfer.[1] These antennas and special pair are held in place in the photosynthetic membrane by a complex network of supramolecular interactions involving primarily H-bonds and coordination linkages.[1] At the laboratory scale, the construction of bio-inspired models is mostly, but not exclusively, designed upon rigid spacers covalently bonded to the chromophores thus rendering the structural parameters reliably accessible, and chlorophylls and bacteriochlorophyls are replaced by zinc(II)porphyrin most of the time.[2] Nature has excluded the use of heavy metals (including the 2nd and 3rd row transition elements) in the design of the photosynthetic machinery.[1] This observation can obviously be rationalized by the observed significant cytotoxicity of these larger atoms,[3] and the presence of the heavy atom effect, which depopulates the singlet state in favor of the triplet where the rate for energy transfer is much slower.[2] One possible question is then "Is this the only reason?" Metal-containing anchoring bridges that are often used in the construction of dyads are the square planar *trans*-Pd(II) and Pt(II) complexes flanked by coordinating ligands.[4] Indeed, literature shows a wealth of examples of dimeric or oligomeric species held together by a Pd(II)- or Pt(II)-containing organometallic and coordination residues, whether these involve the *meso*-, the β-, or both positions of the porphyrin unit.[4] Concurrently, the number of heterodyads held by either Pd or Pt bridge is very limited where a total of 4 examples exists to the best of our knowledge (Figure 1).[4f,s] Moreover, only two of them were analyzed for their energy transfer behaviour.[4s]

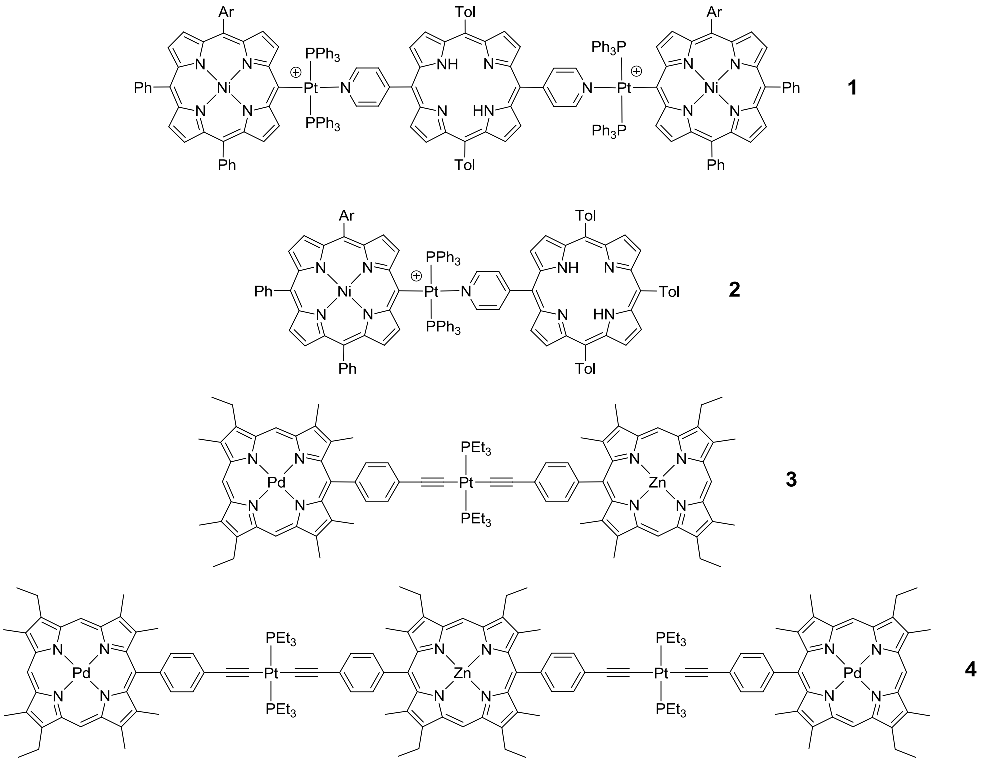

Figure 1. Structures of literature hetero-dyads and triads (Ar = 3,5-*t*Bu_2Ph).

We now report a new example of heterodyad **[Zn-Fb]** taking advantage of porphyrins fused by N-heterocyclic carbene (NHC) ligands and bridged by a *trans*-PdI_2 complex (Figure 2). This dyad has been exhaustively investigated. Despite favorable structural parameters such as the presence of π-conjugation, relatively short center-to-center distance, and non-nil orientation factor of the transition moments, and significant overlap between the donor fluorescence and acceptor absorption, unexpectedly a slow singlet energy transfer rate is observed. This observation is rationalized by the lack of large molecular orbital (MO) overlaps between the frontier MOs of the donor and acceptor units thus preventing an efficient double electron exchange through the *trans*-PdI_2 bridge and by an electronic shielding induced by the presence of this same electron rich linker preventing the two chromophores to fully interact via their transition dipoles.

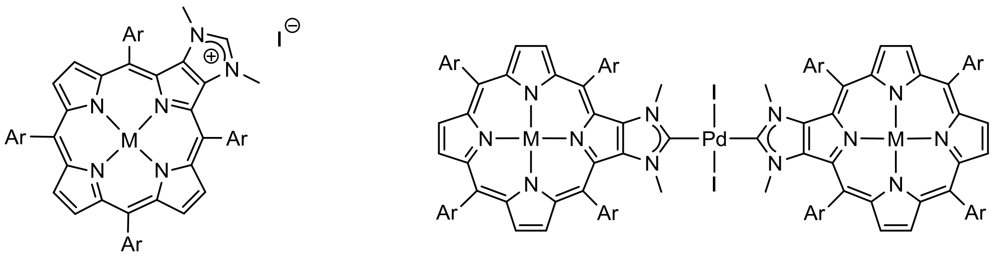

[M] M = H_2 or Zn

Ar = 4-*t*BuPh

[M-M] M = H_2 or Zn

Figure 2. Structures of imidazolium salts **[M]** and dimers **[M-M]** (Ar = 4-*t*BuPh).

3.1.3. Results and Discussion

Synthesis of homo- and heterodimers [M-M]. Imidazolium salts **[M]** (M = Zn and Fb) were obtained in good yields starting from the *meso*-tetra(4-*tert*-butylphenyl)porphyrin (Scheme 1).[5] The mononuclear *trans*-Pd(II) complex **[Fb-Fb]** was selectively obtained in 58% yield by using an excess of the imidazolium salt **[Fb]** (3.4 eq) compared to the starting material $Pd(OAc)_2$. Its parent mass ion peak could be observed by ESI-TOF mass spectrometry at *m/z* = 2175.7 (calcd for $(C_{126}H_{135}I_2N_{12}Pd)^+$ = 2175.8 [$(M + H)^+$]). No signal corresponding to the iminium proton could be detected in the ^1H NMR spectra, thus confirming the formation of the NHC−Pd bonds. ^1H NMR spectroscopy also showed the 2-fold symmetry of the **[Fb-Fb]** complex since (i) signals corresponding to β-hydrogen atoms exhibiting the expected splitting pattern, *i.e.* a pair of doublets (^3J = 4-5 Hz) and one singlet and (ii) two pair of doublets (^3J = 7-8 Hz) corresponding to *meso* aryl protons, were observed. The *trans* geometry around the palladium was confirmed by X-ray diffraction analysis for the corresponding nickel(II) complex **[Ni-Ni]**.[4m] Unfortunately, no suitable single crystals suitable for X-ray diffraction analysis were obtained for **[Fb-Fb]**. However, we observed that **[Ni-Ni]** could be also obtained by heating **[Fb-Fb]** in the presence of $Ni(acac)_2$ in toluene: this metallation reaction indirectly confirmed the *trans* geometry around the palladium of **[Fb-Fb]** (assuming that a total *trans* → *cis* isomerization process is excluded in the course of the metallation reaction). The corresponding *cis*-$[PdI_2(NHC)_2]$ complexes has not been observed in this study. The bulky *meso*-tetraarylporphryrin backbone has undoubtedly a strong influence on the coordination properties of the fused NHC ligands. The *cis*-isomers are usually obtained with small N-substituting groups such as methyl groups. However, this geometry was not observed because of the bulkyness of the *meso*-*t*-butyl aryls. Instead, the *trans* isomers were obtained with these remote bulky groups.[6] The computer modeling below corroborates this hypothesis. The complex **[Zn-Zn]** was easily obtained in 97% yield by metallating **[Fb-Fb]** with $Zn(OAc)_2•2H_2O$ (Scheme 2, top).

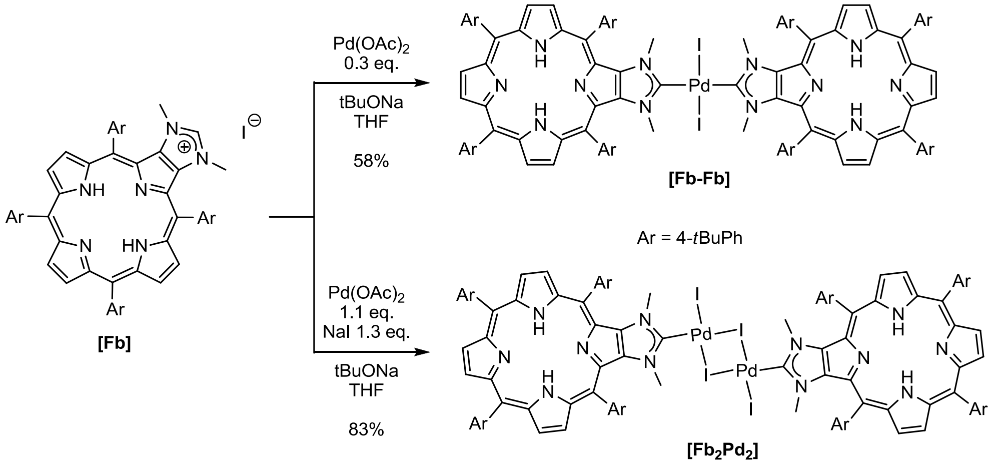

Scheme 1. Synthesis of mononuclear **[Fb-Fb]** and dinuclear **[Fb$_2$Pd$_2$]** complexes (Ar = 4-*t*BuPh).

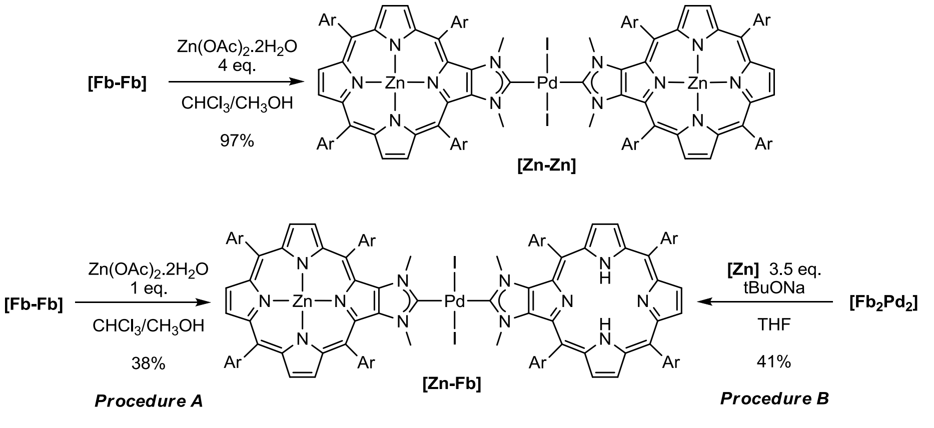

Scheme 2. Synthesis of mononuclear **[Zn-Zn]** and **[Zn-Fb]** (Ar = 4-*t*BuPh).

The synthesis of the heterodyad **[Zn-Fb]** was first performed by metallating complex **[Fb-Fb]** with one equivalent of $Zn(OAc)_2.2H_2O$ (Scheme 2, bottom, procedure A). As expected, a statistical mixture of the three complexes **[Fb-Fb]** **[Zn-Fb]** and **[Zn-Zn]** was obtained.

The desired heterodyad **[Zn-Fb]** was obtained in 38%, but its purification by column chromatography proved to be tedious. Thus, an alternative synthetic strategy taking advantage of the NHC chemistry was adopted. The dinuclear palladium(II) complex [Fb_2Pd_2] was first obtained by using the classical conditions used for the synthesis of dimeric mono−coordinated [$\{PdI(\mu\text{-}I)(NHC)\}_2$] complexes, *i.e.* addition of 1 eq of $Pd(OAc)_2$ and an excess of NaI to a solution of the imidazolium salt **[Fb]** in THF in the presence of *t*BuONa (Scheme 1).[7] Following this procedure, **[Fb_2Pd_2]** was isolated in 83% yield. This complex was characterized by combining several techniques. Mass spectrometry analysis was performed and the parent mass ion peak of **[Fb_2Pd_2]** was observed at *m/z* = 2537.5 (calcd for $(C_{126}H_{135}I_4N_{12}Pd_2)^+$ = 2537.52 [$(M + H)^+$]) in its ESI−TOF mass spectrum. The ^{1}H NMR spectrum of **[Fb_2Pd_2]** is similar to the one of the *trans*-palladium(II) complex **[Fb-Fb]**. However, one doublet due to aromatic protons of the *meso* aryl groups appeared to be broad and split at room temperature. The cross peak observed by 2D NMR spectroscopy (NOESY) between this signal and the singlet at δ = 3.40 ppm showed that this signal is due to aryl groups close to the NHC ligand (see ESI, Figure S20). Variable temperature NMR experiments confirmed the dynamic nature of this phenomenon since sharper signals were observed at 55°C, which split again when the sample was cooled down (see ESI, Figure S21). This behavior is consistent with the slower rotation of the aryl groups when the sample is cooled down. Complex **[Fb_2Pd_2]** was used as starting material for the synthesis of the desired heterodyad **[Zn-Fb]** (Scheme 2) was obtained in 41% yield by reacting **[Fb_2Pd_2]** with imidazolium salt **[Zn]** in the presence of *t*BuONa in THF. As expected, two sets of signals corresponding to the zinc and free base porphyrins were observed for **[Zn-Fb]** by ^{1}H NMR spectroscopy.

DFT computations and structures. In the absence of X-ray structures, DFT computations (B3LYP) were used to address the 3-D structure of **[Zn-Fb]**. The DFT results also allowed us to address the nature of the molecular orbitals (MOs) and excited states simultaneously (below). Interestingly, three conformers, denoted as U-shaped, S-shaped, and twisted were revealed (Figure 3). Their existence is due to obvious *t*-butyl–*t*-butyl steric interactions, and their origins most probably stem from the relative spatial approach of the porphyrin-containing fragments during the coordination reactions (Schemes 1 and 2).

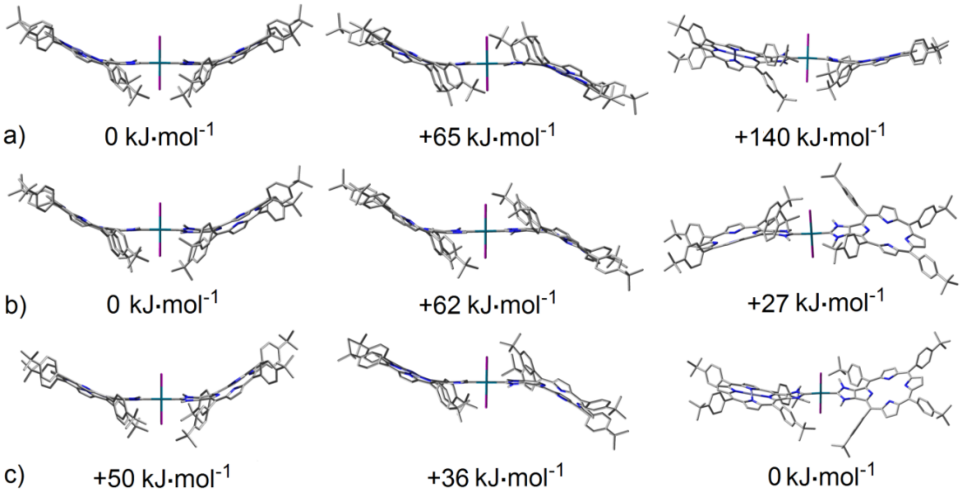

Figure 3. Optimized geometry of a) **[Zn-Zn],** b) **[Fb-Fb],** and c) **[Zn-Fb]** in the U- (left), S-shape (centre) and twisted (right) conformations. The H atoms are omitted for clarity. The lowest energy conformations are set to 0 kJ.mol^{-1}, and the others are destabilized by a given energy relative to the lowest energy conformation.

The relative population of the three conformers remains inaccessible but does not impair the data interpretation. One notes that the computed most stable forms (U- or twisted-shaped) differ from that reported a for **[Ni-Ni]** species identified by X-ray crystallography (i.e. S-shaped).[4m] Their relative energies well exceed the thermal activation energy available at room temperature (2.49 kJ.mol^{-1}) and consequently conversion from one form to other is most unlikely. One concludes that the reported X-ray structure may be the conformer that crystalizes best. Nonetheless in this work, these conformers appear locked based on DFT computations and are all taken into account in the following analysis. Moreover, these optimized geometries show that the *U*-shape would lead to highly unfavourable conformations where the *t*-butyl groups would drastically clash on each other inducing major distortions of the porphyrin macrocycles.

Absorption and fluorescence spectra. The absorption, fluorescence and excitation spectra for **[Zn-Zn]**, **[Fb-Fb]** and **[Zn-Fb]** are shown in Figure 4 (those for **[Zn]**, **[Fb]** are placed in the ESI) and the absorption data are provided in Table 1. The absorption spectra are reminiscent to what is generally encountered for these chromophores with a red shift of ~40 nm both the Soret and Q-bands with respect to zinc(II) *meso*-tetraphenylporphyrin

(ZnTPP) and free base *meso*-tetraphenylporphyrin (H_2TPP).[2] This is easily ascribed to an extension of the π-conjugation onto the imidaz-2-ylidene portion of the chromophores. Based on the maxima of the 0-0 peaks, two main features are highlighted. First, the 0-0 position of the Q-bands and fluorescences of the zinc(II)porphyrin chromophore is placed at a lower wavelength (*i.e.* higher energy) than that for the porphyrin free base indicating that these species are respectively assigned the role of the energy donor and acceptor. Second, no substantial red shift (5 nm) of the absorption and fluorescence bands is observed when going for a monomeric species (**[Zn]** and **[Fb]**) to the dimeric ones (**[Zn-Zn]** and **[Fb-Fb]**) indicating that π-conjugation is minimal across the dimers.

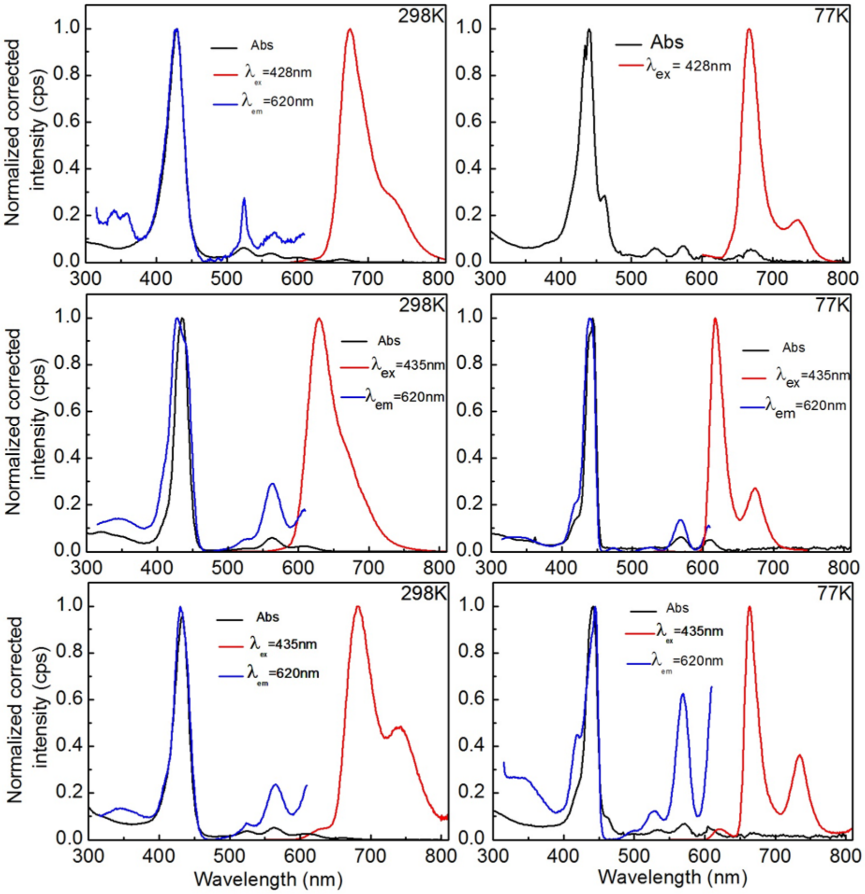

Figure 4. Absorption (black), fluorescence (red) and excitation (blue) spectra of **[Fb-Fb]** (top) **[Zn-Zn]** (centre) and **[Zn-Fb]** (bottom) in 2MeTHF at 298 (left) and 77K (right).

This experimental result indicates that the electronic communication between the two units is minimal. This latter conclusion corroborates the cyclic voltammograms as the oxidation and reduction waves are not split. Indeed, **[Zn-Zn]** is oxidized in two 2-electron steps (E_0 *vs* Fc^+/Fc = +0.32 and +0.57 V) and reduced in two two-electron steps (E_0 *vs* Fc+/Fc = –1.75 and –1.98 V) in comparison with **[Zn]**, which exhibit only 1- electron processes. The absence of splitting strongly suggests that the two porphyrins in **[Zn-Zn]** are isolated and that there is no resultant charge delocalization over the two macrocycles. The splitting of the oxidation and/or reduction waves is commonly noted for dimers with strong interactions between units.[8] Here, both porphyrins are simultaneously oxidized or reduced.

Table 1. Absorption data of **[Zn]**, **[Fb]**, **[Zn-Zn]**, **[Fb-Fb]** and **[Zn-Fb]**.

Compound	λ_{max} (nm)[a]	ε ($M^{-1}.cm^{-1}$)[a]	λ_{max} (nm)[b]
[Zn]	432	464000	439
	563	18000	570
	608	7800	615
[Fb]	428	421500	435
	528	16000	535
	568	9900	574
	595	6100	602
	657	7600	664
[Zn-Zn]	437	657500	444
	561	39800	568
	603	13420	608
[Fb-Fb]	433	562000	440
	527	34100	532
	567	21350	574
	599	12300	608
	661	7600	670
[Zn-Fb]	435	580000	442
	528	20400	532
	563	27700	572
	601	12000	604
	661	4200	664

[a] in 2MeTHF 298K. [b] in 2MeTHF 77K

The presence of fluorescence band at ~620 nm in the **[Zn-Fb]** spectra suggests a residual emission arising from the donor **[Zn]**-chromophore and consequently the singlet energy transfer is not total. The analysis of the energy transfer is presented below.

The interpretation of these spectra and lowest energy excited states has been addressed by analysing the frontier MOs and by computing spectra by time-dependent DFT (TDDFT) calculations. For sake of homogeneity and of symmetry (minimizing distortion of the MOs due to twisting and ring stress) only the S-shape form was used for the computations and analysis. Figure 5 exhibits the frontier MOs for **[Zn-Fb]** whereas those for **[Zn]**, **[Fb]**, **[Zn-Zn]**, and **[Fb-Fb]** are placed in the ESI. Three main observations are made. First, the eight lowest energy frontier MOs (i.e. HOMO-3 to LUMO+3) exhibit the expected typical π-system model for both zinc(II)-containing macrocycle and free base,[9] except that no degeneracy is noted due to the reduction of the local symmetry of the porphyrin ring (from D_{4h} or D_{2h} to C_{2v}) associated with the presence of the carbene-containing attachment. Second, atomic contributions from the carbene fragment to the π-conjugation are also computed for most of these MOs. Third, no significant atomic contributions are computed for the PdI_2 fragment in these low energy frontier MOs (Table 2). Higher contributions are calculated for the higher energy MOs such as HOMO-4 and LUMO+4, but have no contribution in the lowest energy singlet excited states (based on TDDFT computations below).

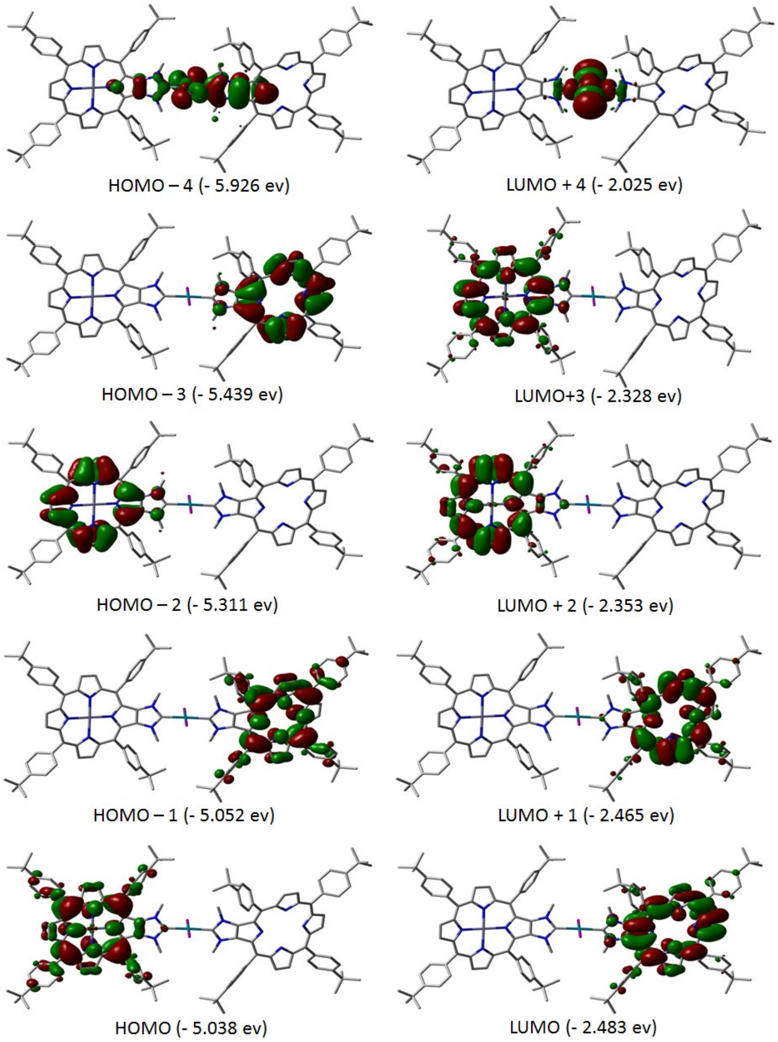

Figure 5. Representation of the frontier MOs for **[Zn-Fb]** (S-shape).

Table 2. Relative atomic contributions of the various fragments in **[Zn-Fb]**.[a][b]

	2I	Pd	[Zn]	Zn	[Fb]	*t*Bu
L+4	**39.44**	**41.16**	9.67	0.02	9.68	0.02
L+3	0.01	0.02	**99.04**	0.23	0.01	0.70
L+2	0.15	0.13	**98.85**	0.24	0.08	0.54
L+1	0.06	0.05	0.05	0.00	**99.08**	0.75
LUMO	0.01	0.02	0.01	0.00	**99.30**	0.67
HOMO	0.13	0.10	**96.95**	1.26	0.10	1.47
H–1	0.01	0.01	0.08	0.00	**98.26**	1.63
H–2	0.02	0.02	**99.88**	0.02	0.01	0.04
H–3	0.03	0.02	0.01	0.00	**99.88**	0.06
H–4	**16.23**	2.94	9.21	0.06	**71.49**	0.06

[a] L = LUMO, H = HOMO, **[Zn]** = Zn-containing porphyrin (except Zn), **[Fb]** = free base porphyrin. [b] The largest contribution (>10%) are in bold.

The nature of the lowest energy singlet excited states has been addressed by TDDFT. The computed positions, oscillator strengths, and major contributions of the first 20 electronic transitions of **[Zn-Fb]** are presented in Table 3 as an example. Tables showing all first 100 electronic transitions for **[Zn]**, **[Fb]**, **[Zn-Zn]**, **[Fb-Fb]** and **[Zn-Fb]** are placed in the ESI. The first four low-energy transitions are computed at 602, 565, 564 and 563 nm. The two lowest and highest energy ones are ππ* transitions respectively centered on the **[Fb]** and **[Zn]** chromophores as easily deduced from their relative contributions (Table 2) and from the calculated positions for **[Zn-Zn]** (565 and 565 nm) and **[Fb-Fb]** (603, 602, 566 and 566 nm; ESI). The computations corroborate the role of the energy donor and acceptor. By tracing the oscillator strength vs wavelengths, a bar graph is plotted, and by assigning 1000 cm^{-1} to each bar, a spectrum (excluding vibronic couplings) is generated (Figure 6). The resulting spectrum is unquestionably reminiscent of the experimental spectrum shown in Figure 4. Compounds **[Zn]**, **[Fb]**, **[Zn-Zn]** and **[Fb-Fb]** exhibit similar shapes also favourably comparing with the experimental spectra. The overall series of computations support the assignments, but also indicate absence of any significant atomic contributions from the Pd atom (Table 2, ≤0.1%).

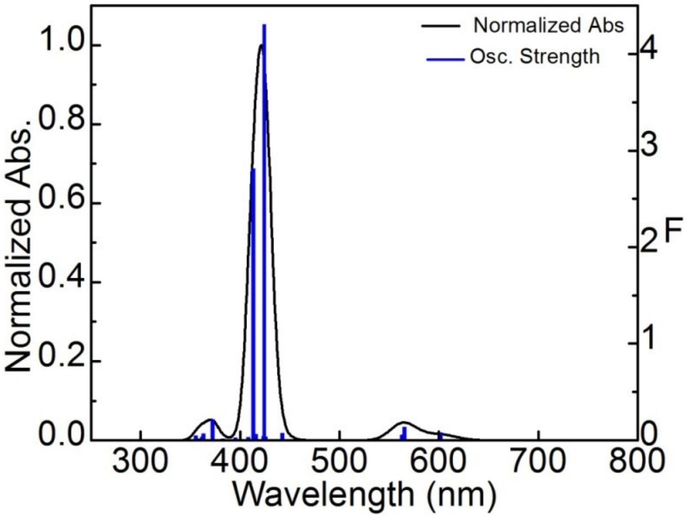

Figure 6. Bar graph showing the oscillator strength as a function of the calculated positions of the electronic transitions (blue) for **[Zn-Fb].** The black line is the generated spectrum when assigning 1000 cm^{-1} for each transition.

Fluorescence lifetimes. The fluorescence lifetimes are summarized in Table 4. The free base-containing chromophores exhibit τ_F values slightly decreasing going from **[Fb]** to **[Fb-Fb]** to **[Zn-Fb]** at both 298 and 77K. Conversely, the zinc(II)porphyrin-containing chromophores exhibit τ_F values that are essentially constant (taking into account the uncertainties) for **[Zn]** and **[Zn-Zn]**, but decreases for **[Zn-Fb]** at both 298 and 77K. Noteworthy, the heavy atom effect of Pd that normally induces a decrease in τ_F is not observed when comparing **[Fb]** with **[Fb-Fb]** and **[Zn]** with **[Zn-Zn]**. This may be explained by the absence of communication either through bond (including conjugation) or through space. Indeed, the atomic contribution of the Pd atom is weak in most frontier π-MOs as exemplified by Figure 5 and Table 2 (for the other compounds see the ESI). The lower τ_F values (in the 50-300 ps range) for **[Zn-Fb]** suggest S_1 energy transfer. In order to unambiguously evidence for this quenching process, ultrafast fluorescence spectroscopic techniques were employed using a Streak camera.

Table 3. Computed positions (λ), oscillator strengths (f) and major contributions of the electronic transitions of **[Zn-Fb]** (H = HOMO, L = LUMO).

λ (nm)	f	Major contributions (%)
601.8	0.08	H-3→L+1 (28), H-1→L (70)
565.3	0.14	H-3→L (30), H-1→L+1 (68)
563.6	0.06	H-2→L+3 (32), H→L+2 (66)
562.5	0.06	H-2→L+2 (35), H→L+3 (64)
522.0	0.00	H→L (100)
516.7	0.00	H→L+1 (100)
490.8	0.00	H-1→L+2 (100)
486.9	0.00	H-1→L+3 (100)
468.6	0.00	H-2→LUMO (100)
467.1	0.00	H→L+4 (96)
464.3	0.00	H-2→L+1 (100)
461.4	0.00	H-1→L+4 (99)
442.5	0.07	H-4→L (77), H-3→L+1 (10)
441.2	0.00	H-5→L+4 (93)
431.1	0.00	H-7→L+4 (39), H-6→L+4 (44)
426.3	0.00	H-3→L+2 (100)
425.6	0.04	H-2→L+4 (96)
424.3		H-3→L (28), H-2→L+3 (34), H-1→L+1 (12),

	4.30	H→L+2 (16)
423.4	0.04	H-3→L+3 (99)
415.9	0.04	H-3→L+1 (29), H-2→L+2 (29), H-1→L (12), H→L+3 (15)

Table 4. Photophysical data of **[Zn]**, **[Fb]**, **[Zn-Zn]**, **[Fb-Fb]** and **[Zn-Fb]** in 2MeTHF.

	298K			77K	
	λ_{em}[a] (nm)	τ_F (ns)[b][c] (cont. %)	Φ_F[c]	λ_{em}[a] (nm)	τ_F (ns)[b][c] (cont. %)
[Zn]	637	0.57±0.10	0.015	633	0.88±0.10
[Zn-Zn]	630	0.65±0.10	0.016	618	1.07±0.10
[Zn-Fb]	675	0.130±0.001(D) 4.55±0.10(A)	0.029	667	0.081±0.001(D) 0.277±0.001(D) 4.88±0.10(A)
[Fb-Fb]	674	4.43±0.64	0.051	667	5.74±0.10
[Fb]	672	5.85±0.10	0.22	665	6.02±0.10

[a] λ_{exc} = 430 nm and λ_{em}(nm) is the monitoring wavelength. [b] λ_{exc} = 430 nm; the detection limit is 100 ps unless indicated otherwise. D = donor; A = acceptor. c) The ϕ_F values were measured with H_2TPP ($\Phi_F = 0.11$).[10] [c] The ultrafast components (< 400 ps) have been measured using a fs laser system and a Streak camera.

Ultrafast fluorescence spectroscopy. The time-resolved fluorescence spectra of **[Zn-Fb]** in 2MeTHF are shown in Figure 7 (top), where the emission signal at 625 nm decreases rapidly with time in the 35 ps to 1 ns time window. The reconstruction of the individual contributions to the overall signal along with the decays and rise traces are shown in Figure 7 (middle and bottom, respectively). In the absence of energy transfer, the reconstruction of the fluorescence spectra should be identical to that observed for **[Zn-Zn]** and **[Fb-Fb]** in Figure 2. However, the reconstructed spectrum of the donor is notoriously deformed with a lower intensity or even a negative value at ~670 nm where the acceptor fluorescence is strong. This indicates that the donor intensity has been “given” to the acceptor providing evidence that energy transfer occurs. The decay and rise traces have been monitored at the three maximums. At the 628 and 724 nm, the fluorescence signals respectively belong to the donor and acceptor without major overlap with the other. Consequently, their lifetimes are easily extracted and placed in Table 4. Note that any values exceeding 1 ns cannot be trusted due to the limit of the technique. At 667 nm, the strong spectral overlap between the donor and acceptor signals gives rise to a decay combining both kinetic behaviours.

Two components at 77K are noted. The reconstructed spectra are relatively similar (red and green traces; Figure 7; middle; right). This is suggestive of two "similar" donor chromophores (since the fluorescence maximum is the same) transferring energy at different rates. Elements of explanations are found in Figure 3 and are discussed below (in Energy transfer analysis).

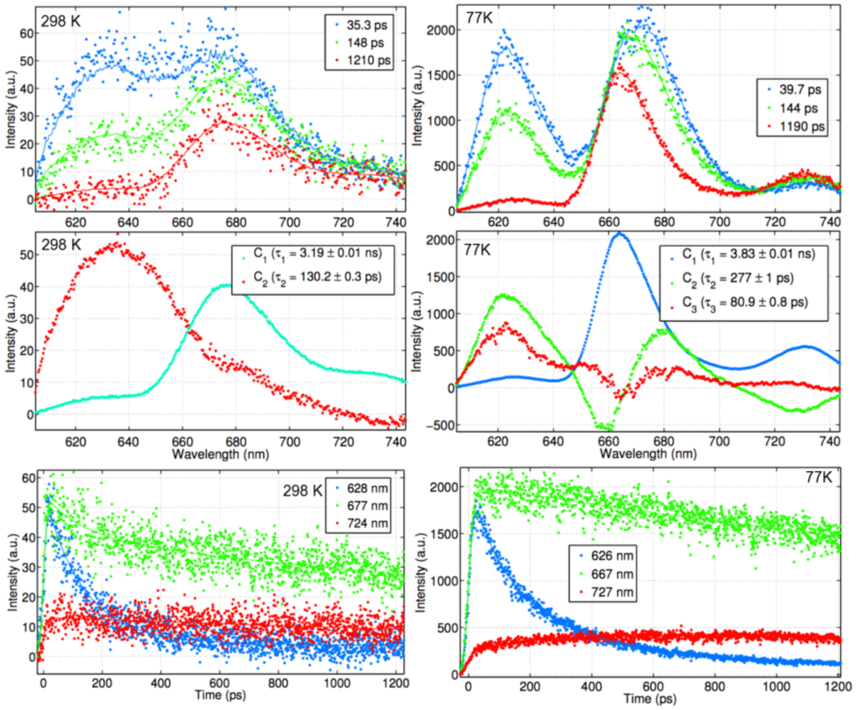

Figure 7. Time resolved fluorescence spectra of **[Zn-Fb]** in 2MeTHF at 298 (left) and 77K (right) using the Streak camera. Top: time-resolved spectra. Middle: reconstructed spectra giving rise to the overall spectra shown above. Bottom: decay and rise traces.

Transient absorption spectroscopy. Further evidence for energy transfer in **[Zn-Fb]** has been provided by ultrafast transient absorption spectroscopy (Figure 8). The 2D map (Frame A) reporting the evolution of the absorbance as a function of time and wavelength at λ_{exc} = 660 nm (*i.e.* in the Q-band of the acceptor chromophore) exhibit a bleach of the Soret bands a strong bleach signal at ~420 nm. At least two intermediates are noted (see the red (~420 nm) and orange (~430 nm) traces). However, at λ_{exc} = 620 nm (*i.e.* in the Q-band of the donor chromophore mainly), one intermediate (orange trace at ~430 nm) disappears quickly and the second intermediate appears later (at ~420 nm; Frame B). This behaviour is characteristic of an energy transfer. The best fit of all the spectra *vs* time requires 3 and 4 individual spectra for λ_{exc} = 660 and 620 nm, respectively. The reconstruction of the spectra exhibits a strong signal at 420 nm (Frames C and D) relaxing at a time scale well exceeding the delay line (< 3.3 ns) and is unquestionably associated with the triplet states of the chromophores. The monitoring of the ΔT/T signal at different wavelengths permits to measure the lifetime of the various intermediates. The species relaxing with a lifetime of 1-2 ns is most likely associated with the S_1 lifetime of the acceptor. The discrepancy with the value in Table 4 (4.55 ns) is due to the strong spectral overlap of the different species relaxing at different rates (i.e. an example of a similar situation is presented above for the monitoring of the overlapping fluorescence at ~670 nm in Figure 4, bottom), and the short delay line available for this time scale (3.3 ns). The species exhibiting a relaxation of ~64 ps appears in the spectra recorded using λ_{exc} = 620 nm (exciting the donor) and is characterized by an obvious rise of the signal at 419 nm (turquoise trace in Frame F) and decay at 435 nm (green trace). Again these traces are absent in Frame E (λ_{exc} = 660 nm; exciting the acceptor only). The discrepancy between the expected 130 ps value is again due to the strong overlap between the various components. Nonetheless, transient absorption measurements provide evidence for energy transfer. The species relaxing with time scales of 12-16 ps are not identified in this work. These are also present for the **[Zn-Zn]** and **[Fb-Fb]**.

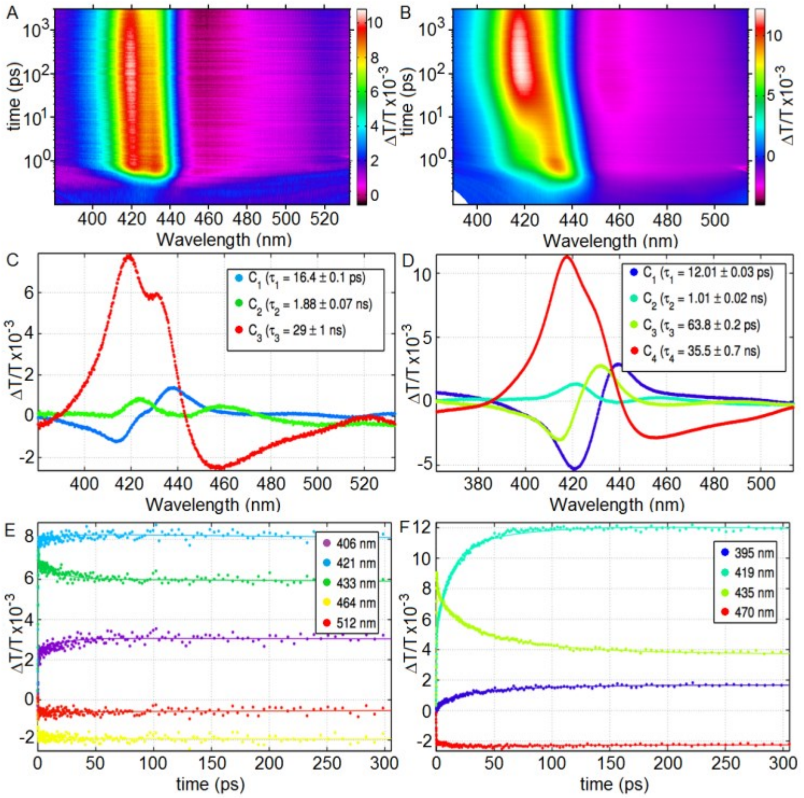

Figure 8. Transient absorption spectra of **[ZnFb]** in 2MeTHF at 298K (left; λ_{exc}= 660, right; 620 nm). Frames A and B: 2D maps of ΔT/T vs wavelength vs time. Frames C and D: reconstruction of the transient spectra of the various intermediates. Frames E and F: decay and rise traces monitored at various wavelengths. Decays > 3 ns are unreliable. The values indicated inside the insets are values extracted from the best fits.

Energy transfer analysis. The rates for S_1 energy transfer, $k_{ET}(S_1)$, can be calculated by $k_{ET}(S_1) = (1/\tau_F)-(1/\tau_F°)$,[2] where τ_F and $\tau_F°$ are respectively the fluorescence lifetime of the donor in the presence and absence of an acceptor. The values for τ_F are 130 ps (298K) and 81 and 277 ps (77K) compute 4.6×10^9, 1.1×10^{10} and 2.7×10^9 s^{-1}, respectively. These k_{ET} values appear similar to the Pt-containing dyads **3** and **4** shown in Figure 1 (**[Pd]***→**[Zn]**; k_{ET} ~ 2 x 10^9 s^{-1}; center-to-center distance = 25.0 Å; optimized geometry by DFT) but fall astonishingly short when compared to traditional benzene-bridged dyads where a 1 to 3 orders of magnitude difference are observed (note that the use of 1,4-benzene for the comparison is to keep the center-to-center distance somewhat similar ~17Å for **[Zn-Fb]** and 13.7 Å for **3** and 4).

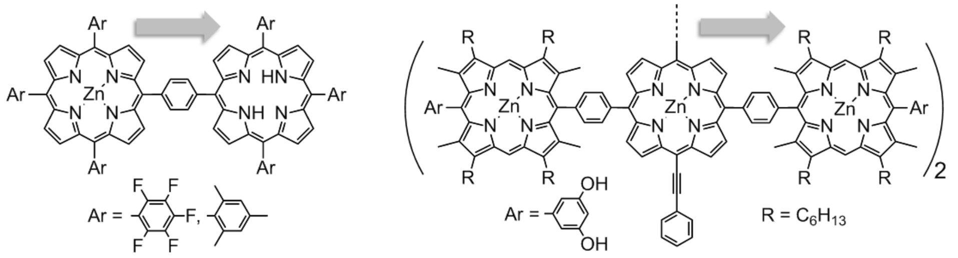

Figure 9. Some structures of dyads bridged by 1,4-benzene groups and their kET values. The arrows indicate the direction of the energy transfer. The center-to-center distance is 13.7 Å according to computer modelling.

Two mechanisms for energy transfer are generally anticipated to operate in the singlet states; *i.e.* Dexter[11] and Förster.[12] The former mechanism involves a double electron exchange between the donor in its singlet excited state and the acceptor in its ground state (i.e. LUMO(donor*)→LUMO(acceptor) and HOMO(donor*)←HOMO(acceptor)) and consequently strongly depends on the degree of orbital overlap between the donor and acceptor.[11] However, Table 2 and Figure 5 clearly indicate that the atomic orbital contribution from the Pd atom is negligible and so no strong d,π-orbital overlap exists between the zinc(II)porphyrin and free base porphyrin chromophores, and so the electronic communication (*i.e.* double electron exchange) is not possible. This concept has clearly been recently verified in detail by one of us.[13]

The other mechanism is commonly called FRET, Förster Resonance Energy Transfer theory.[12]. This theory predicts that for long donor-acceptor interactions, k_{ET} is given by $k_{ET} = k_F°(D) \bullet (\kappa^2/r^6) \bullet cte \bullet \mathbf{J}$, where $k_F°(D)$ is the ratio $\Phi_F°(D)/\tau_F°(D)$ for the donor (D) in the absence of an acceptor (A), r is the center-to-center distance between the donor and the acceptor, κ^2 is an orientation factor between the transition moments of the donor and the acceptor ($\kappa^2 = (\sin\theta_D \bullet \sin\theta_A \bullet \cos\phi - 2\cos\theta_D \bullet \cos\theta_A)^2$ with θ_D and θ_A being the angles formed between the transition moment vectors of D versus the center-to-center axis and of A and this same axis, and ϕ being the dihedral angle made by the two transition moment vectors, and cte is the ratio $9000(\ln 10)/128\pi^5 n^4 N_a$ with n and N_a being the refractive index of the medium (1.406 for THF) and Avogadro's number, respectively. In the case of porphyrin, the transition moments are doubly degenerated with two transition dipoles making an angle of 90°, then κ^2 is given by $\kappa^2 = (|\kappa(\omega)|+|\kappa(\omega+(\pi/2))|)^2/4$, where ω and ω+(π/2) represents ϕ for each component.[14] Finally, the **J** value is given by **J** = $(\int F_D(\nu)\varepsilon_A(\nu)\nu^{-4}d\nu)/(\int F_D(\nu)d\nu)$ (ν is in cm^{-1} units) or by **J** = $(\int F_D(\lambda)\varepsilon_A(\lambda)\lambda^4 d\lambda)/(\int F_D(\lambda)d\lambda)$, (λ is in cm^{-1} units) where F_D is the fluorescence intensity of the donor and ε_A is the absorptivity of the acceptor (ν and λ are expressed in cm^{-1} and nm, respectively). Such a graph is presented in Figure 10 where both possible directions are examined at both temperatures (i.e. **[Zn]*→[Fb]** and **[Zn]←[Fb]***) using the spectroscopic signatures of the homodimers **[Zn-Zn]** and **[Fb-Fb]** as models. The spectral overlaps respectively large and negligible for **[Zn]*→[Fb]** and for **[Zn]←[Fb]***, the energy transfer is essentially unidirectional. Because the absorptivity values are not known at 77K, only the room temperature values for **J** are accessible (Table 5). The **J** values are in line with what has been previously reported.[15]

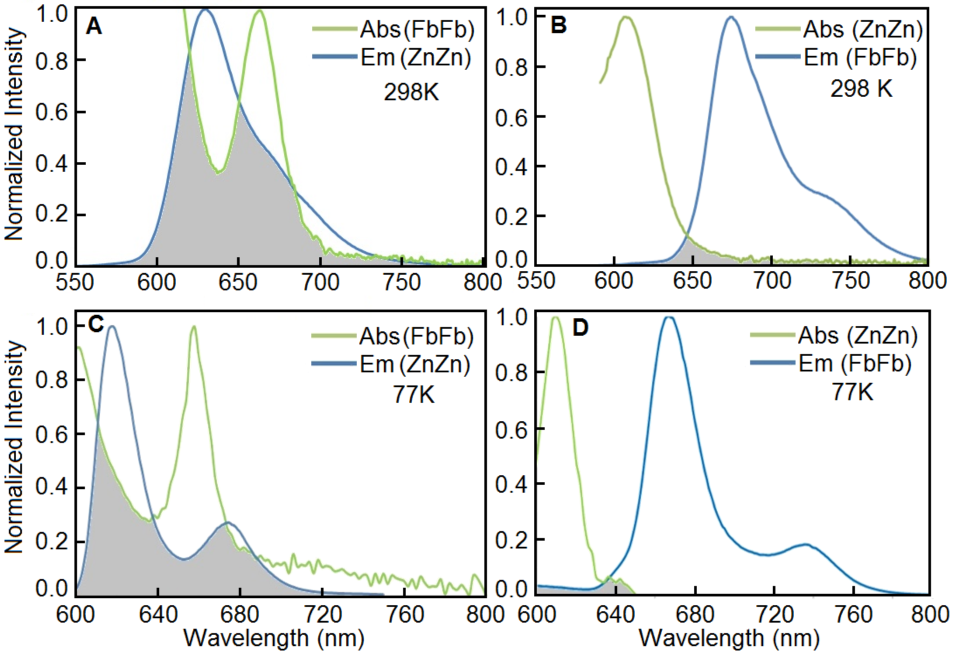

Figure 10. Spectral overlap (grey zone) between the absorption of **[Fb-Fb]** and the fluorescence spectra of **[Zn-Zn]** for the direction **[Zn]*→[Fb]** (left) and the absorption of **[Zn-Zn]** and the fluorescence spectra of **[Fb-Fb]** for the direction **[Zn]←[Fb]*** (right).

Table 5. Structural, spectral and photophysical data for the calculations of k_{ET} of **[Zn-Fb]**.

		S-conformation			
κ^2	J[a]	$\tau_F(D)$	$\Phi_F(D)$	r_{DA}	k_{ET} (s^{-1})
0.81	$2.22 \cdot 10^{14}$ $M^{-1}cm^{-1}nm^4$	0.65 ns	0.016	1.68 nm	$4.35 \cdot 10^{12}$
0.81	$2.27 \cdot 10^{-14}$ $M^{-1}cm^3$	0.65 ns	0.016	$1.68 \bullet 10^{-7}$ cm	$4.46 \cdot 10^{12}$
		U-conformation			
κ^2	J[a]	$\tau_F(D)$	$\Phi_F(D)$	r_{DA}	k_{ET} (s^{-1})
0.79	$2.22 \cdot 10^{14}$ $M^{-1}cm^{-1}nm^4$	0.65 ns	0.016	1.71 nm	$3.82 \cdot 10^{12}$
0.79	$2.27 \cdot 10^{-14}$ $M^{-1}cm^3$	0.65 ns	0.016	$1.71 \bullet 10^{-7}$ cm	$3.91 \cdot 10^{12}$
		Twisted-conformation			
κ^2	J[a]	$\tau_F(D)$	$\Phi_F(D)$	r_{DA}	k_{ET} (s^{-1})
1.3	$2.22 \cdot 10^{14}$ $M^{-1}cm^{-1}nm^4$	0.65 ns	0.016	1.68 nm	$6.99 \cdot 10^{12}$
1.3	$2.27 \cdot 10^{-14}$ $M^{-1}cm^3$	0.65 ns	0.016	$1.68 \bullet 10^{-7}$ cm	$7.15 \cdot 10^{12}$

[a] Calculated using both the nm (first value) and cm^{-1} scales (second value).

Moreover, Table 5 also summarizes the structural, spectral and photophysical data for the calculations of the theoretical k_{ET} of **[Zn-Fb]** at 298K. The predicted values are in the order of (3.8 to 7.2) x 10^{12} s^{-1} depending on the dyad's conformation (Figure 3), and are much larger compared to the experimental values, i.e. (3 to 11) x 10^9 s^{-1}. This time scale is very fast (note that the sub-ps time scale is accessible to us by transient absorption spectroscopy; time resolution = 250 fs). The accuracy of the Förster equation has correctly been criticized for short D•••A distances.[16] We have indeed previously corroborated this effect where discrepancies in the calculated and experimental k_{ET}'s varies from 2 to 32 folds.[17] Interestingly, two time domains are predicted from the calculations of the theoretical k_{ET}'s (4.4 and 3.8) x 10^{12} s^{-1} and 7.0 x 10^{12} s^{-1}. Experimentally, two τ_F values are measured from the decay traces at 77K; 81 and 277 ps. This experimental evidence strongly suggests that at least two species exist in the samples, most likely the S-/U- and twisted-conformers shown in Figure 1. It is more than likely that all three species co-exist at the same time but the similarity in the time scale of the τ_F's and the scattering of the experimental data do not permit for the accurate evaluation for each. Moreover, only one lifetime could be extracted at 298K, again most likely due to the large scattering of the data points. Based on the data presented in Table 5 (calculated k_{ET}'s) and Figure 1 (optimized geometries), it appears clear that the species relaxing the fastest (i.e. 81 ps at 77K) is the twisted species (fastest calculated k_{ET}). Assuming that the fluorescence quantum yields for the zinc-containing chromophore in each individual conformers are the same, or at least very similar, the relative intensity of the red and green traces (~2 *vs* 3) in Figure 4 (middle right) suggests that the presence of the S- and U-shapes is not negligible. Again the resulting calculated theoretical k_{ET} values in Table 5 are far too large to explain the slow k_{ET}'s observed for **[ZnFb].** This begs the question, "what is preventing the singlet energy transfer from occurring?"

Previously, one of us noted a new effect, where placing an unconjugated atom exactly at the shortest distance between a donor and an acceptor dramatically slows down $k_{ET}(S_1)$.[18] Indeed, a simple introduction of a simple H-atom between the C_{meso}•••C_{meso} spacing of a bis(porphyrin) dyad for which the energy transfer proceeds via a through space mechanism mainly operating according to a Förster process,[12] induces a decrease of $k_{ET}(S_1)$ by 20 to 35 fold (Figure 11) while keeping all other structural parameters identical. This notable effect was interpreted as a screening effect where the electric fields of the two chromophores are partially blurred from one another.[18]

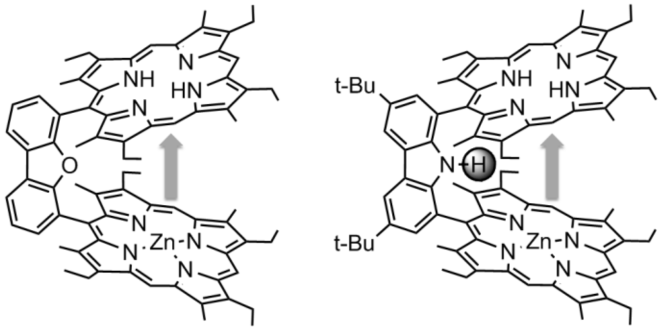

$k_{ET}(S_1)$, 298K:	**5.0×10^9 s^{-1}**	**0.24×10^9 s^{-1}**
$k_{ET}(S_1)$, 77K:	**5.9×10^9 s^{-1}**	**0.16×10^9 s^{-1}**

Figure 11. Structures of two dyads bridged by a dibenzofuran and a carbazole spacer and their k_{ET}'s at 298 and 77K. The arrows indicate the direction of the energy transfer.[18]

In this work, the *trans*-PdI_2 unit obviously bears far more electrons than a proton and its effect is drastically felt as well when comparing the experimental values with those for other linear dyads (Figure 9) and with what theory predicts (Table 5). The calculated electrostatic potential (ESP) map also illustrates this phenomenon where a large electron density is in fact computed on the iodides and surprisingly not on the Pd atom (Figure 12). The reason for this result is still unknown (note that the rich electron density for the Pd atom in compound **3** is clearly visible below). Nonetheless, one can still conclude that this dyad provides, to the best of our knowledge, the second unambiguous piece of evidence for electronic screening effect on k_{ET} (FRET).

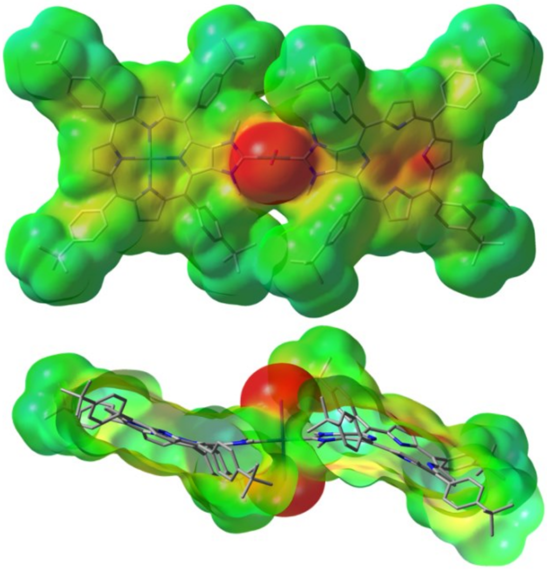

Figure 12. Top and side views of the electron density map of **[Zn-Fb]** extracted from DFT computations. The red and blue regions indicate the area where the electron density is the largest and lowest, respectively. Note that the dicationic Pd(II)-bridge is not in red, and a slice of the ESP map has been removed to allow a better view of the central Pd-atom.

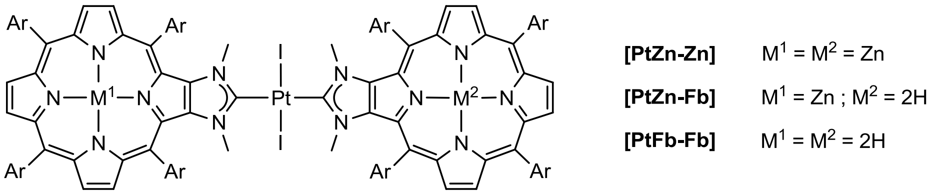

Figure 13. Structures of the computed models containing a *trans*-PtI_2 bridge (Ar = 4-*t*BuPh).

Energy transfer in Pt-contaning bridge. In this work, a focus is placed on the effect of the *trans*-PdI_2 bridge on the efficiency of the S_1 energy transfer. However, this analysis does not address what happens when the heavier Pt atom is used, particularly when rates of ~2×10^9 s^{-1} are reported for compounds **3** and **4**[4s] despite the longer center-to-center separation 25.0 Å (optimized geometry DFT; B3LYP). Notably, the ratio of $1/r^6$ (for 16.8 Å) *vs* $1/r^6$ (for 25.0 Å) is ~11. This means that translating the observed rate ~2×10^9 s^{-1} for **3** and **4** from a center-to-center distance of 25.0 to 16.8 Å, according to a Förster process, would lead to an expected rate, k_{ET} of ~2×10^{10} s^{-1}, which is still faster than what is observed for **[Zn-Fb]**. This point is addressed by DFT computations by comparing the atomic contributions to the frontier MO's of Pt in a series of analogous geometry optimized **[PtZn-Zn]**, **[PtFb-Fb]** and **[PtZn-Fb]** (Figure 13 and SI) and those for compound **3** (Table 6) along with the electrostatic potential maps of **[Zn-Fb]** (Figure 12) and compound **3** (Figure 14).

Table 6. Relative atomic contributions of the various fragments in **[Zn-Fb].**[a][b]

			[PtZn-Zn]			
	[Zn][a]	[Fb][c]	Zn	Pt	I-1	I-2
L+4	2.80	2.82	0.01	**50.04**	**21.90**	**22.43**
L+3	**99.73**	0.02	0.22	0.03	0.01	0.00
L+2	**99.26**	0.16	0.29	0.16	0.03	0.11
L+1	0.14	**99.70**	0.00	0.08	0.02	0.06
LUMO	0.02	**99.95**	0.00	0.02	0.01	0.00
HOMO	**97.82**	0.73	1.07	0.28	0.06	0.03
H–1	0.61	**99.33**	0.01	0.04	0.01	0.00
H–2	**99.90**	0.01	0.03	0.04	0.01	0.01
H–3	0.01	**99.93**	0.00	0.05	0.01	0.01
H–4	0.17	0.22	0.00	**38.21**	**31.47**	**29.93**

				Complex 3			
	Pt	PEt_3	C≡CPh	**[Pd]**	**[Zn]**	Pd	Zn
L+4	**14.03**	**20.95**	**56.59**	4.57	3.53	0.32	0.00
L+3	0.00	0.01	4.48	0.00	**95.31**	0.00	0.19
L+2	0.00	0.00	0.53	0.00	**99.27**	0.00	0.20
L+1	0.00	0.01	4.17	**94.08**	0.00	1.73	0.00
LUMO	0.00	0.00	0.48	**97.77**	0.00	1.75	0.00
HOMO	0.00	0.00	0.10	0.00	**99.89**	0.00	0.00
H–1	0.44	0.02	5.07	0.07	**93.18**	0.00	1.23
H–2	0.17	0.00	0.58	**99.14**	0.09	0.02	0.00
H–3	**25.05**	0.67	**66.55**	3.70	4.01	0.00	0.02
H–4	0.17	0.02	4.01	**95.02**	0.02	0.75	0.00

[a] L = LUMO, H = HOMO. The largest contribution (>10%) are in bold. [b] **[Pd]** = palladium-contaning porphyrin (except Pd), **[Zn]** = Zn-containing porphyrin (except Zn).

The atomic contribution of the Pt atom to the frontier MO's in **[PtZn-Fb]** (Table 6, top) are very low (except for L+4 and H-4). This computational result is similar to that obtained for Pd in **[Zn-Fb]** (Table 2). The conclusion is that DFT predicts that with the metal atomic contribution being negligible, the rate for energy transfer *via* a Dexter process is likely to be very slow. The atomic contribution of the Pt atom in the frontier MO's of compound **3** is also negligible (Table 6, bottom). This result indicates that energy transfer operating via a Dexter mechanism should also be very slow. The rate for triplet energy transfer, which is known to proceed mainly through a Dexter mechanism,[19] for compound **3** is indeed very slow (order of 10^3 s^{-1}).[4s] The main conclusion is that for all three dyads analysed here, the Förster mechanism is the dominant process.

The next question is why the experimental k_{ET} for compound **3** (in proportion of $1/r^6$) appears more efficient than that for **[Zn-Fb]**. The ESP map of compound shares a similar feature to that of **[Zn-Fb]** (using the same electron density colour scaling) i.e. absence of electronic density on the Pt-atom on the bridge. The regions of richer densities are found in the palladium(II)-containing chromophone, the ethynyl groups, and lightly on the nitrogen atoms. The comparison of the ESP maps of the β,β-N,N-carbene-*trans*-PdI_2-β,β-N,N-carbene bridge (Figure 9) *vs* that for C_6H_4-C≡C-*trans*-$Pt(PBu_3)_2$-C≡C-C_6H_4 (Figure 11) clearly shows the former unit bears more electronic density, particularly on the iodides, and thus corroborates the apparent weaker efficiency (for equal $1/r^6$ parameters) of the S_1 energy transfer of **[Zn-Fb]** over compound **3**.

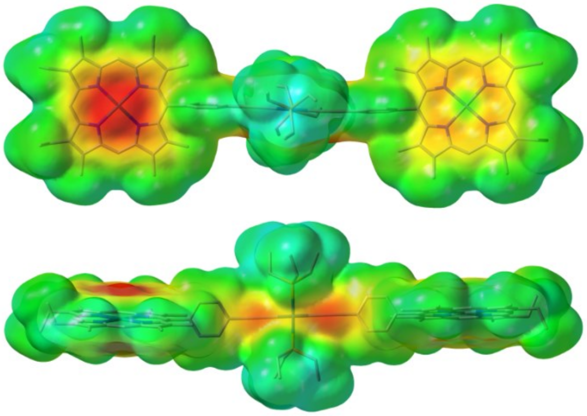

Figure 14. Top and side views of the ESP map of compound 3 extracted from DFT computations. The red and blue regions indicate the area where the electron density is the largest and lowest, respectively. Note that the dicationic Pt(II)-bridge is not in red, and the scaling for this map is identical to that use to generate Figure 9.

Short comment on the triplet states. Triplet energy transfers between porphyrins are also possible and it is known that the Dexter mechanism is the dominant process.[19] Again, the MO's orbital overlap is crucial in analysing $k_{ET}(T_1)$. Based on the energy difference between the optimized geometries by DFT (B3LYP) in the S_0 and T_1 states, the calculated S_0-T_1 energy gaps are 1.303 and 1.298 ev for **[Zn-Zn]** and **[Zn-Fb]**, respectively. The corresponding calculated positions of the 0-0 peaks in the phosphorescence spectra are 951 and 955 nm, respectively, well exceeding the limit of the detector (~830 nm). However, it is possible to make a prediction based on the examination of the frontier MO's of **[Zn-Fb]** (Figure 15; the MO's for **[Zn-Zn]** and **[Fb-Fb]** are placed in the ESI). The assignment of the energy donor and acceptor is readily made by comparing the MO ordering. Indeed, the HSOMO and LSOMO (i.e. highest and lowest semi-occupied molecular orbitals, respectively, and π-systems as well) are clearly located on the free base chromophore only, whereas the HOMO-1 (triplet) and LUMO+1 (triplet) are centered on the zinc-containing unit. This ordering places the triplet states of the zinc-containing unit (donor) above that of the free base (acceptor). More importantly, the atomic contributions of the Pd-containing unit is absent from these MO's meaning that a double electron transfer process is absent or very difficult. These computations predict absence of efficient triplet energy transfer.

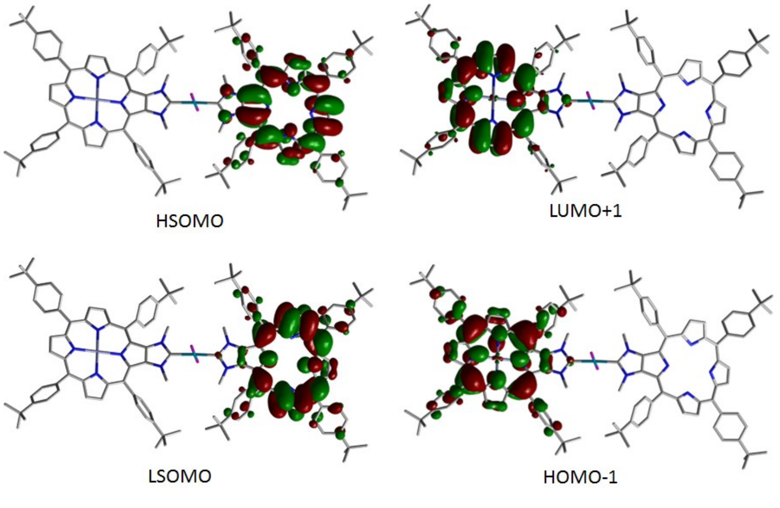

Figure 15. Frontier MOs representations of **[Zn-Fb]** in its lowest energy triplet state.

3.1.4. Conclusion

While the ground state electronic communication in this type of homo- and heterodimers was known for being nil (or negligible) based on previous electrochemical findings for parent compounds,[8] the status of the communication or chromophore-chromophore interactions in the excited states was unknown. Based on the measurements of the τ_F's data at 298 and 77K for the zinc-containing donor in the **[Zn-Fb]** dyad, slow S_1 energy transfer is established, but appears significantly slow when compared to other dyads bearing some similar structural features and to calculated values based on the Förster theory. Based on DFT computations and literature comparisons, both mechanisms, Dexter (double electron exchange) and Förster (dipole-dipole interactions) are either switched off or strongly reduced by the presence of the *trans*-PdI_2 bridge. The absence or very small atomic contribution of the Pd to the frontier MO's (both in the singlet and triplet states) explains the weak contribution of the Dexter process. However, although the number of previous work addressing this phenomenon is extremely limited (only our work), it now appears that screening of the electric fields of the two chromophores occurs, thus blurring them from one another, and consequently preventing strong communications in the S_1 excited states. This work represents a rare example for such a conclusion but appears extremely important when designing photonic devices (i.e. solar cells). Interestingly, Nature stayed away from heavy metals in the Photosystems of plants and photosynthetic bacteria for toxicity reasons, but perhaps also for the sake of the efficiency of the antenna effect.

3.1.5. Experimental Section

Materials.

The synthesis of imidazolium salts **[Zn]** and **[Fb]** is described in reference [5]. Reactions were performed under argon using oven-dried glassware and Schlenk techniques. Palladium acetate (47.5% Pd) was purchased from Acros organics. Dry THF was obtained by distillation over CaH_2 and then Na/benzophenone. Preparative separations were performed by silica gel flash column chromatography (Baeckeroot-Labo 60M) and solvents used as eluents are technical grade. ^1H and $^{13}C\{^1H\}$ NMR spectra were recorded in $CDCl_3$ on Bruker 200 MHz spectrometer. ^1H and $^{13}C\{1H\}$ NMR spectra were calibrated to TMS on the basis of the relative chemical shift of the solvent as an internal standard.

Abbreviations for ^{1}H NMR spectra used are as follows: s, singlet; d, doublet. UV-visible absorption spectra were recorded in $CHCl_3$ with a Perkin Elmer UV-visible spectrophotometer Lambda 35 in quartz cells (Hellma). MALDI-TOF mass spectra were recorded on a Bruker Ultraflex III MS spectrometer using dithranol as a matrix and PEG as internal reference. Elemental analyses were performed at the Service Central d'Analyse du Centre National de la Recherche Scientifique of Solaize (France).

Synthesis

[Fb-Fb]. A solution of the free base imidazolium salt **[Fb]** (47 mg, 4.54x10^{-5} mol) and palladium acetate (3 mg, 1.34 x10^{-5} mol) was prepared in anhydrous THF (7 mL) and was degassed with argon. Then, sodium *tert*-butoxide (5 mg, 5.20x10^{-5} mol) was added and the reaction mixture was stirred for 4 hours at room temperature. After evaporation of THF, the product was isolated by column chromatography on silica gel (eluent: CH_2Cl_2/*n*-pentane from 1:2 to 1:1). Crystallization from CH_2Cl_2/CH_3OH afforded **[Fb-Fb]** in 58% yield (17 mg). **^{1}H NMR (200 MHz, 25°C, $CDCl_3$) :** δ 8.90 (d, *J* = 5.2 Hz, 4H, H_{pyrr}), 8.85 (d, *J* = 5.2 Hz, 4H, H_{pyrr}), 8.73 (s, 4H, H_{pyrr}), 8.43 (d ,*J* = 8.3 Hz, 8H, $H_{Ar\,meso}$), 8.21 (d, *J* = 8.3 Hz, 8H, $H_{Ar\,meso}$), 7.92 (d, *J* = 8.3 Hz, 8H, $H_{Ar\,meso}$), 7.80 (d, *J* = 8.3 Hz, 8H, $H_{Ar\,meso}$), 3.27 (s, 12H, $H_{N\text{-}Me}$), 1.65 (s, 36H, H_{tBu}), 1.62 (s, 36H, H_{tBu}), -2.89 (s, 2H, H_{NH}) ppm. **^{13}C{^{1}H} NMR (50.3 MHz, 25°C, $CDCl_3$) :** δ 181 ($C_{2'}$), 152, 151, 145, 140, 140, 139, 137, 136, 134, 129, 128, 125, 124, 121, 118, 54, 38, 36, 35, 32 ppm. **UV-visible ($CHCl_3$) :** λ_{max} (ε): 433 (562000), 527 (34100), 567 (21350), 599 (12300), 661 nm (7600 L.mol^{-1}.cm^{-1}). **MALDI$^+$ MS :** calculated for $C_{126}H_{133}I_2N_{12}Pd^+$: 2173.79, found: 2173.7 ([M+H]$^+$). **Elem. Ana. :** $C_{126}H_{132}I_2N_{12}Pd\bullet 3.H_2O$: calcd. C 67.90, H 6.24, N 7.54; found C 68.08, H 6.07, N 7.42.

[Zn-Zn]. A solution of the palladium complex **[Fb-Fb]** (100 mg, 4.60 x 10^{-5} mol) and $Zn(OAc)_2\bullet 2H_2O$ (40 mg, 1.82x10^{-4} mol) was prepared in a $CHCl_3$/CH_3OH mixture (18/2 mL) and degassed with argon. Then, the reaction mixture was stirred for 2 hours at 50°C. After evaporation of the solvents, the desired complex was isolated by column chromatography on silica gel (eluent: toluene to chloroform). Crystallization from CH_2Cl_2/CH_3OH afforded the palladium complex **[Zn-Zn]** in 97% yield (103 mg). **^{1}H NMR (200 MHz, 25°C, $CDCl_3$) :** δ 8.93 (s, 4H, H_{pyrr}), 8.92 (d, J = 4.8 Hz, 4H, H_{pyrr}), 8.82

(d, J = 4.8 Hz, 4H, H_{pyrr}), 8.34 (d, J = 8.0 Hz, 8H, $H_{Ar\ meso}$), 8.16 (d, J = 8.0 Hz, 8H, $H_{Ar\ meso}$), 7.85 (d, J = 8.0 Hz, 8H, $H_{Ar\ meso}$), 7.76 (d, J = 8.0 Hz, 8H, $H_{Ar\ meso}$), 3.49 (s, 12H, $H_{N\text{-}Me}$), 1.66 (s, 36H, H_{tBu}), 1.61 (s, 36H, H_{tBu}) ppm. **UV-visible ($CHCl_3$) :** λ_{max} (ε): 437 (657500), 561 (39800), 603 nm (13420 $L.mol^{-1}.cm^{-1}$). **MALDI$^+$ MS** : calculated for $C_{126}H_{128}IN_{12}PdZn_2^+$: 2169.70, found: 2169.7($[M\text{-}I]^+$).

[Fb_2Pd_2]. A solution of the free base imidazolium salt **$1H_2$** (53 mg, $5.12x10^{-5}$ mol), palladium acetate (15 mg, $5.71x10^{-5}$ mol), sodium iodide (10 mg, $6.67x10^{-5}$ mol) was prepared in anhydrous THF (10 mL) and degassed with argon. Then, sodium *tert*-butoxide (6 mg, $6.24x10^{-5}$ mol) was added and the reaction mixture stirred for 4 hours at room temperature. After evaporation of THF, the product was isolated by column chromatography on silica gel (eluent: CH_2Cl_2/*n*-pentane 1:1). Crystallization from CH_2Cl_2/CH_3OH afforded complex **$6H_4$** in 83% yield (54 mg). **^1H NMR (200 MHz, 25°C, $CDCl_3$) :** δ 8.91 (d, *J* = 5.0 Hz, 4H, H_{pyrr}), 8.87 (d, *J* = 5.0 Hz, 4H, H_{pyrr}), 8.73 (s, 4H, H_{pyrr}), 8.44 (d broad, *J* = 8.0 Hz, 4H, $H_{Ar\ meso}$), 8.39 (d broad, *J* = 8.0 Hz, 4H, $H_{Ar\ meso}$), 8.20 (d, *J* = 8.0 Hz, 8H, $H_{Ar\ meso}$), 7.94 (d, *J* = 8.0 Hz, 8H, $H_{Ar\ meso}$), 7.81 (d, *J* = 8.0 Hz, 8H, $H_{Ar\ meso}$), 3.40 (s, 12H, $H_{N\text{-}Me}$), 1.67 (s, 36H, H_{tBu}), 1.62 (s, 36H, H_{tBu}), -2.91 (s, 2H, H_{NH}) ppm. **$^{13}C\{^1H\}$ NMR (50.3 MHz, 25°C, $CDCl_3$) :** δ 167 ($C_{2'}$), 153, 151, 144, 140, 139. 137, 136, 135, 129, 129, 126, 125, 124, 122, 118, 39, 36, 35, 32, 32 ppm. **UV-visible ($CHCl_3$) :** λ_{max} (ε): 431 (716000), 528 (34000), 568 (21000), 599 (12000), 661 nm (9000 $L.mol^{-1}.cm^{-1}$). **MALDI$^+$ MS :** calculated for $C_{126}H_{133}I_4N_{12}Pd_2^+$: 2533.50, found: 2533.5 ($[M+H]^+$). **Elem. Ana. :** $C_{126}H_{132}I_4N_{12}Pd_2{\bullet}H_2O$: calcd. C 59.28, H 5.29, N 6.58; found C 59.44, H 5.31, N 6.48.

[Zn-Fb]. Procedure A. A solution of the palladium complex **[Fb-Fb]** (100 mg, $4.60x10^{-5}$ mol) and $Zn(OAc)_2{\bullet}2H_2O$ (10 mg, $4.56x10^{-5}$ mol) was prepared in a $CHCl_3/CH_3OH$ mixture (18/2 mL) and degassed with argon. Then, the reaction mixture was stirred for 2 hours at 50°C under argon. After evaporation of solvents, the obtained complexes were separated by column chromatography on silica gel (eluent: from toluene to chloroform). Crystallization from CH_2Cl_2/CH_3OH afforded the desired palladium complex **[Zn-Fb]** in 38% yield (39 mg), and also the palladium complex **[Zn-Zn]** in a 25% yield (27 mg) accompanied by the remaining starting material palladium complex **[Fb-Fb]** in a 10% yield

(10 mg). **Procedure B.** A solution of the dinuclear palladium complex **[Fb$_2$Pd$_2$]** (51 mg, 2.01x10^{-5} mol) and the zinc imidazolium salt **[Zn]** (77 mg, 7.01x10^{-5} mol) was prepared in anhydrous THF (20 mL) and degassed with argon. Then, sodium *tert*-butoxide (8 mg, 8.3x10^{-5} mol) was added and the reaction mixture was stirred for 2 days at room temperature. After evaporation of THF, the product was isolated by column chromatography on silica gel (eluent: from toluene to chloroform). Crystallization from CH_2Cl_2/CH_3OH afforded the palladium complex **[Zn-Fb]** in a 41% yield (37 mg). **^{1}H NMR (200 MHz, 25°C, $CDCl_3$) :** δ 8.94 (s, 2H, H_{pyrr}), 8,93 (d „J = 4.8 Hz, 2H, H_{pyrr}), 8.89 (d „J = 4.8 Hz, 2H, H_{pyrr}), 8.88 (d „J = 4.8 Hz, 2H, H_{pyrr}), 8.83 (d „J = 4.8 Hz, 2H, H_{pyrr}), 8.73 (s, 2H, H_{pyrr}), 8.46 (d „J = 8.2 Hz, 4H, $H_{Ar\ meso}$), 8.34 (d, J = 8.2 Hz, 4H, $H_{Ar\ meso}$), 8.22 (d, J = 8.2 Hz, 4H, $H_{Ar\ meso}$), 8.17 (d, J = 8.2 Hz, 4H, $H_{Ar\ meso}$), 7.94 (d, J = 8.2 Hz, 4H, $H_{Ar\ meso}$) 7.85 (d, J = 8.2 Hz, 4H, $H_{Ar\ meso}$), 7.81 (d, J = 8.2 Hz, 4H, $H_{Ar\ meso}$), 7.76 (d, J = 8.2 Hz, 4H, $H_{Ar\ meso}$), 3.46 (s, 6H, $H_{N\text{-}Me}$), 3.32 (s, 6H, $H_{N\text{-}Me}$), 1.67 (s, 36H, H_{tBu}), 1.66 (s, 36H, H_{tBu}), 1.63 (s, 72H, H_{tBu}), -2.85 (s, 2H, H_{NH}) ppm. **UV-visible ($CHCl_3$) :** λ_{max} (ε): 435 (580000), 528 (20400), 563 (27700), 601 (12000), 661 nm (4200 L.mol^{-1}.cm^{-1}). **MALDI$^+$ MS :** calculated for $C_{126}H_{131}N_{12}I_2PdZn^+$: 2235.70, found: 2235.7 ($[M+H]^+$). calculated for $C_{126}H_{130}N_{12}IPdZn^+$: 2107.79, found: 2107.8 ($[M-I]^+$).

Photophysical characterization

Absorption, emission and excitation spectra. All samples were prepared in 2-methyltetrahydrofuran, 2-MeTHF, which was distilled over CaH_2 under nitrogen. Absorption spectra of **[Fb-Fb]**, **[Zn-Zn]** and **[Zn-Fb]** were recorded at 298 and 77 K using a Varian Cary 300 spectrophotometer and a HP-8453 diode array spectrophotometer respectively. Molar absorptivity determination was verified by linear least squares fit of values obtained from at least three independent solutions at varying concentrations with absorbance ranging from 0.01-2.6. Steady-state emission and excitation spectra were recorded at 298 and 77 K in a 1.0 cm capped quartz cell and a 5.0mm(i.d) NMR tube inserted into a liquid nitrogen filled quartz EPR dewar, respectively. Emission spectra were obtained by exciting at the lowest energy absorption maxima using a Horiba Jobin Yvon Fluorolog spectrofluorometer equipped with double monochromators. Experimental Details.

Fluorescence quantum yield and lifetimes. The measurements of the emission quantum yields were performed in 2MeTHF at 298K. Three different measurements (i.e. different solutions) were prepared for each photophysical datum (quantum yields and lifetimes). For 298K measurements samples were prepared under inert atmosphere (in a glove box, $P_{O2} <$ 25 ppm). The sample and the standard concentrations were adjusted to obtain an absorbance of 0.05 or less. This absorbance was adjusted to be the same as much as possible for the standard and the sample for a measurement. Each absorbance value was measured five times for better accuracy in the measurements of the quantum yields. The equation $\Phi_s = \Phi_r(F_r/F_s)(I_s/I_r)(n_s/n_r)^2$ was used to calculate the relative quantum yield of each of the sample, where Φ_r is the absolute quantum yield of the reference, n is the refractive index of the solvent, F is the absoptance ($F= 1\text{-}10^{-A}$, where A is the absorbance) at the excitation wavelength, and I is the integrated area under the corrected emission curve. The subscripts s and r refer to the sample and reference, respectively. A solution of meso-tetraphenylporphyrin (H_2TPP) in 2MeTHF (Φ_F = 0.11) [10] was used as the external reference. The emission lifetimes in the 1 to 10 ns range were measured on a TimeMaster model TM-3/2003 apparatus from PTI. The source was a nitrogen laser with high-resolution dye laser (fwhm~1400 ps) and the excited lifetimes were obtained from deconvolution or distribution lifetimes analysis. Time resolved photoluminescence measurement was done by using Titan-sapphir with regenerative amplificator as the laser source and Axis Photonique Inc. AXIS-TRS Streak camera was used as a detector. The data analyses were made using open source software named Glotaran 1.3. This technique allows for the reliable measurements of fluorescence lifetime between 8 ps and 2 ns. Any lifetime above this value is not accurate.

Femptosecond transient absorption spectroscopy. The fs transient spectra and decay profiles were acquired on an homemade system using the SHG of a Soltice (Spectra Physics) Ti-Sapphire laser (λ_{exc} = 398 nm; FWHM = 75 ps; pulse energy = 0.1 μJ/pulse, rep. rate = 1 kHz; spot size ~ 500 μm), a white light continuum generated inside a Sapphire window and a custom made dual CCD camera of 64 x 1024 pixels sensitive between 200 and 1100 nm (S7030, Spectronic Devices). The delay line permitted to probe up to 4 ns with an accuracy of ~4 fs. The results were analysed with the program Glotaran (http://glotaran.org) permitting to extract a sum of independent exponentials ($I(\lambda,t) = C_1(\lambda)\bullet\exp(-t/\tau_1)+C_2(\lambda)\bullet\exp(-t/\tau_2)+\ldots$) that fits the whole 3D transient map.

Fast kinetic fluorescence measurements*:* The search for short components ($8ps < \tau_F < 1$ ns) of the fluorescence decays were performed using the output of an OPA (OPA-800CF, Spectra-Physics) operating at λ_{exc} = 490 nm, pulse width of 90 ps, rep. rate = 1 kHz, pulse energy = 1.6 μJ/pulse, spot size ~2 mm, and a Streak Camera (Axis-TRS, Axis Photonique Inc.) with less than 6 and 8 ps time resolution respectively at 298 and 77K. The results were also globally analysed with the program Glotaran (http://glotaran.org) permitting to extract a sum of independent exponentials ($I(\lambda,t) = C_1(\lambda)\bullet\exp(-t/\tau_1)+C_2(\lambda)\bullet\exp(-t/\tau_2)+\ldots$).

Computational Methodology. All density functional theory (DFT) calculations were performed with Gaussian 09[20] at the Université de Sherbrooke with the MP2 supercomputer supported by *Le Réseau Québécois De Calculs Hautes Performances*. The DFT geometry optimisations well as TD-DFT calculations[21-30] were carried out using the B3LYP method. 6-31g* basis sets were used for the porphyrin macrocycles. 3-21g* basis sets were used for the phenyl groups of the porphyrin and *tert*-butyl groups attached to the phenyl. VDZ (valence double ζ) with SBKJC effective core potentials were used for Zn, Pd, Pt and I.

Acknowledgements

PDH thanks the Natural Sciences and Engineering Research Council of Canada (NSERC), le Fonds de recherche du Québec sur la Nature et la Technologie (FRQNT), and the Centre en matériaux optiques et photoniques de l'Université de Sherbrooke (CEMOPUS) for fundings.

References

[1] Advances in Photosynthesis and Respiration, Vol. 13 Light-Harvesting Antennas in Photosynthesis. (Eds: B. R. Green, W. W. Parson), Kluwer, Boston, (2003), pp. 1-493.

[2] P. D Harvey, C. Stern, R. Guilard, in *Handbook of Porphyrin Science With Applications to Chemistry, Physics, Materials Science, Engineering, Biology and Medicine*, Vol. 11 (Eds: K. M. Kadish, K. M. Smith, R. Guilard), World Scientific Publishing: Singapore, (2011), pp. 1-179.

[3] a) W. A. Stirk, J. van Staden, *Curr. Top. Plant Biol.,* (2003), 4, 151-158; b) J. J. Rodriguez-Mercado, M. A. Altamirano-Lazano*, Drug and Chem. Tox.,* (2013), **36,** 369-383; c) M. Mkandawire, J. A. Teixeira da Silva, E. G. Dudel, *Critical Rev. Environ. Sci. Technol.,* (2014), **44**, 154-197; d) Q. Zhao, C. Huang, F. Li, *Chem. Soc. Rev*., (2011), **40**, 2508-2524.

[4] a) H. Furuta, K. Youfu, H. Maeda, A. Osuka, Atsuhiro, *Angew. Chem. Int. Ed.,* (2003), **42**, 2186-2188; b) P. J. Chmielewski, I. Schmidt, *Inorg. Chem.,* (2004), **43**, 1885-1894; c) S. Yamaguchi, T. Katoh, H. Shinokubo, A. Osuka, *J. Am. Chem. Soc.,* (2008), **130**, 14440-14441; d) J. Song, N. Aratani, J. H. Heo, D. Kim, H. Shinokubo, A. Osuka, *J. Am. Chem. Soc.,* (2010), **132**, 11868-11869; (e) H. Furuta, N. Kubo, H. Maeda, T. Ishizuka, Tomoya, A. Osuka, H. Nanami, T. Ogawa, *Inorg. Chem.,* (2000), **39**, 5424-5425; f) R. D. Hartnell, D. P. Arnold, *Organometallics*, (2004), **23**, 391-399; g) J. Haumesser, J.-P. Gisselbrecht, J. Weiss, R. Ruppert, *Chem. Commun.,* (2012), **48**, 11653-11655; h) Y. Matano, K. Matsumoto, H. Hayashi, Y. Nakao, T. Kumpulainen, V. Chukharev, N. V. Tkachenko, H. Lemmetyinen, S. Shimizu, N. Kobayashi, D. Sakamaki, A. Ito, K. Tanaka, H. Imahori, *J. Am. Chem. Soc.,* (2012), **134**, 1825-1839; i) Y. Matano, K. Matsumoto, Y. Nakao, H. Uno, S. Sakaki, H. Imahori, *J. Am. Chem. Soc.,* (2008), **130**, 4588-4589; j) S. Richeter, C. Jeandon, J.-P. Gisselbrecht, R. Graff, R. Ruppert, H. J. Callot, *Inorg. Chem.,* (2004), **43**, 251-263; k) S. Richeter, C. Jeandon, J.-P. Gisselbrecht, R. Ruppert, H. J. Callot, *J. Am. Chem. Soc.,* (2002), **124**, 6168-6179; l) S. Richeter, C. Jeandon, C. Sauber, J.-P. Gisselbrecht, R. Ruppert, H. J. Callot, *J. Porphyrins Phthalocyanines,* (2002), **6**, 423-430; m) S. Richeter, A. Hadj-Aïssa, C. Taffin, A. van der Lee, D. Leclercq, *Chem. Commun.,*

(2007), 2148-2150; (n) Y.-J. Chen, S.-S. Chen, S.-S. Lo, T.-H. Huang, C.-C. Wu, G.-H. Lee, S.-M. Peng, C.-Y. Yeh, *Chem. Commun.,* (2006), 1015-1017; (o) G. Langlois, S. M. Aly, C. P. Gros, J.-M. Barbe, P. D. Harvey*, New J. Chem.,* (2011), **35**, 1302-1314; p) A. Ferri, G. Polzonetti, S. Licoccia, R. Paolesse, D. Favretto, P. Traldi, M. V. Russo, *J. Chem. Soc., Dalton Trans*., (1998), **23**, 4063-4070; q) L. Liu, D. Fortin, P. D. Harvey, *Inorg. Chem.,* (2009), **48**, 5891-5900; r) F.-L. Jiang, D. Fortin, P. D. Harvey, *Inorg. Chem.,* (2010), **49**, 2614-2623; s) D. Bellows, S. M. Aly, C. P. Gros, M. El Ojaimi, J.-M. Barbe, R. Guilard, P. D. Harvey, *Inorg. Chem.,* (2009), **48**, 7613-7629; t) D. Bellows, T. Goudreault, S. M. Aly, D. Fortin, C. P. Gros, J.-M. Barbe, P. D. Harvey, *Organometallics,* (2010), **29**, 317-325; u) Y. Takao, T. Takeda, J.-Y. Watanabe, J.-I. Setsune, *Organometallics,* (1999), **18**, 2936-2938.

[5] J.-F. Lefebvre, D. Leclercq, J.-P. Gisselbrecht, S. Richeter, *Eur. J. Org. Chem.,* (2010), 1912-1920.

[6] a) W. A. Herrmann, M Elison, J. Fischer, C.; Köcher, G. R. J. Artus, *Angew. Chem. Int. Ed., (*1995), **34**, 2371-2374; b) W. A. Herrmann, M Elison, J. Fischer, C. Köcher, G. R. J. Artus, *Chem. Eur. J.,* (1996), **2**, 772-780; c) D. M. Khramov, E. L. Rosen, J. A. V. Er, P. D. Vut, V. M. Lynch, C. W. Bielawski, *Tetrahedron,* (2008), **64**, 6853-6862.

[7] a) W. A. Herrmann, V. P. W. Böhm, C. W. K. Gstöttmayr, M. Grosche, C.-P. Reisinger, T. Weskamp, *J. Organomet. Chem.,* (2001), 616-628; b) Y. Han, D. Yuan, Q. Teng, H. V. Huynh, *Organometallics,* (2011), **30,** 1224-1230.

[8] V. S.-Y. Lin, S. G. DiMagno, M. J. Therien, *Science,* (1994), **264**, 1105-1111.

[9] *Porphyrins Excited States and Dynamics* (Eds: M. Gouterman, P. M. Rentzepis, K. D. Straub), American Chemical Society, Washington DC, (1986**)**.

[10] F. Nifiatis, J. C. Athas, K. D. D. Gunaratne, Y. Gurung, K. M. Monette, P. J. Shivokevich; *The Open Spectroscopy Journal,* (2011), **5**, 1-12.

[11] D.L. Dexter, *J. Chem. Phys.,* (1953), **21**, 836-850.

[12] T. Förster, *Ann. Phys.,* (1948), **2**, 55-75.

[13] A. M. Soliman, M. Abdelhameed, E. Zysman-Colman, P. D. Harvey, *Chem. Commun.,* (2013), **49**, 5544-5546.

[14] a) A. Osuka, K. Maruyama, I. Yamazaki, N. Tamai, *Chem. Phys. Let*., (1990**)**, **165**, 392-396; b) J. Mårtensson, *Chem. Phys. Let.,* (1994), **229**, 449-456.

[15] D. Bai, A. C. Benniston, J. Hagon, H. Lemmetyinen, N. V. Tkachenko, R. W. Harrington, *Phys. Chem. Chem. Phys.,* (2013), **15**, 9854-9861.

[16] a) Y. R. Khan, T. E. Dykstra, G. D. Scholes, *Chem. Phys. Let.,* (2008), **461**, 305-309; b) G. D. Scholes, *Annu. Rev. Phys. Chem.,* (2003), **54,** 57-87, c) C. Curutchet, B. Mennucci, G. D. Scholes and D. Beljonne, *J. Phys. Chem. B,* (2008), **112,** 3759-3766; d) D. Beljonne, C. Curutchet, G. D. Scholes, R. J. Silbey, *J. Phys. Chem. B,* (2009), **113**, 6583-6599.

[17] B. Brizet, N. Desbois, A. Bonnot, A. Langlois, A. Dubois, J.-M. Barbe, C. P. Gros, C. Goze, F. Denat, P. D. Harvey, *Inorg. Chem.,* (2014), **53**, 3392-3403.

[18] C. P. Gros, S. M. Aly, M. E. Ojaimi, J.-M. Barbe, F. Brisach, A. S. Abs-El-Aziz, R. Guilard, P. D. Harvey, *J. Porphyrins Phthalocyanines*, (2007), **11**, 244-257.

[19] S. Faure, C. Stern, E. Espinosa, R. Guilard, P. D. Harvey, *Chem. Eur. J.,* (2005), **11**, 3469.

[20] M. J. Frisch, G. W. Trucks, H. B. Schlegel, G. E. Scuseria, M. A. Robb, J. R. Cheeseman, J. A. Montgomery, Jr., T. Vreven, K. N. Kudin, J. C. Burant, J. M. Millam, S. S. Iyengar, J. Tomasi, V. Barone, B. Mennucci, M. Cossi, G. Scalmani, N. Rega, G. A. Petersson, H. Nakatsuji, M. Hada, M. Ehara, K. Toyota, R. Fukuda, J. Hasegawa, M. Ishida, T. Nakajima, Y. Honda, O. Kitao, H. Nakai, M. Klene, X. Li, J. E. Knox, H. P. Hratchian, J. B. Cross, V. Bakken, C. Adamo, J. Jaramillo, R. Gomperts, R. E. Stratmann, O. Yazyev, A. J. Austin, R. Cammi, C. Pomelli, J. W. Ochterski, P. Y. Ayala, K. Morokuma, G. A. Voth, P. Salvador, J. J. Dannenberg, V. G. Zakrzewski, S. Dapprich, A. D. Daniels, M. C. Strain, O. Farkas, D. K. Malick, A. D. Rabuck, K. Raghavachari, J. B. Foresman, J. V. Ortiz, Q. Cui, A. G. Baboul, S. Clifford, J. Cioslowski, B. B. Stefanov, G. Liu, A. Liashenko, P. Piskorz, I. Komaromi, R. L. Martin, D. J. Fox, T. Keith, M. A. Al-

Laham, C. Y. Peng, A. Nanayakkara, M. Challacombe, P. M. W. Gill, B. Johnson, W. Chen, M. W. Wong, C. Gonzalez, and J. A. Pople, Gaussian, Inc., Wallingford CT, (2004).

[21] P. Hohenberg, W. Kohn, *Phys. Rev.,* (1964), **136**, B864-871.

[22] P. Hohenberg, W. Kohn. *J. Phys. Rev.,* (1965), **140**, A1133-1138.

[23] *Density-functional theory of atoms and molecules,* (Eds: R.G. Parr and W. Yang), Oxford Univ. Press, Oxford, (1989).

[24] *The Challenge of d and f Electrons,* (Eds*:* D. R. Salahub and M. C. Zerner) American Chemical Society, Washington DC, (1989).

[25] R. Bauernschmitt, X. Ahlrichs, *Chem. Phys. Lett.,* (1996), **256,** 454-464.

[26] M. E. Casida, C. Jamorski, K. C. Casida, D. R Salahub, *J. Chem. Phys.,* (1998), **108**, 4439-4449.

[27] R. E. Stratmann, G. E. Scuseria, M. J. Frisch, *J. Chem. Phys.,* (1998), **109**, 8218–8224.

[28] C. Lee, W. Yang, R. G. Parr, *Phys. Rev. B*, (1988), **37**, 785-789.

[29] B. Miehlich, A. Savin, H. Stoll, *Preuss. Chem. Phys. Lett.,(* 1989), **157**, 200-206.

[30] A. D. Becke, *J. Chem. Phys.,* (1993), **98**, 5648-5652.

3.2. SUPPORTING INFORMATION

Unexpected Drastic Decrease in the Excited State Electronic Communication Between Porphyrine Chromophores Covalently Linked by a Palladium(II) Bridge

Mohammed Abdelhameed,[a] Paul-Ludovic Karsenti,[a] Adam Langlois,[a] Jean-François Lefebvre,[b] Sébastien Richeter,*[c] Romain Ruppert*[b] and Pierre D. Harvey*[a]

Table of Contents:

Structures of the studied compounds

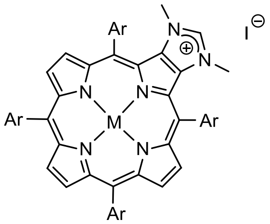

[Fb]: M = 2H, Ar = 4-*t*BuPh

[Zn]: M = Zn, Ar = 4-*t*BuPh

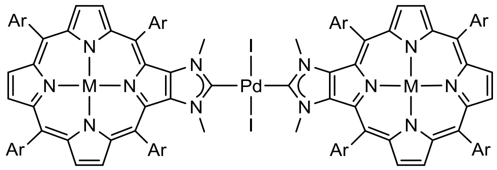

[Fb-Fb]: $M_1 = M_2 = 2H$, Ar = 4-*t*BuPh

[Zn-Fb]: M_1= Zn, $M_2 = H_2$, Ar = 4-*t*BuPh

[Zn-Zn]: $M_1 = M_2$ = Zn, Ar = 4-*t*BuPh

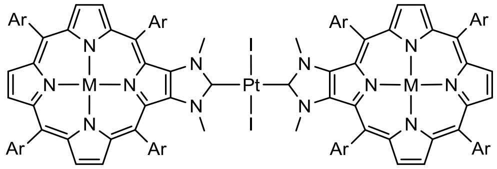

[PtFb-Fb]: $M_1 = M_2 = 2H$, Ar = 4-*t*BuPh

[PtZn-Fb]: M_1= Zn, $M_2 = H_2$, Ar = 4-*t*BuPh

[PtZn-Zn]: $M_1 = M_2$ = Zn, Ar = 4-*t*BuPh

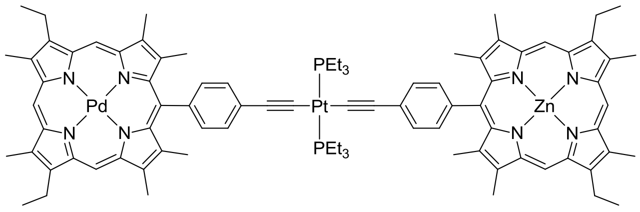

[Zn-Pt-Pd]:

The singlet optimized structures

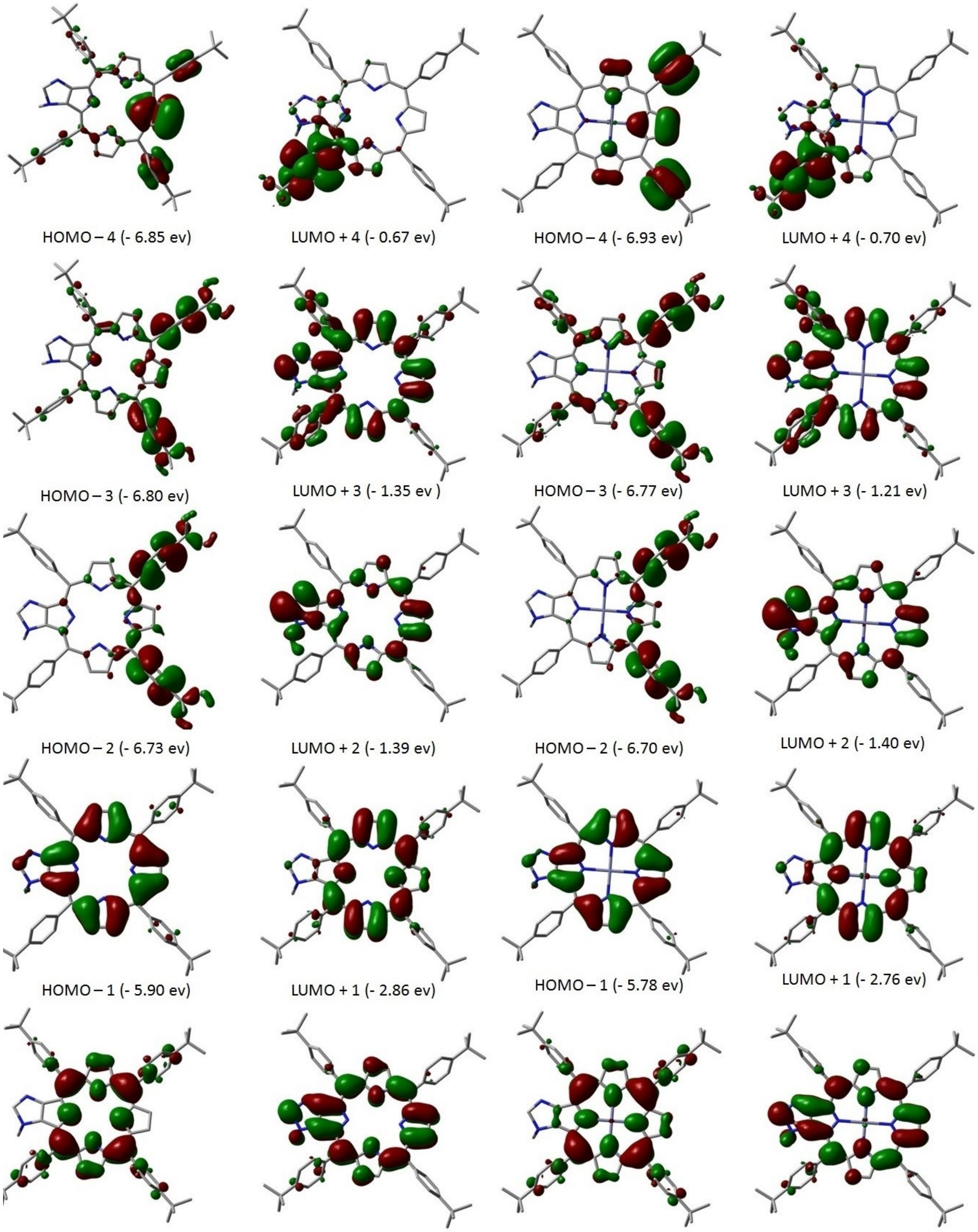

HOMO – 4 (- 6.85 ev)
LUMO + 4 (- 0.67 ev)
HOMO – 4 (- 6.93 ev)
LUMO + 4 (- 0.70 ev)

HOMO – 3 (- 6.80 ev)
LUMO + 3 (- 1.35 ev)
HOMO – 3 (- 6.77 ev)
LUMO + 3 (- 1.21 ev)

HOMO – 2 (- 6.73 ev)
LUMO + 2 (- 1.39 ev)
HOMO – 2 (- 6.70 ev)
LUMO + 2 (- 1.40 ev)

HOMO – 1 (- 5.90 ev)
LUMO + 1 (- 2.86 ev)
HOMO – 1 (- 5.78 ev)
LUMO + 1 (- 2.76 ev)

HOMO (- 5.46 ev)
LUMO (- 2.96 ev)
HOMO (- 5.54 ev)
LUMO (- 2.81 ev)

Figure S1. Representation of the frontier MOs for **[Fb]** and **[Zn]**.

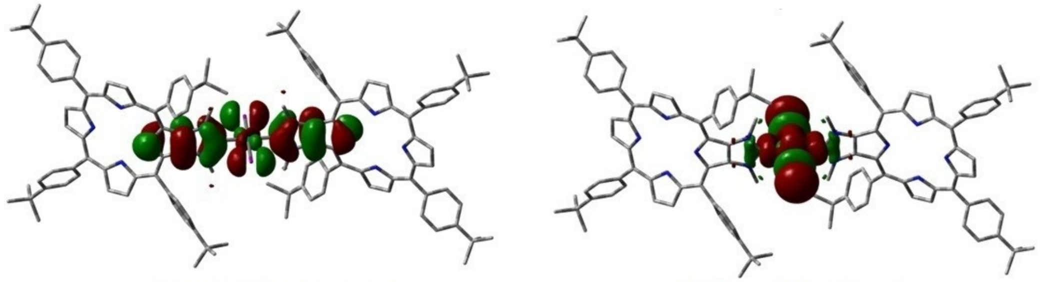

HOMO – 4 (- 5.88 ev) LUMO + 4 (- 2.0 ev)

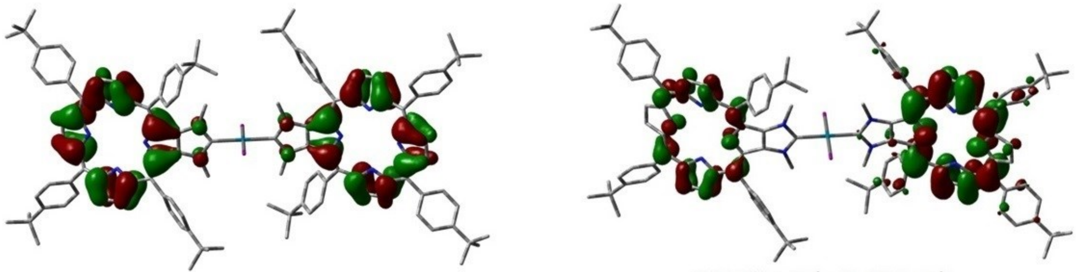

HOMO – 3 (- 5.44 ev) LUMO + 3 (- 2.460 ev)

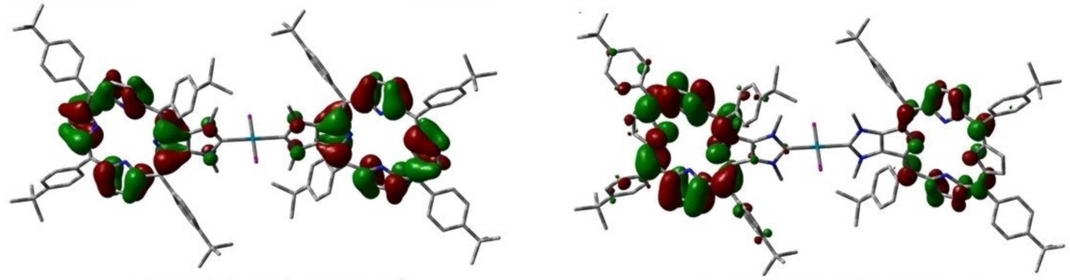

HOMO – 2 (- 5.44 ev) LUMO + 2 (-2.464 ev)

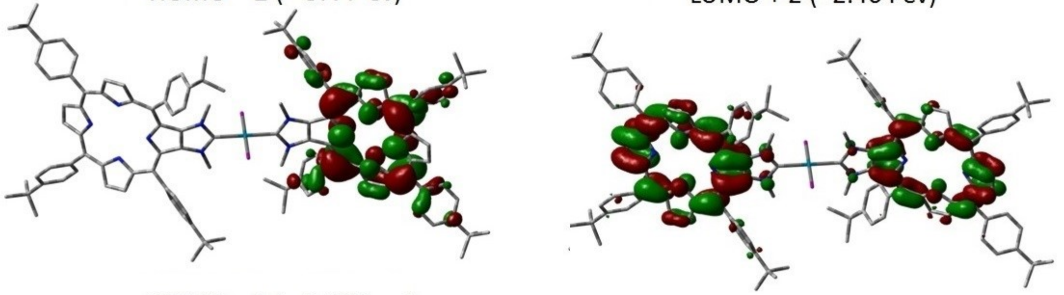

HOMO – 1 (- 5.049 ev) LUMO + 1 (- 2.48 ev)

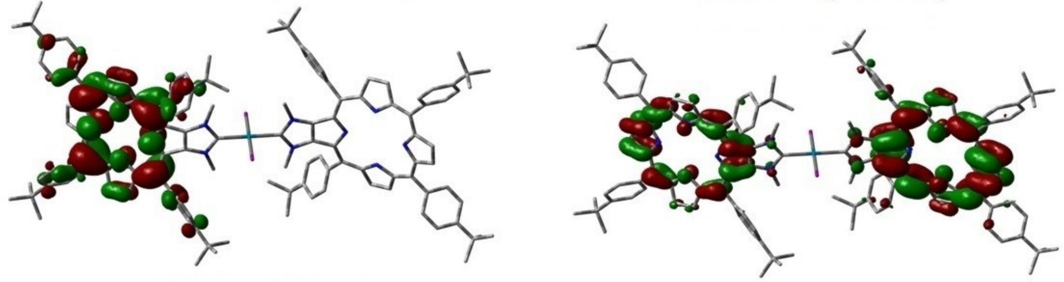

HOMO (- 5.047 ev) LUMO (- 2.48 ev)

Figure S2. Representation of the frontier MOs for **[Fb-Fb]**.

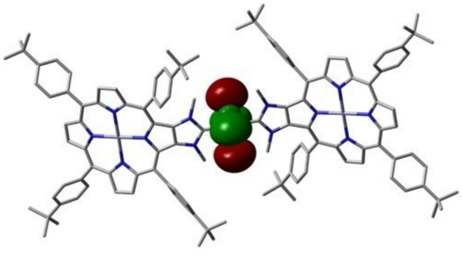

HOMO – 4 (- 5.97ev)

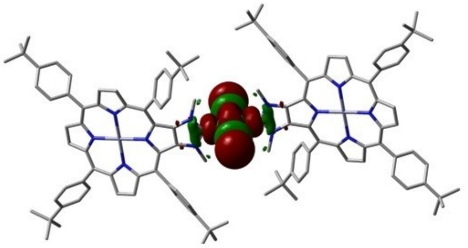

LUMO + 4 (- 2.04 ev)

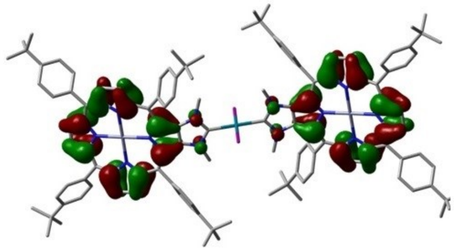

HOMO – 3 (- 5.32 ev)

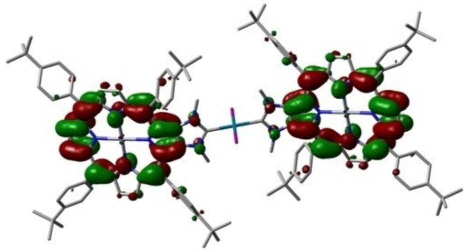

LUMO +3 (- 2.335 ev)

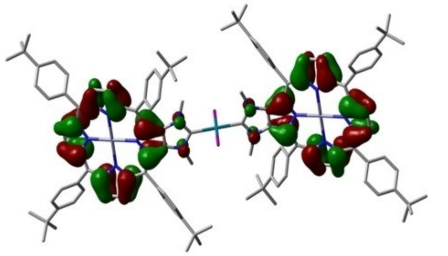

HOMO – 2 (- 5.31 ev)

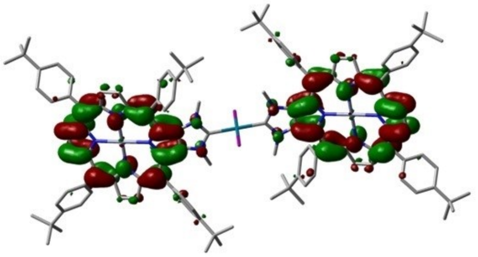

LUMO + 2 (- 2.34 ev)

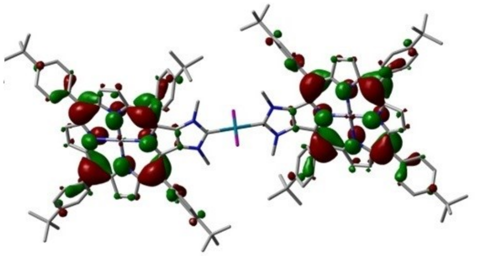

HOMO – 1 (- 5.04 ev)

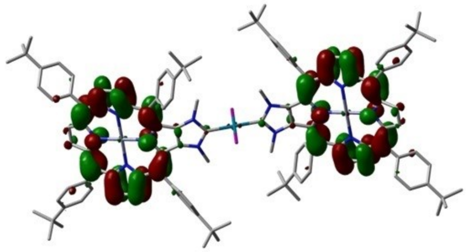

LUMO + 1 (- 2.35 ev)

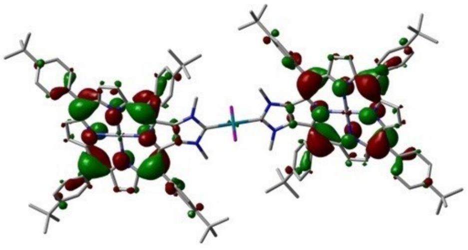

HOMO (- 5.03 ev)

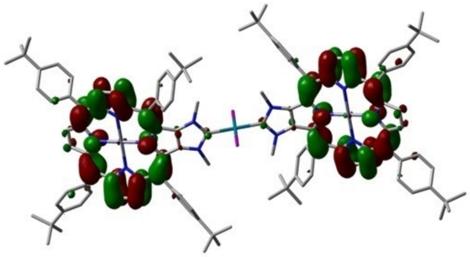

LUMO (- 2.36 ev)

Figure S3. Representation of the frontier MOs for **[Zn-Zn]**.

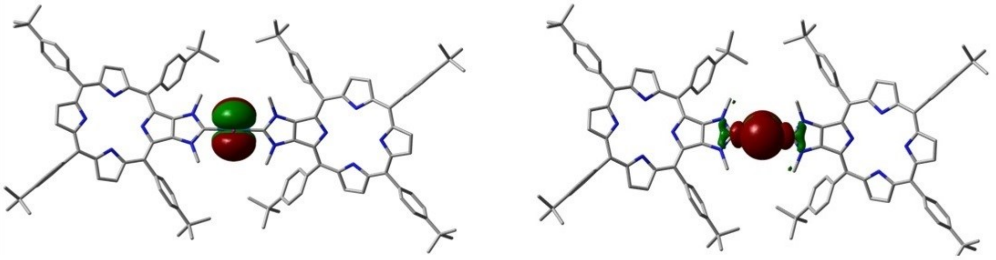

HOMO – 4 (- 5.78 ev)

LUMO + 4 (- 1.74 ev)

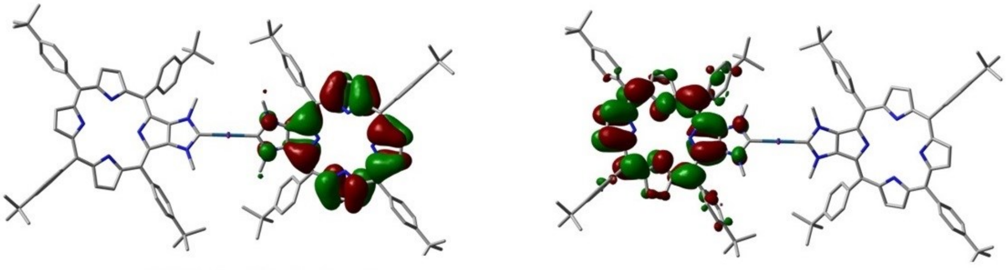

HOMO – 3 (- 5.44 ev)

LUMO + 3 (- 2.42 ev)

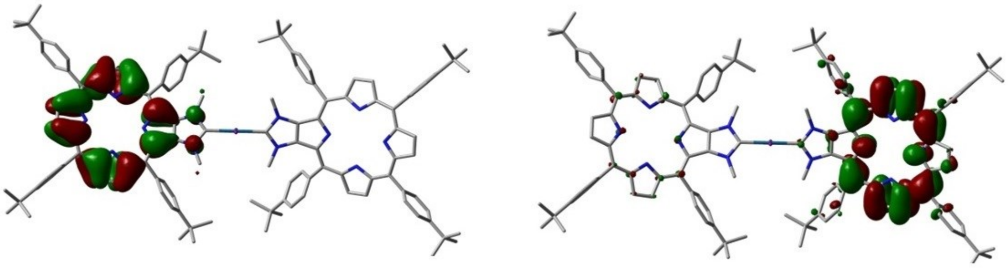

HOMO – 2 (- 5.40 ev)

LUMO + 2 (- 2.46 ev)

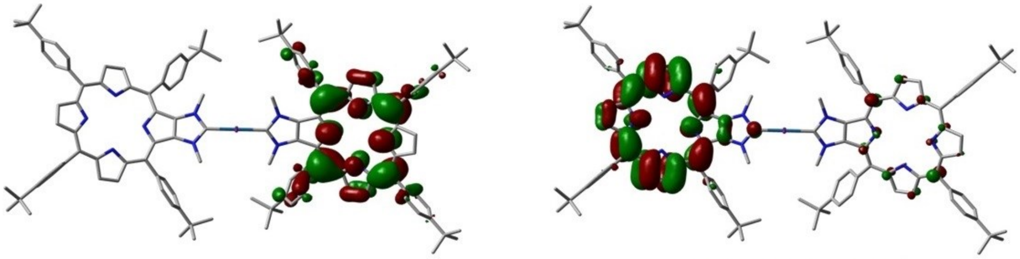

HOMO – 1 (- 5.14 ev)

LUMO + 1 (- 2.48 ev)

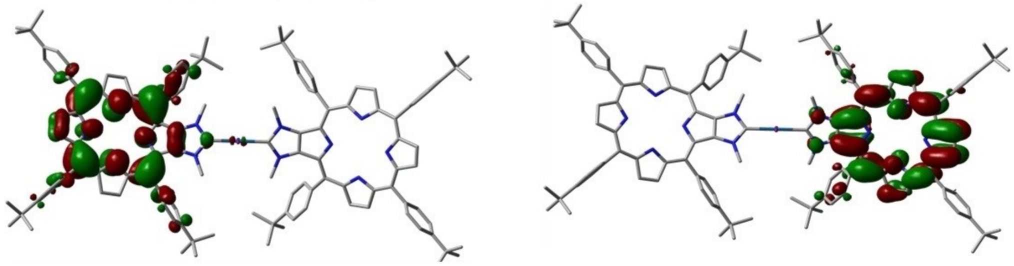

HOMO (- 5.13 ev)

LUMO (- 2.48 ev)

Figure S4. Representation of the frontier MOs for **[PtFb-Fb]**.

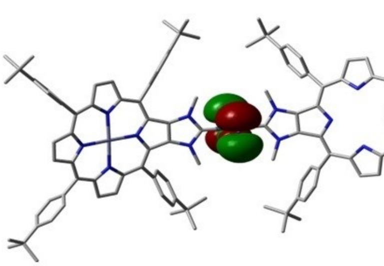
HOMO – 4 (- 5.75 ev)

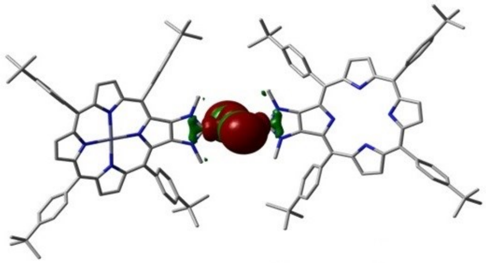
LUMO + 4 (- 1.69 ev)

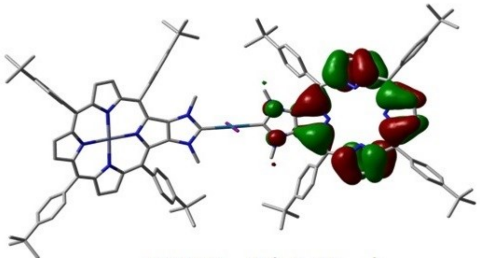
HOMO – 3 (- 5.43 ev)

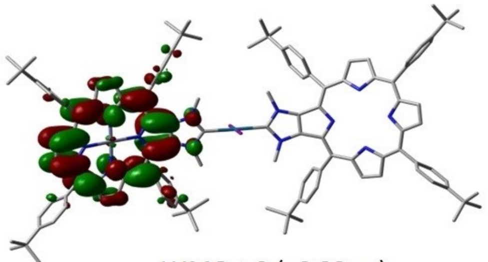
LUMO + 3 (- 2.32 ev)

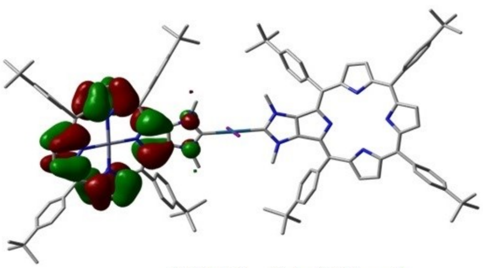
HOMO – 2 (- 5.31 ev)

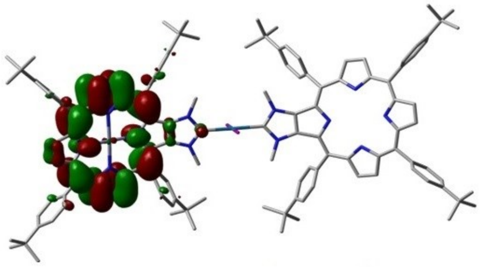
LUMO + 2 (- 2.34 ev)

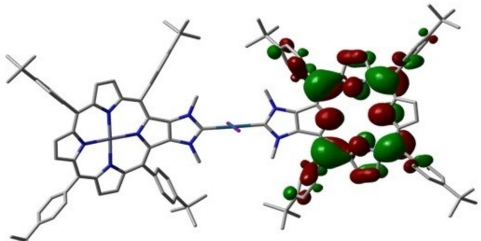
HOMO – 1 (- 5.13 ev)

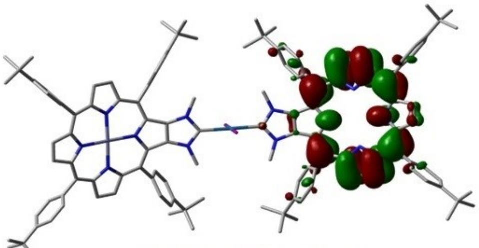
LUMO + 1 (- 2.45 ev)

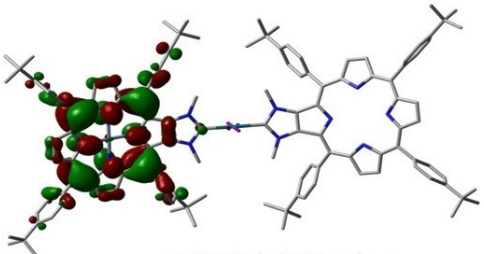
HOMO (- 5.11 ev)

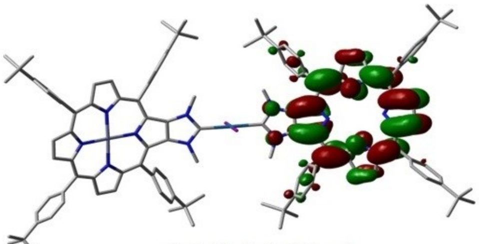
LUMO (- 2.48 ev)

Figure S5. Representation of the frontier MOs for **[PtZn-Fb]**.

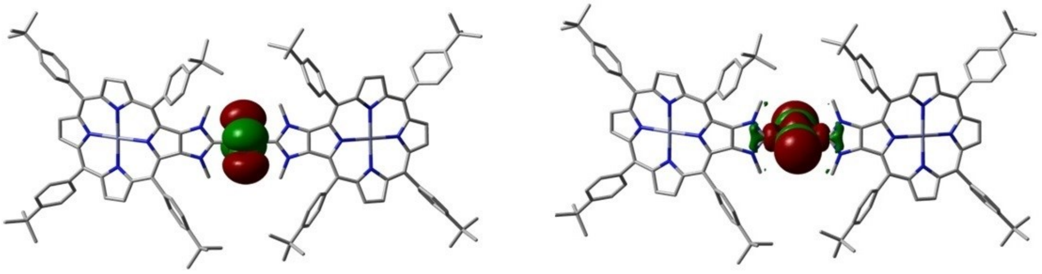

HOMO – 4 (- 5.77 ev)

LUMO + 4 (- 1.72 ev)

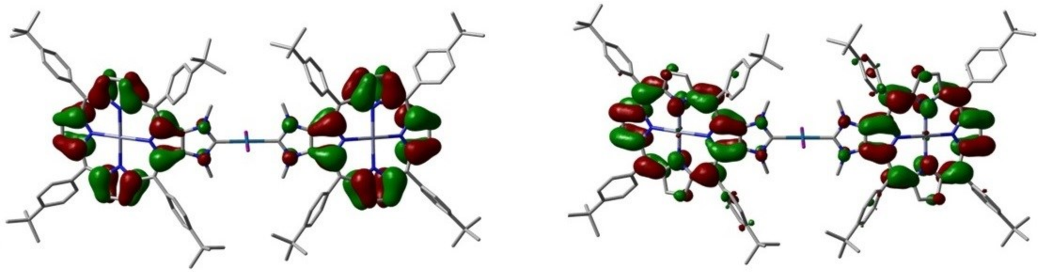

HOMO – 3 (- 5.31 ev)

LUMO + 3 (- 2.33 ev)

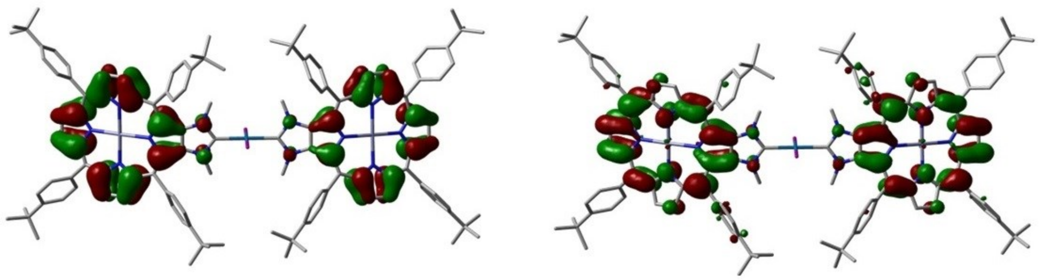

HOMO – 2 (- 5.31 ev)

LUMO + 2 (- 2.33 ev)

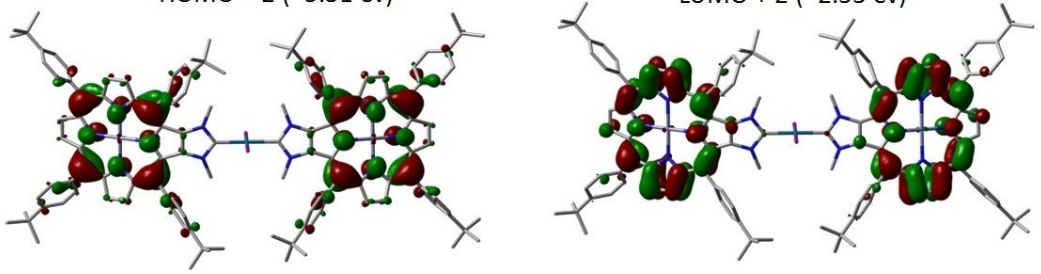

HOMO – 1 (- 5.08 ev)

LUMO + 1 (- 2.34 ev)

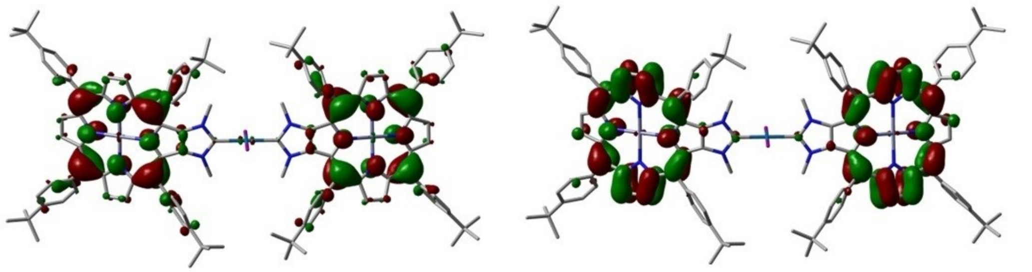

HOMO (- 5.07 ev)

LUMO (- 2.35 ev)

Figure S6. Representation of the frontier MOs for **[PtZn-Zn]**.

Atomic Contributions to the MOs

The tables below shows the % electronic contributions over given molecular fragments from HOMO - 4 to LUMO + 4. H and L refers to the HOMO and LUMO orbitals respectively. The fragments listed on the left of the table. The fragment exhibiting the largest atomic contributions is in bold.

Table S1. Relative atomic contributions of the various fragments in **[Fb-Fb]**.[a]

	2I	Pd	**[Fb1]**	**[Fb2]**	*t*Bu
L+4	**39.52**	**41.33**	9.54	9.59	0.02
L+3	0.03	0.06	**23.70**	**75.46**	0.75
L+2	0.09	0.05	**75.40**	**23.70**	0.76
L+1	0.01	0.01	**65.96**	**33.35**	0.68
LUMO	0.01	0.02	**33.40**	**65.89**	0.67
HOMO	0.01	0.02	**98.29**	0.03	1.65
H-1	0.01	0.02	0.03	**98.30**	1.64
H-2	0.02	0.02	**46.52**	**53.38**	0.06
H-3	0.03	0.01	**53.43**	**46.47**	0.06
H-4	11.18	3.38	**42.10**	**43.28**	0.06

Table S2. Relative atomic contributions of the various fragments in **[Zn-Zn]**.[b]

	2I	Pd	**[Zn1]**	Zn atom 1	**[Zn2]**	Zn atom 2	*t*Bu
L+4	**39.46**	**40.98**	9.75	0.02	9.75	0.02	0.01
L+3	0.01	0.01	**49.16**	0.11	**49.52**	0.11	1.08
L+2	0.01	0.02	**49.15**	0.11	**49.51**	0.11	1.08
L+1	0.14	0.18	**48.89**	0.12	**49.43**	0.12	1.11
LUMO	0.19	0.09	**48.92**	0.12	**49.46**	0.12	1.09
HOMO	0.08	0.16	**47.84**	0.63	**48.50**	0.63	2.17
H-1	0.17	0.02	**47.84**	0.64	**48.51**	0.64	2.18
H-2	0.01	0.02	**49.83**	0.01	**49.95**	0.01	0.16
H-3	0.03	0.01	**49.83**	0.01	**49.95**	0.01	0.16
H-4	75.53	24.26	0.10	0.00	0.10	0.00	0.02

Table S3. Relative atomic contributions of the various fragments in **[PtFb-Fb]**.[a]

	[Fb1]	**[Fb2]**	Pt	I 1	I 2
L+4	3.07	3.06	**49.87**	**21.52**	**22.48**
L+3	**99.90**	0.05	0.04	0.01	0.00
L+2	5.60	**94.28**	0.09	0.01	0.02
L+1	**91.45**	8.12	0.24	0.05	0.18
LUMO	2.34	**97.57**	0.05	0.01	0.02
HOMO	**98.81**	0.59	0.44	0.11	0.06
H-1	0.45	**99.51**	0.03	0.01	0.00
H-2	**99.88**	0.02	0.06	0.03	0.02
H-3	0.02	**99.88**	0.06	0.03	0.01
H-4	0.27	0.22	**37.69**	**31.44**	**30.38**

Table S4. Relative atomic contributions of the various fragments in **[PtZn-Zn]**.[b]

	[Zn1]	**[Zn2]**	Zn atom 1	Zn atom 2	I 1	I 2	Pt
L+4	3.01	3.01	0.01	0.01	**21.74**	**22.45**	**49.77**
L+3	**51.97**	**47.78**	0.11	0.12	0.00	0.00	0.02
L+2	**47.78**	**51.94**	0.12	0.11	0.01	0.00	0.04
L+1	**49.82**	**49.76**	0.13	0.13	0.01	0.01	0.14
LUMO	**49.62**	**49.70**	0.14	0.14	0.04	0.21	0.15
HOMO	**47.90**	**50.57**	0.59	0.56	0.00	0.01	0.37
H-1	**50.61**	**47.94**	0.58	0.61	0.13	0.05	0.08
H-2	**39.38**	**60.55**	0.02	0.01	0.00	0.00	0.04
H-3	**60.52**	**39.37**	0.01	0.02	0.02	0.01	0.05
H-4	0.13	0.13	0.00	0.00	**31.44**	**30.51**	**37.78**

a) **[Fb1], [Fb2] and [Fb]** : The free base porphyrin. b) **[Zn1], [Zn2] and [Zn]** : Zn-containing porphyrin (except Zn).

The TDDFT Electronic Transition Tables

Table S5. The electronic transitions of **[Fb]:**

λ(nm)	f	Major contributions (%)	λ(nm)	f	Major contributions (%)
622.6	0.15	H-1→L+1 (15), H→L (84)	316.4	0.00	H→L+3 (76)
554.7	0.01	H-1→L (44), H→L+1 (55)	314.6	0.02	H-13→L (45), H-10→L+1 (32), H→L+3 (11)
429.0	0.44	H-1→L+1 (53), H→L+2 (34)	311.0	0.00	H-9→L+1 (83)
423.7	1.73	H-1→L (52), H→L+1 (39)	310.2	0.11	H-14→L (34), H-13→L (24), H-10→L+1 (22)
408.3	0.01	H-4→L (83)	309.4	0.09	H-14→L (44), H-13→L (14), H-10→L+1 (25), H-9→L+1 (10)
405.4	0.12	H-2→L (96)	304.2	0.01	H-15→L+1 (48), H-13→L+1 (13), H-12→L+1 (13), H-11→L+1 (18)
395.0	0.05	H-3→L (89)	302.3	0.02	H-15→L+1 (37), H-11→L+1 (53)
382.6	0.59	H-2→L+1 (18), H-1→L+1 (14), H→L+2 (40)	301.1	0.01	H-12→L+1 (73), H-11→L+1 (15)
372.4	0.02	H-7→L (31), H-2→L+1 (55)	297.7	0.01	H-15→L+1 (12), H-13→L+1 (72)
370.0	0.16	H-7→L (43), H-2→L+1 (22)	293.4	0.10	H-14→L+1 (89)
367.2	0.05	H-5→L (85)	288.4	0.01	H-16→L (21), H-2→L+2 (35), H-1→L+3 (33)
365.8	0.00	H-8→L (39), H-7→L (10), H-6→L (36)	286.1	0.00	H-2→L+2 (55), H-1→L+3 (14), H→L+4 (22)
364.8	0.01	H-8→L (37), H-6→L (44)	285.7	0.00	H-1→L+3 (17), H→L+4 (63)
360.4	0.00	H-4→L+1 (46), H-3→L+1 (51)	281.8	0.04	H-4→L+2 (71), H→L+5 (17)
357.1	0.04	H-4→L+1 (49), H-3→L+1 (36)	281.5	0.03	H-4→L+2 (15), H→L+5 (74)
344.4	0.12	H-12→L (15), H-10→L (21), H-1→L+2 (36)	281.3	0.00	H-3→L+2 (86)
343.3	0.08	H-9→L (79)	278.4	0.00	H→L+6 (88)
341.8	0.05	H-12→L (26), H-1→L+2 (30)	276.7	0.01	H-18→L (11), H-12→L+2 (20), H-8→L+2 (10), H-7→L+2 (33)
339.3	0.00	H-12→L (13), H-6→L+1 (31), H-5→L+1 (48)	274.9	0.01	H-17→L (54), H-16→L+1 (29)
339.1	0.02	H-6→L+1 (45), H-5→L+1 (46)	274.2	0.00	H-16→L (27), H-8→L+2 (15), H-7→L+2 (15)
334.5	0.01	H-7→L+1 (90)	273.8	0.03	H-16→L (19), H-7→L+2 (31), H-1→L+3 (11)
333.2	0.30	H-12→L (25), H-10→L (39), H-6→L+1 (10)	270.8	0.01	H→L+7 (91)
331.9	0.13	H-11→L (77)	267.9	0.01	H-8→L+2 (23), H-5→L+2 (41)
327.2	0.01	H-15→L (88)	267.1	0.02	H-8→L+2 (25), H-5→L+2 (43)
323.5	0.11	H-8→L+1 (79)	265.9	0.01	H-6→L+2 (81)

Table S6. The electronic transitions of **[Zn]:**

λ(nm)	f	Major contributions (%)	λ(nm)	f	Major contributions (%)
585.2	0.15	H-1→L+1 (16), H→L (83)	324.5	0.00	H-13→L (90)
555.4	0.00	H-1→L (47), H→L+1 (51)	321.5	0.02	H-11→L+1 (23), H-10→L+1 (40), H-8→L+1 (20)
428.2	0.44	H-1→L+1 (53), H→L (10), H→L+2 (32)	314.9	0.17	H-14→L (47), H-11→L+1 (31), H-10→L+1 (12)
425.2	1.67	H-1→L (48), H→L+1 (41)	313.3	0.19	H-14→L (41), H-11→L+1 (30), H-10→L+1 (14)
394.0	0.04	H-2→L (98)	310.7	0.00	H→L+3 (89)
390.1	0.00	H-8→L (20), H-7→L (51), H-6→L (20)	303.0	0.00	H-12→L+1 (94)
387.6	0.19	H-3→L (71), H→L+2 (18)	300.7	0.02	H-15→L (65), H-7→L+2 (11)
377.2	0.64	H-3→L (23), H-1→L+1 (14), H→L+2 (39)	295.3	0.00	H-13→L+1 (93)
372.6	0.04	H-8→L (22), H-4→L (68)	289.3	0.07	H-14→L+1 (51), H-1→L+3 (37)
364.7	0.02	H-2→L+1 (90)	287.7	0.03	H-14→L+1 (35), H-2→L+2 (21), H-1→L+3 (20), H→L+4 (13)
362.7	0.03	H-7→L (23), H-6→L (55), H-5→L (10)	286.4	0.01	H-2→L+2 (70), H-1→L+3 (17)
360.5	0.00	H-8→L+1 (23), H-7→L+1 (47), H-6→L+1 (20)	285.1	0.03	H-1→L+3 (11), H→L+4 (70)
358.5	0.02	H-9→L (10), H-5→L (73)	282.8	0.02	H-3→L+2 (86)
356.2	0.07	H-8→L (31), H-7→L (10), H-4→L (15), H-3→L+1 (11), H-1→L+2 (21)	281.1	0.01	H→L+5 (87)
355.0	0.04	H-8→L (13), H-3→L+1 (46), H-1→L+2 (17)	277.8	0.00	H-15→L (21), H-8→L+2 (11), H-7→L+2 (35), H-6→L+2 (19)
351.6	0.02	H-9→L (54), H-1→L+2 (18)	276.6	0.00	H-6→L+2 (15), H→L+6 (66)
349.1	0.02	H-11→L (52)	275.7	0.01	H-17→L+1 (11), H-16→L (50), H→L+6 (15)
347.6	0.11	H-10→L (59)	275.1	0.01	H-7→L+2 (24), H-6→L+2 (45), H→L+6 (12)
346.2	0.11	H-10→L (12), H-9→L (18), H-9→L+1 (11), H-5→L+1 (12), H-1→L+2 (17)	273.0	0.00	H-4→L+2 (77)
341.9	0.04	H-4→L+1 (79)	271.8	0.01	H-17→L (49), H-16→L (10), H→L+7 (10)
339.8	0.01	H-11→L (27), H-9→L+1 (16), H-5→L+1 (24)	270.4	0.01	H→L+7 (85)
333.4	0.00	H-12→L (90)	268.5	0.01	H-9→L+2 (26), H-5→L+2 (54)
329.6	0.03	H-7→L+1 (20), H-6→L+1 (18), H-5→L+1 (45)	267.9	0.00	H-10→L+2 (25), H-8→L+2 (41), H-7→L+2 (10), H-5→L+2 (12)
327.8	0.01	H-10→L+1 (16), H-8→L+1 (48)	265.2	0.02	H-1→L+4 (86)

Table S7. The electronic transitions of **[Fb-Fb]:**

λ(nm)	f	Major contributions (%)	λ(nm)	f	Major contributions (%)
603.1	0.01	H-3→L+2 (14), H-2→L+3 (10), H-1→L (11), H→L (18), →L+1 (37)	405.6	0.02	H-3→L+4 (88)
602.3	0.15	H-3→L+3 (14), H-2→L+2 (10), H-1→L (36), H-1→L+1 (19), →L+1 (10)	405.5	0.00	H-9→L+4 (52), H-3→L+4 (10)
566.2	0.18	H-3→L+1 (13), →L+2 (51), →L+3 (15)	400.3	0.00	H-5→L (90)
565.5	0.07	H-3→L (12), H-1→L+2 (16), H-1→L+3 (49)	400.2	0.00	H-5→L+1 (90)
520.0	0.00	→L (66), →L+1 (34)	393.9	0.00	H-5→L+2 (100)
519.5	0.00	H-1→L (34), H-1→L+1 (66)	393.3	0.00	H-5→L+3 (100)
513.9	0.00	H-1→L+2 (75), H-1→L+3 (24)	392.6	0.00	H-7→L+4 (16), H-4→L+4 (76)
513.9	0.00	H→L+2 (23), →L+3 (76)	387.9	0.00	H-7→L+1 (12), H-6→L (17), H-6→L+1 (32), H-4→L (11), H-4→L+1 (22)
458.7	0.00	H-1→L+4 (13), →L+4 (86)	387.6	0.00	H-7→L (13), H-6→L (32), H-6→L+1 (16), H-4→L (21), H-4→L+1 (11)
458.2	0.00	H-1→L+4 (86), →L+4 (13)	382.5	0.00	H-7→L+2 (11), H-6→L+2 (40), H-6→L+3 (20), H-4→L+2 (23)
447.8	0.00	H-3→L (35), H-3→L+1 (18), H-2→L (32), H-2→L+1 (15)	382.0	0.00	H-7→L+3 (10), H-6→L+2 (22), H-6→L+3 (39), H-4→L+3 (23)
447.8	0.00	H-3→L (16), H-3→L+1 (30), H-2→L (18), H-2→L+1 (36)	380.3	0.00	H-7→L (78), H-6→L+1 (15)
444.4	0.04	H-6→L (23), H-4→L (27), H-4→L+1 (28)	380.2	0.00	H-7→L+1 (79), H-6→L (14)
444.2	0.08	H-6→L+1 (24), H-4→L (28), H-4→L+1 (26)	375.7	0.00	H-8→L (64), H-8→L+1 (30)
443.5	0.00	H-3→L+2 (33), H-3→L+3 (12), H-2→L+2 (36), H-2→L+3 (15)	375.6	0.00	H-8→L (30), H-8→L+1 (64)
443.2	0.00	H-3→L+2 (10), H-3→L+3 (42), H-2→L+3 (36)	375.1	0.01	H-8→L+4 (17), H-7→L+2 (64), H-6→L+3 (11)
439.5	0.00	H-5→L+4 (96)	374.4	0.00	H-7→L+3 (80)
433.7	0.00	H-7→L+4 (76), H-4→L+4 (16)	373.8	0.02	H-8→L+4 (72), H-7→L+2 (16)
424.5	4.39	H-3→L+1 (30), H-2→L (29), H-1→L+3 (10), →L+2 (10)	372.6	0.04	H-13→L+1 (27), H-12→L (44)
417.5	0.14	H-6→L+2 (15), H-6→L+3 (10), H-4→L+2 (59)	372.2	0.41	H-13→L (30), H-13→L+1 (13), H-12→L+1 (34)
417.4	0.06	H-6→L+2 (11), H-6→L+3 (14), H-4→L+3 (62)	369.5	0.00	H-8→L+2 (98)
416.6	0.02	H-3→L+2 (28), H-2→L+3 (27)	368.9	0.00	H-8→L+3 (94)
415.1	0.01	H-9→L+4 (16), H-3→L (25), H-2→L+1 (25)	362.6	0.05	H-6→L+4 (95)
413.5	2.83	H-3→L+3 (28), H-2→L+2 (25)	357.3	0.02	H-13→L+3 (16), H-12→L+3 (33), H-11→L+3 (16)
405.8	0.00	H-2→L+4 (96)	357.2	0.02	H-13→L+2 (33), H-13→L+3 (11), H-12→L+2 (21), H-10→L+2 (12)

Table S8. The electronic transitions of **[Zn-Zn]:**

λ(nm)	f	Major contributions (%)	λ(nm)	f	Major contributions (%)
565.2	0.15	H-3→L+3 (16), H-2→L+2 (16), H-1→L+1 (33), H→L (35)	382.0	0.00	H-5→L+1 (30), H-5→L+4 (54)
564.9	0.00	H-3→L+2 (16), H-2→L+3 (16), H-1→L (33), H→L+1 (33)	381.0	0.03	H-7→L+1 (24), H-5→L (62)
564.3	0.00	H-3→L (17), H-2→L+1 (17), H-1→L+2 (32), H→L+3 (33)	379.1	0.00	H-7→L (18), H-5→L+1 (35), H-5→L+4 (38)
563.8	0.12	H-3→L+1 (17), H-2→L (18), H-1→L+3 (32), H→L+2 (33)	378.5	0.00	H-4→L (16), H-4→L+2 (83)
495.4	0.00	H-1→L (50), H→L+1 (50)	378.3	0.00	H-4→L+3 (98)
495.4	0.00	H-1→L+1 (51), H→L (49)	378.2	0.00	H-4→L (83), H-4→L+2 (16)
492.1	0.00	H-1→L+2 (50), H→L+3 (50)	377.3	0.00	H-4→L+1 (97)
492.1	0.00	H-1→L+3 (50), H→L+2 (50)	375.4	0.01	H-8→L+4 (87)
472.1	0.00	H→L+4 (95)	363.5	0.00	H-6→L+2 (57), H-5→L+2 (33)
468.0	0.00	H-1→L+4 (99)	363.4	0.00	H-6→L+3 (57), H-5→L+3 (33)
445.7	0.00	H-3→L (50), H-2→L+1 (50)	362.5	0.01	H-7→L+1 (11), H-6→L (62), H-5→L (21)
445.7	0.00	H-3→L+1 (49), H-2→L (50)	362.2	0.00	H-20→L+1 (18), H-19→L (18), H-8→L (47)
443.1	0.00	H-3→L+3 (49), H-2→L+2 (50)	361.9	0.17	H-20→L (20), H-19→L+1 (19), H-8→L+1 (40)
443.1	0.00	H-3→L+2 (50), H-2→L+3 (50)	361.7	0.00	H-7→L (13), H-6→L+1 (60), H-5→L+1 (24)
440.4	0.00	H-4→L+4 (95)	361.1	0.00	H-20→L+3 (14), H-19→L+2 (13), H-8→L+2 (59)
427.8	0.00	H-6→L+4 (82)	361.0	0.13	H-20→L+2 (14), H-19→L+3 (13), H-8→L+3 (59)
427.4	0.00	H-2→L+4 (90)	351.9	0.00	H-11→L (31), H-10→L+1 (30)
427.2	0.05	H-3→L+4 (97)	351.9	0.02	H-11→L+1 (30), H-10→L (32)
425.2	4.24	H-3→L+3 (32), H-2→L+2 (31), H-1→L+1 (15), H→L (14)	351.4	0.02	H-7→L+1 (48), H-7→L+4 (13), H-6→L (22)
416.5	0.00	H-3→L (29), H-2→L+1 (32), H-1→L+2 (16), H→L+3 (16)	350.8	0.00	H-7→L (56), H-6→L+1 (30)
416.2	0.00	H-3→L+2 (28), H-2→L+3 (28), H-1→L (14), H→L+1 (14)	350.3	0.00	H-7→L+2 (53), H-6→L+3 (28), H-5→L+3 (11)
413.6	2.93	H-3→L+1 (32), H-2→L (29), H-1→L+3 (16), H→L+2 (16)	350.3	0.00	H-7→L+3 (55), H-6→L+2 (28), H-5→L+2 (12)
404.6	0.00	H-15→L+4 (46), H-9→L+4 (34)	350.1	0.00	H-20→L+1 (13), H-19→L (17), H-8→L (48)
394.6	0.00	H-7→L+2 (33), H-6→L+3 (11), H-5→L+3 (53)	349.8	0.06	H-20→L (11), H-19→L+1 (13), H-8→L+1 (45)
394.5	0.06	H-7→L+3 (32), H-6→L+2 (11), H-5→L+2 (53)	349.3	0.00	H-20→L+3 (18), H-19→L+2 (22), H-8→L+2 (39)

Theoretical UV-Vis Spectra

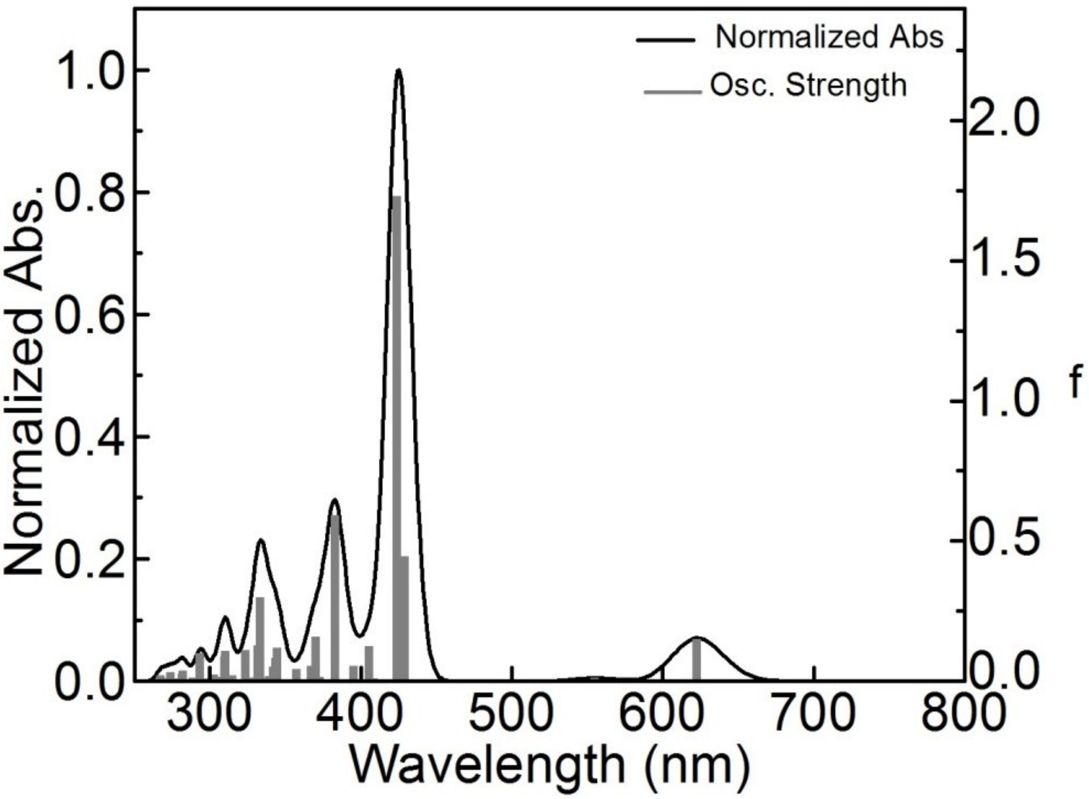

Figure S7. Bar graph showing the oscillator strength as a function of the calculated positions of the electronic transitions (gray) for **[Fb]**. The black line is the generated spectrum when assigning 1000cm^{-1} for each transition.

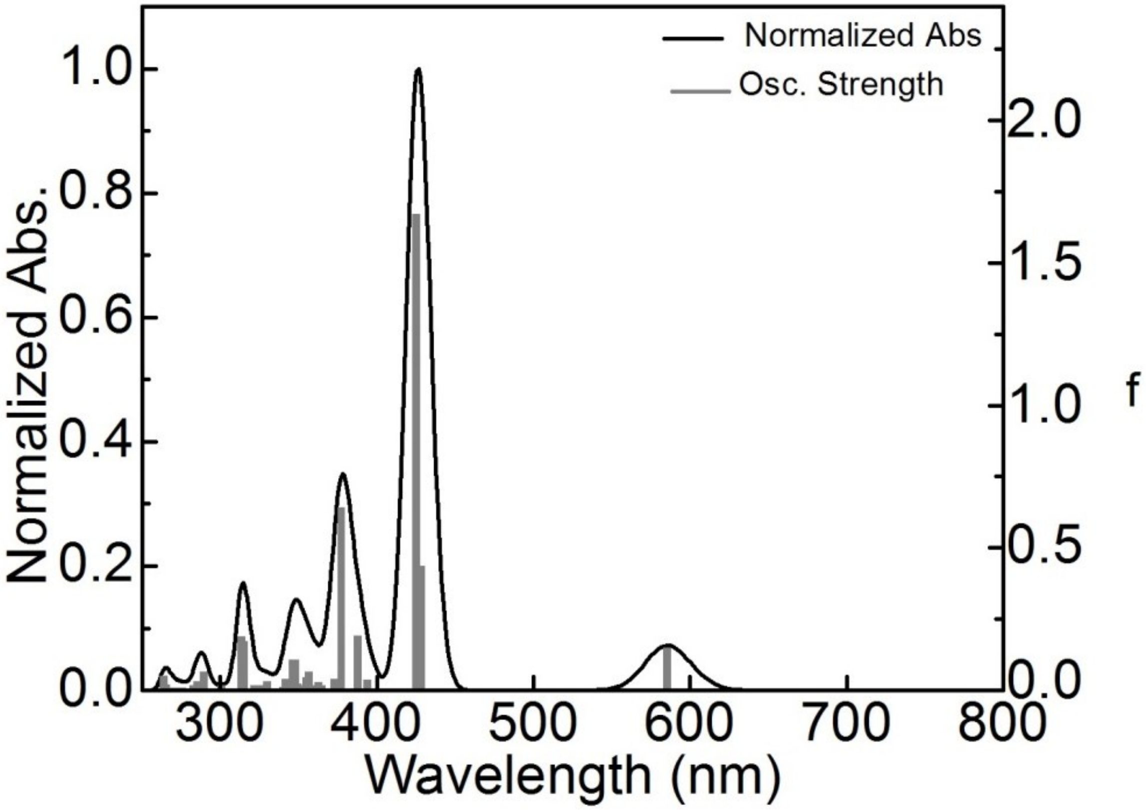

Figure S8. Bar graph showing the oscillator strength as a function of the calculated positions of the electronic transitions (gray) for **[Zn]**. The black line is the generated spectrum when assigning 1000cm^{-1} for each transition.

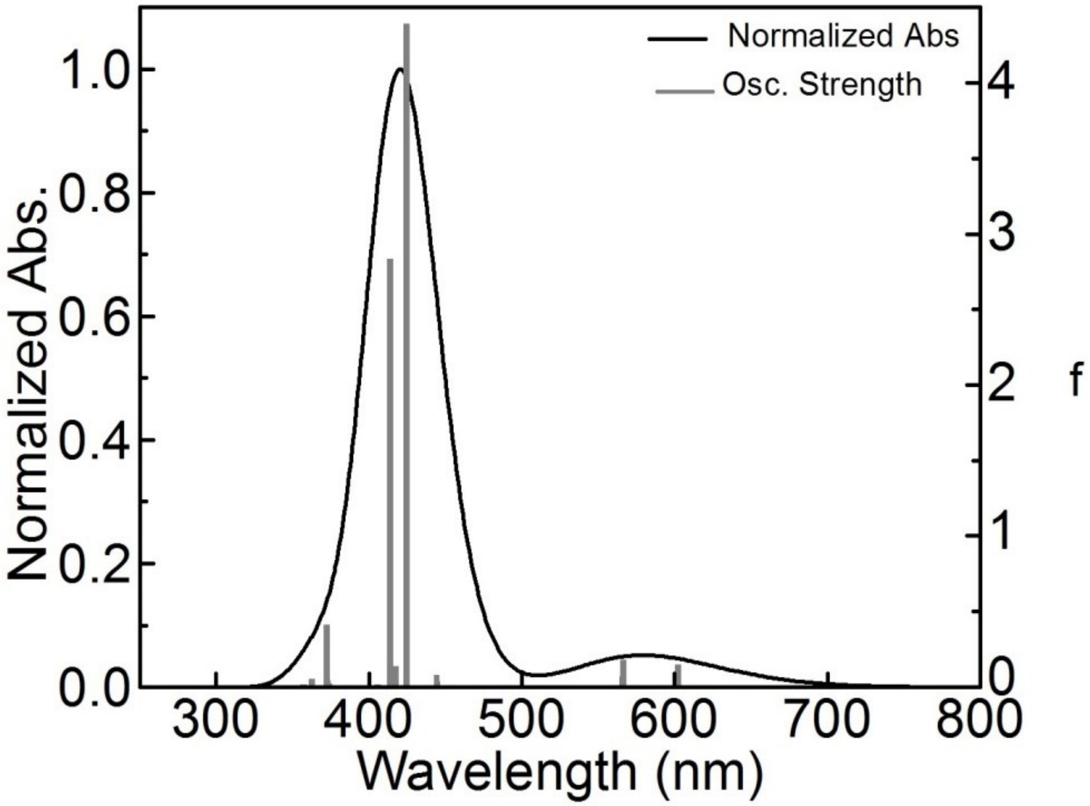

Figure S9. Bar graph showing the oscillator strength as a function of the calculated positions of the electronic transitions (gray) for **[Fb-Fb]**. The black line is the generated spectrum when assigning 1000 $\mathrm{cm^{-1}}$ for each transition.

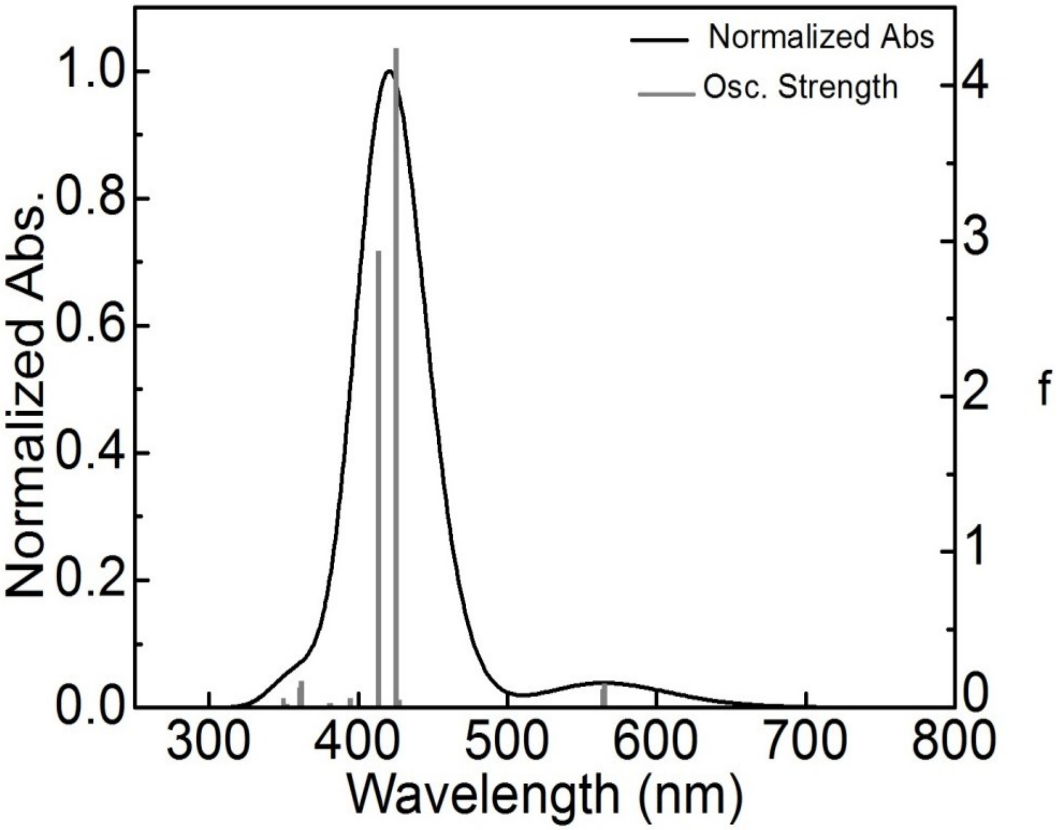

Figure S10. Bar graph showing the oscillator strength as a function of the calculated positions of the electronic transitions (gray) for **[Zn-Zn]**. The black line is the generated spectrum when assigning 1000cm^{-1} for each transition.

The Triplet Optimized Structure

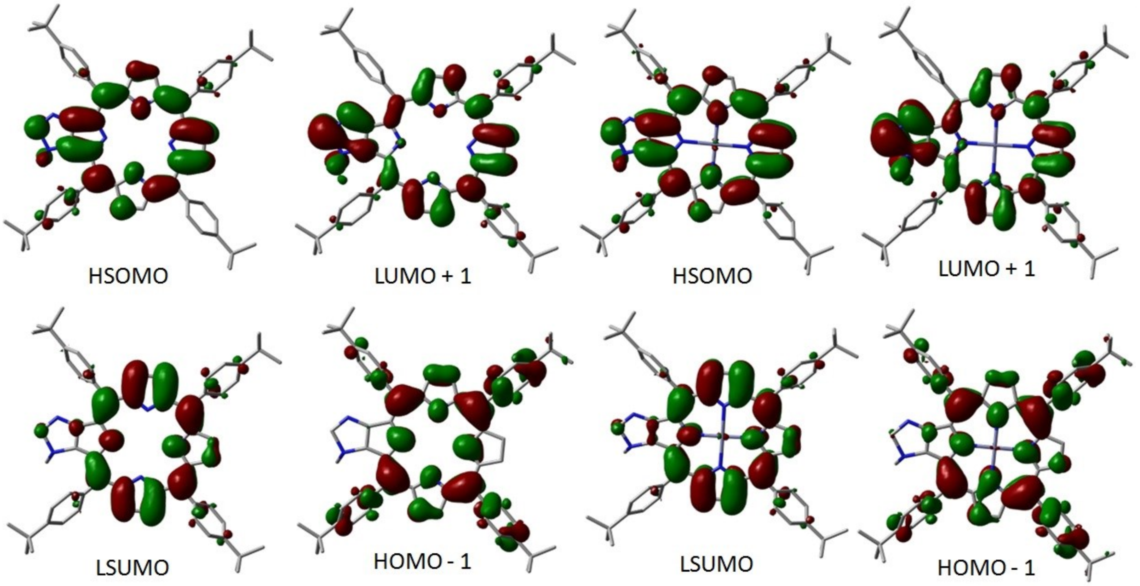

Figure S11. Frontier MO representations of the **[Fb]** and **[Zn]** in their lowest energy triplet states.

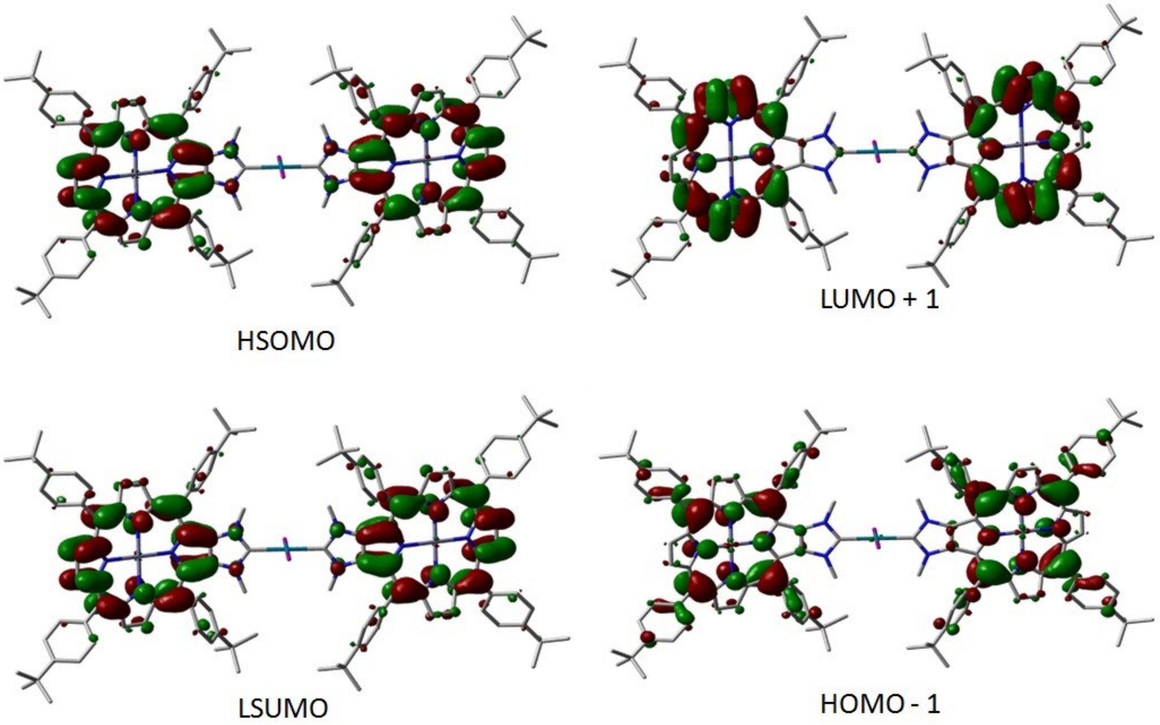

Figure S12. Frontier MO representations of the **[Zn-Zn]** in its lowest energy triplet state.

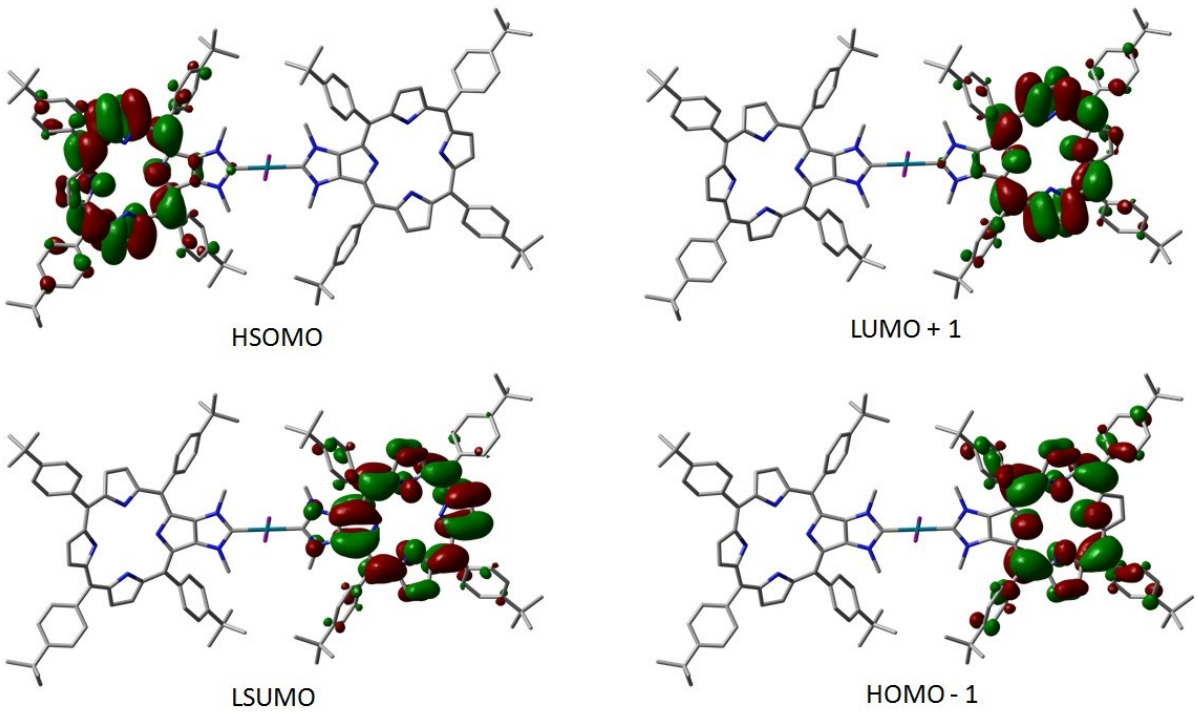

Figure S13. Frontier MO representations of the **[Fb-Fb]** in its lowest energy triplet state.

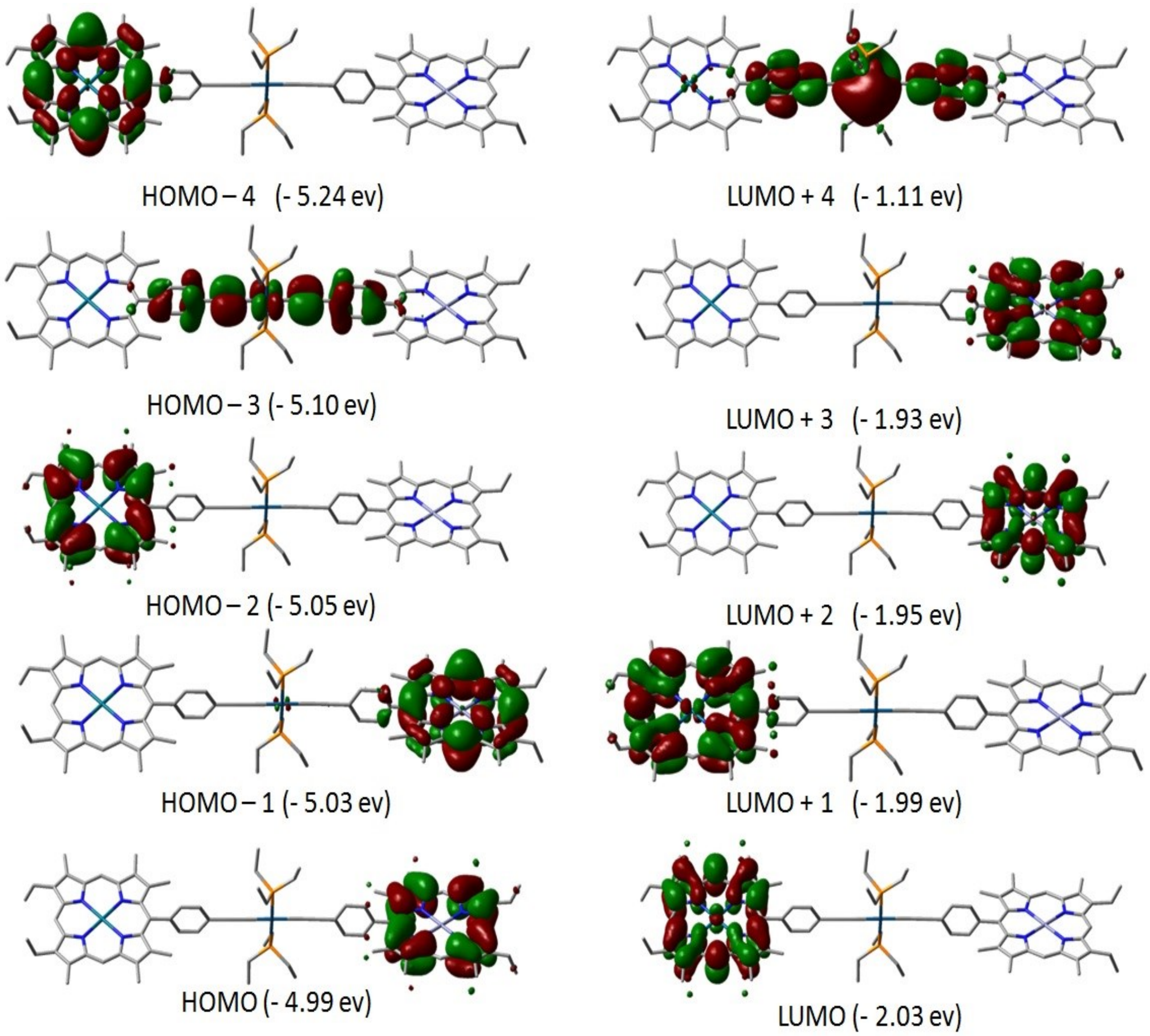

HOMO – 4 (- 5.24 ev)

LUMO + 4 (- 1.11 ev)

HOMO – 3 (- 5.10 ev)

LUMO + 3 (- 1.93 ev)

HOMO – 2 (- 5.05 ev)

LUMO + 2 (- 1.95 ev)

HOMO – 1 (- 5.03 ev)

LUMO + 1 (- 1.99 ev)

HOMO (- 4.99 ev)

LUMO (- 2.03 ev)

Figure S14. Representation of the frontier MOs for compound **[Zn-Pt-Pd]**, (Pd is turquoise).

^{1}H NMR spectra

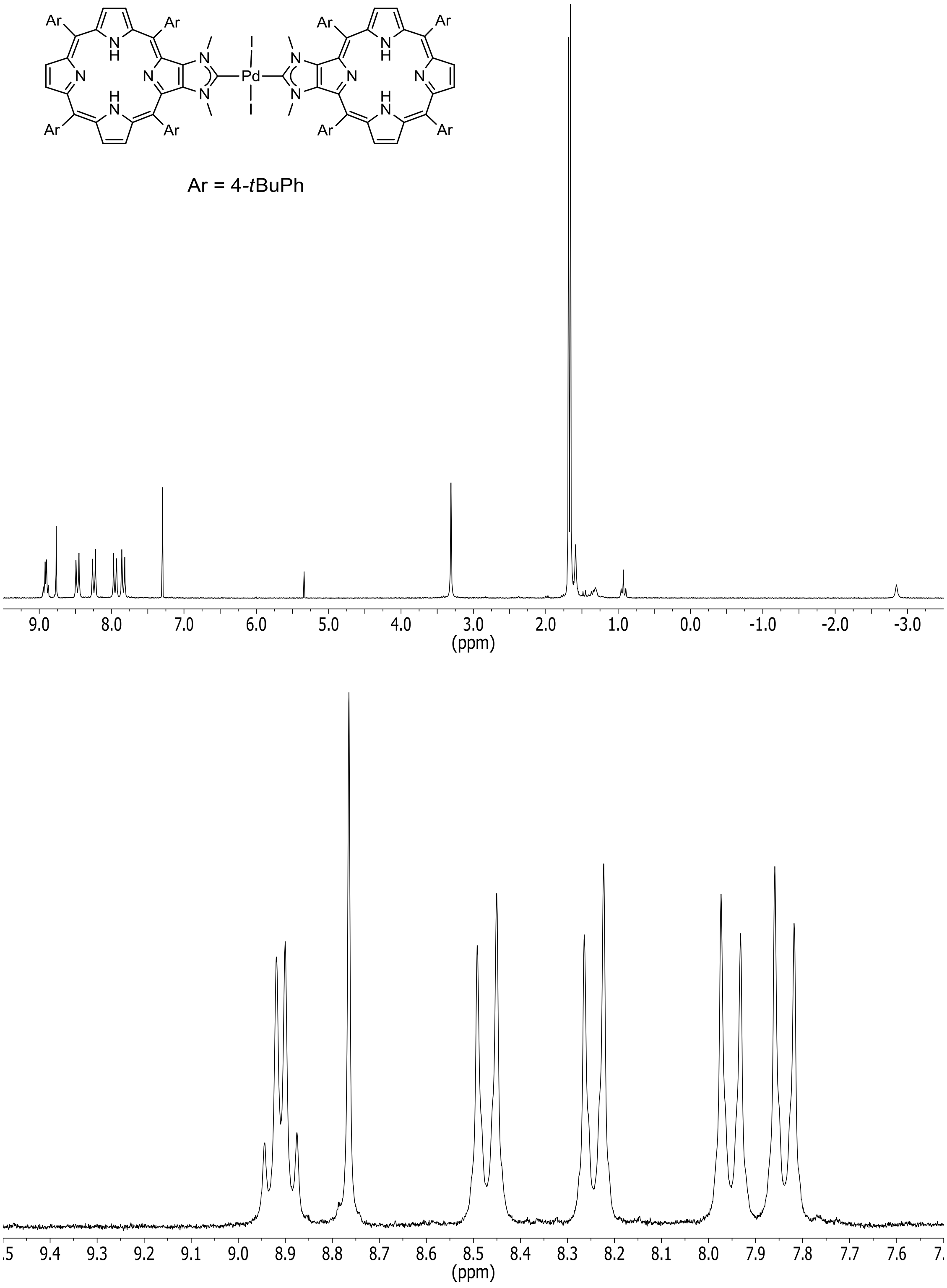

Figure S15. ^{1}H NMR spectrum of **[Fb-Fb]** (200 MHz, 25°C, $CDCl_3$).

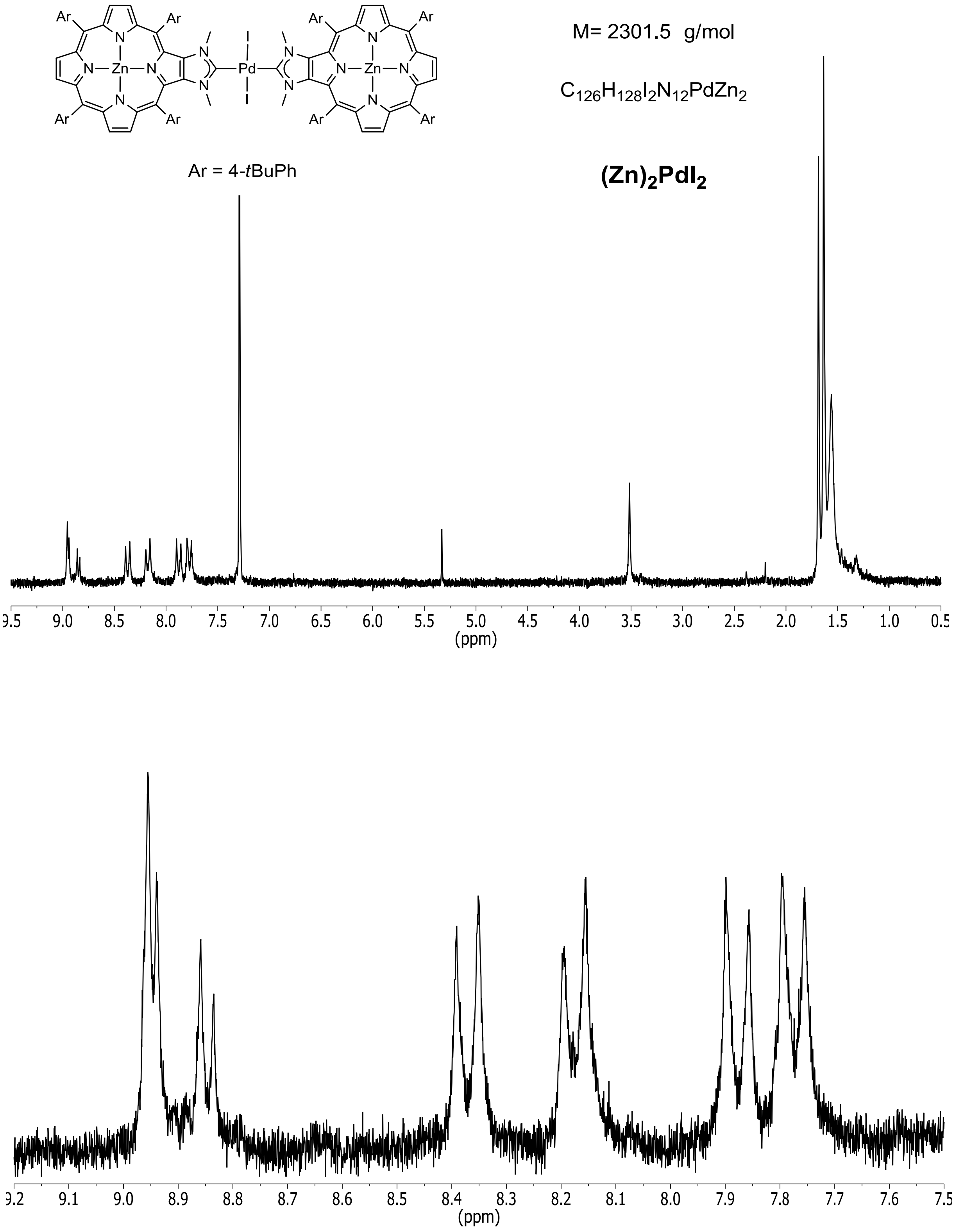

Figure S16. ^{1}H NMR spectrum of **[Zn-Zn]** (200 MHz, 25°C, $CDCl_3$).

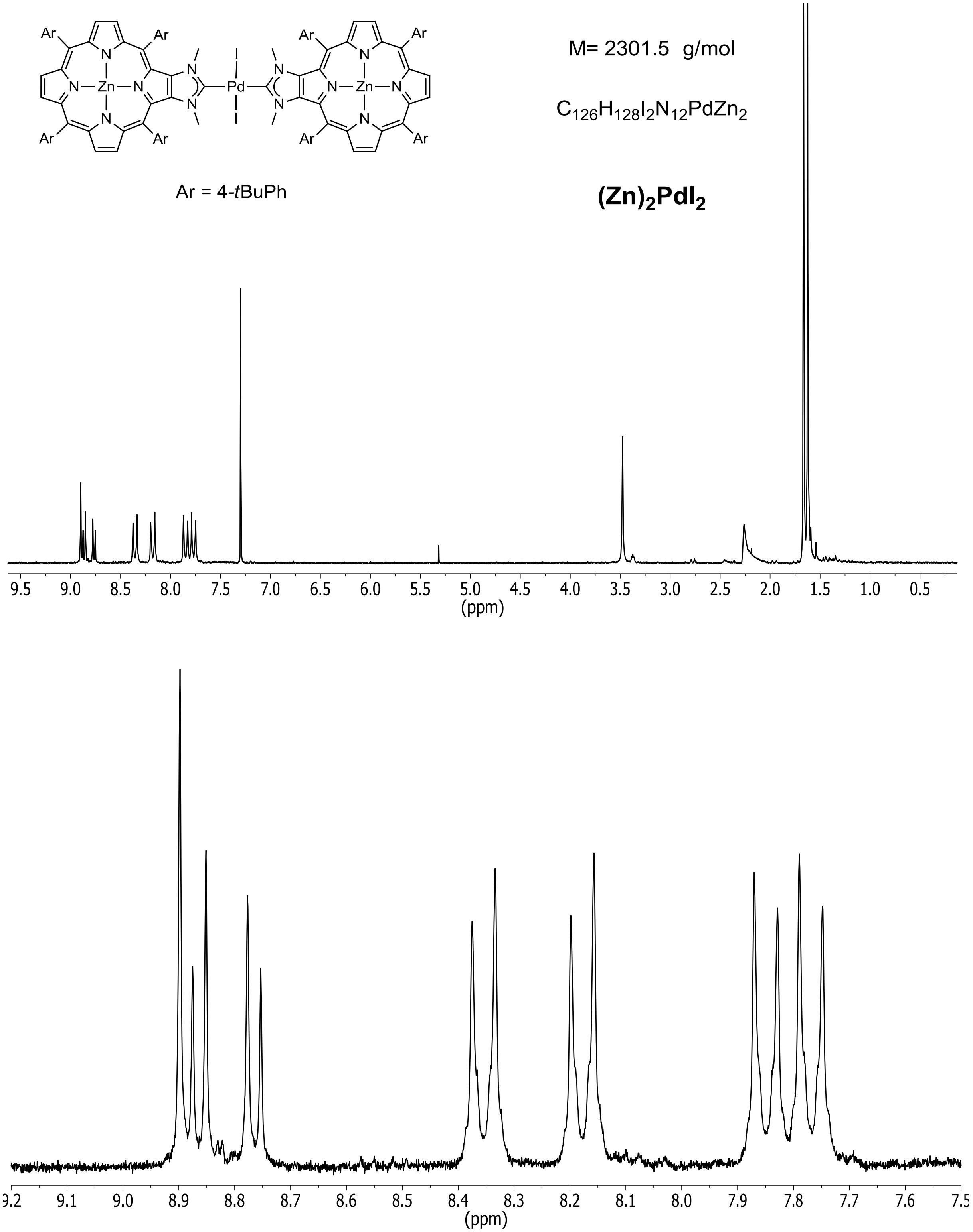

Figure S17. ^{1}H NMR spectrum of **[Zn-Zn]** (200 MHz, 25°C, $CDCl_3$ + 5% CD_3OD).

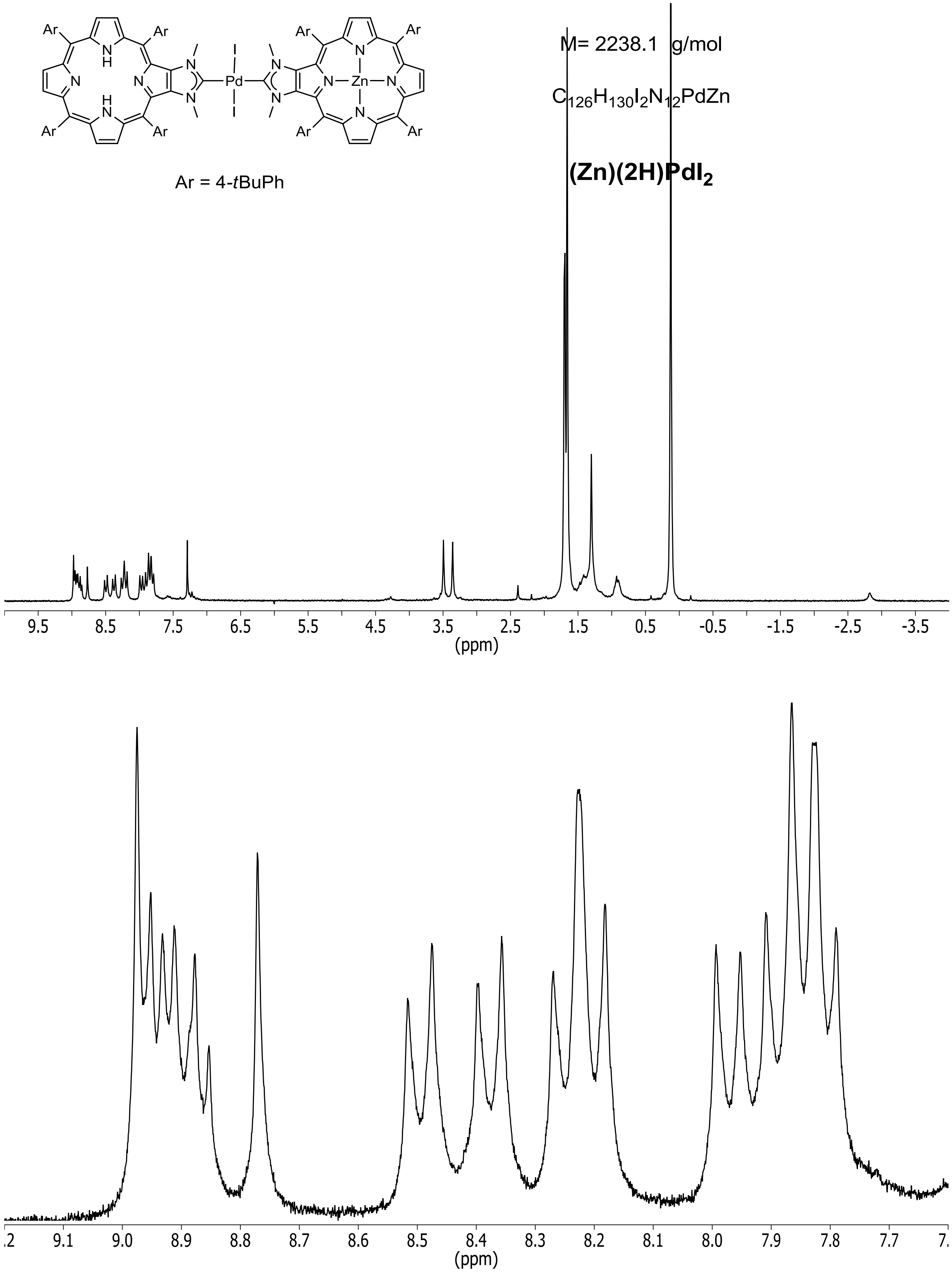

Figure S18. ^{1}H NMR spectrum of **[Zn-Fb]** (200 MHz, 25°C, $CDCl_3$).

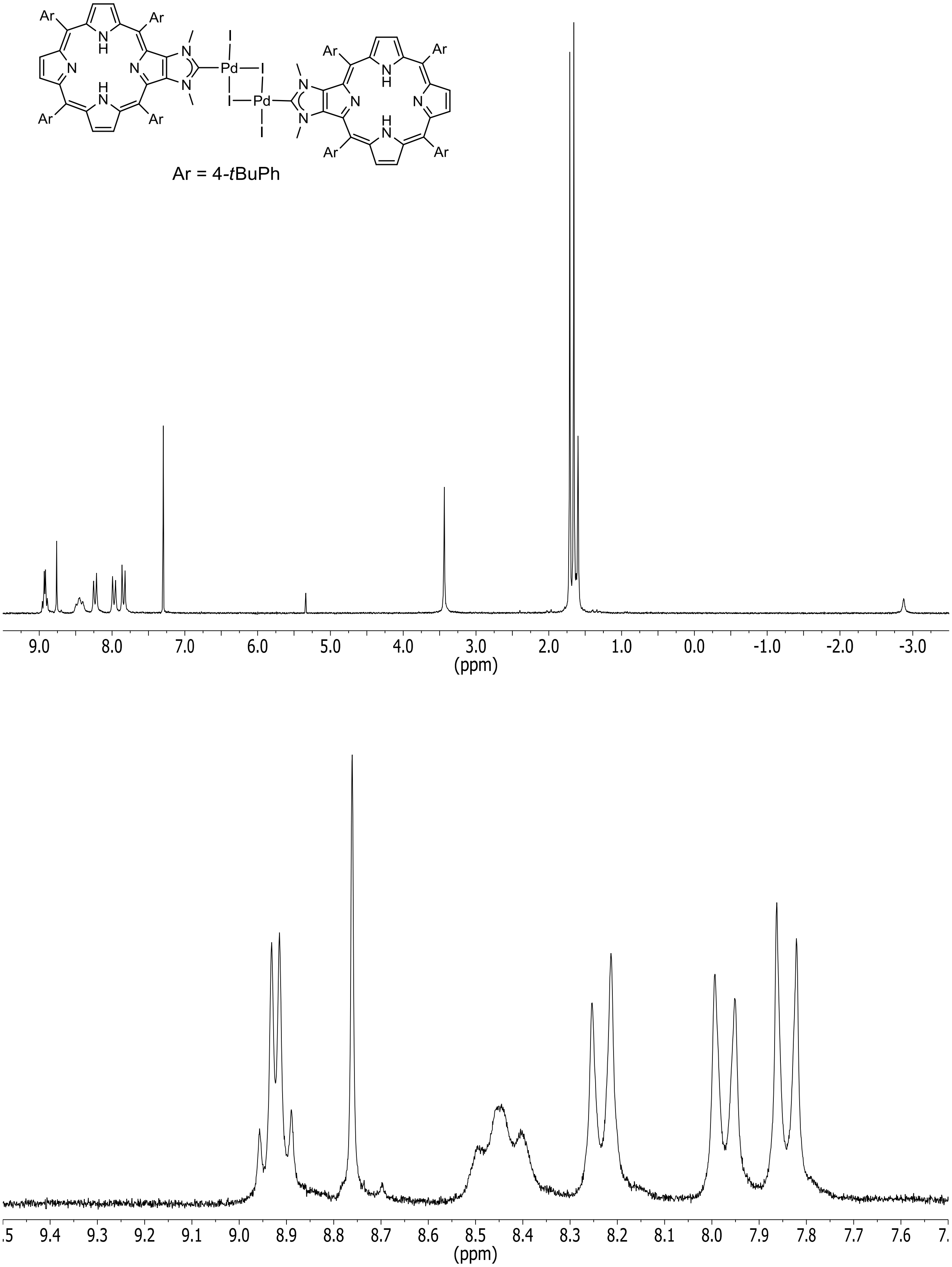

Figure S19. ^{1}H NMR spectrum of **[Fb$_2$Pd$_2$]** (200 MHz, 25°C, CDCl$_3$).

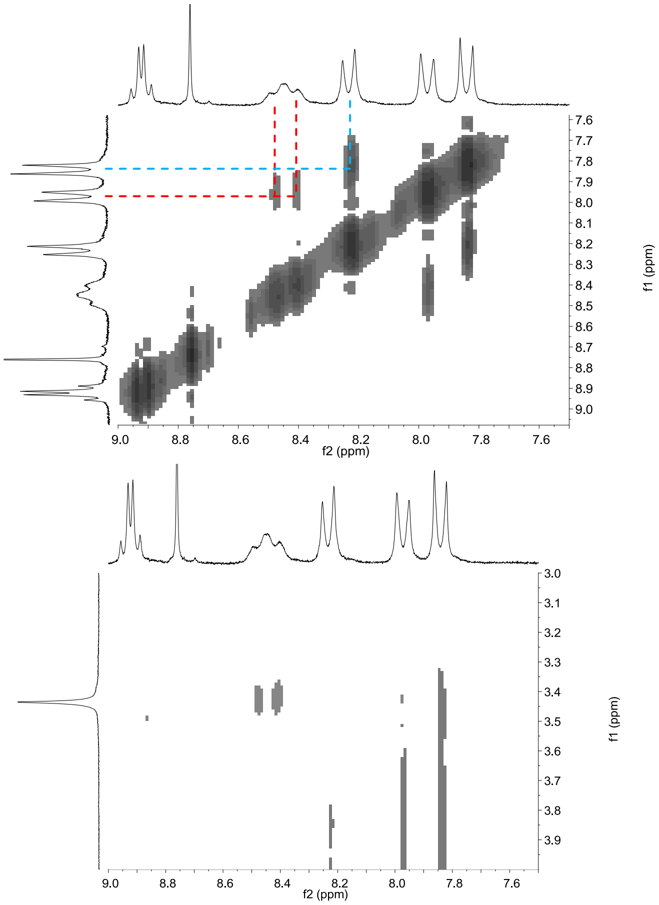

Figure S20. ^{1}H 2D NMR ($CDCl_3$, 200 MHz, 25°C) spectra COSY (left side) and NOESY (right side) of **[Fb_2Pd_2]**.

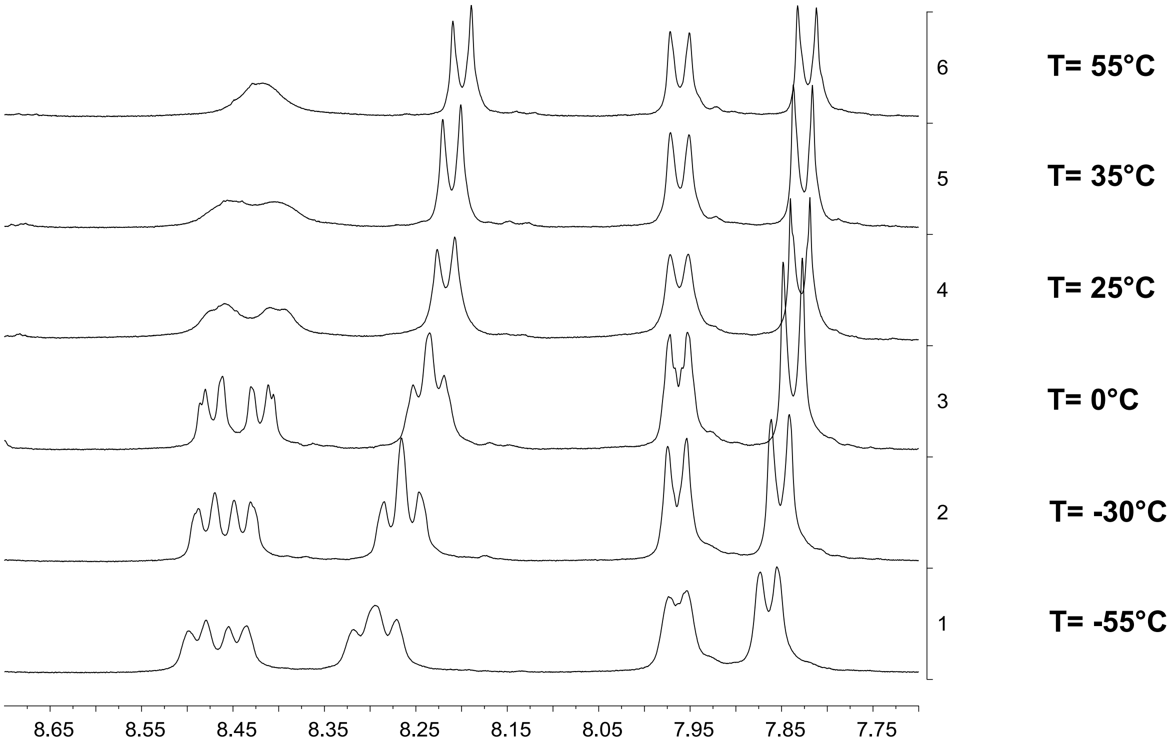

Figure S21. Variable temperature ^{1}H NMR ($CDCl_3$, 400 MHz) spectra of **[Fb_2Pd_2]**.

CHAPTER 4

ULTRAFAST ENERGY TRANSFER IN A Pd(II)-BRIDGED BISPORPHYRIN DYAD.

This chapter reports an ultrafast energy transfer in a bisporphyrin dyad, composed of a zinc(II)porphyrin (donor) and the corresponding free base porphyrin, linked together by a β,β-linked trans-$Pd(NH)_2(C{=}O)_2$.

This work has been submitted in *JACS* by Mohammed Abdelhameed, Paul-Ludovic Karsenti, Sébastien Richeter, Romain Ruppert and Pierre D. Harvey. (Manuscript number: ja-2014-061774 on 19th of June, 2014)

The synthesis part has been carried out at the Université de Strasbourg and Université Montpellier by Dr. Sébastien Richeter and Dr. Romain Ruppert.

The second part of the work was carried out by me. This part involves spectroscopic and photophysical measurements including the absorption and emission spectra, emission quantum yields and lifetimes as well as the DFT (density functional theory) and TDDFT (time-dependent density functional theory) computations. The lifetime measurements using transient absorption spectroscopy and Streak camera were done by Paul-Ludovic Karsenti. I did the measurements, analyses and discussion of the photophysical parameters under the supervision of Dr. Pierre D. Harvey, Dr. Sébastien Richeter and Dr. Romain Ruppert. I wrote the first draft of the manuscript and Prof. Harvey finalized the manuscript.

4.1. Manuscript

Ultrafast Energy Transfer In A Pd(II)-Bridged Bisporphyrin Dyad.

Mohammed Abdelhameed,[a] Paul-Ludovic Karsenti,[a] Sébastien Richeter,*[b] Romain Ruppert*[c] and Pierre D. Harvey*[a]

[a] Département de Chimie, Université de Sherbrooke, 2550 Boulevard de l'Université, Sherbrooke, Québec, Canada J1K 2R1, Fax: Tel: E-mail:

[b] Institut Charles Gerhardt de Montpellier, UMR CNRS 5253, Université Montpellier 2,
CC 1701, Place E. Bataillon, 34095 Montpellier Cedex 05 (France).
E-mail:

[c] Institut de Chimie, UMR CNRS 7177, Université de Strasbourg 1 rue Blaise Pascal,
67000, Strasbourg.
E-mail:

4.1.1. Abstract

An energy transfer dyad composed of a zinc(II)porphyrin (donor) and a free base porphyrin (acceptor) rigidly held together by a β,β-linked *trans*-Pd(NH)$_2$(C=O)$_2$ unit exhibits ultrafast singlet energy transfer, $k_{ET} = 1.5 \times 10^{12}$ s^{-1}, drastically contrasting with other metallo-bridged examples showing much slower rates ((2 to 11) x 10^9 s^{-1}). This fast rate is due to significant MO coupling of the donor and acceptor chromophores and non-nil atomic contribution of the Pd-atom in the frontier MOs, hence ensuring π-conjugation.

4.1.2. Introduction

Energy transfer (ET) is one of the key photophysical events that takes place in the antenna effect in photosynthetic bacteria and plants.[1] From a theoretical stand point, the Förster Resonance ET (FRET) theory is often used to analyze experimental findings,[2] but often fails to fully explain the observed processes (*i.e.* the calculated ET rates, k_{ET} do not match the measured data).[3] This discrepency has been pointed out before,[4] and the FRET theory is considered as an approximation that performs well for long distances between the donor and acceptor, but does poorly at shorter spacings. Models are often utilized to study these

ET phenomena and models with reliably addressable geometries commonly use rigid carbon-based linkers.[1b] However several examples of metallo-bridged oligoporphyrins were also described in the literature,[5] and some of them show significant electronic communication between individual porphyrins in homo-dimers in the ground state.[6]. We now report a new dyad linked by a Pd(II) bridge (**[Fb-Zn]**, Scheme 1), which favors ground state electronic communication.[6b]

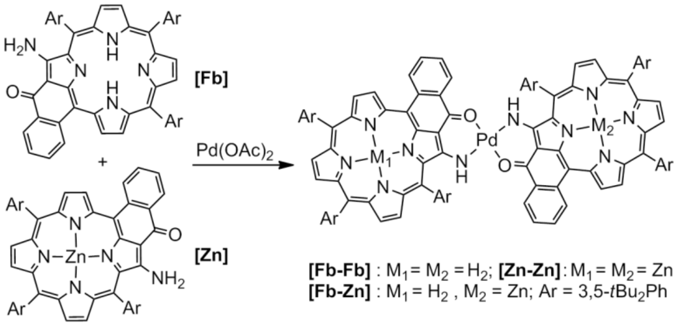

Scheme 1. Structures of the palladium(II) bridged dimers and dyad.

However, communication across this link in the excited state is not known and can be addressed from the rate of ET, k_{ET}. In this respect, we reported two porphyrin-containing dyads linked by a Pt(II)- or Pd(II)-containing fragment respectively for **1**[7] and **2**,[8] (Scheme 2). Both metallo-bridged dyads **1** (~2 x 10^9) and **2** ((3 to 11) x 10^9 s^{-1}) show slow k_{ET}. In both cases, the lack of Pt and Pd orbital contributions to the π-system of the frontier MOs dramatically restricts the electronic communication between the donors and the acceptors (*i.e.* no Dexter mechanism;[9] double electron exchange).[8] The lack of Pt atomic contribution in the semi-occupied MOs in the triplet states was previously identified as the main reason for the absence of ET in **Ir-Pt-Zn** (**Ir** = [(1-phenyl-pyridine)$_2$(bipyridine)Ir]$^+$ (donor); **Zn** = zinc(II)porphyrin (acceptor); **Pt** = *trans*-Pt(PBu$_3$)$_2$(C≡C)$_2$).[10] The slow ET for dyad **2** was explained by an electric field screening effect of the transition moments of the donor and the acceptor. These results led to the seemingly constant conclusion that the metal-bridge has a negative impact on k_{ET}. This work reports a spectacular exception to this trend. The dyad **[Fb-Zn]**, which is built upon **[Zn]** and **[Fb]** linked by a single Pd(II) ion, exhibits the fastest k_{ET} (~ 1.5 x 10^{12} s^{-1}) for metallo-bridged bis-porphyrins.

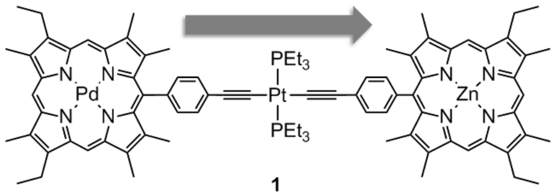

1

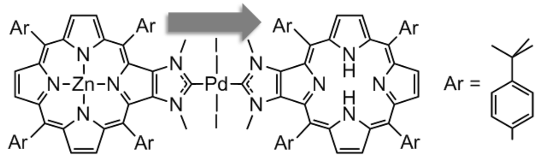

2

Scheme 2. Structures of the two previously reported metallo-bridged dyads. The arrows show the direction of the energy transfers.

4.1.3. Results and discussion

Synthesis: The dyads linked by Pd(II) were readily synthesized by a statistical reaction between **[Fb], [Zn]** and Pd(OAc)$_2$ leading to the two known homodyads **[Zn-Zn]** and **[Fb-Fb]**,[6b] and the desired dyad **[Fb-Zn],** which were isolated by chromatography and fully characterized (ESI).

The absorption and fluorescence spectra (Figs. 1 and 2) and photophysical data (Table 1) of **[Fb-Zn]** and the model compounds have been studied at 298 and 77K (additional data are in the ESI). Bathochromic shifts were found in the absorption and fluorescence spectra going from **[Fb]** to **[Fb-Fb]** (~30 nm) and from **[Zn]** to **[Zn-Zn]** (~20 nm). These shifts provide evidence for conjugation across the Pd(II) bridge. Based on these data, the donor (**[Zn]**) and acceptor (**[Fb]**) moiety were assigned. The fluorescence lifetimes, τ_F, for **[Fb]** (~8.8 ns) and **[Zn]** (~0.9 ns) are similar respectively to those of H$_2$TPP (10.6 ns) and of ZnTPP (2.0 ns),[11] although somewhat shorter. The τ_F data drastically decrease when going from **[Fb]** to **[Fb-Fb]** (~two orders) and from **[Zn]** to **[Zn-Zn]** (~one order of magnitude), due to a strong heavy atom effect, which enhances the intersystem crossing process (S_1~>T_1). These results further confirm the efficient electronic communication between the π-systems of the porphyrins across the Pd(II) bridge. The fluorescence of the **[Zn]** and **[Fb]** chromophores is obvious in the spectra of the dyad **[Fb-Zn]** but only the **[Fb]** (acceptor) component (~60 ps) could be detected by the Streak camera (Fig. 2) meaning that the τ_F value for **[Zn]** (donor) is < 3 ps (*i.e.* under the time resolution limit). Indeed, 9 ps after the laser pulse, the fluorescence peak of the **[Zn]** disappeared completely (Fig. 2) with respect to the steady state spectrum (Fig. 1).

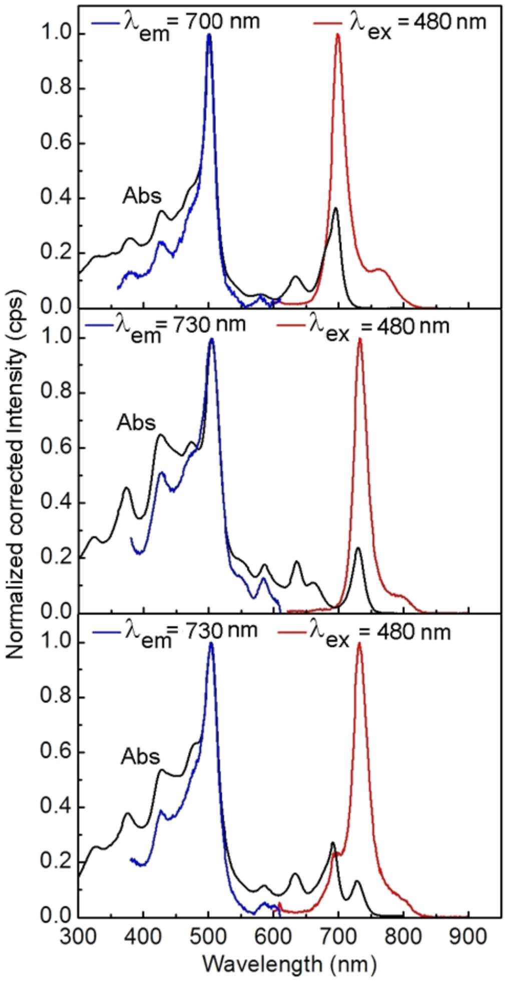

Figure 1. Absorption (black), fluorescence (red) and excitation (blue; limit of the instrument = 610 nm) spectra of respectively (top to bottom) **[Zn-Zn], [Fb-Fb]**, and **[Fb-Zn]** in 2MeTHF at 298 K (the 77 K data are in the ESI).

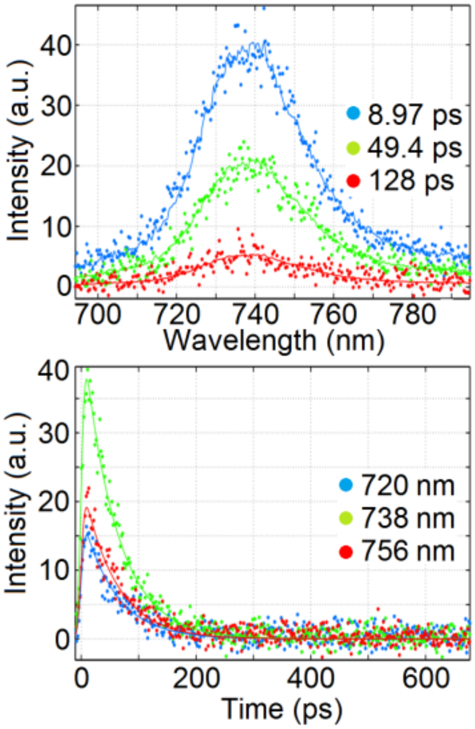

Figure 2. Top: Time resolved emission spectra of **[Fb-Zn]** in 2MeTHF at 298 K. Bottom: Decay traces of the **[Fb-Zn]** fluorescence (the 77 K data are in the ESI).

The drastic decrease of τ_F from ~40 to <3 ps of the **[Zn]** donor going from **[Zn-Zn]** to **[Fb-Zn]** can only be explained by S_1 ET. The good superposition of the excitation and absorption spectra indicates that the ET is indeed very efficient. In order to extract this lifetime, transient absorption spectroscopy was used and three intermediates were clearly observed (Fig. 3). The long-lived species (ms time scale) is unambiguously a $T_1 \rightarrow T_n$ species (most likely that for **[Fb]**). This lifetime cannot be considered accurate because of the limitation of the delay line (3.3 ns).

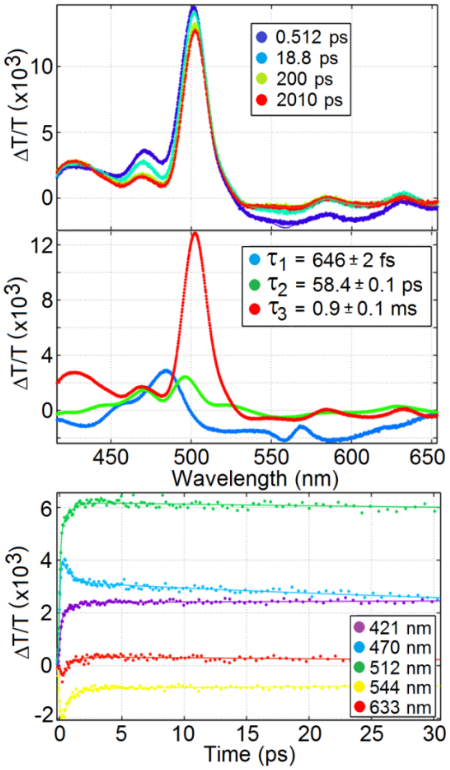

Figure 3. Top: Time evolution of the transient absorption spectra of **[Fb-Zn]** in 2MeTHF at 298 K. The signals above and below 0 are respectively the bleached and transient signals. Middle: Deconvolution of the individual components necessary to explain the transient spectra. Their lifetimes are given in the inset. Bottom: decay and rise traces of the transient spectra at various wavelengths.

Table 1. Fluorescence lifetimes and quantum yields (in 2-MeTHF).

Code	Chro.	λ_F (nm)	τ_F (298 K)	Φ_F	λ_F (nm)	τ_F (77 K)
Fb	**[Fb]**	717	8.76±0.04 ns	0.056	705	10.45 ±0.12 ns
Zn	**[Zn]**	690	0.85±0.03 ns	0.031	685	1.14±0.06 ns
FbFb	**[Fb]**	732	59.7±0.1 ps	0.0014	727	98.1±0.1 ps
ZnZn	**[Zn]**	699	42.2±0.2 ps	0.0011	700	85.5±0.1 ps
FbZn	**[Zn]**	698	< 3 ps	-	704	not measured
	[Fb]	733	57.4±0.1 ps	0.0011	728	not measured

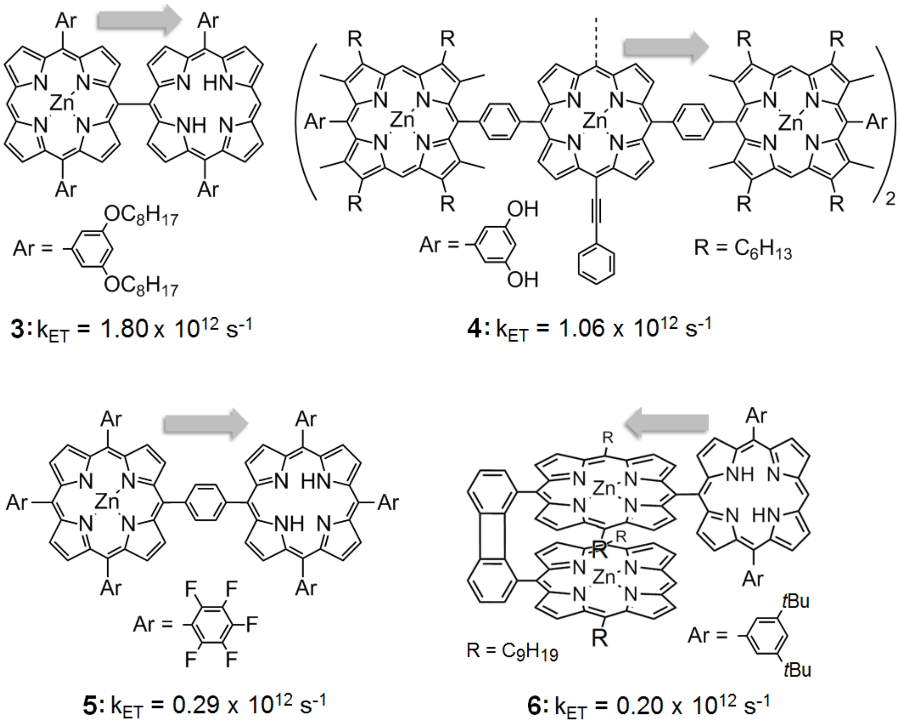

3: k_{ET} = 1.80 x 10^{12} s^{-1}

4: k_{ET} = 1.06 x 10^{12} s^{-1}

5: k_{ET} = 0.29 x 10^{12} s^{-1}

6: k_{ET} = 0.20 x 10^{12} s^{-1}

Scheme 3. Comparison of various dyads and their k_{ET}'s. The arrows indicate the direction of the S_1 ET.

The second species, which relaxes at 58.4 ps, is the **[Fb]** in the S_1 state that is readily assigned based on its τ_F (57.4±0.1ps) and the red-shifted position of the bleached Soret band of the **[Fb]** chromophore (green trace) compared to that for **[Zn]** (blue trace). Finally, the transient decaying at 646 fs is the **[Zn]** S_1 species. This value compares favorably to that reported by Kim, Osuka, *et al.* on the *meso-meso*-bonded dyad **3** (k_{ET} = (550 fs)$^{-1}$; Scheme 3),[12] and indicates an ultrafast ET. For **[Fb-Zn]**, the rate, $k_{ET}(S_1)$, is extracted from $k_{ET} = (1/\tau_F)-(1/\tau_F°) = 1.5 \times 10^{12}$ s^{-1}, where τ_F and $\tau_F°$ are respectively the lifetime of the donor in the presence (646 fs) and in the absence of an acceptor (42.2 ps for **[Zn-Zn]**). The efficiency is given by Eff = $((1/\tau_F)-(1/\tau_F°))/(1/\tau_F)$ = 98% for **[Fb-Zn]**. This rate compares favorably to the fastest carbon-based "side-by-side" dyads **3**[12], **4**[13] and **5**[14] (Scheme 3), placing it the second fastest rate among porphyrins. However, this k_{ET} drastically contrasts with those measured for the metallo-bridged dyads **1** (~2 x 10^9 s^{-1})[7] and **2** ((3 to 11) x 10^9 s^{-1}).[8] Although the longer center-to-center distance in **1** (25.0) and **2** (17) compared to **[Fb-Zn]** (14.5 Å) may partially explain the slower k_{ET} for **1**, the reason for the much slower k_{ET} for **2** cannot be simply explained using this structural parameter only.

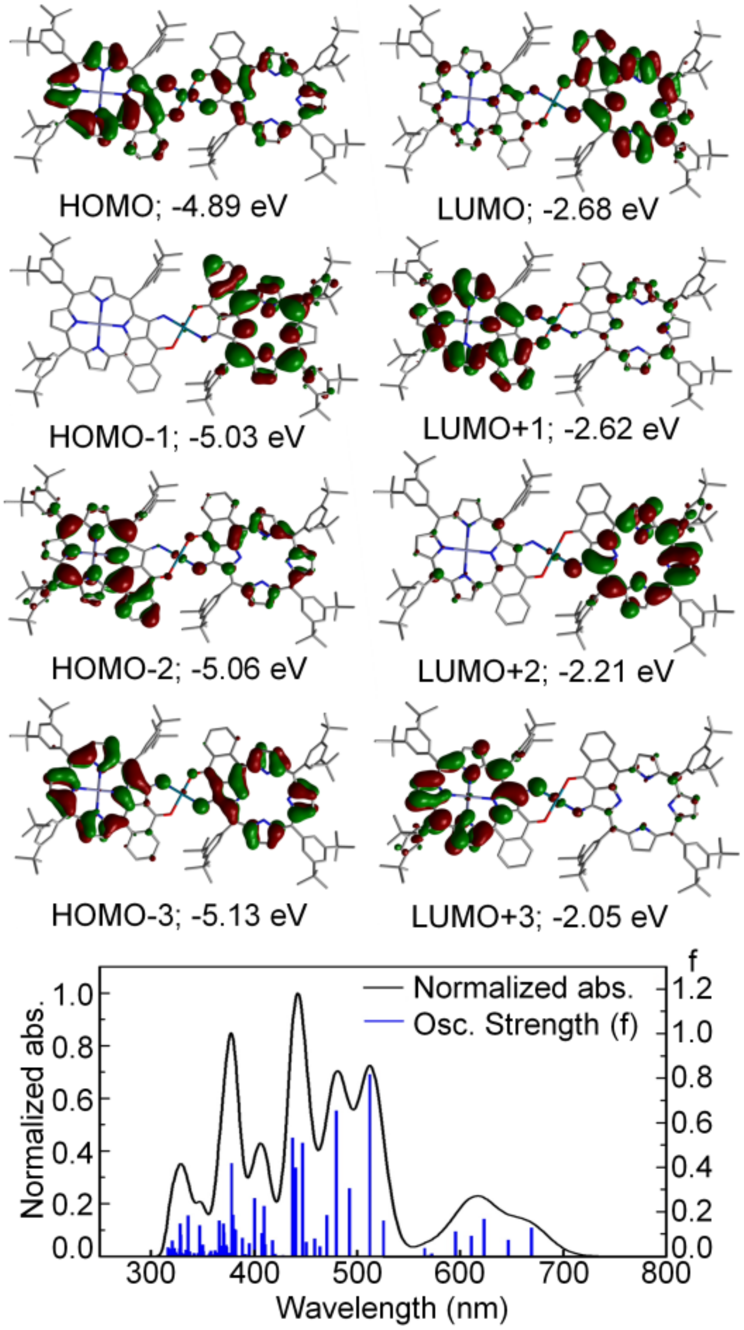

Figure 4. Representation of the frontier MOs for **[Fb-Zn]**. Bottom. Bar graph reporting the calculated oscillator strengths (f) as a function of the positions of the electronic transition (blue). The black trace is the same but applying a thickness of 1000 cm^{-1} to each bar. The tables showing the contribution for each transition for **[Fb-Zn]**, **[Zn-Zn]**, and **[Fb-Fb]** are placed in the ESI. No vibronic transition is included in these calculations.

Recently, one of us investigated the ET process for the *meso*-*meso*-bonded dyad **6** (k_{ET} = (5.1 ps)$^{-1}$).[15] DFT computations revealed a substantial frontier MO coupling between the donor (**Fb**) and acceptor (**[Zn$_2$]**) π-systems. Concurrently and to the best of our knowledge, there was no other report stressing a correlation between a fast k_{ET} and MO coupling. Conversely, no MO coupling was noted for dyads **1** and **2**, and no atomic contribution of the Pd-bridge in **2** was found.[8] This latter observation indicates that the ET does not operate via a Dexter mechanism in **1** and **2**, hence contributing in slowing down k_{ET} (*i.e.* $k_{ET}^{total} = k_{ET}^{Förster} + k_{ET}^{Dexter}$;[16] where k_{ET}^{Dexter} is negligible). The frontier MOs of [**Fb-Zn]** (optimized geometry by DFT; B3LYP; Fig. 4; top) exhibit extensive coupling between the donor and acceptor. Notably, the atomic contributions calculated for the HOMO exhibit significant atomic contributions on the donor and acceptor, as well as the Pd(II) ion (Table 2). Furthermore, TDDFT computations generated a bar graph reporting the oscillator strength (f) *vs* the position of the pure electronic transitions (Fig. 4; bottom). By applying a thickness of 1000 cm^{-1} to each bar, a spectrum is formed, which is similar to the experimental one (Fig. 1). This result provides strong support that significant MO coupling and atomic contributions of the bridging Pd(II) ion are other key factors influencing k_{ET} in **[Fb-Zn]**. Previous electrochemical findings for an isostructural bis(nickel(II)porphyrin) species (*i.e.* similar to **[Zn-Zn]**) also established the presence of a strong coupling between the two **[Ni]** chromophores.[6b]

Table 2. Atomic contributions (%) of the frontier MOs of **[Fb-Zn]**.[a]

Fragment	Pd	Zn	**[Zn]**-Zn[b]	[Fb][b]	R groups
L+4	**40.20**	0.04	**29.23**	**30.37**	0.15
L+3	0.82	0.19	**91.44**	7.17	0.39
L+2	0.54	0.01	7.37	**91.70**	0.38
L+1	1.00	0.21	**83.58**	14.74	0.47
LUMO	0.18	0.03	**14.39**	**84.98**	0.41
HOMO	4.64	0.06	**65.01**	**30.01**	0.28
H-1	0.18	0.02	2.00	**97.08**	0.72
H-2	0.83	0.81	**73.63**	**24.06**	0.67
H-3	0.44	0.29	**55.09**	**43.83**	0.35
H-4	8.29	0.09	**47.59**	**43.18**	0.84

[a] L = LUMO, H = HOMO. The largest contribution (>10%) are in bold. [b] **[Zn]**-Zn = Zn-containing porphyrin (except Zn), **[Fb]** = free base porphyrin.

4.1.4. Conclusion

This work reported the fastest k_{ET} for a dyad linked by a metal ion, and the ET rate compares favorably with the fastest rate reported (*i.e.* directly bonded dyad). The non-nil atomic contribution of the bridging Pd(II) to the π-systems probably explains this fact. This contribution permits the Dexter mechanism to operate efficiently, thanks to a significant overlap between frontier MOs of the donor and the acceptor. This observation is, to the best of our knowledge, only the second one reported so far. In the present case, the absence of ancillary ligands on the bridging Pd(II) also prevents an *electric field screening* effect (no "spectator" atom nor groups are placed between the donor and the acceptor), which is now known to dramatically decrease k_{ET} values. Consequently, the ET processes that are commonly analyzed by the Förster (FRET) and Dexter theories now appear conceptually more complicated than initially. This research provides significant insights on the many parameters that influence k_{ET}. These results represent a valuable addition to the data bank used to predict k_{ET}, and consequently to direct future designs aimed at ET processes.

4.1.5. Experimental Section

Synthesis of dyad [Fb-Zn]. A solution of **[Fb]** (25 mg, 0.025 mmol), **[Zn]** (27 mg, 0.025 mmol), and palladium(II) acetate (6 mg, 0.026 mmol) in toluene was heated under argon at 80°C for 16 h. TLC monitoring of the advancement showed that the reaction was almost complete. After evaporation of the solvent, the hetero dyad was isolated by column chromatography on silica gel together with the two known homodimers[6b] (eluent: cyclohexane/dichloromethane). Crystallization from CH_2Cl_2/CH_3OH afforded the palladium complex **[Fb-Zn]** in about 30% yield (16 mg, 0.0075 mmol). Spectral data of **[Fb-Zn]** are placed in ESI.

REFERENCES

[1] a) Advances in Photosynthesis and Respiration, Vol. 13 Light-Harvesting Antennas in Photosynthesis. (Eds: B. R. Green, W. W. Parson), Kluwer, Boston, (2003), pp. 1-493; b) P. D. Harvey, C. Stern, R. Guilard, in Handbook of Porphyrin Science With Applications to Chemistry, Physics, Materials Science, Engineering, Biology and Medicine, Vol. 11 (Eds: K. M. Kadish, K. M. Smith, R. Guilard), World Scientific Publishing: Singapore, (2011), pp. 1-179.

[2] T. Förster, *Ann. Phys.,* (1948), **2**, 55-75.

[3] B. Brizet, N. Desbois, A. Bonnot, A. Langlois, A. Dubois, J.-M. Barbe, C. P. Gros, C. Goze, F. Denat, P. D. Harvey, *Inorg. Chem.,* (2014), **53**, 3392-3403.

[4] a) G. D. Scholes, *Annu. Rev. Phys. Chem.,* (2003), **54**, 57-87; b) C. Curutchet, B. Mennucci, G. D. Scholes, D. Beljonne, *J. Phys. Chem. B,* (2008), **112**, 3759-3766; c) D. Beljonne, C. Curutchet, G. D. Scholes, R. J. Silbey, *J. Phys. Chem. B,* (2009), **113**, 6583-6599.

[5] Selected examples: a) H. Furuta, K. Youfu, H. Maeda, A. Osuka, *Angew. Chem.,* 2003, **115**, 2236-2238; *Angew. Chem. Int. Ed.,* (2003), **42**, 2186-2188; b) P. J. Chmielewski, I. Schmidt, *Inorg. Chem*., (2004), **43**, 1885-1894; c) R. D. Hartnell, D. P. Arnold, *Organometallics,* (2004), **23**, 391-399; d) S. Richeter, A. Hadj-Aïssa, C. Taffin, A. van des Lee, D. Leclercq, *Chem. Commun*., (2007), 2148-2150; e) J. Haumesser, J.-P. Gisselbrecht, J. Weiss, R. Ruppert, *Chem. Commun.,* (2012), **48**, 11653-11655.

[6] a) S. Richeter, C. Jeandon, R. Ruppert, H. J. Callot, *Chem. Commun.,* (2001), 91-92; b) S. Richeter, C. Jeandon, J.-P. Gisselbrecht, R. Ruppert, H. J. Callot, *J. Am. Chem. Soc.,* (2002), **124**, 6168-6179; c) S. Richeter, C. Jeandon, J.-P. Gisselbrecht, R. Graff, R. Ruppert, H. J. Callot, *Inorg. Chem.,* (2004), **43**, 251-263; d) Y.-J. Chen, S.-S. Chen, S.-S. Lo, T.-H. Huang, C.-C. Wu, G.-H. Lee, S.-M. Peng, C.-Y. Yeh, *Chem. Commun.,* (2006), 1015-1017; e) S. Yamaguchi, T. Katoh, H. Shinokubo, A. Osuka, *J. Am. Chem. Soc*., (2008), **130**, 14440-14441; f) Y. Matano, K. Matsumoto, Y. Nakao, H. Uno, S. Sasaki, H. Imahori, *J. Am. Chem. Soc.,* (2008), **130**, 4585-4589; g) Y. Matano, K. Matsumoto, H.

Hayashi, Y. Nakao, T. Kumpulainen, V. Chukharev, N. V. Tkachenko, H. Lemmetyinen, S. Shimizu, N. Kabayashi, D. Sakamaki, A. Ito, K. Tanaka, H. Imahori, *J. Am. Chem. Soc.,* (2012), **134**, 1825-1839.

[7] D. Bellows, S. M. Aly, C. P. Gros, M. El Ojaimi, J.-M. Barbe, R. Guilard, P. D. Harvey, *Inorg. Chem.,* (2009), **48**, 7613-7629.

[8] M. Abdelhameed, P.-L. Karsenti, A. Langlois, J.-F. Lefebvre, S. Richeter, R. Ruppert, P. D. Harvey, *accepted*

[9] D.L. Dexter, *J. Chem. Phys.,* (1953), **21**, 836-850.

[10] A. M. Soliman, M. Abdelhameed, E. Zysman-Colman, P. D. Harvey, *Chem. Commun.,* (2013), **49**, 5544-5546.

[11] E. G. Azenha, A. C. Serra, M. Pineiro, M. M. Pereira, J. Seixas de Melo, L. G. Arnaut, S. J. Formosinho, A.M.d'A. Rocha Gonsalves, *Chem. Phys.,* (2002), **280**, 177-190.

[12] H. S. Cho, D. H. Jeong, M.-C. Yoon, Y. H. Kim, Y.-R. Kim, D. Kim, S. C. Jeong, S. K. Kim, N. Aratani, H. Shinmori, A. Osuka, *J. Phys. Chem. A,* (2001), **105***,* 4200-4210.

[13] S. Akimoto, T. Yamazaki, I. Yamazaki, A. Nakano, A. Osuka, *Pure Appl. Chem*., (1999), **71**, 2107-2115.

[14] S. I. Yang, R. K. Lammi, J. Seth, J. A. Riggs, T. Arai, D. Kim, D. F. Bocian, D. Holten, J. S. Lindsey, *J. Phys. Chem. B,* (1998), **102**, 9426-9436.

[15] M. Filatov, F. Laquai, D. Fortin, R. Guilard, P. D. Harvey, *Chem. Comm.,* (2010), **48,** 9176-9178**.**

[16] S. Faure, C. Stern, R. Guilard, P. D. Harvey, *J. Am. Chem. Soc*., (2004), **126**, 1253-1261.

4.2. SUPPORTING INFORMATION

Ultrafast Energy Transfer in a Pd(II)-Bridged Bisporphyrin Dyad

Mohammed Abdelhameed, Paul-Ludovic Karsenti, Sébastien Richeter, Romain Ruppert and Pierre D. Harvey

Table of Contents:

Experimental Section.

Experimental Section

Materials

The synthesis of the porphyrins **[Fb]** and **[Zn],** and homo-dimers **[Fb-Fb]** and **[Zn-Zn]** was described earlier.[1] The reactions were performed under argon using oven-dried glassware and Schlenk techniques. Palladium acetate was purchased from Alfa Aesar. Dry toluene was obtained by distillation over Na/benzophenone. Preparative separations were performed by silica gel flash column chromatography (Merck SI 60, 40-63 μm). Dichloromethane (distilled over CaH_2) and cyclohexane used as eluents were obtained from Aldrich. ^1H and $^{13}C\{^1H\}$ NMR spectra were recorded in $CDCl_3$ on Bruker Avance 400 or 500 MHz spectrometer. ^1H and $^{13}C\{1H\}$ NMR spectra were calibrated to TMS on the basis of the relative chemical shift of the solvent as an internal standard. Abbreviations for ^1H NMR spectra used are as follows: s, singlet; d, doublet. UV-visible absorption spectra were recorded in $CHCl_3$ with an Agilent diode-array UV-visible spectrophotometer HP 8453. ESI mass spectra were recorded on a Bruker MicroTOF spectrometer.

Synthesis of dyad **[Fb-Zn]**, **Procedure A.** A solution of the palladium complex **[Fb-Fb]** (25 mg, $1.2x10^{-5}$ mol) and $Zn(OAc)_2•2H_2O$ (3 mg, $1.3x10^{-5}$ mol) was prepared in a $CHCl_3/CH_3OH$ mixture (18/2 mL) and degassed with argon. Then, the reaction mixture was stirred for 2 hours at 50°C under argon. Although TLC analysis showed the presence of the three expected dimers, [Fb-Fb], [Fb-Zn] and **[Zn-Zn]**, and the desired dyad **[Fb-Zn]** could never be obtained pure even after several chromatographic purifications.

Procedure B. A solution of **[Fb]** (25 mg, 0.025 mmol), **[Zn]** (27 mg, 0.025 mmol), and palladium(II) acetate (6 mg, 0.026 mmol) in toluene was heated under argon at 80°C for 16 h. TLC monitoring of the advancement showed that the reaction was almost complete. After evaporation of the solvent, the dyad was isolated by column chromatography on silica gel together with the two known homodimers (eluent: cyclohexane/dichloromethane). Crystallization from CH_2Cl_2/CH_3OH afforded the palladium complex **[Fb-Zn]** in about 30% yield (16 mg, 0.0075 mmol). **^{1}H NMR** (400 MHz, 25°C, $CDCl_3$): δ 9.38 (d, J = 4.8 Hz, 1H, H_{pyrr}), 9.36 (d, J = 4.8 Hz, 1H, H_{pyrr}), 8.90 (d, J = 7.6 Hz, 1H, H_{cyclPh}) 8.88 (d, 1H, J = 7.6 Hz, H_{cyclPh}) 8.72 (d, J = 4.8 Hz, 1H, H_{pyrr}), 8.70 (d, J = 4.8 Hz, 1H, H_{pyrr}), 8.61 (2d, J

= 7.6 Hz, 2H, H_{cyclPh}), 8.57 (d, J = 4.8 Hz, 1H, H_{pyrr}), 8.51 (d, J = 4.8 Hz, 1H, H_{pyrr}), 8.49 (d, J = 4.8 Hz, 1H, H_{pyrr}), 8.45 (d, J = 4.8 Hz, 1H, H_{pyrr}), 8.42 (d, J = 4.8 Hz, 1H, H_{pyrr}), 8.41 (d, J = 4.8 Hz, 1H, H_{pyrr}), 8.30 (s, 1H, $H_{N\text{-}H}$), 8.27 (t, J = 1.6 Hz, 1H, $H_{Ar\text{-}para}$), 8.26 (t, J = 1.6 Hz, 1H, $H_{Ar\text{-}para}$), 8.21 (s, 1H, $H_{N\text{-}H}$), 8.11 (d, J = 4.8 Hz, 1H, H_{pyrr}), 8.06 (d, J = 1.6 Hz, 1H, $H_{Ar\text{-}ortho}$), 8.05 (d, J = 1.6 Hz, 1H, $H_{Ar\text{-}ortho}$), 8.02 (d, J = 1.6 Hz, 1H, $H_{Ar\text{-}ortho}$), 7.99 (d, J = 1.6 Hz, 1H, $H_{Ar\text{-}ortho}$), 7.95 (d, J = 1.6 Hz, 1H, $H_{Ar\text{-}ortho}$),7.93 (d, J = 1.6 Hz, 1H, $H_{Ar\text{-}ortho}$), 8.1-7.9 (m, 4H, H_{cyclPh}) 7.78 (t, J = 1.6 Hz, 1H, $H_{Ar\text{-}para}$), 7.77 (t, J = 1.6 Hz, 1H, $H_{Ar\text{-}para}$), 7.73 (t, J = 1.6 Hz, 1H, $H_{Ar\text{-}para}$), 7.72 (t, J = 1.6 Hz, 1H, $H_{Ar\text{-}para}$), 1.59 (s, 36H, H_{tBu}), 1.53 (s, 36H, H_{tBu}), 1.48 (s, 18H, H_{tBu}), 1.47 (s, 18H, H_{tBu}), -0.3 (broad, 2H, H_{NH}) ppm. UV-visible (CH_2Cl_2): λ_{max} (ε): 374 (59600), 428 (85400), 478 (sh, 102200), 504 (160000), 586 (17900), 634 (24200), 672 (sh, 25300), 691 (34500), 727 nm (19300 $L.mol^{-1}.cm^{-1}$). **ESI MS** : calculated for $C_{138}H_{150}N_{10}O_2PdZn^+$: 2149.03, found: 2149.034. Calculated for $C_{138}H_{152}N_{10}O_2PdZn^{2+}$ ($M+2H^+/2$): 2151.04/2, found:1075.02.

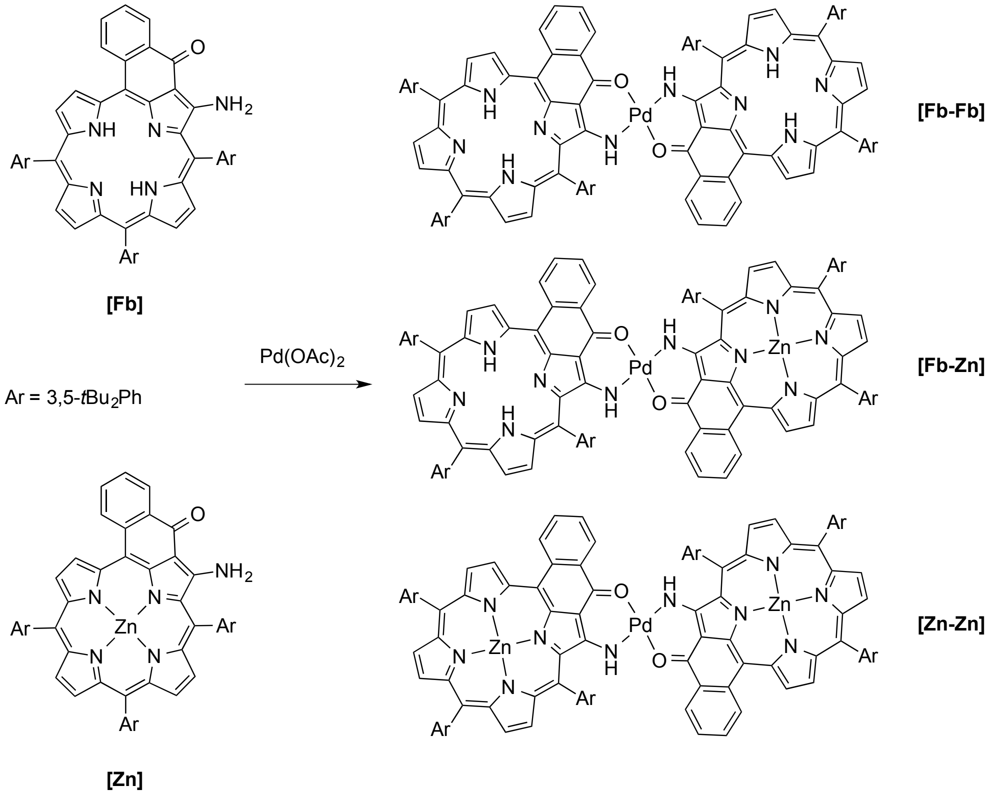

Scheme 1. Synthesis of dyads **[Zn-Zn], [Fb-Zn]** and **[Fb-Fb].**

Fluorescence quantum yield and lifetimes. The measurements of the emission quantum yields were performed in 2MeTHF at 298K. Three different measurements (i.e. different solutions) were prepared for each photophysical datum (quantum yields and lifetimes). For 298K measurements samples were prepared under inert atmosphere (in a glove box, $P_{O2} <$ 25 ppm). The sample and the standard concentrations were adjusted to obtain an absorbance of 0.05 or less. This absorbance was adjusted to be the same as much as possible for the standard and the sample for a measurement. Each absorbance value was measured five times for better accuracy in the measurements of the quantum yields. The equation $\Phi_s = \Phi_r(F_r/F_s)(I_s/I_r)(n_s/n_r)^2$ was used to calculate the relative quantum yield of each of the sample, where Φ_r is the absolute quantum yield of the reference, n is the refractive index of the solvent, F is the absortance ($F= 1\text{-}10^{-A}$, where A is the absorbance) at the excitation wavelength, and I is the integrated area under the corrected emission curve. The subscripts s and r refer to the sample and reference, respectively. A solution of *meso*-tetraphenylporphyrin (H_2TPP) in 2MeTHF ($\Phi_F = 0.11$)[2] was used as the external reference. The emission lifetimes in the 1 to 10 ns range were measured on a TimeMaster model TM-3/2003 apparatus from PTI. The source was a nitrogen laser with high-resolution dye laser (fwhm~1400 ps) and the excited lifetimes were obtained from deconvolution or distribution lifetimes analysis. Time resolved photoluminescence measurement was done by using Titan-sapphir with regenerative amplificator as the laser source and Axis Photonique Inc. AXIS-TRS Streak camera was used as a detector. This detector allowed measurement in the time window of 3 ps to ~3 ns (see below). The data analyses were made using open source software named Glotaran 1.3. This technique allows for the reliable measurements of fluorescence lifetime between 8 ps and 2 ns. Any lifetime above this value is not accurate.

Femptosecond transient absorption spectroscopy. The fs transient spectra and decay profiles were acquired on an homemade system using the SHG of a Soltice (Spectra Physics) Ti-Sapphire laser (λ_{exc} = 398 nm; FWHM = 75 ps; pulse energy = 0.1 μJ/pulse, rep. rate = 1 kHz; spot size ~ 500 μm), a white light continuum generated inside a Sapphire window and a custom made dual CCD camera of 64 x 1024 pixels sensitive between 200 and 1100 nm (S7030, Spectronic Devices). The delay line permitted to probe up to 4 ns with an accuracy of ~4 fs. The results were analysed with the program Glotaran (*http://glotaran.org*) permitting to extract a sum of independent exponentials ($I(\lambda,t) = C_1(\lambda)\bullet\exp(-t/\lambda_1)+C_2(\lambda)\bullet\exp(-t/\lambda_2)+\ldots$) that fits the whole 3D transient map.

Fast kinetic fluorescence measurements: The search for short components (3 ps < τ_F <~3 ns) of the fluorescence decays were performed using the output of an OPA (OPA-800CF, Spectra-Physics) operating at λ_{exc} = 635 nm, pulse width of 90 ps, rep. rate = 1 kHz, pulse energy = 1.6 µJ/pulse, spot size ~2 mm, and a Streak Camera (Axis-TRS, Axis Photonique Inc.) with less than 3 and 8 ps time resolution respectively at 298 and 77K. The results were also globally analysed with the program Glotaran (*http://glotaran.org*) permitting to extract a sum of independent exponentials ($I(\lambda,t) = C_1(\lambda)\bullet\exp(-t/\tau_1)+C_2(\lambda)\bullet\exp(-t/\tau_2)+\ldots$).

Computational Methodology. Computational Methodology. All density functional theory (DFT) calculations were performed with Gaussian 09[2] at the Université de Sherbrooke with the MP2 supercomputer supported by Le Réseau Québécois De Calculs Hautes Performances. The DFT [3-6] geometry optimisations well as TD-DFT calculations [7-9] were carried out using the B3LYP method.[10-12] 6-31g* basis sets [13-19] were used for the porphyrin macrocycles. 3-21g*[20-25] basis sets were used for the phenyl groups of the porphyrin and tert-butyl groups attached to the phenyl. VDZ (valence double ζ) with SBKJC effective core potentials [26-28] were used for Zn, Pd. The calculated absorption spectra, were obtained from GaussSum 2.1.[29] No solvent field was applied. It was not necessary for the purpose of this work.

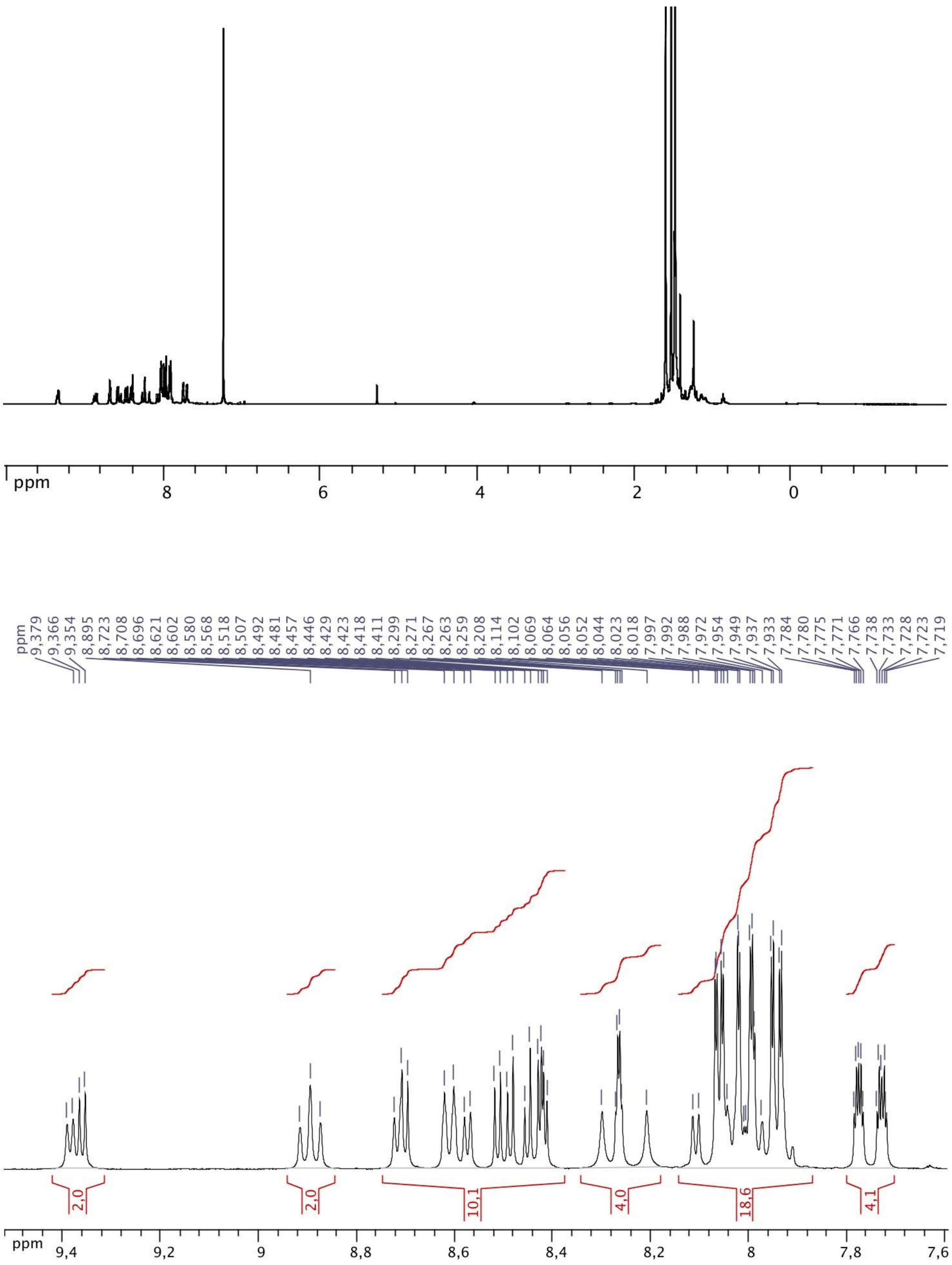

Figure S1: ^{1}H NMR of **[Fb-Zn]** (bottom: expansion of the aromatic region).

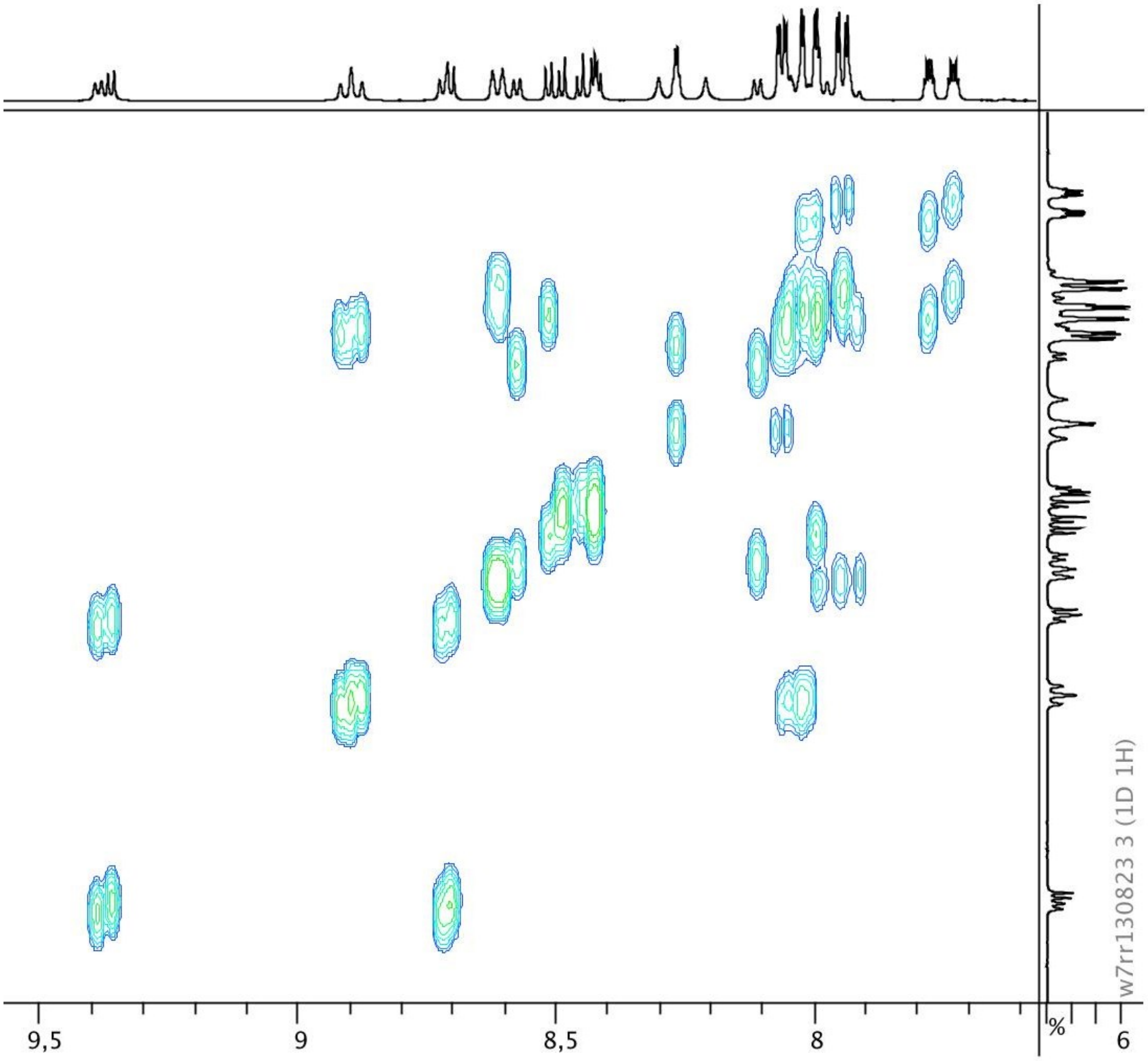

Figure S2: ^{1}H-^{1}H COSY spectrum of **[Fb-Zn]** (aromatic region only).

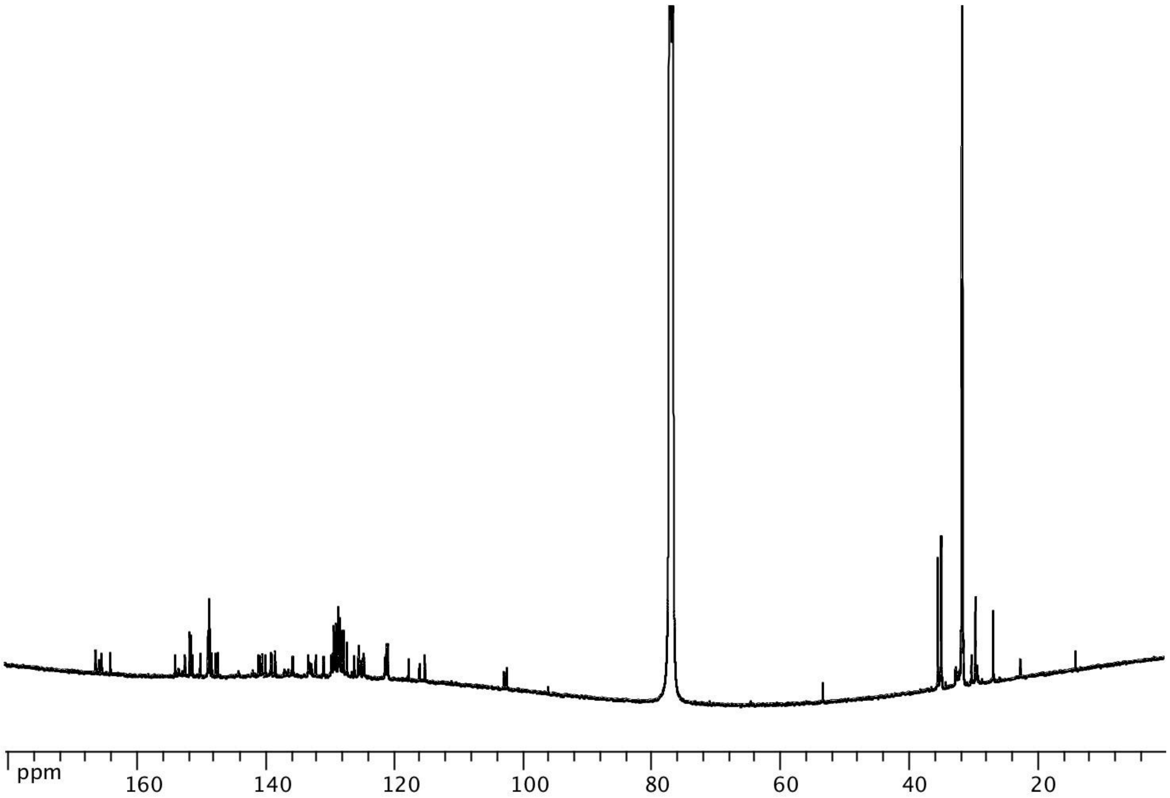

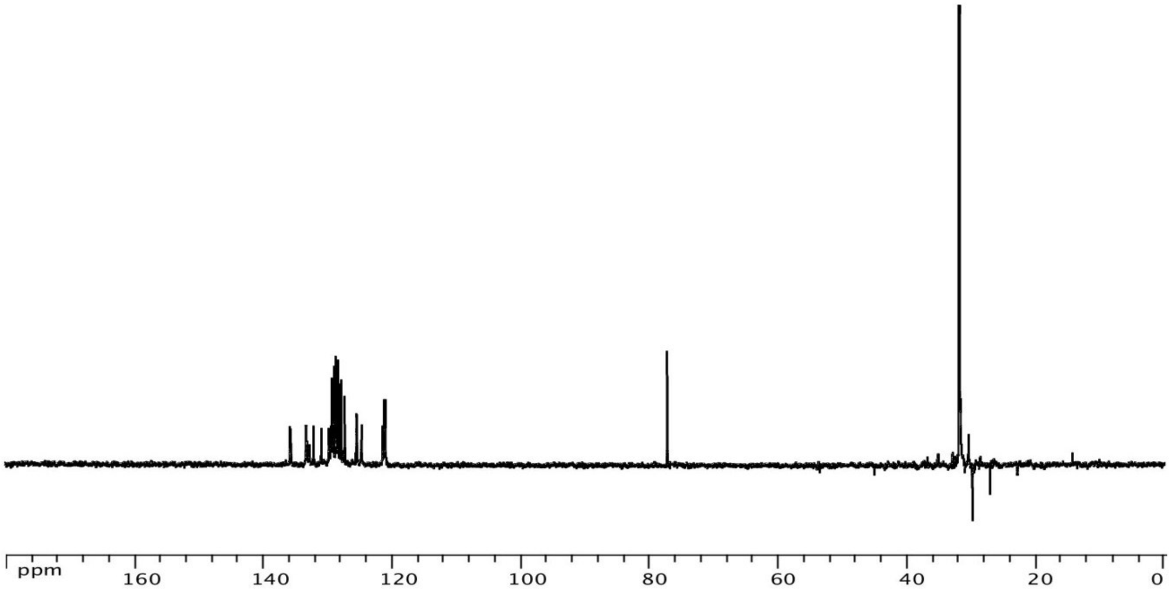

Figure S3: ^{13}C (top) and DEPT135 (bottom) of **[Fb-Zn]** (cryo, 125 MHz).

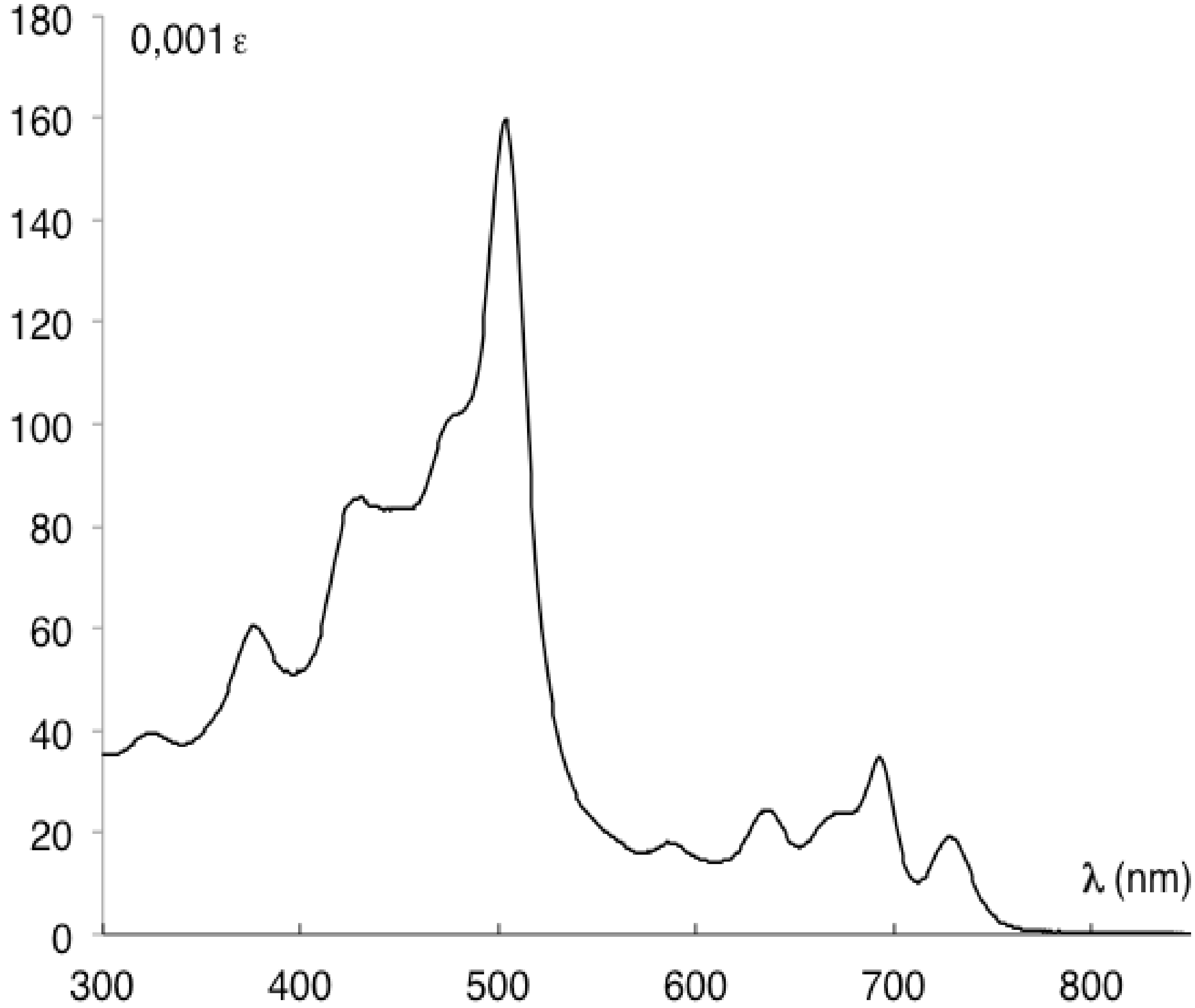

Figure S4. Absorption spectrum of **[Fb-Zn]** in CH_2Cl_2.

Acquisition Parameter

Source Type	ESI	Capillary	4500 V	Nebulizer	0.4 Bar	Corona	195 nA
Ion Polarity	Positive	Set Capillary Exit	100.0 V	Dry Gas	4.0 l/min	Set Hexapole RF	220.0 V
n/a	n/a	Set Skimmer 1	50.0 V	Dry Heater	180 °C	APCI Heater	514 °C

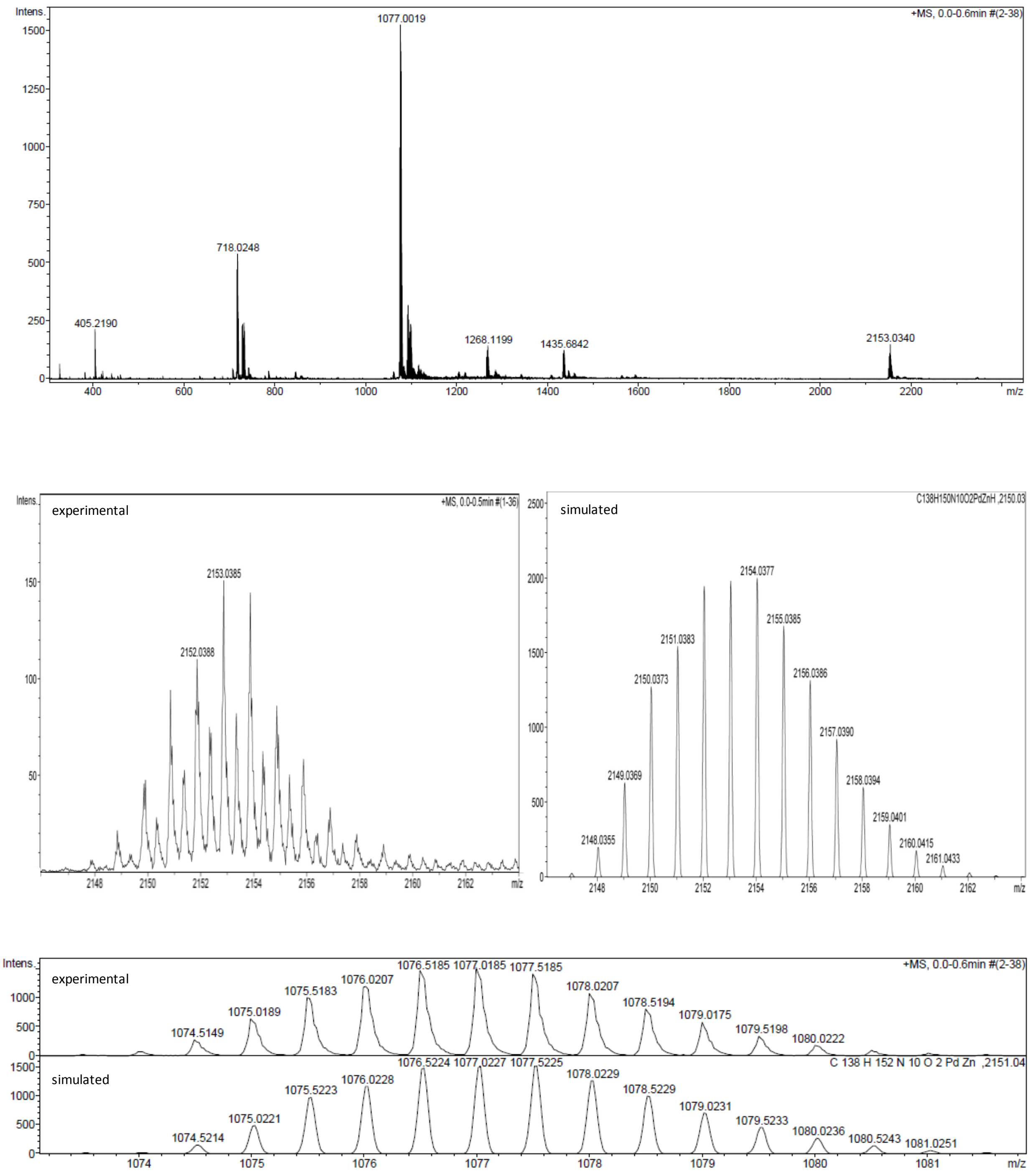

Meas. m/z	#	Formula	Score	m/z	err [mDa]	err [ppm]	mSigma	rdb	e⁻ Conf	N-Rule
1075.5183	1	C 138 H 152 N 10 O 2 Pd Zn	100.00	1075.5223	3.9	3.7	67.5	68.0	even	ok

Figure S5. Experimental and simulated mass spectra (ESI mass) of **[Fb-Zn]**.

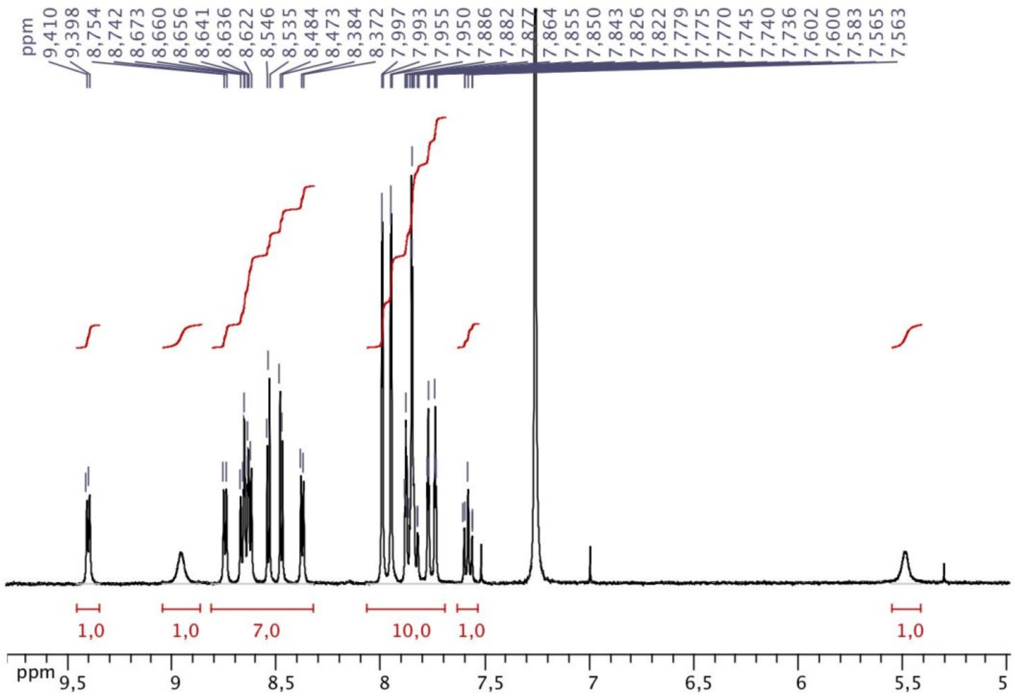

Figure S6. ^{1}H NMR of **[Fb]** (aromatic part).

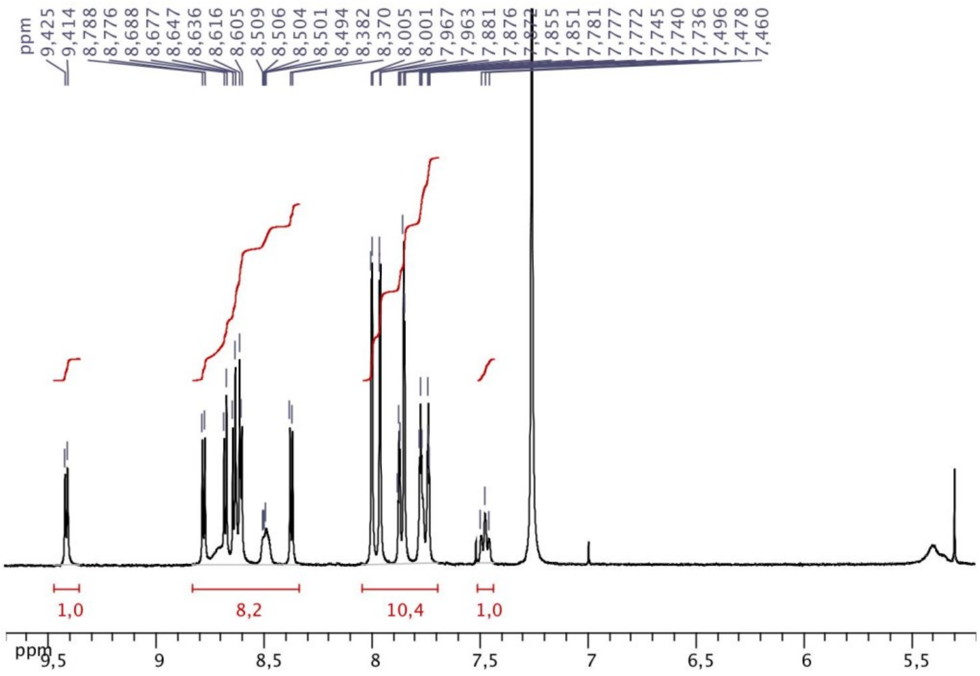

Figure S7. ^{1}H NMR of **[Zn]** (aromatic part).

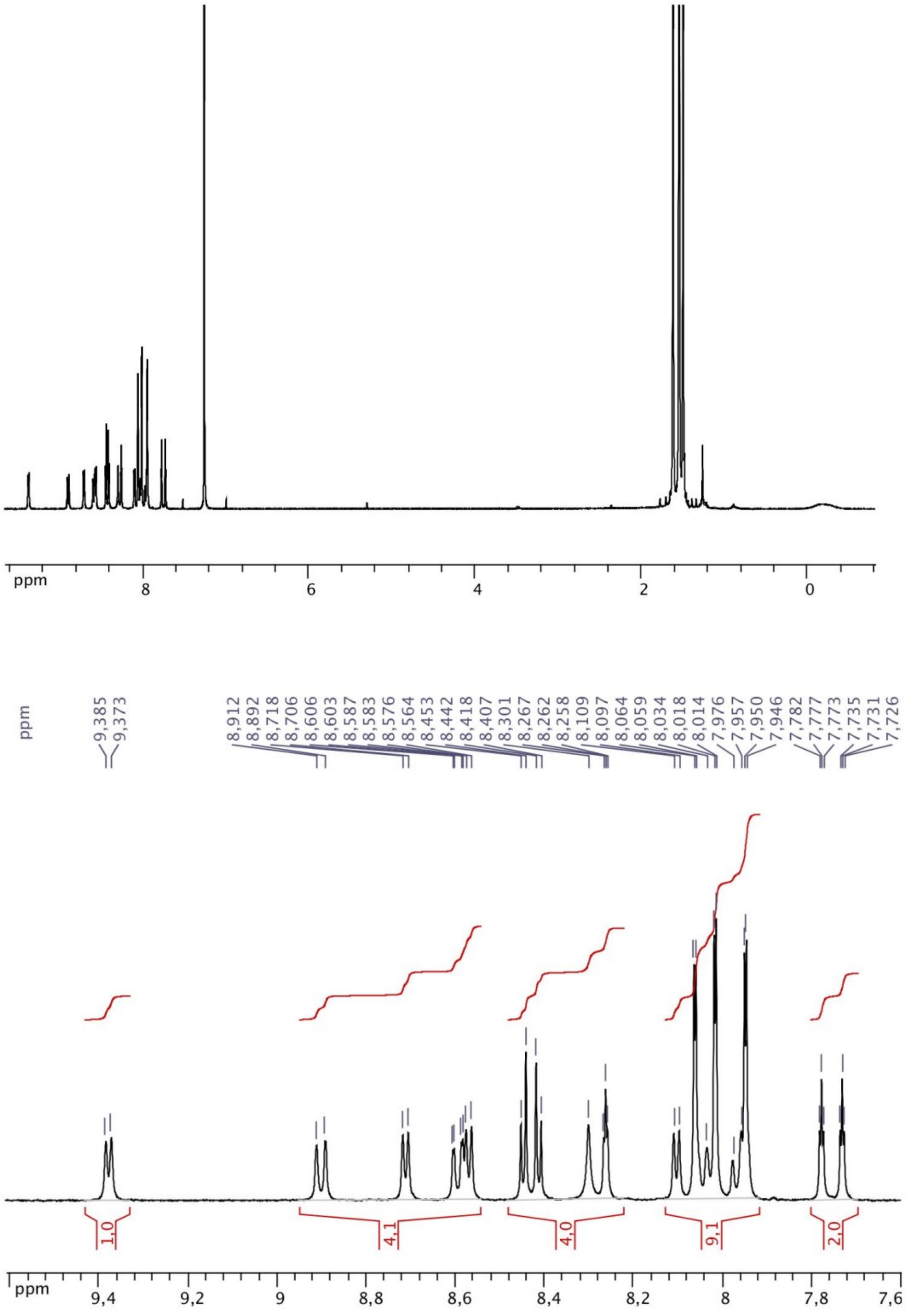

Figure S8. ^{1}H NMR of **[Fb-Fb]** (aromatic part at the bottom).

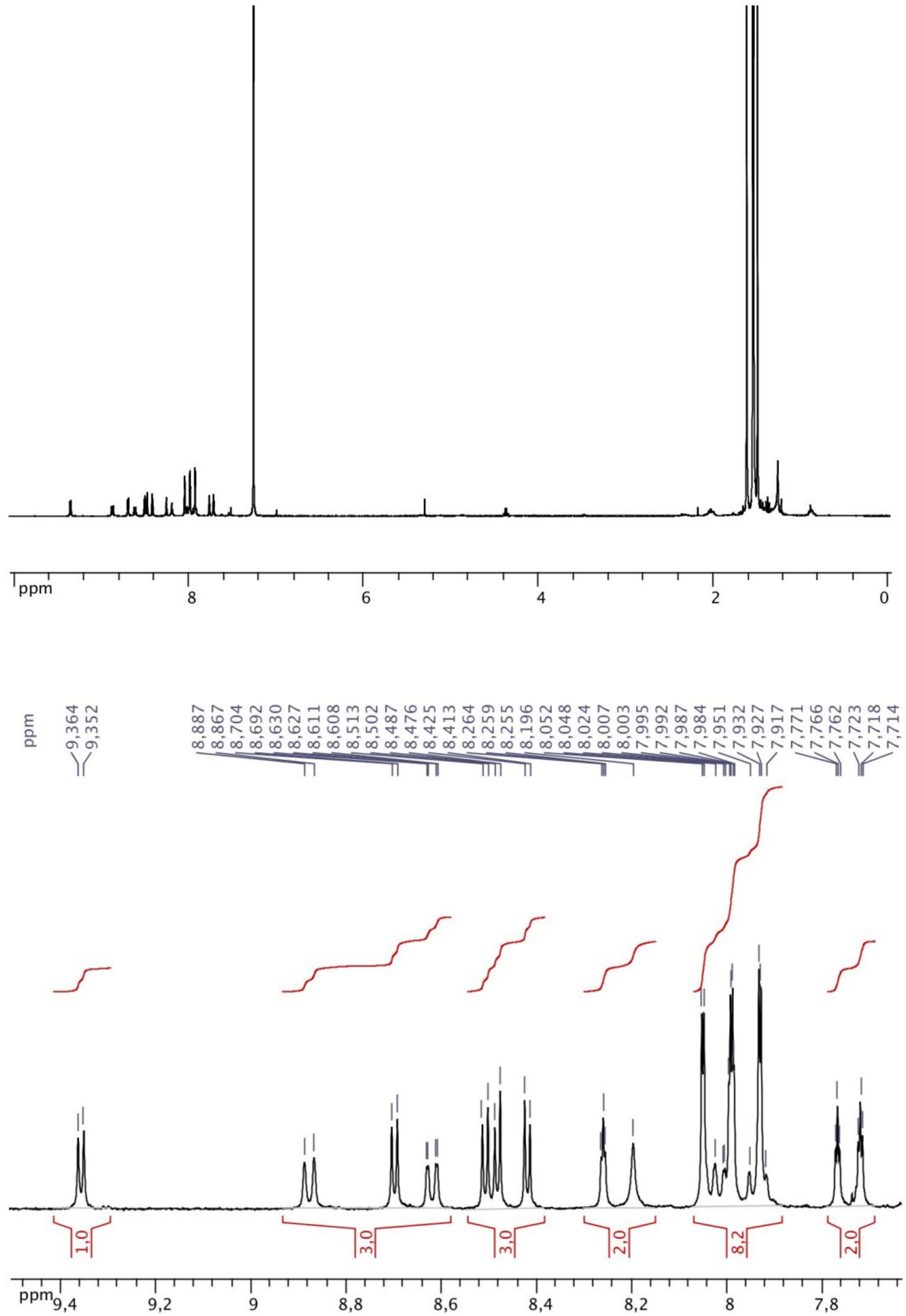

Figure S9. ^{1}H NMR of **[Zn-Zn]** (bottom: expansion of the aromatic region).

Table S1. Absorption data.

Compound	**λ_{max} (nm), ε ($M^{-1}.cm^{-1}$) in CH_2Cl_2 at 298 K**	**λ_{max} (nm) at 77 K in 2MeTHF**
[Zn]	382 (42100), 466 (170900), 608 (13300), 664 (31900).	388, 476, 562, 624, 664.
[Fb]	315 (28200), 371 (46200), 394 (47300), 456 (107800), 571 (9100), 617 (21500), 711 (8500).	372, 396, 450, 568, 616, 706.
[Zn-Zn]	378 (75800), 428 (100800), 500 (246000), 634 (31100), 674 (53700), 696 (75400).	380, 428, 508, 592, 636, 698.
[Fb-Fb	375 (85000), 429 (119000), 475 (11900), 507 (182000), 588 (31500), 639 (34300), 660 (25300), 730 (39000).	378, 426, 478, 508, 588, 638, 728.
[Fb-Zn]	374 (59600), 428 (85400), 503 (160000), 586 (17900), 634 (24200), 691 (34500), 727 (19300).	378, 446, 484, 512, 592, 638, 694, 728.

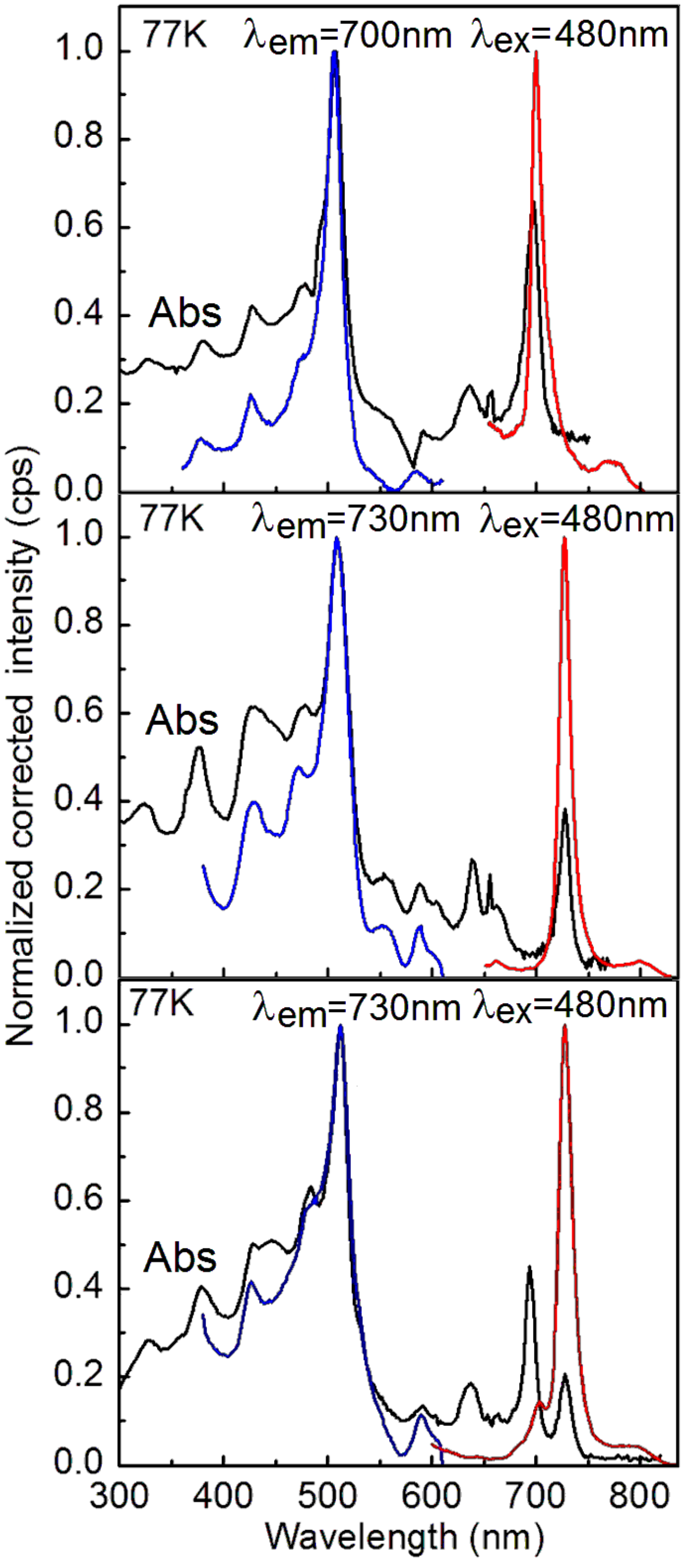

Figure S10. Absorption (black), fluorescence (red) and excitation (blue) spectra of **[Zn-Zn]** (top), **[Fb-Fb]** (centre) and **[Fb-Zn]** (bottom) in 2MeTHF at 77K.

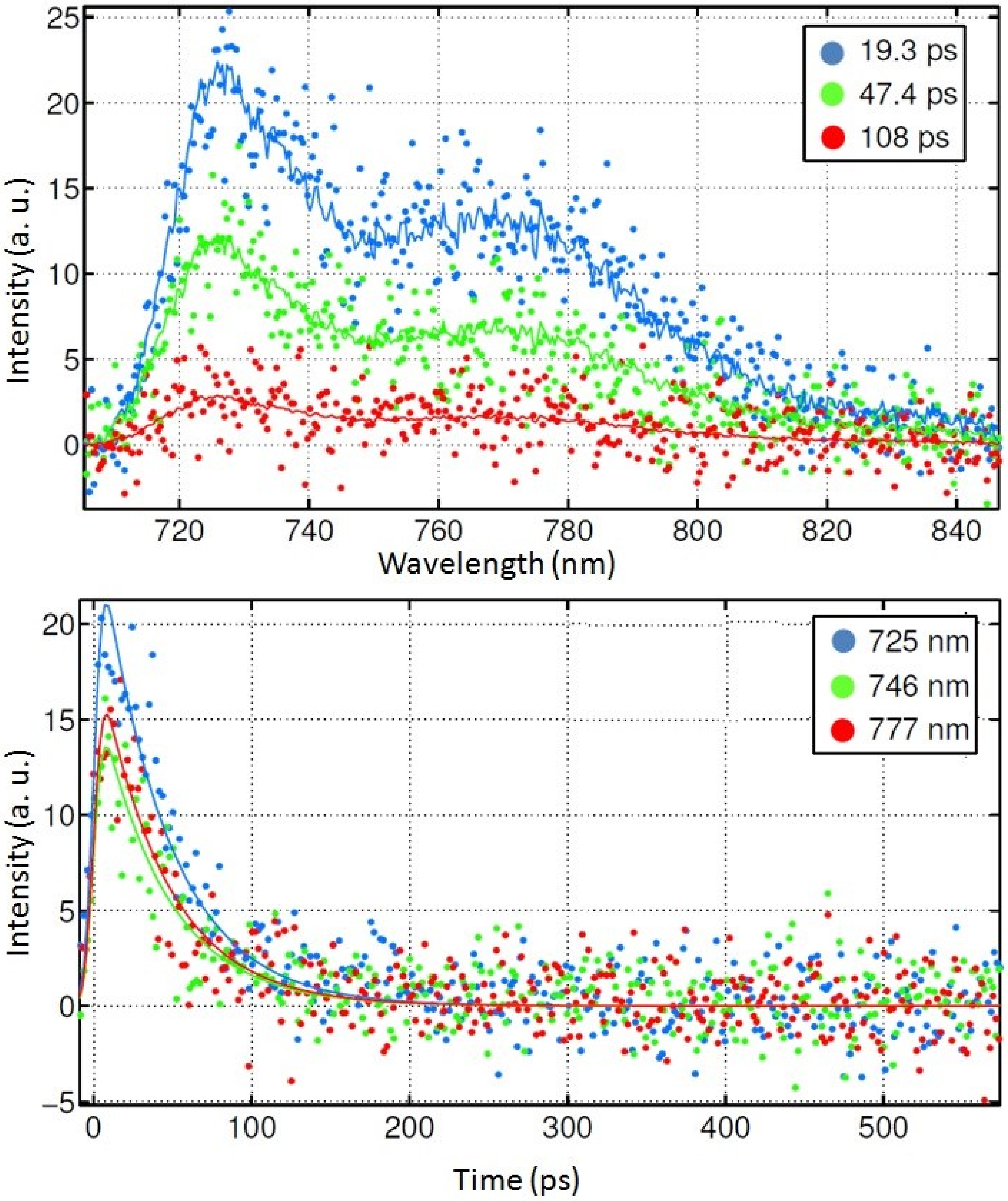

Figure S11.Time resolved fluorescence spectra of **[Zn-Zn]** in 2MeTHF at 298K using the Streak camera. Top: time-resolved spectra. Bottom: decay traces. The best fits are all monoexponential.

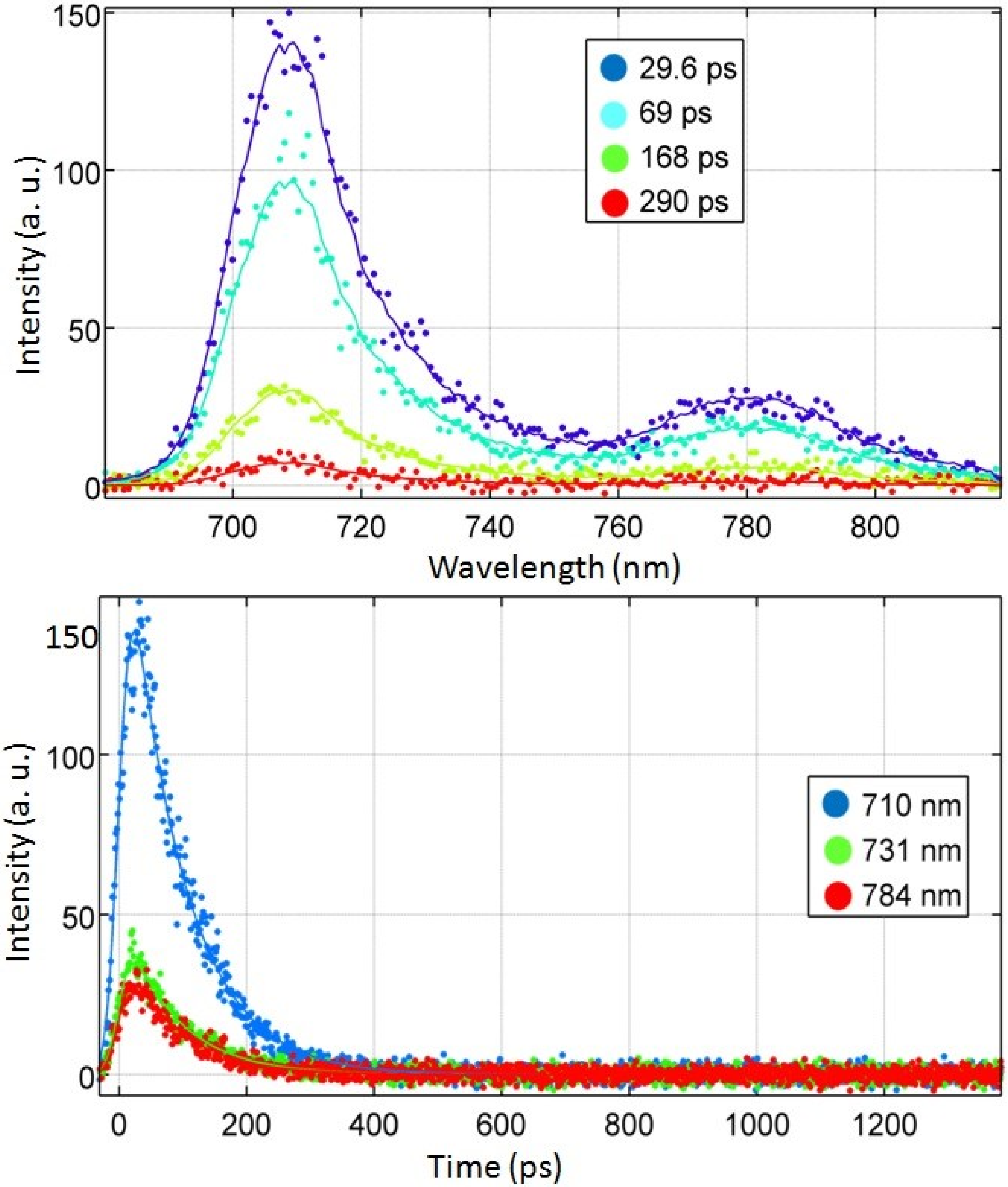

Figure S12.Time resolved fluorescence spectra of **[Zn-Zn]** in 2 MeTHF at 77K using the Streak camera. Top: time-resolved spectra. Bottom: decay traces. The best fits are all monoexponential.

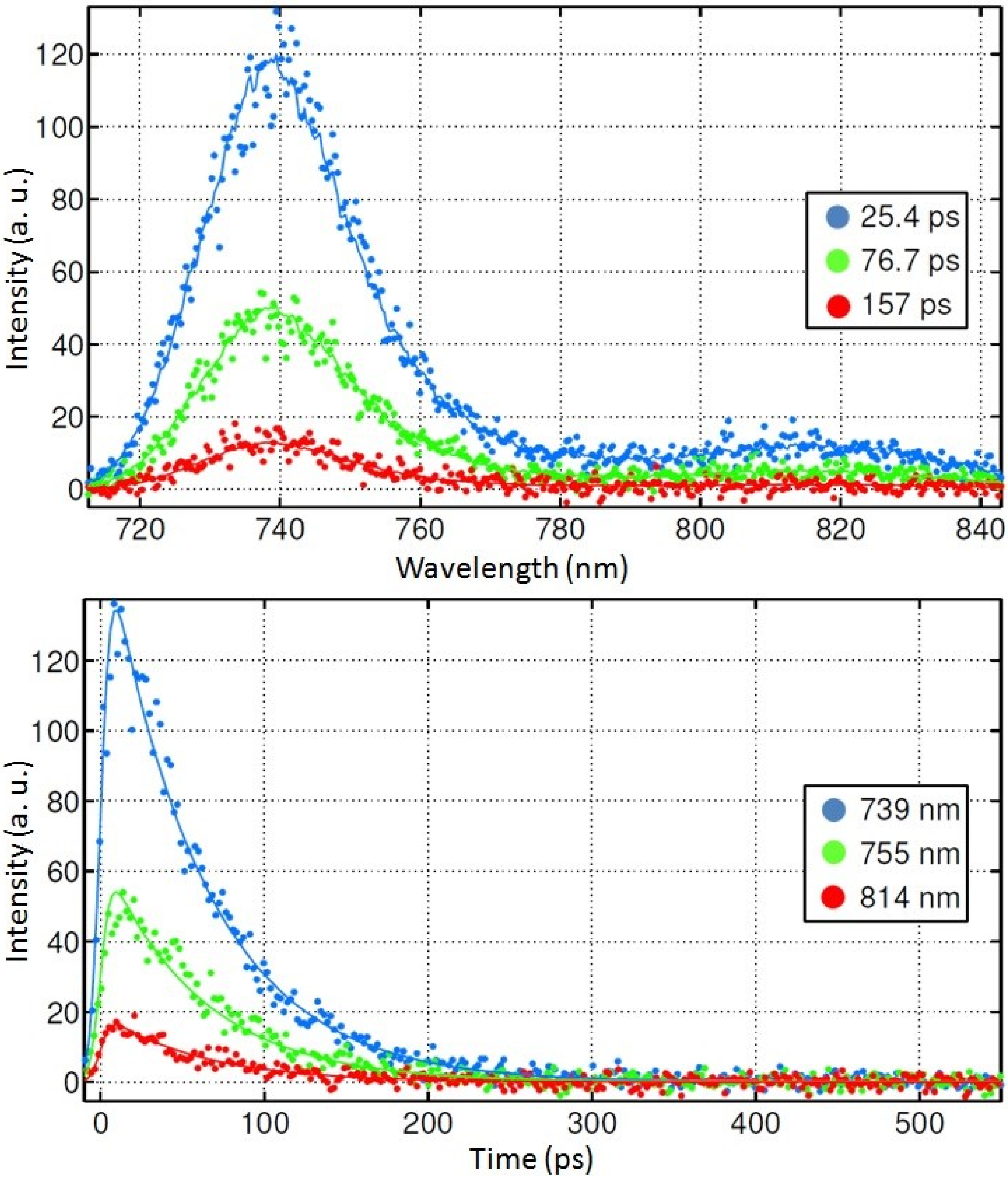

Figure S13.Time resolved fluorescence spectra of **[Fb-Fb]** in 2 MeTHF at 298K using the Streak camera. Top: time-resolved spectra. Bottom: decay and rise traces.

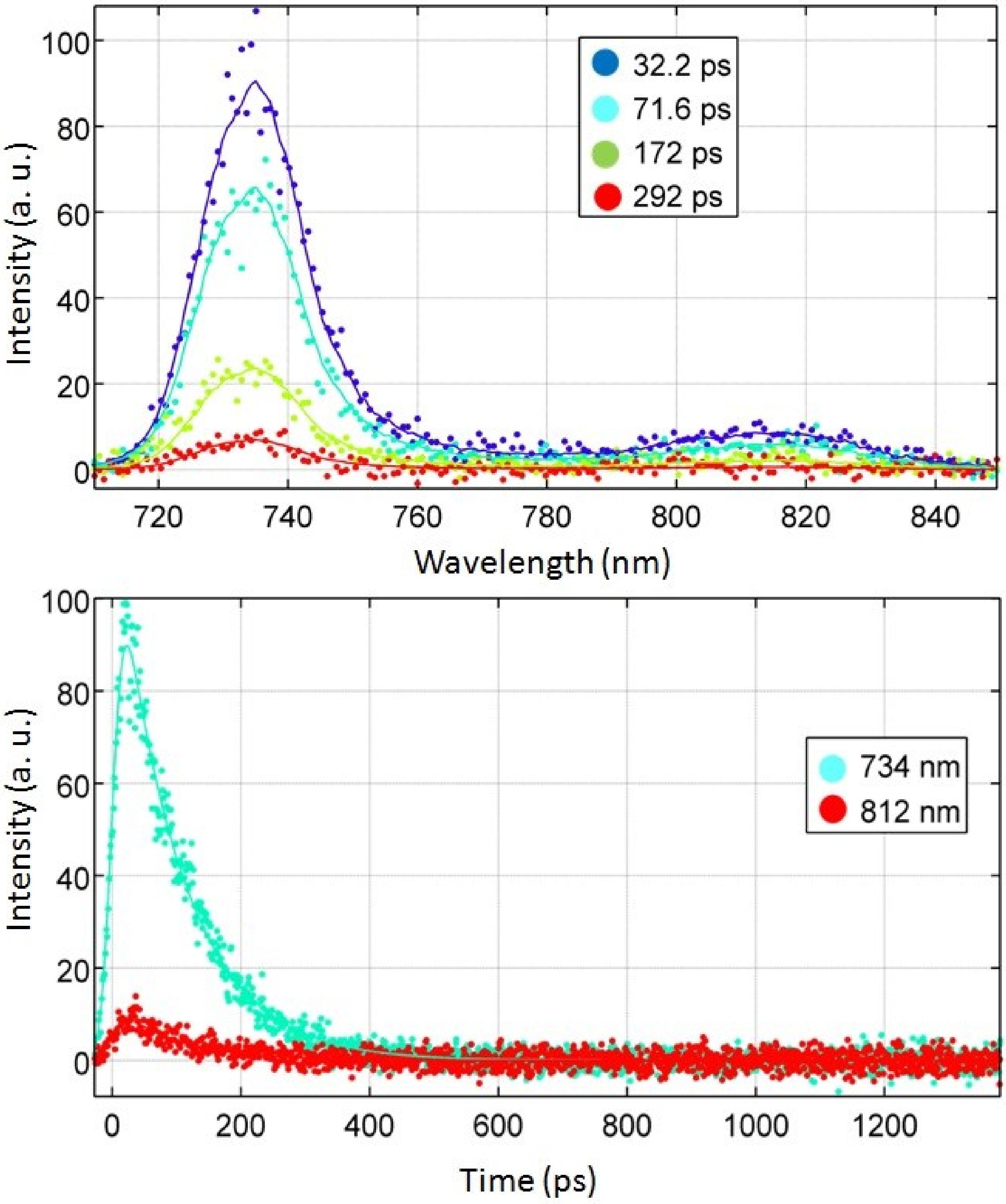

Figure S14.Time resolved fluorescence spectra of **[Fb-Fb]** in 2 MeTHF at 298K using the Streak camera. Top: time-resolved spectra. Bottom: decay traces. The best fits are all monoexponential.

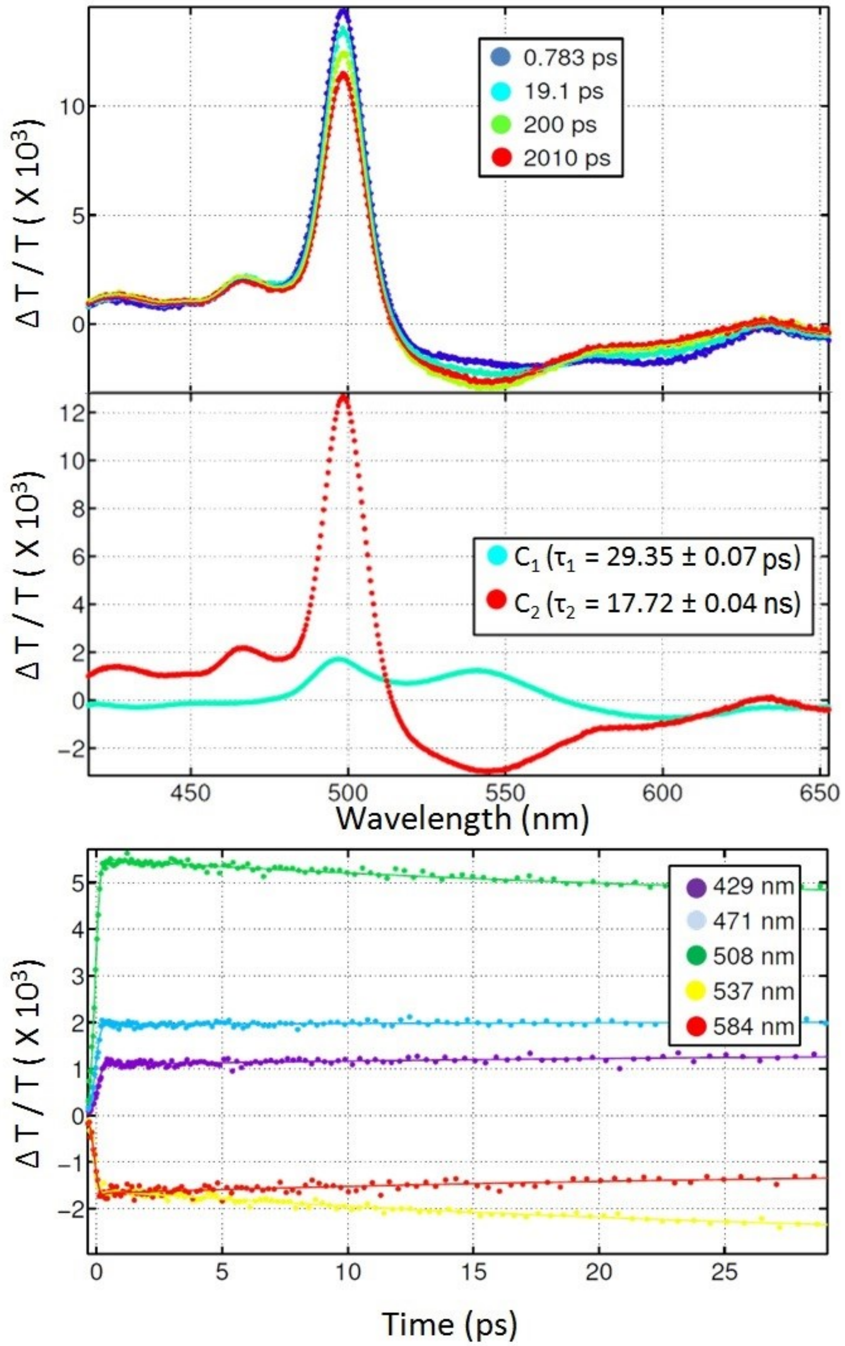

Figure S15. Transient absorption spectra of **[Zn-Zn]** in 2MeTHF at 298K (up), reconstruction of the transient spectra of the various intermediates (middle) and decay and rise traces monitored at various wavelengths (bottom). The fast decays and rise traces are due to the direct absorption of the laser light (<<1ps). The values indicated inside the insets (middle frame) are values extracted from the best fits. The value at ~29.4 ps is the S_1 transient (τ_F measured on the Streak camera is 43 ps). The transient relaxing at 17.7 ns is the triplet state, T_1. This value should not be considered accurate because of the delay line used (3.3 ns).

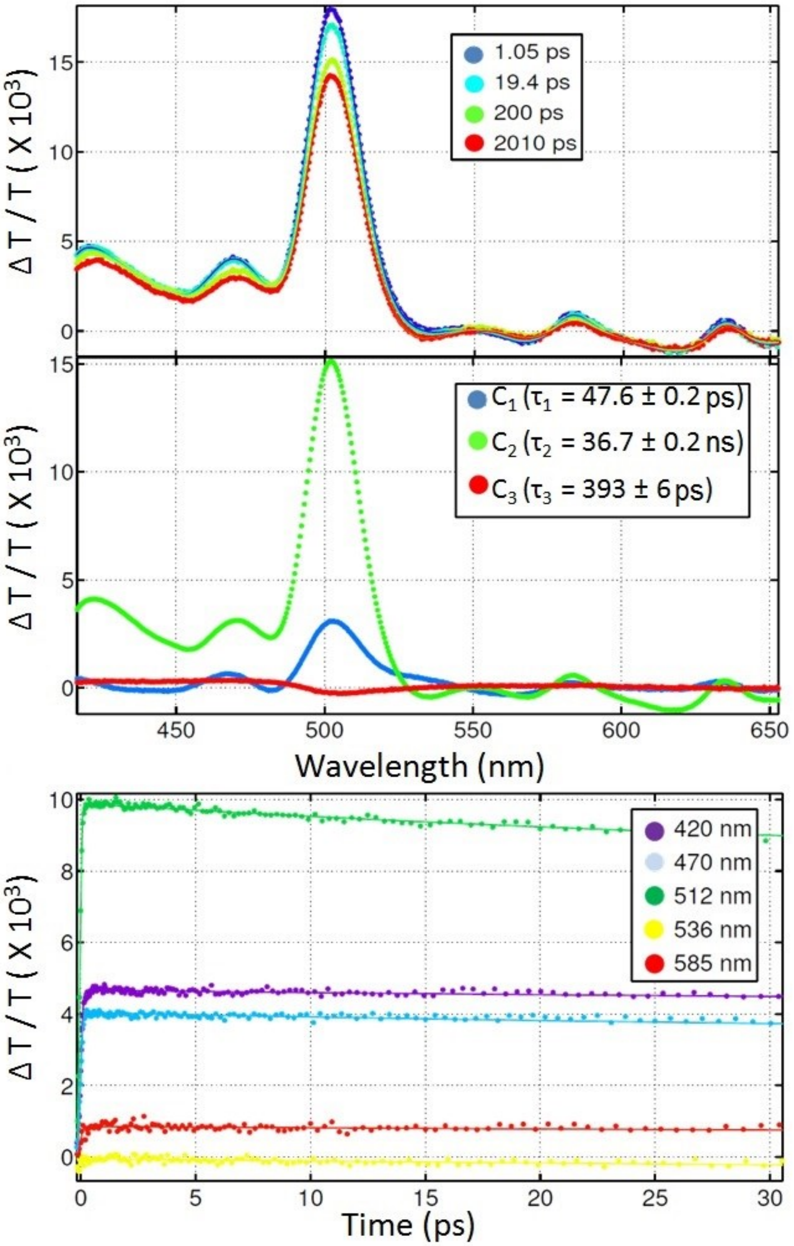

Figure S16. Transient absorption spectra of **[Fb-Fb]** in 2MeTHF at 298K (up), reconstruction of the transient spectra of the various intermediates (middle) and decay and rise traces monitored at various wavelengths (bottom). The values indicated inside the insets (middle frame) are values extracted from the best fits. The species relaxing at ~48 ps is associated with the S_1 transient. (τ_F measured on the Streak camera is 59.7 ps). The transient at relaxing at 36.7 ns is the triplet state, T_1. This value should not be considered accurate because of the delay line used (3.3 ns). The component with a relaxation time of 0.39 ns is very weak and may very likely be unreal.

Optimized geometries in the ground state and frontier MO representations

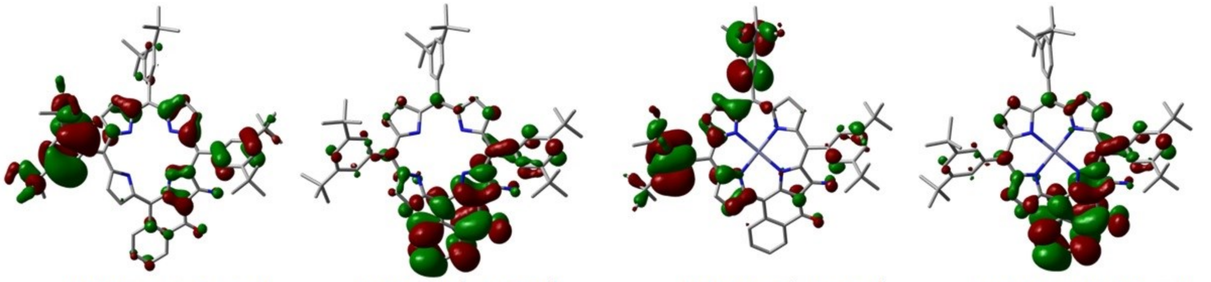

HOMO - 4 (- 7.53 ev)
LUMO + 4 (- 1.97 ev)
HOMO - 4 (- 7.50 ev)
LUMO + 4 (- 1.99 ev)

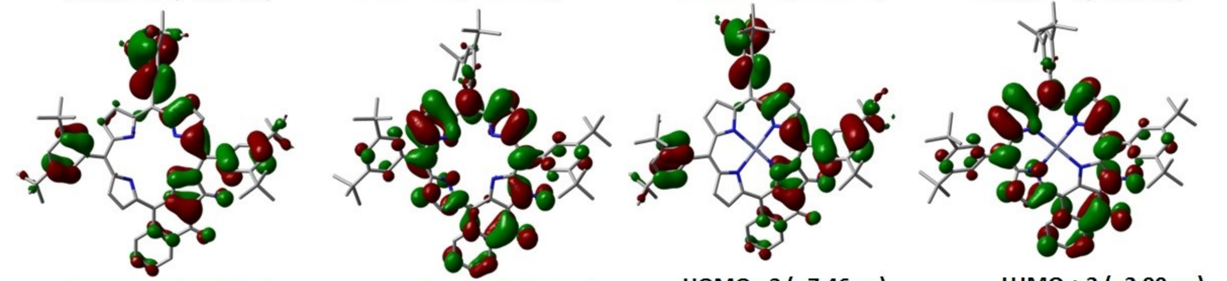

HOMO - 3 (- 7.46 ev)
LUMO + 3 (- 2.97 ev)
HOMO - 3 (- 7.46 ev)
LUMO + 3 (- 2.90 ev)

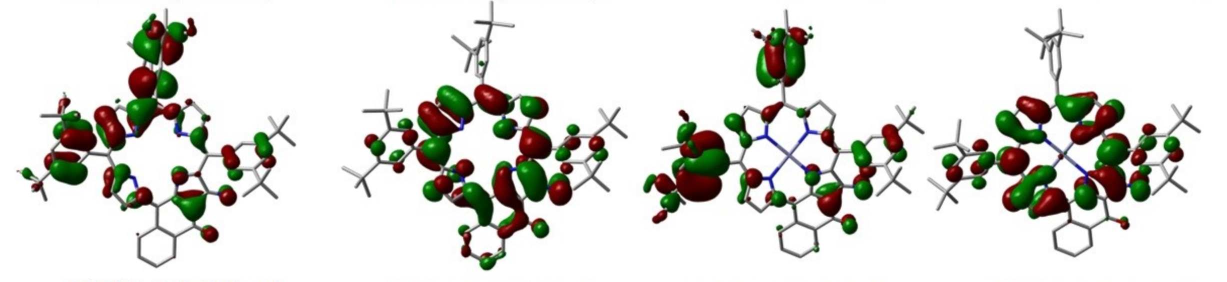

HOMO - 2 (- 7.41 ev)
LUMO + 2 (- 3.97 ev)
HOMO - 2 (- 7.40 ev)
LUMO + 2 (- 3.83 ev)

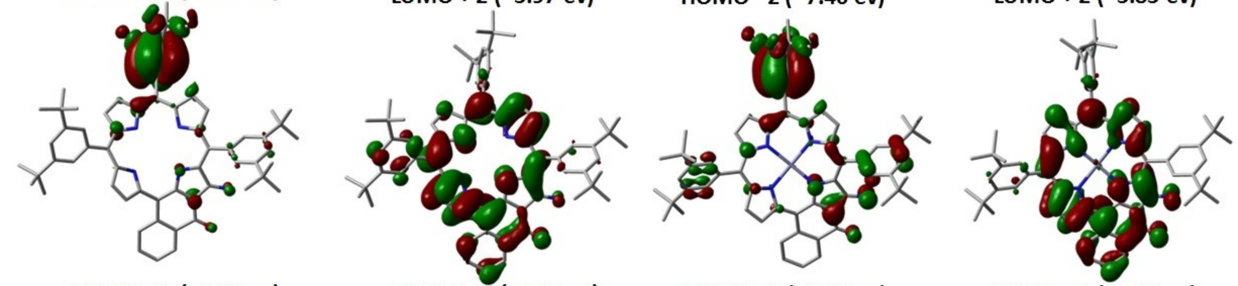

HOMO - 1 (- 7.30 ev)
LUMO + 1 (- 4.26 ev)
HOMO - 1 (- 7.34 ev)
LUMO + 1 (- 4.24 ev)

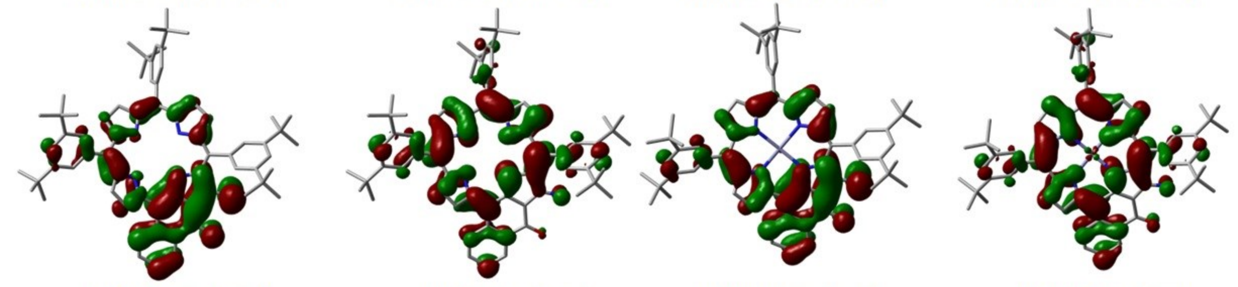

HOMO (- 6.76 ev)
LUMO (- 5.61 ev)
HOMO (- 6.76 ev)
LUMO (- 5.65 ev)

Figure S17. Representation of the frontier MOs for **[Fb]** (left) and **[Zn]** (right).

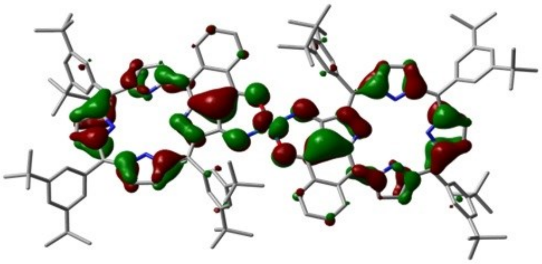

HOMO - 4 (- 5.82 ev)

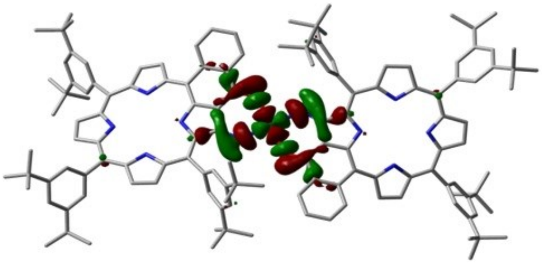

LUMO + 4 (- 1.64 ev)

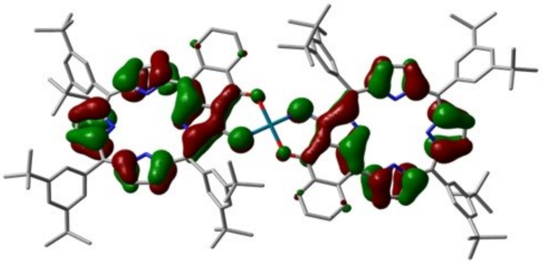

HOMO - 3 (- 5.16 ev)

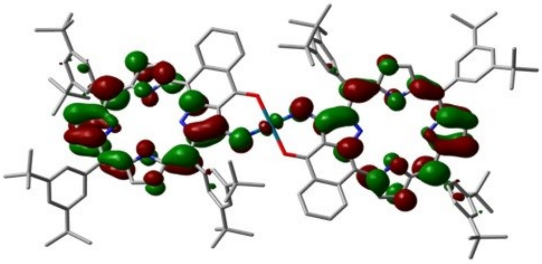

LUMO + 3 (- 2.17 ev)

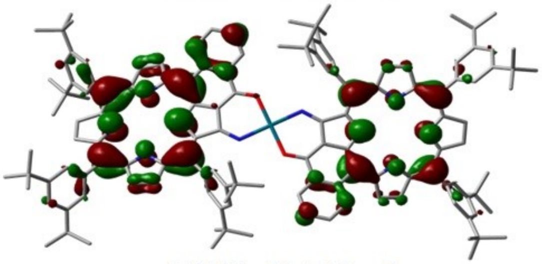

HOMO - 2 (- 5.02 ev)

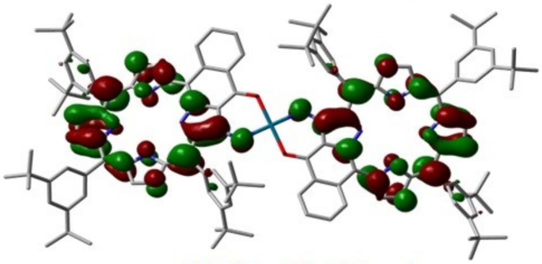

LUMO + 2 (- 2.25 ev)

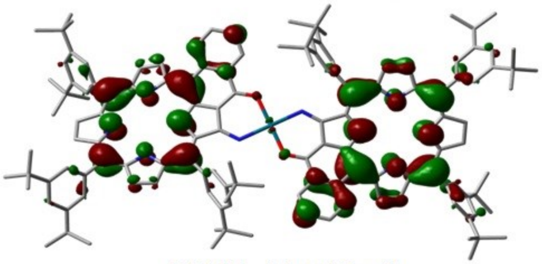

HOMO - 1 (- 5.02 ev)

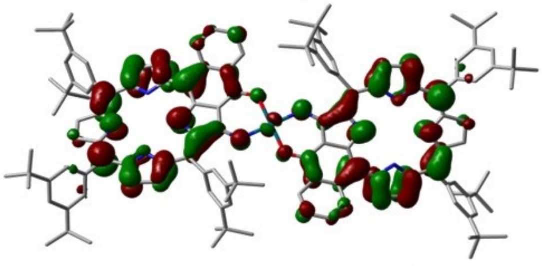

LUMO + 1 (- 2.66 ev)

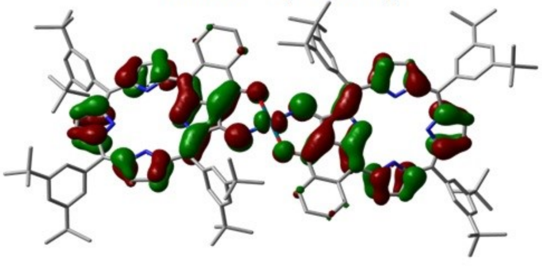

HOMO (- 4.93 ev)

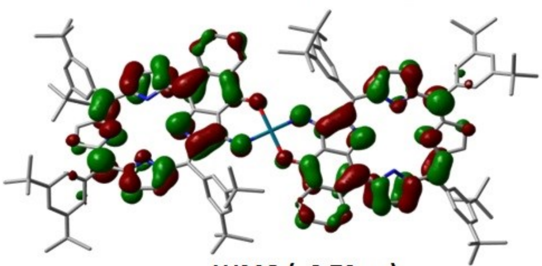

LUMO (- 2.70 ev)

Figure S18. Representation of the frontier MOs for **[Fb-Fb]**.

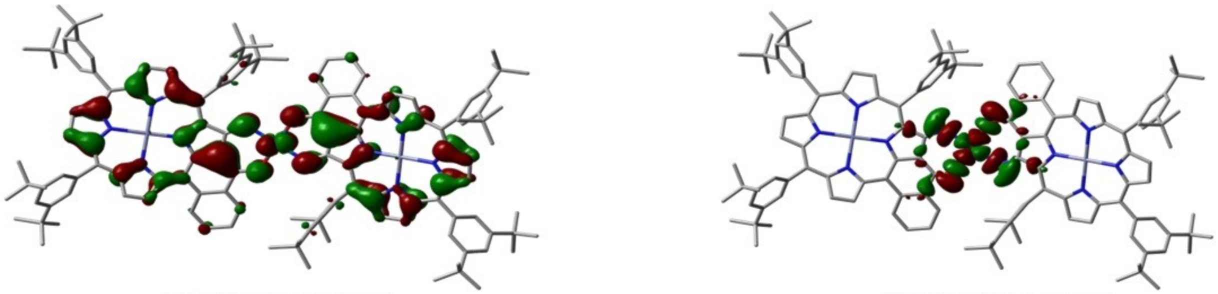

HOMO - 4 (- 5.76 ev) **LUMO + 4 (- 1.62 ev)**

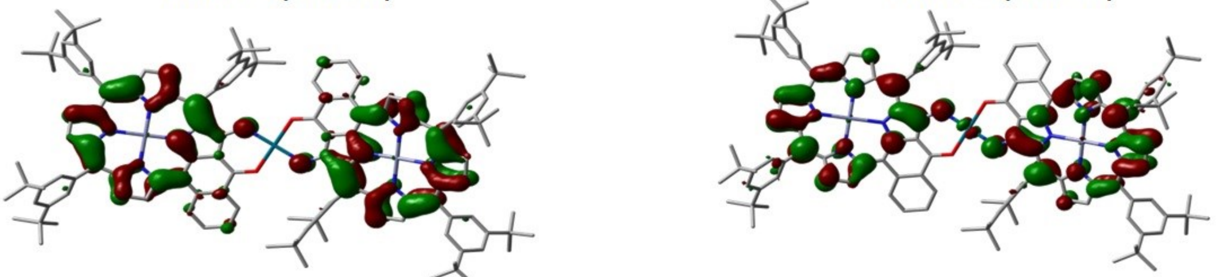

HOMO - 3 (- 5.12 ev) **LUMO + 3 (- 2.02 ev)**

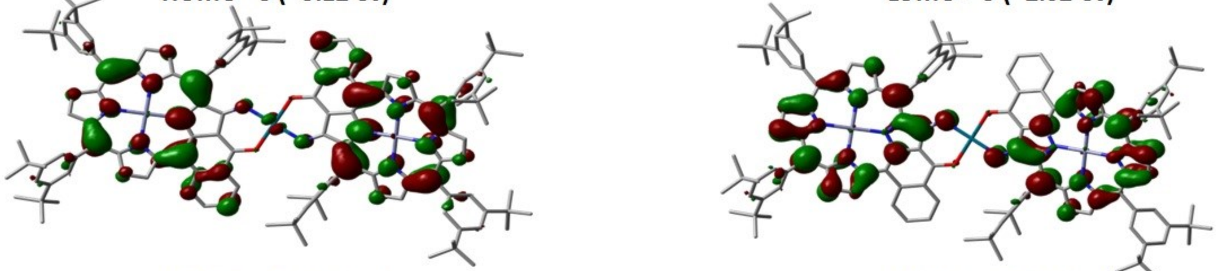

HOMO - 2 (- 5.07 ev) **LUMO + 2 (- 2.10 ev)**

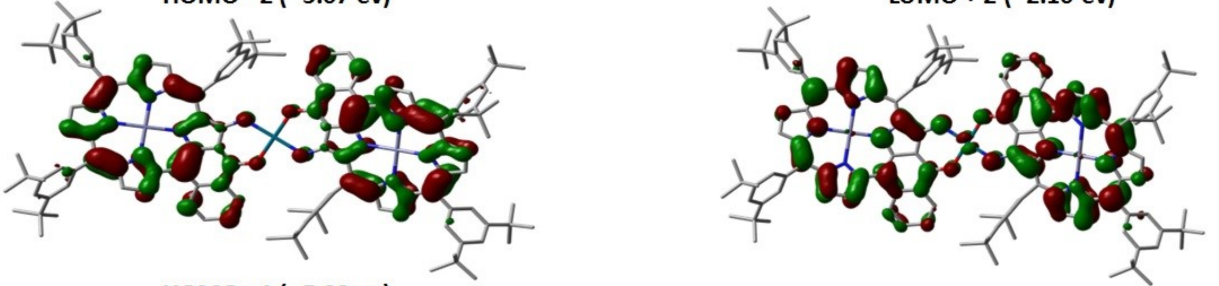

HOMO - 1 (- 5.02 ev) **LUMO + 1 (-2.60 ev)**

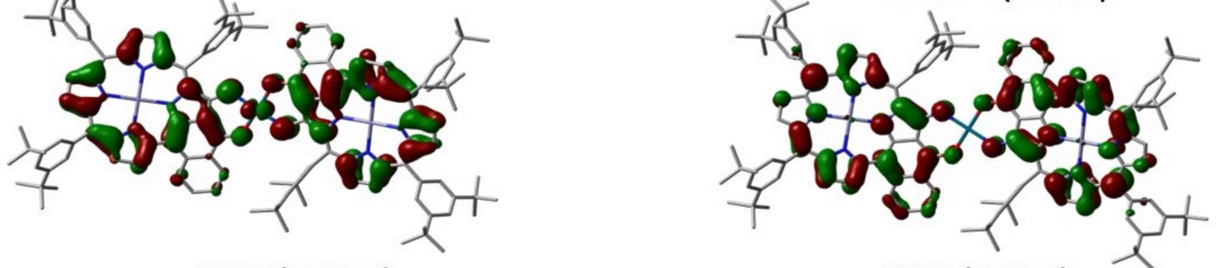

HOMO (- 4.86 ev) **LUMO (-2.65 ev)**

Figure S19. Representation of the frontier MOs for **[Zn-Zn]**.

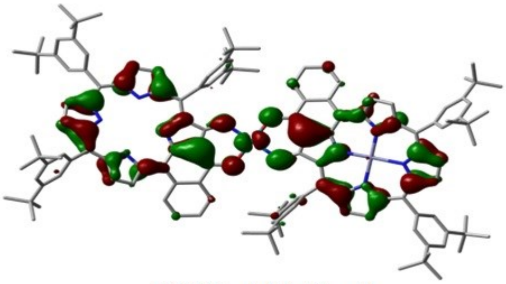

HOMO - 4 (-5.80 ev)

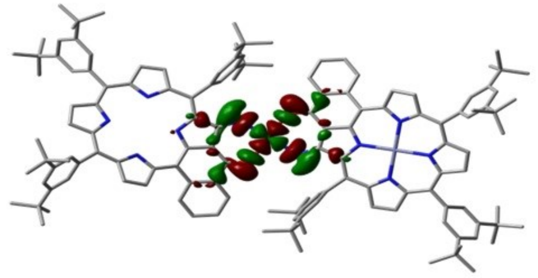

LUMO + 4 (-1.63 ev)

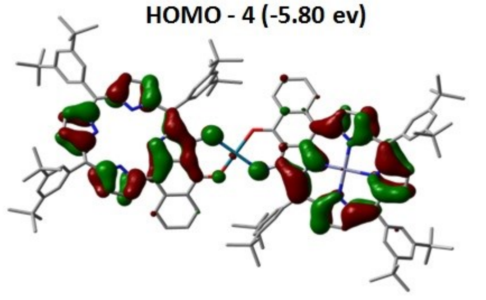

HOMO - 3 (-5.13 ev)

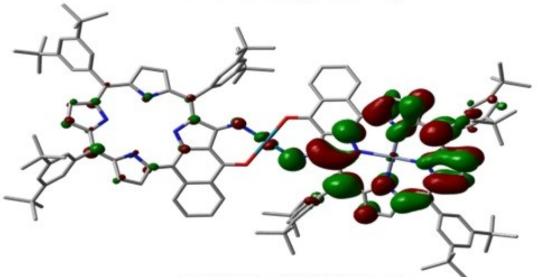

LUMO + 3 (-2.05 ev)

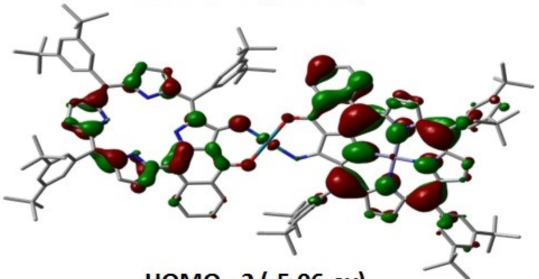

HOMO - 2 (-5.06 ev)

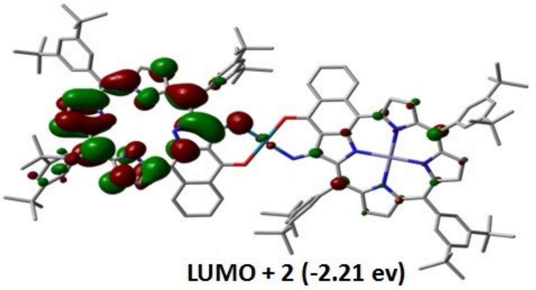

LUMO + 2 (-2.21 ev)

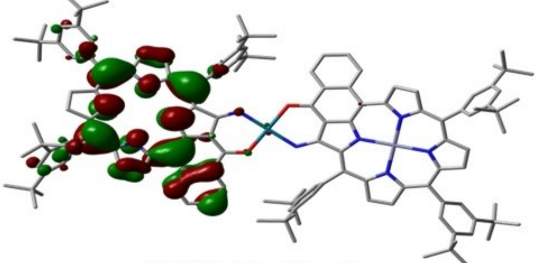

HOMO-1 (-5.03 ev)

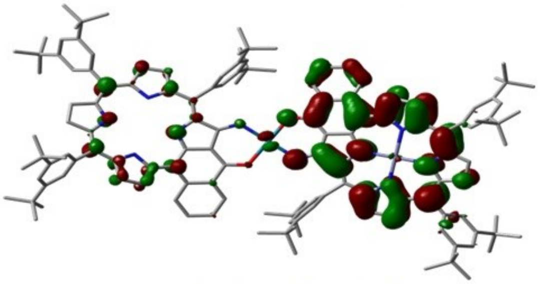

LUMO + 1 (-2.62 ev)

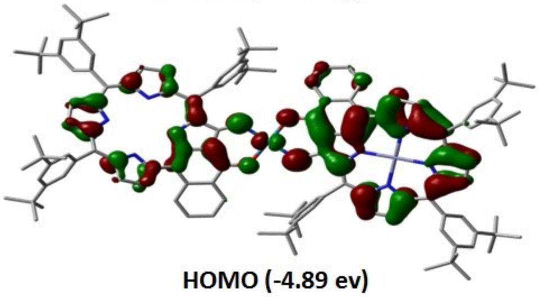

HOMO (-4.89 ev)

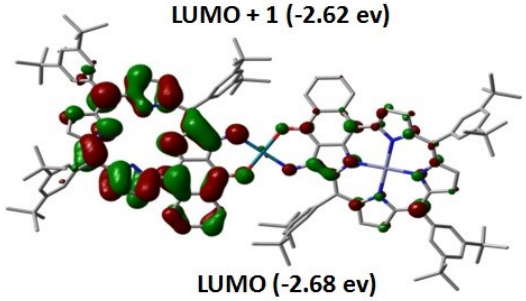

LUMO (-2.68 ev)

Figure S20. Representation of the frontier MOs for **[Fb-Zn]**, the HOMO+4 and LUMO-4 are new in comparison with Fig. 4 in the text.

Atomic Contributions to the MOs

The tables below show the % electronic contributions over given molecular fragments from HOMO-4 to LUMO+4. H and L refer to the HOMO and LUMO orbitals respectively. The fragments are listed on the left of the table. The fragments exhibiting the largest atomic contributions (i.e. > 10%) are highlighted in grey.

Table S2. Relative atomic contributions of the various fragments in **[Fb-Fb]**.[a]

	H-4	H-3	H-2	H-1	HOMO	LUMO	L+1	L+2	L+3	L+4
Pd	7.72	0.43	0.01	0.22	5.42	0.05	1.01	0.37	0.96	39.02
[Fb1]	45.59	49.72	57.71	41.45	47.09	50.47	48.57	50.07	48.88	30.41
[Fb2]	45.79	49.53	41.59	57.56	47.29	49.08	49.92	49.18	49.80	30.41
*t*Bu groups	0.90	0.32	0.69	0.77	0.20	0.40	0.49	0.38	0.36	0.17

a) **[Fb1]** and **[Fb2]** are the free base porphyrin chromophores.

Table S3. Relative atomic contributions of the various fragments in **[Zn-Zn]**.[a]

	H-4	H-3	H-2	H-1	HOMO	LUMO	L+1	L+2	L+3	L+4
Pd	8.90	0.13	1.03	0.24	4.54	0.05	1.25	0.41	0.95	40.72
Zn 1	0.08	0.36	0.54	0.24	0.04	0.12	0.12	0.10	0.10	0.04
Zn 2	0.08	0.34	0.55	0.25	0.04	0.12	0.13	0.10	0.11	0.04
[Zn1]	45.01	50.24	48.15	49.17	47.29	50.56	48.13	50.28	48.45	29.53
[Zn2]	45.14	48.53	49.00	49.46	47.79	48.74	49.90	48.70	50.00	29.53
*t*Bu groups	0.79	0.40	0.73	0.64	0.29	0.41	0.47	0.41	0.39	0.14

a) **[Zn1]** and **[Zn2]** are Zn-containing porphyrin chromophores minus the Zn atom.

Table S4. Relative atomic contributions of the various fragments in **[Fb-Zn]**.[a]

	H-4	H-3	H-2	H-1	HOMO	LUMO	L+1	L+2	L+3	L+4
Pd	8.29	0.44	0.83	0.18	4.64	0.18	1.00	0.54	0.82	40.20
Zn	0.09	0.29	0.81	0.02	0.06	0.03	0.21	0.01	0.19	0.04
[Zn]-Zn	47.59	55.09	73.63	2.00	65.01	14.39	83.58	7.37	91.44	29.23
[Fb]	43.18	43.83	24.06	97.08	30.01	84.98	14.74	91.70	7.17	30.37
*t*Bu groups	0.84	0.35	0.67	0.72	0.28	0.41	0.47	0.38	0.39	0.15

a) **[Fb]** and **[Zn]**-Zn are respectively the free base porphyrin and Zn-containing porphyrin chromophores minus the Zn atom.

Computed Electronic Transitions by TDDFT

Table S5. Calculated position of the pure electronic transitions, oscillator strength (f) and major contributions to the transitions for the first 100 transitions of **[Fb]**.

λ(nm)	f	Major contributions (%)	λ(nm)	f	Major contributions (%)
1885.104708	0.0153	H→L (99%)	412.6862718	0.0272	H-7→L+1 (17%), H-6→L+1 (56%)
1011.778494	0.0147	H-1→L (98%)	410.9763214	0.0658	H-25→L (12%), H-24→L (36%), H-3→L+2 (14%)
939.3388639	0.0329	H-3→L (27%), H-2→L (63%)	407.7460343	0.0037	H-3→L+2 (33%), H-2→L+2 (38%)
855.1164676	0.0396	H-4→L (85%)	406.7694772	0.002	H-7→L+1 (54%), H-6→L+1 (29%)
845.0336467	0.1552	H-3→L (67%), H-2→L (25%)	405.598458	0.0196	H-14→L (80%)
772.8189032	0.0179	H-7→L (27%), H-6→L (64%)	398.570536	0.0919	H-15→L (65%)
751.2775655	0.0834	H-8→L (46%), H-7→L (26%), H-5→L (22%)	395.9610904	0.0179	H-16→L (18%), H-4→L+2 (63%)
723.1035614	0.2646	H-8→L (33%), H-5→L (58%)	393.9731066	0.0615	H-16→L (60%), H-4→L+2 (11%)
710.7506113	0.0738	H-8→L (17%), H-7→L (40%), H-6→L (29%)	388.7843733	0.0054	H-19→L (83%), H-18→L (12%)
642.1012825	0.0029	H-10→L (94%)	386.9279925	0.1426	H-17→L (51%), H-5→L+2 (14%)
628.2408748	0.0066	H-9→L (98%)	384.6352815	0.1029	H-17→L (12%), H-6→L+2 (40%), H-5→L+2 (21%)
580.1747152	0.2406	H-11→L(22%), H→L+1 (68%)	383.5524722	0.0058	H-20→L (74%)
528.2180327	0.2888	H-11→L(56%), H→L+1(12%), H→L+2 (25%)	382.4049616	0.0443	H-22→L (10%), H-18→L (11%), H-7→L+2 (35%), H-6→L+2 (19%)
492.1145377	0.1766	H-12→L (40%), H-11→L(10%), H→L+2 (37%)	380.6672909	0.0505	H-22→L (17%), H-21→L (25%), H-18→L (11%), H-7→L+2 (14%)
489.0282674	0.1252	H-12→L(54%), H→L+2 (23%)	378.1939927	0.0875	H-21→L (21%), H-8→L+2 (24%), H-5→L+2 (10%)
476.2728052	0.06	H-1→L+1 (94%)	377.399661	0.0348	H-21→L (22%), H-7→L+2 (13%), H-6→L+2 (16%),

					H-5→L+2 (28%)
471.4733112	0.0127	H-13→L (95%)	375.661546	0.0625	H-21→L (19%), H-8→L+2 (32%), H-7→L+2 (15%)
458.1285764	0.1694	H-2→L+1 (85%)	373.7815395	0.0349	H-9→L+1 (85%)
452.2958436	0.0138	H-3→L+1 (88%)	369.7794048	0.0705	H-10→L+1 (68%)
444.4803063	0.0756	H-4→L+1 (86%)	364.1320939	0.0503	H-23→L (30%), H→L+3 (44%)
436.7609703	0.0224	H-22→L (36%), H-18→L (24%), H-15→L (15%)	361.425305	0.0391	H-23→L (67%), H→L+3 (20%)
430.4827493	0.0094	H-8→L+1 (50%), H-8→L+2 (14%), H-7→L+1 (14%)	357.0537284	0.0215	H-25→L (43%), H-24→L (37%)
428.13404	0.0638	H-1→L+2 (83%)	353.9145257	0.0125	H-26→L (61%), H-25→L (24%)
418.8626238	0.0385	H-3→L+2 (24%), H-2→L+2 (27%), H-1→L+2 (13%)	351.7257777	0.0078	H-27→L (51%), H-26→L (23%)
414.7987174	0.0177	H-8→L+1 (10%), H-5→L+1 (73%)	350.4234946	0.0087	H-10→L+2 (87%)

Table S6. Calculated position of the pure electronic transitions, oscillator strength (f) and major contributions to the transitions for the first 100 transitions of **[Zn]**.

λ(nm)	**f**	**Major contributions (%)**	**λ(nm)**	**f**	**Major contributions (%)**
2080.257326	0.0136	H→L (100%)	414.4659244	0.0224	H-16→L (79%)
1016.00702	0.0213	H-1→L (93%)	408.9160179	0.0022	H-7→L+1 (82%)
976.7851307	0.0079	H-3→L (10%), H-2→L (82%)	405.9969109	0.0334	H-17→L (57%), H-1→L+2 (17%)
915.1412507	0.0219	H-4→L (35%), H-3→L (49%), H-2→L (12%)	402.3473524	0.0572	H-18→L (35%), H-17→L (33%), H-1→L+2 (24%)
848.3293646	0.1976	H-4→L (61%), H-3→L (35%)	399.0451775	0.0288	H-18→L (38%), H-1→L+2 (41%)
816.9159692	0.0257	H-6→L (90%)	397.7649555	0.0419	H-19→L (17%), H-2→L+2 (59%)
791.6693483	0.2494	H-5→L (90%)	396.3915105	0.0044	H-20→L (17%), H-19→L (58%)
745.7195756	0.0433	H-7→L (72%)	393.8104267	0.0052	H-20→L (78%), H-19→L (18%)
722.9349075	0.017	H-8→L (88%)	391.3244852	0.1853	H-3→L+2 (65%)
629.3570388	0.0061	H-9→L (88%)	387.2059233	0.0432	H-21→L (79%), H-4→L+2 (11%)
615.2408527	0.0019	H-10→L(63%), H→L+1 (16%)	385.1490685	0.0894	H-22→L (39%), H-4→L+2 (35%)
599.7355809	0.0029	H-11→L (86%)	382.2634786	0.0974	H-22→L (35%), H-4→L+2 (37%)
595.8159289	0.0002	H-12→L (94%)	375.3772038	0.1038	H-6→L+2 (84%)

570.0121219	0.0473	H-13→L(62%), H→L+1 (33%)	374.538068	0.0203	H-5→L+2 (82%)
521.7714697	0.5097	H-13→L (30%), H-10→L(20%), H→L+1 (34%)	368.91019	0.0243	H-12→L+1 (14%), H-11→L+1 (18%), H-9→L+1 (44%)
505.4149307	0.0816	H-14→L (80%)	367.6412544	0.0232	H-10→L+1 (29%), H-9→L+1 (20%), H→L+3 (18%)
483.724149	0.286	H→L+2 (83%)	366.6518901	0.0008	H-23→L (88%)
469.3849347	0.0316	H-1→L+1 (95%)	363.3743747	0.0095	H-25→L (16%), H-24→L (69%)
459.0785228	0.0644	H-3→L+1 (21%), H-2→L+1 (73%)	362.0162831	0.0128	H-25→L (69%), H-24→L (24%)
452.0484801	0.0078	H-3→L+1 (72%), H-2→L+1 (22%)	360.6263428	0.0106	H-27→L (12%), H-12→L+1 (21%), H-10→L+1 (14%), H→L+3 (25%)
442.0240887	0.0388	H-4→L+1 (92%)	359.2262173	0.0903	H-7→L+2 (68%)
429.082321	0.0306	H-5→L+1 (88%)	357.3521736	0.0163	H-26→L (79%)
423.90364	0.0508	H-15→L (21%), H-6→L+1 (54%)	355.528164	0.0356	H-11→L+1 (10%), H-9→L+1 (14%), H→L+3 (31%)
419.0891585	0.0793	H-15→L (39%), H-6→L+1 (32%)	352.666221	0.0324	H-27→L (33%), H-12→L+1 (25%), H-11→L+1 (26%)
416.4987122	0.0039	H-8→L+1 (67%)	349.3078736	0.0598	H-27→L (23%), H-13→L+1 (14%), H-12→L+1 (21%), H-11→L+1 (18%)

Table S7. Calculated position of the pure electronic transitions, oscillator strength (f) and major contributions to the transitions for the first 100 transitions of **[Fb-Fb]**.

λ(nm)	**f**	**Major contributions (%)**	**λ(nm)**	**f**	**Major contributions (%)**
671.1233985	0.1727	H→L (76%)	410.7176488	0.0395	H-4→L+3 (11%), H-2→L+5 (33%), H-1→L+6 (23%)
659.4858332	0.0077	H→L+1 (67%)	409.5102941	0.0665	H-5→L (29%), H→L+6 (26%)
626.2417246	0.2777	H-2→L+1 (22%), H-1→L(51%), H→L+2 (12%)	403.4077459	0.3658	H-5→L+1 (43%), H→L+5 (32%)
621.0345454	0.0071	H-2→L (48%), H-1→L+1(24%), H→L+1 (10%)	392.0793645	0.0002	H-7→L (42%), H-6→L+1 (34%)
589.8070341	0.0007	H-3→L (32%), H-2→L (16%), H-1→L+1(34%), H→L+1 (11%)	391.5840334	0.0078	H-7→L+1 (38%), H-6→L (52%)

585.6281547	0.0009	H-2→L+1 (60%), H-1→L (36%)	388.991738	0.0143	H-20→L+4 (14%), H-12→L+4 (15%), H→L+6 (25%)
582.1633875	0.0004	H-3→L (38%), H-2→L (19%), H-1→L+1 (29%)	383.1376287	0.0443	H-2→L+6 (32%), H-1→L+5 (39%), H-1→L+6 (13%)
578.226549	0.1031	H-3→L+1 (66%), H→L (10%)	382.9719424	0.0145	H-2→L+5 (28%), H-2→L+6 (12%), H-1→L+6 (36%)
524.6195432	0.3358	H→L+2(22%), H→L+4 (57%)	382.1221002	0.0051	H-12→L (48%)
515.0306843	1	H→L+2(61%), H→L+4 (20%)	381.9102287	0.5795	H-4→L+2 (35%), H-2→L+6 (17%)
500.1546518	0.0234	H-2→L+2(32%), H→L+3 (37%)	380.433681	0.3875	H-9→L+1 (19%), H-8→L (28%), H-4→L+2 (15%)
490.7510158	0.5459	H-4→L (15%), H-3→L+1 (22%), H-1→L+2 (50%)	379.8625468	0.0053	H-9→L (36%), H-8→L+1 (28%)
486.4762483	0.0334	H-3→L+2 (15%), H-2→L+2(21%), H→L+3 (40%)	379.061198	0.0438	H-4→L+3 (18%), H-3→L+5 (33%)
478.1647446	0.0088	H-2→L+2 (21%), H-1→L+3 (66%)	378.6791382	0.0016	H-12→L+1 (43%), H-9→L+1 (10%), H-8→L (14%)
477.4466137	0.0649	H-2→L+3 (67%), H-1→L+2 (21%)	374.6625669	0.039	H-11→L+1 (21%), H-10→L (33%), H-3→L+6 (27%)
457.655076	0.0006	H-4→L+1 (17%), H-3→L+2 (53%)	374.617285	0.009	H-11→L (14%), H-10→L+1 (10%), H-4→L+3 (21%), H-3→L+5 (15%)
455.888133	0.2256	H-4→L (31%), H-3→L+3 (43%)	372.6468595	0.2654	H-14→L+1 (11%), H-13→L (13%), H-3→L+6 (50%)
445.4704536	1.3564	H-4→L (29%), H-3→L+3 (41%)	372.3782449	0.0602	H-11→L (22%), H-10→L+1 (18%), H-3→L+5 (25%)
438.5685767	0.1565	H-4→L+1 (35%), H-3→L+2(14%), H→L+6 (11%)	371.0742746	0.0942	H-21→L+4 (18%), H-4→L+4 (33%)
425.1245942	0.0032	H-3→L+4 (59%), H-2→L+4 (27%)	371.0187528	0.0554	H-14→L (21%), H-13→L+1 (25%)
423.5126785	0.0259	H-1→L+4 (91%)	370.9410503	0.1177	H-14→L (14%), H-14→L+1 (19%), H-13→L (19%)
419.3301202	0.0008	H-3→L+4 (18%), H-2→L+4 (54%)	367.3798051	0.023	H-20→L+1 (21%), H-15→L (55%)
417.1854256	0.0202	H-5→L (35%), H-4→L+1 (15%), H-2→L+4(14%),	366.0889262	0.0004	H-20→L (31%), H-19→L (15%), H-15→L+1 (43%)

		H→L+6 (14%)			
415.9118975	0.3751	H-5→L+1(17%), H→L+5 (47%)	363.5235344	0.0011	H-18→L (25%), H-16→L (28%), H-16→L+1 (24%)
412.6450664	0.0697	H-5→L+1 (25%), H-4→L+2 (15%), H-2→L+6 (18%), H-1→L+5 (28%)	363.4595938	0.0015	H-18→L (16%), H-18→L+1 (12%), H-17→L (23%), H-17→L+1 (17%), H-16→L (14%)

Table S8. Calculated position of the pure electronic transitions, oscillator strength (f) and major contributions to the transitions for the first 100 transitions of **[Zn-Zn]**.

λ(nm)	**f**	**Major contributions (%)**	**λ(nm)**	**f**	**Major contributions (%)**
659.4156826	0.1928	H→L (90%)	402.922676	0.0011	H-19→L+1 (17%), H-18→L (12%), H-13→L+1 (19%), H-12→L (26%)
645.6120425	0.001	H→L+1 (85%)	402.8572155	0.0008	H-19→L (19%), H-18→L+1 (11%), H-13→L (23%), H-12→L+1 (21%)
611.3576757	0.0289	H-2→L+1 (21%), H-1→L (49%)	399.327933	0.3324	H-5→L+1 (43%), H→L+5 (33%)
611.1768542	0.363	H-3→L+1 (14%), H-2→L(54%), H→L+2 (12%)	396.8355684	0.1337	H-4→L+2 (22%), H-3→L+6 (11%), H-2→L+5 (32%)
587.1257122	0.0051	H-3→L (36%), H-2→L+1 (11%), H-1→L (30%)	395.1534187	0.0011	H-4→L+3 (14%), H-3→L+5 (17%), H-2→L+6 (27%), H-1→L+5 (18%)
582.8749783	0.0853	H-1→L+1 (78%)	387.7993702	0.0155	H-25→L+4 (14%), H-12→L+4 (16%), H→L+6 (32%)
558.1315235	0.0002	H-3→L (38%), H-2→L+1 (54%)	382.9364569	0.029	H-7→L (15%), H-7→L+1 (21%), H-6→L (39%)
554.1897758	0.0223	H-3→L+1 (59%), H-2→L (32%)	382.5937686	0	H-7→L (32%), H-6→L (10%), H-6→L+1 (30%)
527.2072826	0.0482	H-4→L+4(15%), H→L+4 (74%)	379.5369536	0.0008	H-10→L (10%), H-9→L+1 (11%), H-8→L (26%)
496.6087344	1.525	H→L+2 (77%)	379.3279383	0.0056	H-9→L (12%), H-8→L+1 (13%), H-1→L+5 (25%)
476.1264848	0.0001	H-1→L+2(35%), H→L+3 (53%)	378.0325537	0.0469	H-9→L (10%), H-1→L+5 (36%)

471.4912406	0.0197	H-4→L+1 (29%), H-3→L+2 (18%), H-2→L+3(13%), H→L+3 (16%)	377.3537151	0.1068	H-24→L+4 (12%), H-4→L+4 (41%), H→L+4 (14%)
470.8824027	0.3559	H-4→L (42%), H-2→L+2 (31%)	376.5400329	0.0482	H-10→L (20%), H-9→L+1 (11%), H-8→L (15%), H-1→L+6 (10%)
453.7857281	0.1988	H-4→L (24%), H-2→L+2 (40%), H-1→L+3 (21%)	376.2886177	0.0106	H-11→L (20%), H-10→L+1 (13%), H-9→L (21%), H-8→L+1 (14%)
447.6902457	0.8459	H-4→L (18%), H-1→L+3 (59%)	375.8095742	0.2852	H-1→L+6 (54%)
445.9832253	0.0279	H-4→L+1 (36%), H-3→L+2 (31%)	373.3763074	0.0015	H-25→L (18%), H-19→L+1 (12%), H-18→L (13%), H-12→L (36%)
443.2567182	0.0019	H-2→L+3 (55%), H-1→L+2 (23%)	372.0206939	0.6007	H-4→L+2 (30%), H-2→L+5 (25%)
440.6259743	0.055	H-3→L+2 (35%), H-2→L+3 (12%), H-1→L+2 (16%)	370.1326586	0.0411	H-25→L+1 (11%), H-19→L (17%), H-18→L+1 (10%), H-12→L+1 (30%)
435.7172259	0.5881	H-3→L+3 (73%), H-2→L+2 (14%)	368.4278398	0.0024	H-15→L (18%), H-14→L+1 (17%), H-2→L+6 (18%)
431.741953	0.0016	H-3→L+4 (12%), H-1→L+4 (80%)	367.6630587	0.1045	H-15→L+1 (11%), H-14→L (18%), H-10→L (11%), H-4→L+2 (10%)
421.4110215	0.0002	H-2→L+4 (92%)	366.9991908	0.006	H-3→L+5 (47%), H-2→L+6 (34%)
411.7679729	0.0074	H-5→L (53%), H-4→L+1 (11%), H-3→L+4(13%), H→L+6 (10%)	365.8080921	0.002	H-4→L+3 (42%)
411.4946453	0.0022	H-5→L (10%), H-3→L+4 (69%), H-1→L+4 (12%)	365.6786216	0.1277	H-3→L+6 (72%), H-2→L+5 (18%)
409.3345328	0.2817	H-5→L+1(38%), H→L+5 (42%)	365.0756357	0.0021	H-19→L (10%), H-15→L+1 (12%), H-13→L (37%)
407.0098373	0.0496	H-25→L+4 (15%), H-12→L+4 (17%), H-5→L(12%), H→L+6 (27%)	364.0786299	0.012	H-18→L (11%), H-17→L (10%), H-15→L (17%), H-13→L+1 (18%)

Table S9. Calculated position of the pure electronic transitions, oscillator strength (f) and major contributions to the transitions for the first 100 transitions of **[Fb-Zn]**.

λ(nm)	f	Major contributions (%)	λ(nm)	f	Major contributions (%)
669.059072	0.1282	HOMO→LUMO (74%)	407.5851824	0.1034	H-5→L+1(29%), HOMO→L+6 (30%)
646.757103	0.0732	HOMO→L+1 (82%)	403.0274571	0.0012	H-18→L+1 (26%), H-11→LUMO (10%), H-11→L+1 (40%)
623.0631521	0.1681	H-1→LUMO (64%)	400.2948912	0.261	H-5→L+1(41%), HOMO→L+5 (23%)
610.6951859	0.0919	H-2→LUMO (35%), H-2→L+1(33%), HOMO→L+3 (12%)	395.2038016	0.0574	H-4→L+3 (15%), H-3→L+6 (10%), H-2→L+5 (12%), H-2→L+6 (37%)
595.5583468	0.1119	H-3→LUMO(34%), H-2→LUMO(16%), H-2→L+1 (17%)	391.6335101	0.0086	H-6→LUMO (81%)
572.5919579	0.0127	H-3→LUMO(20%), H-3→L+1 (11%), H-2→LUMO(11%), H-2→L+1 (15%), H-1→L+1 (35%)	388.4798265	0.0828	H-11→L+4(11%), HOMO→L+6 (32%)
569.3054304	0.0043	H-3→LUMO (13%), H-2→L+1 (20%), H-1→L+1 (53%)	382.9364569	0.0051	H-7→LUMO (17%), H-7→L+1 (61%)
565.5142157	0.037	H-3→L+1 (52%), H-2→LUMO (27%)	382.0279061	0.1187	H-11→LUMO (10%), H-3→L+5 (10%), H-2→L+5 (19%)
525.5981035	0.1593	H-4→L+4(12%), HOMO→L+2(11%), HOMO→L+4 (64%)	380.7374298	0.123	H-15→LUMO (10%), H-14→LUMO (13%), H-11→LUMO (20%)
512.3490088	0.8171	HOMO→L+2(74%), HOMO→L+4 (10%)	379.7927298	0.0375	H-9→LUMO (47%), H-2→L+5 (10%)
492.4663832	0.3043	H-4→LUMO (18%), H-3→LUMO (12%), H-1→L+2 (46%)	379.5485723	0.186	H-9→LUMO (26%), H-8→L+1 (12%), H-4→L+2 (16%)
479.7002888	0.6537	H-2→L+2(41%), HOMO→L+3 (41%)	378.1363201	0.4172	H-8→L+1 (17%), H-4→L+2 (15%), H-2→L+5 (16%)
470.3464971	0.1851	H-4→L+1 (15%), H-3→L+2 (17%), H-2→L+2 (18%), HOMO→L+3 (15%)	376.4371406	0.0153	H-10→L+1 (34%), H-8→L+1 (26%)
464.0615961	0.0449	H-4→LUMO (16%), H-2→L+2 (21%), H-2→L+3 (35%)	374.0521832	0.0118	H-12→LUMO (26%), H-3→L+5 (26%), H-2→L+5 (15%)
458.9086007	0.0797	H-4→LUMO (16%), H-3→L+2 (39%),	373.5788135	0.0034	H-4→L+4 (30%)

		H-1→L+3 (11%)			
450.7501514	0.0633	H-1→L+3 (80%)	373.2751367	0.042	H-12→LUMO (24%), H-3→L+5 (10%), H-1→L+6 (28%)
447.1574157	0.5091	H-4→LUMO (18%), H-4→L+1 (22%), H-2→L+3 (24%)	372.8261514	0.051	H-3→L+5 (15%), H-2→L+6 (11%), H-1→L+6 (52%)
440.4224953	0.3975	H-4→LUMO (12%), H-4→L+1 (23%), H-3→L+2 (10%)	371.296528	0.0101	H-18→L+1 (17%), H-11→L+1 (21%)
437.4081377	0.5312	H-3→L+3 (59%), H-2→L+3 (12%)	370.8966634	0.1074	H-14→LUMO (10%), H-3→L+6 (24%)
428.1488246	0.0041	H-3→L+4 (30%), H-2→L+4 (43%), H-1→L+4 (12%)	370.4533783	0.1464	H-15→LUMO (32%), H-14→LUMO (24%), H-12→LUMO (10%)
420.425014	0.0111	H-3→L+4 (16%), H-1→L+4 (75%)	367.4560228	0.047	H-13→L+1 (20%), H-3→L+6 (21%)
417.9871102	0.0713	H-5→LUMO (44%), HOMO→L+5 (24%)	366.6410476	0.0147	H-15→LUMO (14%), H-14→LUMO (18%), H-11→LUMO (11%)
415.326734	0.0004	H-3→L+4 (40%), H-2→L+4 (47%)	365.9808621	0.1605	H-4→L+3 (31%), H-3→L+6 (24%)
410.8265239	0.0538	H-4→L+2 (18%), H-1→L+5 (58%)	364.2069697	0.0161	H-15→L+1 (14%), H-13→L+1 (14%)
409.7674477	0.2264	H-5→LUMO (30%), HOMO→L+5 (31%)	362.9701289	0.0031	H-19→LUMO (26%), H-17→LUMO (58%)

Graphs representing the computed oscillator strengths vs the positions of the electronic transitions for [Zn-Zn] and [Fb-Fb].

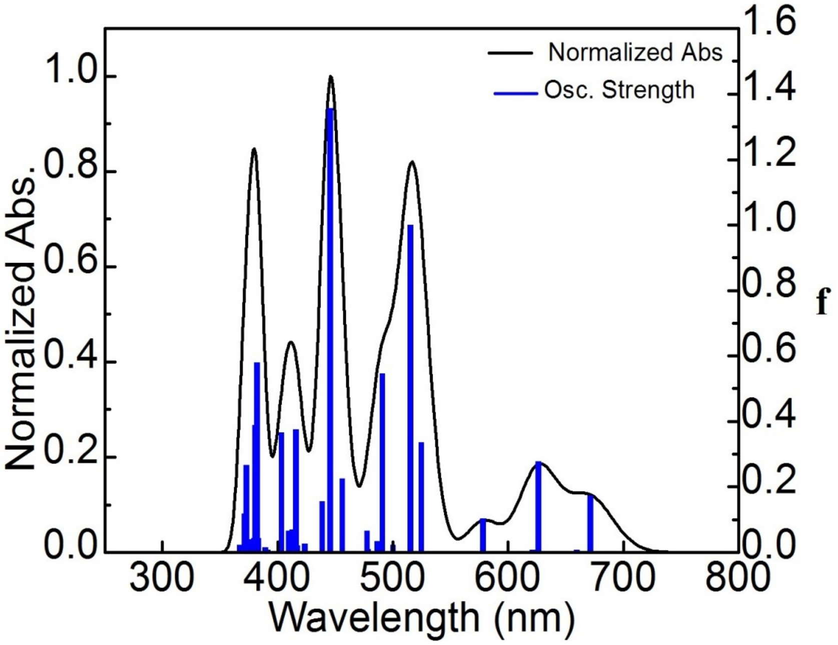

Figure S21. Bar graph showing the oscillator strength, f, as a function of the calculated positions of the electronic transitions (blue) for **[Fb-Fb]**. The black line is the generated spectrum when assigning 1000 cm^{-1} for each transition.

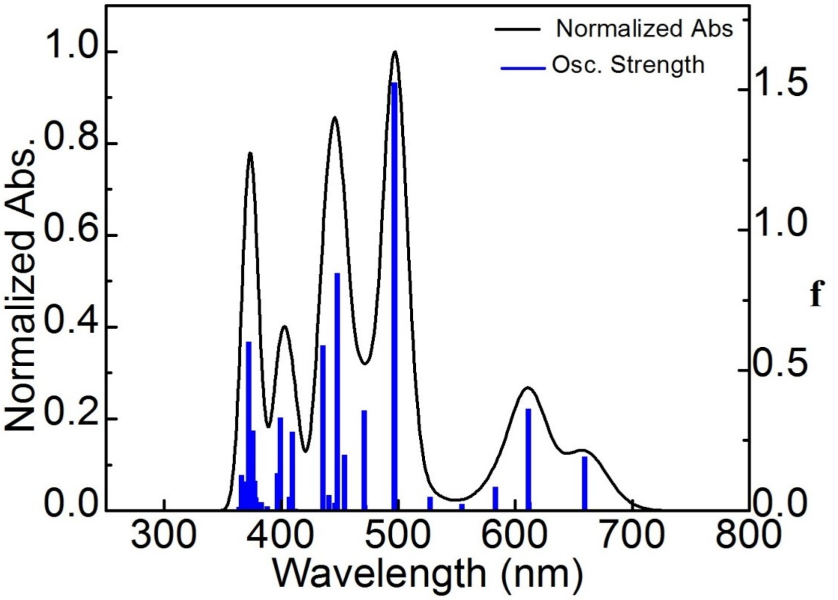

Figure S22. Bar graph showing the oscillator strength, f, as a function of the calculated positions of the electronic transitions (blue) for **[Zn-Zn]**. The black line is the generated spectrum when assigning 1000 cm^{-1} for each transition.

References

[1] S. Richeter, C. Jeandon, J.-P. Gisselbrecht, R. Ruppert, H. J. Callot, *J. Am. Chem. Soc.,* (2002), **124**, 6168–6179.

[2] M. J. Frisch et al. Gaussian, Inc., Wallingford CT,(2004).

[3] P. Hohenberg and W. Kohn, *Phys. Rev.*, (1964), **136**, B864–871.

[4] P. Hohenberg and W. Kohn., *J. Phys. Rev.,* (1965), **140**, A1133–1138.

[5] R.G. Parr and W. Yang, Density-functional theory of atoms and molecules, Oxford Univ. Press: Oxford, (1989).

[6] D. R. Salahub and M. C. Zerner, The Challenge of d and f Electrons, *Amer. Chem. Soc.* Washington, D.C., (1989).

[7] R. Bauernschmitt and X. Ahlrichs, *Chem. Phys. Lett.,* (1996), **256**, 454–464.

[8] M. E. Casida, C. Jamorski, K. C. Casida and D. R Salahub, *J. Chem. Phys.,* (1998), **108**, 4439–4449.

[9] R. E. Stratmann, G. E. Scuseria and M. J. Frisch, *J. Chem. Phys.,* (1998), **109**, 8218–8224.

[10] C. Lee,W. Yang and +R. G. Parr, *Phys. Rev. B*, (1988), **37**, 785–789.

[11] B. Miehlich, A. Savin, H. Stoll and H, *Preuss. Chem. Phys. Lett.,* (1989), **157**, 200–206.

[12] A. D. Becke, *J. Chem. Phys.,* (1993), **98**, 5648–5652.

[13] R. Ditchfield, W. J. Hehre, and J. A. Pople, *J. Chem. Phys.*, (1971), **54**, 724-728.

[14] W. J. Hehre, R. Ditchfield, and J. A. Pople, *J. Chem. Phys.*, (1972), **56**, 2257-2261.

[15] P. C. Hariharan and J. A. Pople, *Mol. Phys.*, (1974), **27**, 209-214.

[16] M. S. Gordon, *Chem. Phys. Lett.,* (1980), **76**, 163-168.

[17] P. C. Hariharan and J. A. Pople, *Theo. Chim. Acta*, (1973), **28**, 213-222.

[18] J.-P. Blaudeau, M. P. McGrath, L. A. Curtiss, and L. Radom, *J. Chem. Phys.*, (1997), **107**, 5016-5021.

[19] M. M. Francl, W. J. Pietro, W. J. Hehre, J. S. Binkley, D. J. DeFrees, J. A. Pople, and M. S. Gordon, *J. Chem. Phys.,* (1982), **77**, 3654-3665.

[20] J. S. Binkley, J. A. Pople, W. J. Hehre, *J. Am. Chem. Soc.,* (1980), **102**, 939-947.

[21] M. S. Gordon, J. S. Binkley, J. A. Pople, W. J. Pietro, W. J. Hehre, *J. Am. Chem. Soc.,* (1982), **104**, 2797-2803.

[22] W. J. Pietro, M. M. Francl, W. J. Hehre, D. J. Defrees, J. A. Pople, , J. S. Binkley, *J. Am. Chem. Soc.*, (1982), **104**, 5039-5048.

[23] K. D. Dobbs, W. J. Hehre, *J. Comp. Chem.*, (1986), **7**, 359-378.

[24] K. D. Dobbs, W. J. Hehre, *J. Comp. Chem.*, (1987), **8**, 861-879.

[25] K. D. Dobbs, W. J. Hehre, *J. Comp. Chem.*, (1987), **8**, 880-893.

[26] N. Godbout, D. R. Salahub, J. Andzelm, and E. Wimmer., *Can. J. Chem.*, (1992), **70**, 560- 571.

[27] SBKJC ECP EMSL Basis Set Exchange Library.

[28] W.J. Stevens, M. Krauss, H. Basch, and P. G. Jasien., *Can. J. Chem.*, (1992), **70**, 612-630.

[29] N.M. O'Boyle, A.L.Tenderholt, and K.M. Langner., *J. Comp. Chem.,* (2008), **29**, 839-845.

CHAPTER 5

Bis-α-(amino(4-ethynylbenzene(trimethylsilane)(R))bis(4-ethynylbenzene (trimethyl - silane)) quinone diimine (R = H, Boc) as potential building blocks for conjugated porphyrin dye-containing polymers exhibiting low-energy band gaps.

This work will be submitted to *Journal of Inorganic and Organometallic Polymers and Materials* in the special issue dedicated to Dr. Ben Zhong Tang for his outstanding contribution in the field of metal-containing polymers by Mohammed Abdelhameed and Pierre D. Harvey.

The synthesis and second part of the work was carried out by myself. The second part involves spectroscopic and photophysical measurements including the absorption and emission spectra, emission quantum yields and lifetimes as well as the DFT (density functional theory) and TDDFT (time-dependent density functional theory) computations. I did the measurements, analyses and discussion of the photophysical parameters under the supervision of Dr. Pierre D. Harvey. I wrote the first draft of the manuscript and Prof. Harvey finalized the manuscript.

5.1. Manuscript

Bis-α-(amino(4-ethynylbenzene(trimethylsilane)(R))bis(4-ethynylbenzene (trimethyl - silane)) quinone diimine (R = H, Boc) as potential building blocks for conjugated porphyrin dye-containing polymers exhibiting low-energy band gaps.

Mohammed Abdelhameed,[a] and Pierre D. Harvey*[a]

[a] Département de Chimie, Université de Sherbrooke, 2550 Boulevard de l'Université, Sherbrooke, Québec, Canada J1K 2R1, Fax: Tel: E-mail:

5.1.1. Introduction

Photosystems are functional and supramolecular units of protein complexes involved in the photosynthetic process that carry out the primary photochemistry of photosynthesis which, amongst other things, involves the absorption of light and the transfers of energy and electrons. There are two types of photosystems, photosystem II and photosystem I, **PSII** and **PSI**, respectively. **PSII** is an integral membrane protein composed of two protein subunits known as **D1** and **D2**, i.e. a dimer. The principal function of **PSII** is to absorb light through antennas, composed of chlorophyll *a* molecules (Chart 1) at an optimal wavelength of 680 nm, then transport the excitation energy towards a special pair (also composed of chlorophyll *a*) and to use the absorbed energy (4 photons in fact) to oxidize two molecules of water to form one molecule of molecular oxygen. The four electrons removed from the water molecule during this process are transferred via an electron transport chain to photosystem I.[1,2]

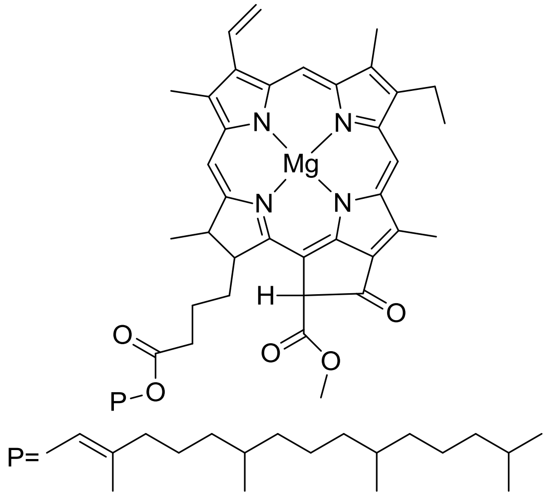

Chart 1. The structure of **chlorophyll *a***

Another important component of the photosynthetic process is the plastoquinone, **PQ**, which functions as a one or two electron acceptor/donor to carry the electrons from **PSII** to the cytochrome *bf* complex. Upon excitation, by the absorption of a photon, chlorophyll *a* rapidly transfers an electron to a nearby pheophytin *a*. Pheophytin *a* is a chlorophyll *a* molecule in which the magnesium atom has been replaced by two protons. The electron is then transferred to the plastoquinone (**PQ**) which is reduced to form plastoquinol (**PQH**) (Chart 2). The plastoquinol then transfers its electron through an electron transport chain that terminates at **PSI**.[2]

Plastoquinone **Plastoquinol**

Chart 2. Structures of **Plastoquinone** and **Plastoquinol**.

Designing metalloporphyrin-containing polymers with very low band gap for potential applications in bulk hetero-junction solar cells has been a topic of interest to researchers for quite some time.[3-7] In our laboratory, we tried to design low band gap polymers that are inspired from the natural photosynthetic machinery. The first reported polymer of this type,

P1 (Chart 3), was built on an electron rich (zinc(II)porphyrin) unit and a poor (quinone diimine) center, which are respectively similar structurally to chlorophyll *a* and **PQ,** showed a charge transfer band (CT; zinc(II)porphyrin → quinone diimine).[8] An example of an unconjugated polymer that also showed low band gap was composed of a zinc(II)porphyrin unit that was incorporated in the backbone of a quinone-containing polymer (at the α-position), **P2**, (Chart 3) (Xiaorong Wang, PhD candidate in our laboratory; unpublished results) showed a very similar charge transfer band from (zinc(II)porphyrin → quinone diamine).

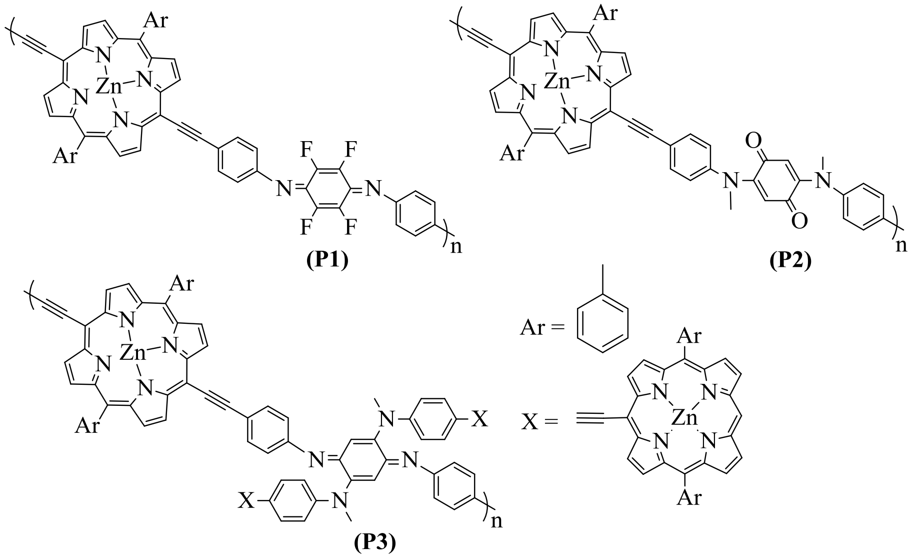

Chart 3. Structure of polymers **P1, P2** and **P3**

To further understanding of the charge transfer processes occurring in polymers **P1** and **P2**, the synthesis of a polymer that combines both the conjugated and unconjugated motifs within the same assembly, **P3**, is necessary. The synthesis of the compound **TAI-Por,** Chart 4, was proposed as a model compound for **P3** (Chart 3). The Boc group, *tert*-butyloxycarbonyl, is used as a protecting group for the amine fragment during the following steps of the synthesis, but also can be investigated as being a group left permanently onto the backbone of the target polymer, therefore on the model compound as well. The syntheses are shown in Scheme 1.

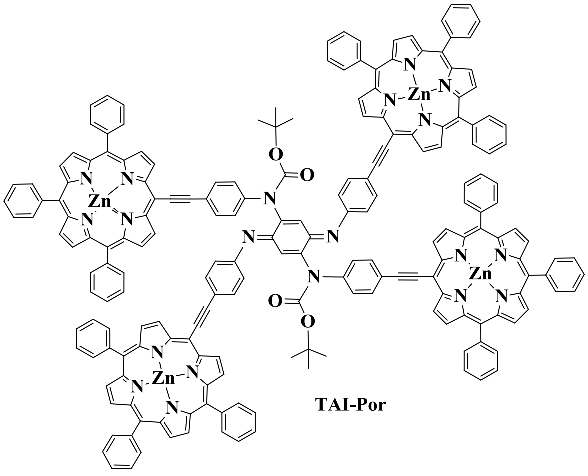

Chart 4. The Structure of **TAI-Znpor**

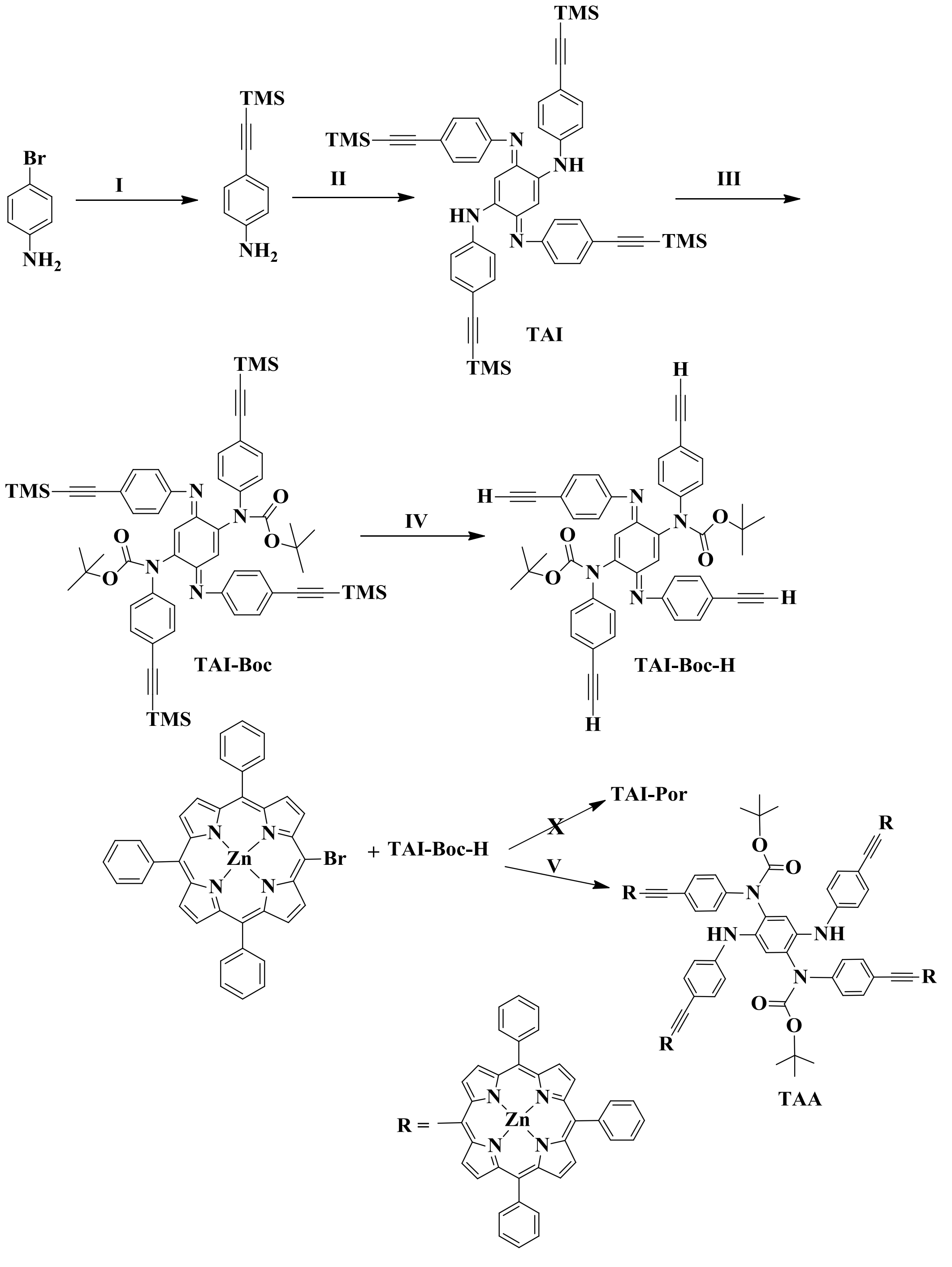

I = ≡—TMS, $Pd(PPh_3)_2Cl_2$, CuI, Et_3N; **II** = $C_6H_4(=O)_2$, Et_3N, $TiCl_4$, **III** = Di-*tert*-butyl dicarbonate (Boc_2O), 4-Dimethylaminopyridine (DMAP), **IV**= Tetra-n-butylammonium fluoride (TBAF), MeOH, **V** = $Pd(PPh_3)_2Cl_2$, CuI, Et_3N.

Scheme 1. Synthesis of **TAA.**

According to the synthetic scheme outlined in Scheme 1, the compound **TAI** was synthesized starting with one equivalent of 1,4-benzoquinone and seven equivalent of 4-((trimethylsilyl)ethynyl)aniline in the presence of triethylamine. The reaction mixture was dissolved in chlorobenzene and the $TiCl_4$ catalyst was then added to it. The solution was stirred at 60^{o} C for 10 h. The crude product was subjected to flash chromatography which gave the desired compound as an orange solid. The recovered product was analysed using ^{1}H NMR, UV-Vis and mass spectroscopy which confirmed obtaining **TAI** as a pure solid. The two secondary amine groups of **TAI** had to be protected before performing the Sonogashira coupling to get the final target compound, to avoid any reactions that might occur with the protons of the amine and to allow the reaction between the four terminal acetylene groups and the 5,10,15-(triphenyl)-20-bromo-porphyrin to occur. The protection of the secondary amine of **TAI** was performed using the **Boc** group, *tert*-butyloxycarbonyl, to give **TAI-Boc**. The latter compound, **TAI-Boc**, was synthesized by stirring (1.35 mmol) of **TAI**, (5.11 mmol) of di-*tert*-butyl dicarbonate and (1.36 mmol) of 4-dimethylaminopyridine in THF for 20 hrs at room temperature. The compound was purified on silica gel to give the product as a red solid. The ^{1}H NMR and mass spectrometry confirmed obtaining the pure compound. The four trimethylsilyl groups, TMS, were then removed from **TAI-Boc** by adding 1.2 ml of tetra-n-butylammonium fluoride to 250 mg of **TAI-Boc** in THF. Then, the crude product was purified over a silica plug to give compound **TAI-Boc-H.** Then, a Sonogashira coupling with 5,10,15-(triphenyl)-20-bromo-porphyrin was performed. An amount equivalent to 0.013 mmol of **TAI-Boc-H** was added to a mixture solution of THF/ Et_3N (60:40) under argon, then amounts equivalent to 0.007 mmol of $Pd(PPh_3)_2Cl_2$ and 0.003 mmol of CuI were added to the mixture. The 5,10,15-(triphenyl)-20-bromo-porphyrin (0.087 mmol) was then added. The mixture was stirred for 24 h at 60^{o} C. The crude product was then subjected to chromatography purification on silica gel. However, the target compound was unfortunately not obtained. Instead, the completely reduced form of the desired target was isolated as a red solid where the two imine groups have been reduced to secondary amine groups to give the compound **TAA**.

5.1.2. Spectroscopy of TAI, TAI-Boc and the model compound TAA.

The UV-Vis absorption spectrum of **TAI** at room temperature, which is composed of a bis(4-ethynlypenyl)quinonediimine where the protons in the 2 and 5 positions of the central quinone have been substituted with two 4-ethynylanaline groups, shows a charge transfer **(CT)** band at λ_{max}= 415. Upon adding the *tert*-butyloxycarbonyl (**Boc**) protecting group to protect the secondary amines, forming **TAI-Boc**, the charge transfer band maximum was red shifted to λ_{max}= 491 (Figure 1). The demonstration of the presence of the CT interactions is made below, using DFT computations.

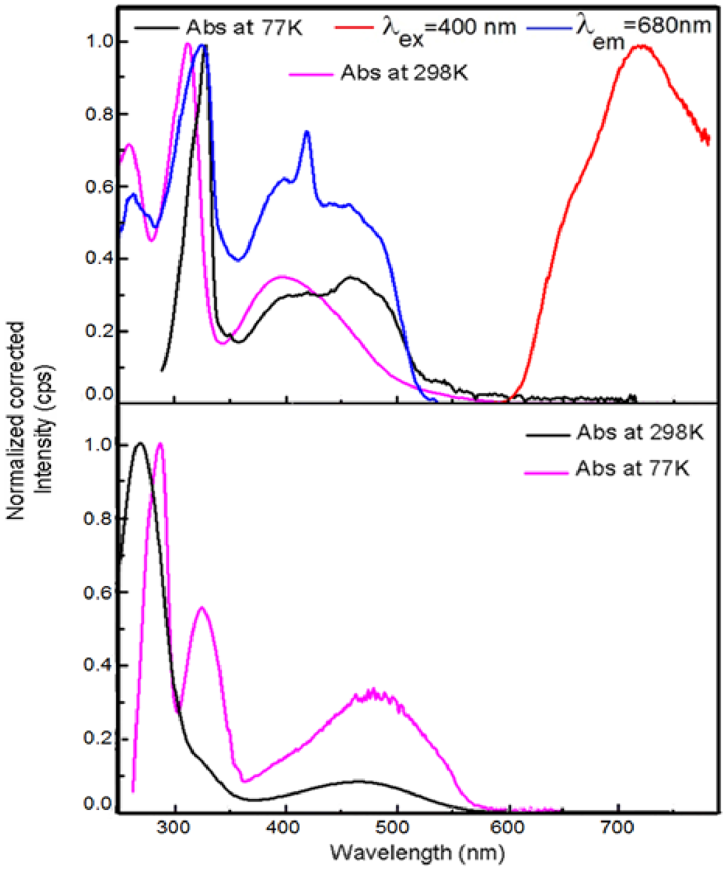

Figure 1. Absorption at 298K (black), at 77K (purple), emission (red) and the excitation (blue) spectra at 77K of **TAI** (up) and **TAI-Boc** (bottom) in 2MeTHF.

The spectroscopic analyses of both compounds, **TAI** and **TAI-Boc,** revealed that the compound **TAI** is luminescent at 77K (Figure 1) but not at room temperature or its emission is too weak to be observed. The compound **TAI-Boc** is not luminescent at both temperatures.

The emission lifetime for **TAI** in 2MeTHF at 77K is 1.62 ns (Figure 2) which suggests that the nature of the luminescence at λ_{max} = 770 nm is fluorescence. The excitation spectrum exhibits a good superposition between this absorption indicating that this emission arises from the absorbing species (not an impurity). This lifetime may appears surprising at first glance since the Stoke shift, Δ, seems very large (absorption = 500 nm; fluorescence = 700 nm; 5700 cm^{-1}) and could be better associated with a phosphorescence. However, the 77 K spectrum of **TAI** reveals a weak shoulder extending all the way to 600 nm, which appears somewhat barely perceptible at 298K as well (Figure 1). Then, the true Stoke shift may be much smaller, consequently more in line with what is expected for a fluorescence. The TDDFT results below corroborate these findings.

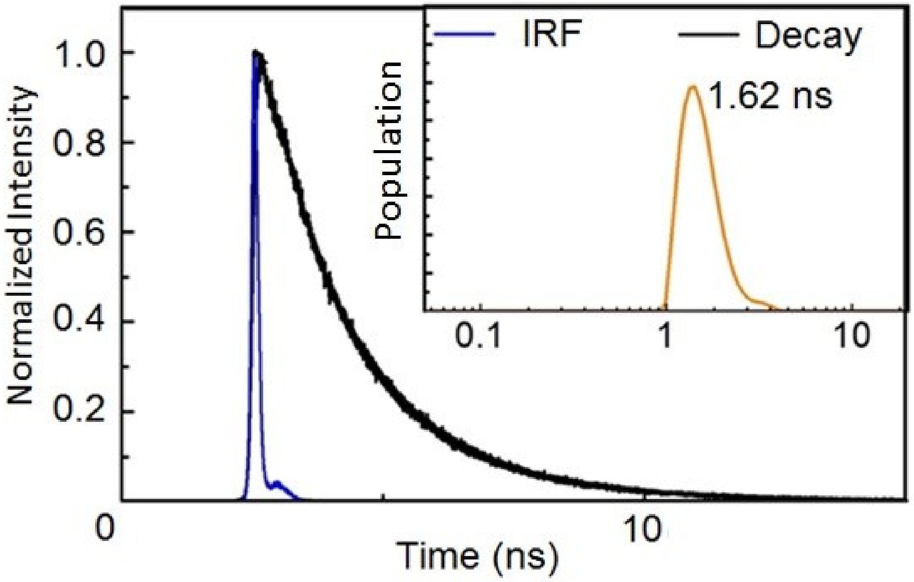

Figure 2. The decay (black), lamp profile (IRF; blue) curves of **TAI** in 2MeTHF at 77K. Inset: population of lifetimes used to fit the decay using the ESM (orange). The maximum of this distribution is the most probable lifetime.

5.1.3. DFT Computations

In order to explain this rather unusual result, two approaches were used. First, a large Stoke shift is always due to a large excited state distortion (deformation of the molecule in the excited state). This is performed by comparing the structures of the model compound in the ground and triplet excited state (since the singlet is not accessible; DFT does not compute well the geometry in the S_1 state because of the strong magnetic coupling of the two single electrons). If there is no major excited state distortion, then there should not be large Stoke shift. Second, one can compute the energy difference between the ground and excited state in order to have an approximate idea where the phosphorescence should take place. This is now addressed below in Table 1.

The calculated phosphorescence wavelength of **TAI** that was obtained from the difference between the singlet and triplet total energy using the singlet S_0 and triplet T_1 optimized geometry structures of **TAI** predicted to have the phosphorescence peak at 1956 nm (Table 1). Although this is an approximation, this position is very low and not accessible with our detector, and the band observed in the 700-800 nm range is unquestionably fluorescence. Consequently, the nature of the luminescence of **TAI** observed at λ_{max} = 770 nm is assigned to a fluorescence.

Table 1. The calculated phosphorescence energy and wavelength for compound **TAI.**

Calculated parameters	Emission
S_0 total energy (a.u.)	-3315.9688
T_1 total energy (a.u.)	-3315.9455
S_0-T_1 energy gap (a.u.)	0.0233
phosphorescence position (eV)	0.634
phosphorescence position (nm)	1956

a.u. = atomic units in Hartree.

The excited state distortion normally responsible for the large Stoke shift was also addressed by DFT computations, notably when comparing the ground (S_0) and the lowest energy triplet excited state (T_1) optimized geometries. Because of the presence of several single bonds, bond angles and dihedral angles are most likely to undergo the largest changes. Several angles and dihedral angles between the S_0 and T_1 geometries of **TAI** are presented in Table 2 (the remainder of the data, including bond distances is placed in the ESI). The triplet state is in fact computed (instead of S_1) because again DFT does not handle the optimized geometry very well because of the strong magnetic coupling between the unpaired electrons in the single excited state. Instead, the T_1 state is addressed assuming that the excited state distortion may be applied to the S_1 state. The computational results show that the bond lengths do not experience any lengthening or shrinkage (see ESI), which is fully consistent with the presence of an extended π-system. The bond angles (Table 2; the atom numbering used for the analysis is placed in Chart 5) do not change very much as well. Therefore, the excited state distortion, at least in the triplet state, is not large, and it is very likely that the excited state distortion be similar in the S_1 state. However, some dihedral angles experience large changes (Table 2). No analysis of this type was performed for **TAI-Boc** was performed, expecting a similar conclusion.

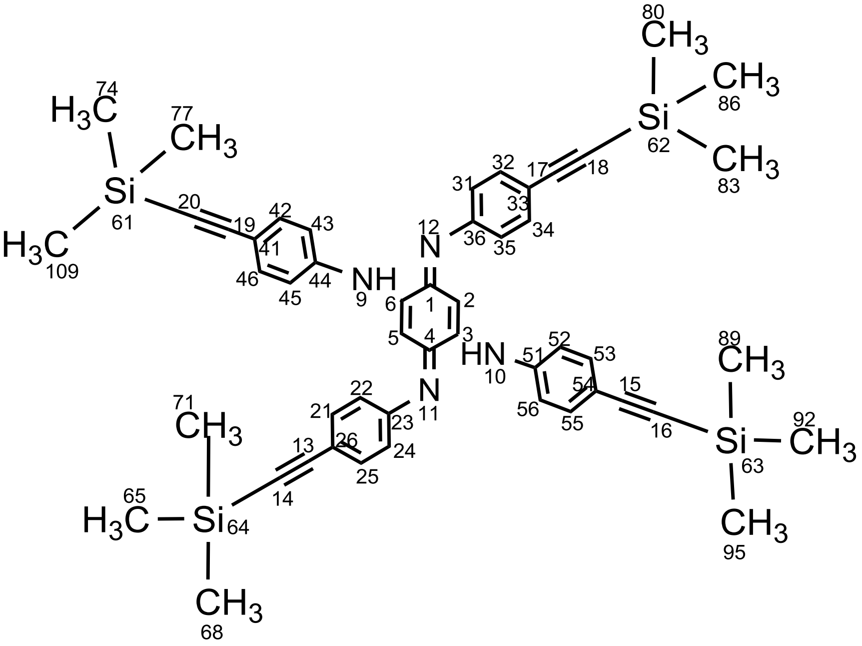

Chart 5. The atom numbering of **TAI.**

Table 2. The S_0-T_1 bond difference, Δ Bond, distorted angles and dihedral angles for both singlet and triplet optimized geometries of **TAI. NA, NB and NC** are adjacent atoms to the studied atom, **X**, where the bond length was determined between **NA** and **X**. The angles were determined between **NA, NB** and **X** while the dihedral angles were determined between **NA, NB, NC** and **X**. (See Chart 5 for the atoms numbering in **TAI**).

Atom	**Adjacent atoms**				**S_0**	**T_1**	**S_0**	**T_1**
X	**NA**	**NB**	**NC**	**Δ Bond**	**Angle**	**Angle**	**Dihedral**	**Dihedral**
C13	11	4	3	0.032	135.7	126.0	163.2	138.4
C14	13	11	4	-0.001	171.3	179.3	-144.1	162.3
C15	10	3	2	0.021	125.4	133.9	53.7	-18.6
C16	15	10	3	0.001	171.4	179.2	116.6	151.5
C19	9	6	5	-0.004	136.8	135.4	39.0	10.5
C20	19	9	6	0.002	171.6	179.2	109.4	-160.0
C23	11	4	3	0.050	128.6	122.7	169.3	137.9
C24	23	11	4	-0.023	116.9	117.0	146.0	168.3
C26	21	13	11	-0.003	29.5	0.9	11.3	-16.7
C31	12	1	2	0.008	145.8	150.9	32.6	11.8
C32	31	12	1	0.004	152.3	152.3	-78.7	-55.0
C41	19	9	6	0.003	4.9	0.8	-80.9	22.1
C42	41	19	9	0.002	119.8	121.0	-63.0	-0.6
C44	9	6	5	0.004	133.7	132.7	30.9	10.8
C51	10	3	2	0.045	121.5	131.2	50.0	-18.7
C52	51	10	3	-0.010	121.8	124.2	-108.7	-20.2
Si61	20	19	9	0.002	175.0	179.9	5.4	-134.0
Si62	18	17	12	0.003	178.6	179.8	15.3	-169.2
Si63	16	15	10	0.006	174.4	179.7	-5.4	-154.6
Si64	14	13	11	-0.004	176.3	179.9	8.7	-175.0
C65	64	14	13	0.003	108.6	108.2	100.0	0.1
C68	64	14	13	0.004	108.1	108.2	-19.5	-120.0
C74	61	20	19	0.003	107.7	108.6	46.5	128.4
C77	61	20	19	0.004	108.6	108.7	-72.6	8.4
C83	62	18	17	0.002	108.9	108.8	-136.0	81.2
C86	62	18	17	0.001	108.5	108.8	-16.0	-158.9
C89	63	16	15	-0.001	109.4	108.5	156.7	5.3
C92	63	16	15	0.002	108.2	108.8	-82.6	125.3
C95	63	16	15	0.003	107.6	109.0	36.3	-114.7

Assignment of the fluorescent state

In order to address the nature of the fluorescent state, DFT and TDDFT were used for the assignment. First the frontier molecular orbitals, MOs, were examined for the optimized geometries of both compounds (**TAI** and **TAI-Boc**; Figure 3 and 4, respectively).

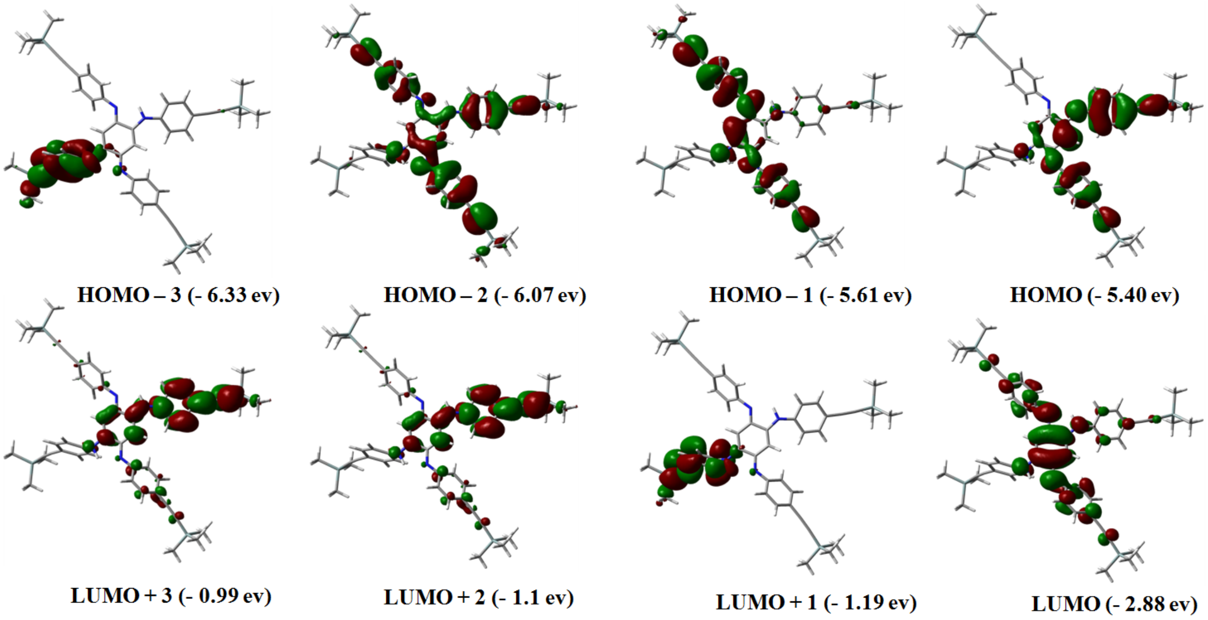

Figure 3. Representation of the frontier MOs of **TAI**.

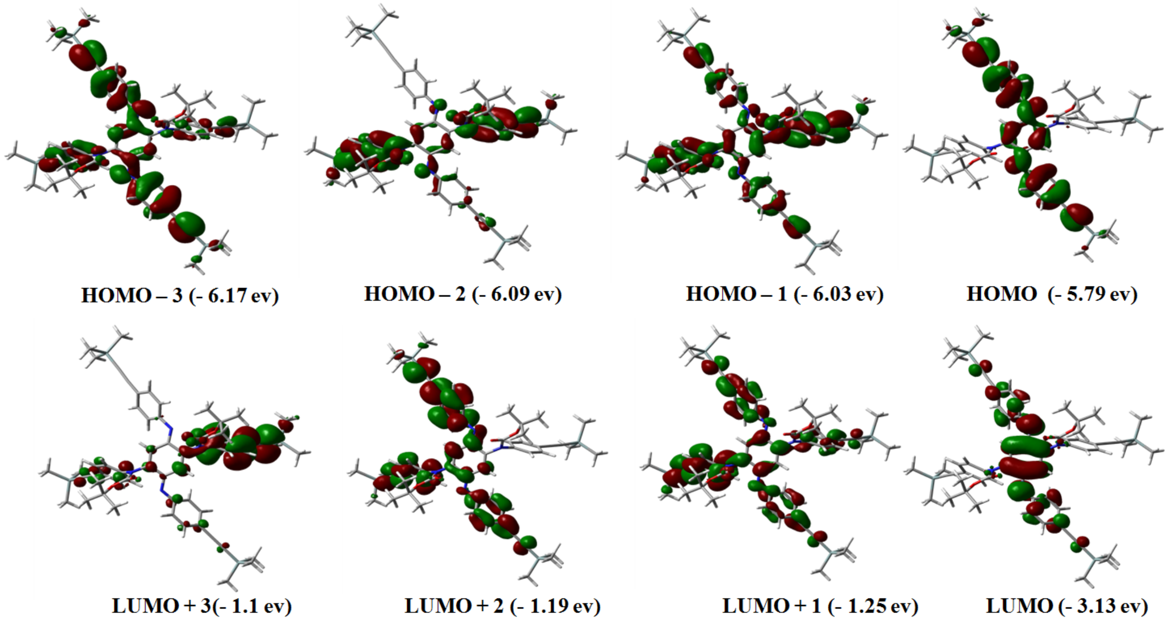

Figure 4. Representation of the frontier MOs of **TAI-Boc**.

The highest occupied molecular orbital (HOMO) and lowest unoccupied molecular orbital (LUMO) exhibit both π-systems where the atomic contributions are mainly localized on one imine phenylacetylene and one amine phenylacetylene residues for **TAI** and on two quinone diimine bis(phenylacetylene) for **TAI-Boc** for the HOMO. The relative atomic contributions to each MO for the frontier MOs are summarized in Table 3. The main transition to monitor is the HOMO→LUMO transition based on the TDDFT results presented below. The two model compounds behave somewhat differently. Indeed, the change in atomic contributions in the HOMO→ LUMO transition for **TAI** is focused on one of the NH-C_4H_4-CC-$SiMe_3$ residue (electron richer) and one of the =N-C_4H_4-CC-$SiMe_3$ arm to the two =N-C_4H_4-CC-$SiMe_3$ fragments and the central benzoquinone diimine unit (electron poorer). This transition is unsurprisingly a charge transfer (CT). Conversely, the HOMO for **TAI-Boc** is composed mainly of the two (=N-C_4H_4-CC-$SiMe_3$) fragments and the LUMO comprises these two same units and the central benzoquinone diimine. This means that the contributions for the electron richer units NH-C_4H_4-CC-$SiMe_3$ are negligible, leading to the conclusion that the Boc pendant group isolate the amino-groups. In a previous work on a polymer analogous to **P2** (Chart 3),[9] there was a clear demonstration that the nitrogen lone pair secured a good electronic communication across the polymer chain. Based on DFT results, this phenomenon appears to repeat itself here for **TAI**. However, this is not the case for **TAI-Boc**. One possible explanation is that the lone pair is strongly conjugated with the Boc unit (i.e. **:**N-C=O ↔ N^+=C-O**:**$^-$) and can no longer support the communication between the NH-C_4H_4-CC-$SiMe_3$ arm and the benzoquinone diimine central residue.

Consequently, the nature of the S_1 excited state is a CT for both model compounds but the presence of Boc in **TAI-Boc** makes the resulting CT bound to be different from that found in **TAI**. This difference is consistent in the difference in band shape in the absorption spectra (Figure 1), and may be at the origin of the lack of fluorescence in **TAI-Boc**.

Table 3. Relative atomic contributions of the various units (major components are in BOLD).

TAI	H-4	H-3	H-2	H-1	HOMO	LUMO	L+1	L+2	L+3	L+4
benzoquinone ring	**28.1**	3.7	10.7	17.4	18.9	**36.1**	3.6	13.5	13.6	10.3
NH-C$_4$H$_4$-CC-SiMe$_3$ (1)	9.2	1.2	19.7	4.6	**53.3**	8.1	0.1	2.6	**75.8**	4.8
NH-C$_4$H$_4$-CC-SiMe$_3$ (2)	**28.3**	**93.1**	7.6	8.8	3.4	5.2	**95.3**	1.1	2.5	4.4
=N-C$_4$H$_4$-CC-SiMe$_3$ (1)	1.5	1.7	**46.5**	18.1	**24.2**	**26.3**	0.6	**39.2**	5.6	**39.6**
=N-C$_4$H$_4$-CC-SiMe$_3$ (2)	**32.9**	0.2	15.4	**51.1**	0.2	**24.2**	0.4	**43.6**	2.6	**40.9**

TAI-R (R = **Boc**)	H-4	H-3	H-2	H-1	HOMO	LUMO	L+1	L+2	L+3	L+4
benzoquinone ring	14.9	10.8	4.7	10.0	14.8	**38.0**	11.1	12.2	5.4	9.1
NR-C$_4$H$_4$-CC-SiMe$_3$ (1)	19.9	7.4	**35.5**	**46.8**	2.2	2.5	9.3	1.3	**81.9**	2.2
NR-C$_4$H$_4$-CC-SiMe$_3$ (2)	**22.3**	13.3	**52.1**	**25.1**	1.8	2.7	**55.0**	**29.2**	7.8	1.6
=N-C$_4$H$_4$-CC-SiMe$_3$ (1)	**21.2**	**30.8**	1.6	9.7	**46.0**	**28.5**	14.4	**43.0**	1.4	**29.6**
=N-C$_4$H$_4$-CC-SiMe$_3$ (2)	**21.7**	**37.7**	6.1	8.4	**35.2**	**28.2**	10.2	14.2	3.6	**57.5**

The lowest energy electronic transitions for **TAI** and **TAI-Boc** were computed by TDDFT methods. The ten first transitions for both models are listed in Table 4, and the first 100 transition are placed in the ESI. In this work, the transition of interest is the lowest-energy S$_1$ transitions. In both cases, the HOMO→LUMO contribution represents the major part of the transition (> 88%). Because the calculated positions of the lowest energy transition are well isolated from the next one in energy makes the assignment much less ambiguous as described above.

Table 4. Computed positions of 10 first electronic transitions, oscillator strength (f) and the major contributions for **TAI** (left) and **TAI-Boc** (right) (see ESI for the 100 transtions).

λ(nm)	f	Major contributions (%)	λ(nm)	f	Major contributions (%)
606.9	0.168	H→L (94)	562.7	0.865	H→L (88)
541.5	0.989	H-1→L (92)	527.5	0.004	H-1→L (97)
457.4	0.062	H-2→L (93)	508.4	0.128	H-2→L (89)
424.3	0.155	H-4→L (88)	492.6	0.021	H-3→L (92)
413.9	0.048	H-3→L (93)	367.1	0.058	H-5→L (69)
347.7	0.442	H-14→L (11), H-5→L (75)	360.6	0.143	H-7→L (11), H-5→L (12), H-4→L (56)
336.3	0.004	H-6→L (93)	355.9	0.053	H-10→L (12), H-7→L (62)
334.7	0.057	H-7→L (82)	352.5	0.006	H-10→L (38), H-9→L (36)
326.3	0.034	H-14→L (53), H→L+2 (16)	351.6	0.141	H-14→L (14), H-9→L (27), H-8→L (23), H-7→L (14)
325.7	0.028	H-11→L (64), H-8→L (20)	347.8	0.007	H-10→L (30), H-9→L (17), H-8→L (38)

The plots of the computed oscillator strength (f) versus the positions of the first 100 transitions provide bar graphs (blue lines; Figure 5). By assigning a thickness of a 1000 cm^{-1}, a spectrum is generated, excluding any vibronic couplings. Three observations can be made. First, again the lowest energy bands are as follow λ(**TAI-Boc**) > λ(**TAI**), and corroborates the experimental spectra of Figure 1. Second, some other features are depicted in the 400-550 nm window, again as seen in the experimental spectra. Third, the computed relative intensity (i.e. f) of the low energy transitions (λ > 400 nm), is higher than that for those placed at lower wavelengths (i.e. λ < 400 nm). This third observation is not yet explained. Nonetheless, the qualitative feature computed by DFT and TDDFT corroborate the experimental findings and help providing a reasonable assignment of the lowest energy S_1 state of this moiety.

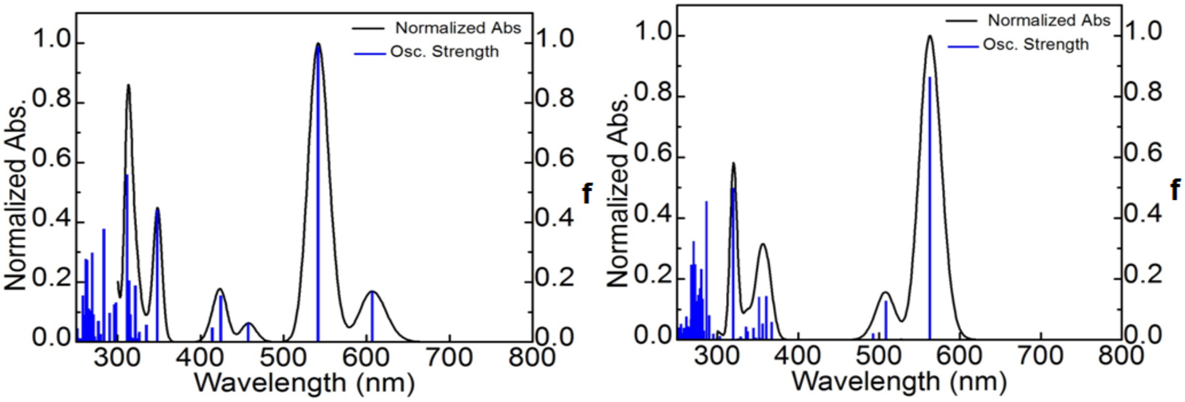

Figure 5. Bar graph showing the oscillator strength, f, as a function of the calculated positions of the electronic transitions (blue) for **TAI** (left) and **TAI-Boc** (right). The black line is the generated spectrum when assigning 1000 cm^{-1} for each transition.

5.1.4. Photophysical characterization of the final product TAA.

The UV-Vis absorption, excitation and emission spectra of **TAA** at 298 K (Figure 6) exhibit a strong absorption at 422 (Soret), two Q bands in the 540-600 range, and an emission at 602 nm. While **P1** and **P2 (Chart 3)** exhibit low-energy CT bands, the spectra are characteristic of **ZnTPP**, zinc(II)tetraphenylporphyrin, as illustrated in Figure 7. There is no evidence for a CT bands for **TAA**. The presence of the quinone diimine is clearly necessary for CT interactions.

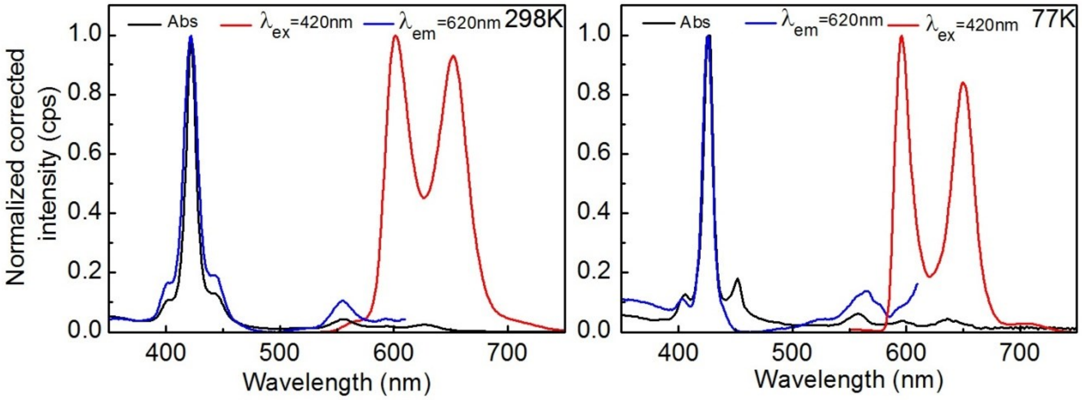

Figure 6. The absorption (black), excitation (blue) and fluorescence (red) spectra of **TAA** in 2MeTHF at 298 (left) and 77 K (right).

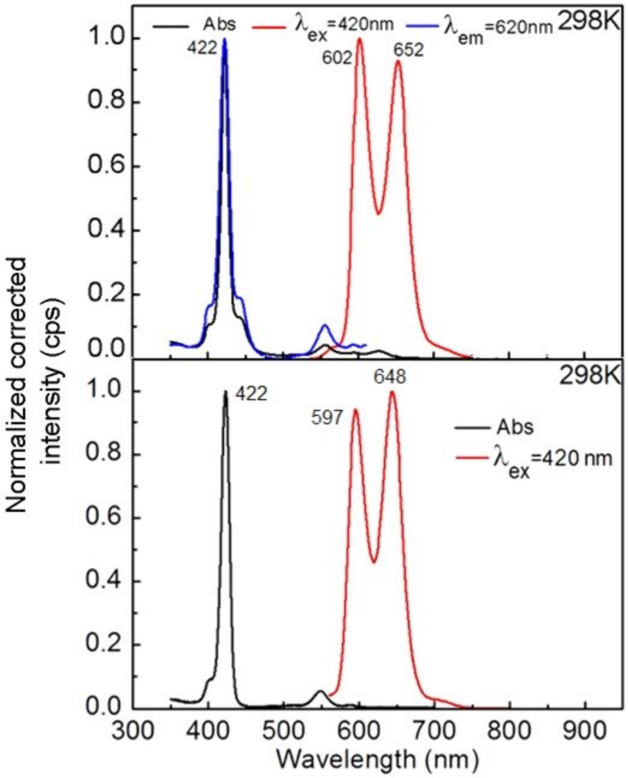

Figure 7. The absorption (black), fluorescence (red) and the excitation (blue) spectra at 298K of **TAA** (top) and **ZnTPP** (bottom).

The fluorescence lifetimes, τ_F, of **TAA** at 77 and 298 K are respectively 2.0 and 1.3 ns, a time scale which is typical for a **ZnTPP**-like chromophore (Table 5).[10] The fluorescence quantum yield of **TAA** is 0.029, which is very similar to 0.033 of **ZnTPP**.[11] Hence, the photophysical and spectroscopic results led to the deduction that there is clearly no CT interaction between the various arms of the molecules and between the arms and the central electron rich benzene.

Table 5. Emission lifetimes and quantum yield of compound **TAA**.

Compound	298 K		77 K
	τ_F (ns)	Φ_F	τ_F (ns)
TAA	1.31±0.08 [a]	0.029[b]	1.99±0.06 [a]
ZnTPP	1.75±0.02[11]	0.033[11]	2.0±0.001[11]

a= The lifetime measurement was carried out at $\lambda_{\text{excitation}}$ = 590 nm , $\lambda_{\text{emission}}$ =650 nm.
b= Quantum yield was measured in 2MeTHF at 298 K, using ZnTPP as a reference.[11]

5.1.5. Conclusion

The compounds **TAI** and **TAI-Boc** exhibit charge transfer which occurs from the terminal arms to be more localized on the central benzoquinone ring. The compound **TAI-Boc** showed a more red shifted charge transfer absorption band maximum than **TAI**. The compound **TAA** showed absence of charge transfer due to the broken conjugation

5.1.6. Experimental Section

Materials

$TiCl_4$ (Aldrich), 4-((Trimethylsilyl)ethynyl)aniline (Aldrich), triethylamine, (Et_3N; Aldrich), 1,4-benzoquinone (Aldrich), CuI (Aldrich), $PdCl_2(PPh_3)_2$ (Aldrich), $Pd(PPh_3)_2Cl_2$ (Aldrich), di-*tert*-butyl dicarbonate , (Boc_2O; Aldrich), 4-Dimethylaminopyridine (DMAP; Aldrich), Tetra-n-butylammonium fluoride (TBAF, Aldrich) and 5,10,15-(triphenyl)-20-bromo-porphyrin (Porphychem) were commercially available and were used as received. All reactions were performed in Schlenk-tube flasks under argon atmosphere. All flasks were dried in an oven to eliminate moisture.

Synthesis

TAI. An amount equivalent to (1.33 g, 7 mmol) of 4-((trimethylsilyl)ethynyl)aniline was dissolved in chlorobenzene and placed in a three-necked round bottomed flask, 1.4 mL (10 mmol) of triethylamine, and 0.16 ml (1.5 mmol) of $TiCl_4$ were added to the flask using a syringe. A 108.1 mg quantity (1 mmol) of 1,4-benzoquinone was dissolved in a minimum amount of chlorobenzene and added dropwise to the solution. The solution was stirred at 60 ^{o}C for 10 h. The mixture was left to cool to room temperature, filtered, and washed with warm chlorobenzene twice. The solution was evaporated. The solid was dissolved in CH_2Cl_2, washed three times with water, dried with $MgSO_4$, and filtered. The product was purified on a silica column with CH_2Cl_2/Hexanes (1:2) as the eluent to give the desired compound. Yield: 580 mg (70%). IR (KBr)/cm^{-1} ν : 3297 (N-H), 2155 (C≡C), 1593 (C=N). ^{1}H NMR (400 MHz, CD_2Cl_2): 8.30 (2 H, s), 7.44 (8 H, d), 6.95 (8 H, d), 6.24 (2 H, s), 0.25 (36 H, d), m/z (EI): calculated for $C_{50}H_{56}N_4Si_4^+$: 825.36, Found: 825.36 (M+).

TAI-Boc. To a solution of **TAI** (1.11 g, 1.35 mmol) in THF (40 ml) under argon at 21^{o}C, Di-*tert*-butyl dicarbonate, Boc_2O (1.12 g, 5.11 mmol) was added. The solution was cooled on ice bath followed by addition of 4-Dimethylaminopyridine, DMAP, (297 mg, 1.36 mmol). The resulting mixture solution was stirred at 21° C for 24 h was evaporated. The crude product was subject to chromatography purification on silica gel, eluent CH_2Cl_2 / hexane (2:1) to give the product as a red solid. Yield: 535 mg (60%). IR (KBr)/cm^{-1} ν : 3303 (N-H), 2161 (C≡C), 1742 (C=O), 1599 (C=N). ^{1}H NMR (400 MHz, CD_2Cl_2): 7.40 (8 H, dd), 7.16 (4 H, d), 6.77 (2 H, s), 6.68 (4 H, d), 1.40 (18 H, s),0.25 (36 H, d), m/z (EI): calculated for $C_{60}H_{72}N_4O_4Si_4^+$:1025.46, Found: 1025.24 (M+).

TAI-Boc-H. To a solution of **TAI-Boc** (250 mg, 0.245 mmol) in THF (100 ml), Tetra-n-butylammonium fluoride (1.2 ml, 1 M in THF), TBAF, was added dropwise. The mixture was stirred at room temperature for 12 h, the solution evaporated under reduced pressure and dissolved in DCM. The solution was washed with a saturated NH_4Cl solution, 3 times with water and dried over anhydrous $MgSO_4$. The desired compound was purified over a silica plug, eluent CH_2Cl_2: hexane (1:1). ^{1}H NMR (400 MHz, CD_2Cl_2): 7.43 (8 H, m), 7.20 (4 H, m), 6.80 (2 H, s), 6.70 (4 H, m), 3.38 (4H, m), 1.44 (18 H, s), m/z (EI): calculated for $C_{48}H_{40}N_4O_4^+$:737.3, Found: 737.3 (M+).

TAA. To a solution of **TAI-Boc-H** (9.6 mg, 0.013 mmol) in THF (100 ml) under argon, an amount equivalent to (5 mg, 0.007 mmol) of $Pd(PPh_3)_2Cl_2$**,** (0.6 mg, 0.003 mmol) of CuI and Et_3N (40 ml) were added. The mixture was stirred for 10 mins before adding the 5,10,15-(triphenyl)-20-bromo-porphyrin (54 mg, 0.087 mmol). The mixture was stirred for 24 h at 60^o C and was evaporated under reduced pressure. The crude product was dissolved in CH_2Cl_2 and was then subject to chromatography purification on silica gel, eluent CH_2Cl_2: Hexane (3:1). Yield: 1.9 mg (6 %). ^1H NMR (400 MHz, CD_2Cl_2): 7.87 (8 H, d), 7.66 (14 H, m), 7.62 (8 H, d), 7.59 (8 H, m), 7.52 (8 H, d), 7.09 (12 H, d), 6.99 (26 H, m), 6.82 (14 H, m), 6.51 (12 H, d), 5.69 (2 H, s), 1.45 (18 H, s). m/z (MALDI-TOF): calculated for $C_{200}H_{130}N_{20}O_4Zn_4$: 3138.77, Found: 3138.73 (M).

Photophysical characterization

Absorption, emission and excitation spectra. All samples were prepared in 2-methyltetrahydrofuran, 2-MeTHF, which was distilled over CaH_2 under nitrogen. Absorption spectra were recorded at 298 and 77 K using a Varian Cary 300 spectrophotometer and a HP-8453 diode array spectrophotometer respectively. Steady-state emission and excitation spectra were recorded at 298 and 77 K in a 1.0 cm capped quartz cell and a 5.0mm(i.d) NMR tube inserted into a liquid nitrogen filled quartz EPR dewar, respectively. Emission spectra were obtained by exciting at the lowest energy absorption maxima using a Horiba Jobin Yvon Fluorolog spectrofluorometer equipped with double monochromators.

Fluorescence quantum yield and lifetimes. The measurements of the emission quantum yields were performed in 2MeTHF at 298K. Three different measurements (i.e. different solutions) were prepared for each photophysical datum (quantum yields and lifetimes). For 298K measurements samples were prepared under inert atmosphere (in a glove box, $PO_2 <$ 25 ppm). The sample and the standard concentrations were adjusted to obtain an absorbance of 0.05 or less. This absorbance was adjusted to be the same as much as possible for the standard and the sample for a measurement. Each absorbance value was measured five times for better accuracy in the measurements of the quantum yields. The equation $\Phi_s = \Phi_r(F_r/F_s)(I_s/I_r)(n_s/n_r)^2$ was used to calculate the relative quantum yield of each of the sample, where Φr is the absolute quantum yield of the reference, n is the refractive index of the solvent, F is the absoptance (F= $1\text{-}10^{-A}$, where A is the absorbance) at the excitation wavelength, and I is the integrated area under the corrected emission curve. The subscripts s and r refer to the sample and reference, respectively. A solution of meso-tetraphenylporphyrin (ZnTPP) in 2MeTHF ($\Phi_F = 0.033$)[11] was used as the external reference. The emission lifetimes in the 1 to 10 ns range were measured on a TimeMaster model TM-3/2003 apparatus from PTI. The source was a nitrogen laser with high-resolution dye laser (fwhm~1400 ps) and the excited lifetimes were obtained from deconvolution or distribution lifetimes analysis.

References

1- Egbert J. Boekema, Henny van Roon, Jan F. L. van Breemen and Jan P. Dekker, *Eur. J. Biochem*, (1999), **266**, 444 - 452.

2- A. W. Rutherford and P. Faller, *Philos. Trans. R. Soc. Lond.* B Biol. Sci., (2003), **358**, 245–253.

3- W. Zhou, P. Shen, B. Zhao, P. Jiang, L. Deng and S. Tan, *J. Polym. Sci.,* Part A: *Polym. Chem.*, (2011), **49**, 2685-2692.

4- X. Xu, H. Chen, E. Huo, X. Cai, Y. Li and Q. Jiang, *Polym. Bull.*, (2008), **60**, 7-14.

5- N. Wang, F. Lu, C. Huang, Y. Li, M. Yuan, X. Liu, H. Liu, L. Gan, L. Jiang and D. Zhu, J. Polym. Sci., Part A: *Polym. Chem.,* (2006), **44**, 5863-5874.

6- J. Zhao, B. Li and Z. Bo, *Chin. Sci. Bull.,(* 2006), **51**, 1287-1295.

7- K. Takahashi, Y. Takano, T. Yamaguchi, J.-I. Nakamura, C. Yokoe, K. Murata and Kazuhiko, *Synth. Met.*, (2005), **155**, 51-55.

8- S. Lamare, S. M. Aly, D. Fortin and P. D. Harvey, *Chem. Comm.*, (2011), **47**, 10942–10944.

9- X. Wang, D. Fortin, G. Brisarda and P. D. Harvey, *Chem. Comm.*, (2014), **50**, 350-352.

10- P. D. Harvey. In The Porphyrin Handbook; K. M. Kadish, K. M. Smith, R. Guilard, Eds., Academic Press, San Diego, (2003), **18**, 113.

11- E. G. Azenha, A. C. Serra, M. Pineiroa, M. M. Pereira, J. Seixas de Melo, L. G. Arnaut, S. J. Formosinho and A.M.d'A. Rocha Gonsalves, *Chem. Phys.*, (2002), **280**, 177–190.

5.2. SUPPORTING INFORMATION

Bis-α-(amino(4-ethynylbenzene(trimethylsilane)(R))bis(4-ethynylbenzene-(trimethylsilane))quinone diimine (R = H, Boc) as potential building blocks for conjugated porphyrin dye-containing polymers exhibiting low-energy band gaps.

Table of Contents:

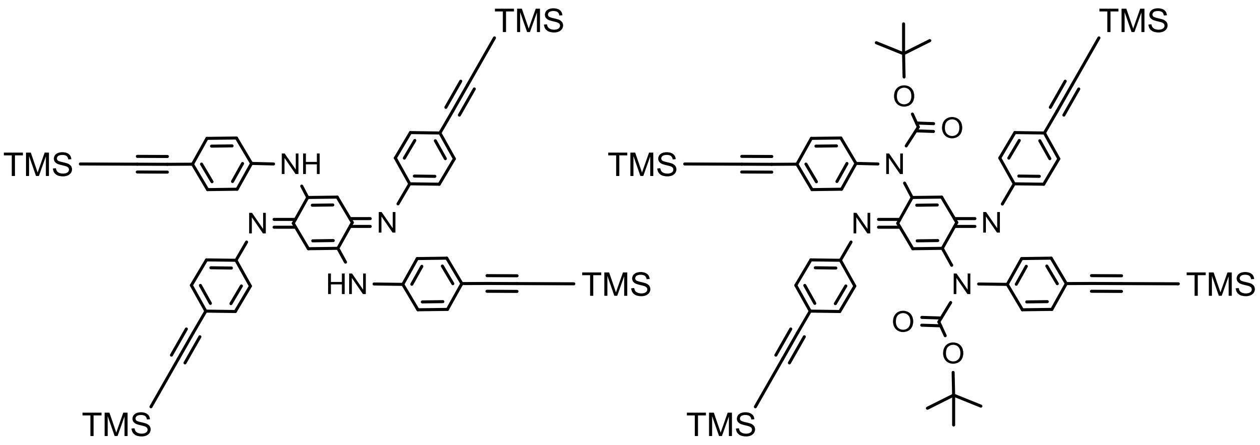

TAI **TAI-Boc**

Figure S1. The structures of **TAI** and **TAI-Boc**.

DFT Calculation Procedure

All density functional theory (DFT) calculations were performed with Gaussian 09[1] at the Université de Sherbrooke with the MP2 supercomputer supported by Le Réseau Québécois De Calculs Hautes Performances. The DFT [2-5] geometry optimisations well as TD-DFT calculations [6-8] were carried out using the B3LYP method.[9-11] 6-31g* basis sets [12-18] were used for **TAI** and **TAI-Boc**. The calculated absorption spectra, were obtained from GaussSum 2.1.[19]

Images of the optimised structure

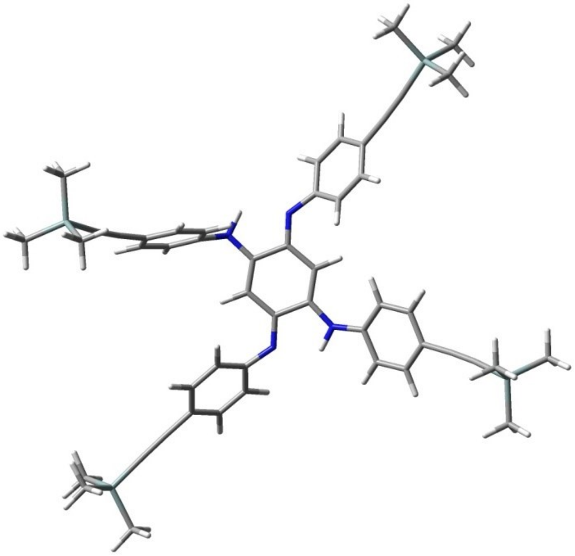

TAI

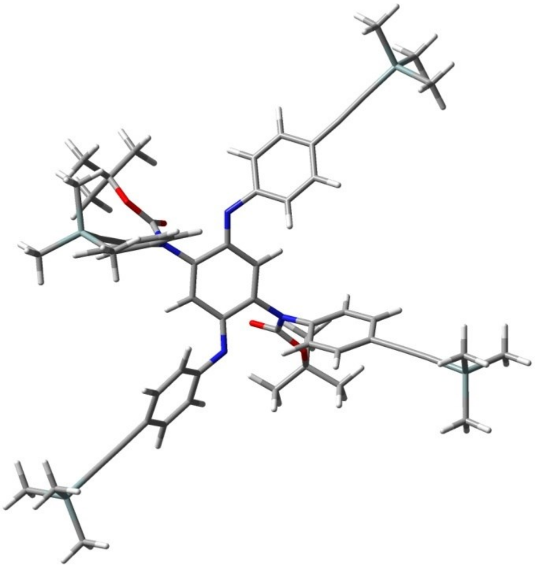

TAI-Boc

Figure S2. The optimized structures of **TAI** (up) and **TAI-Boc** (bottom).

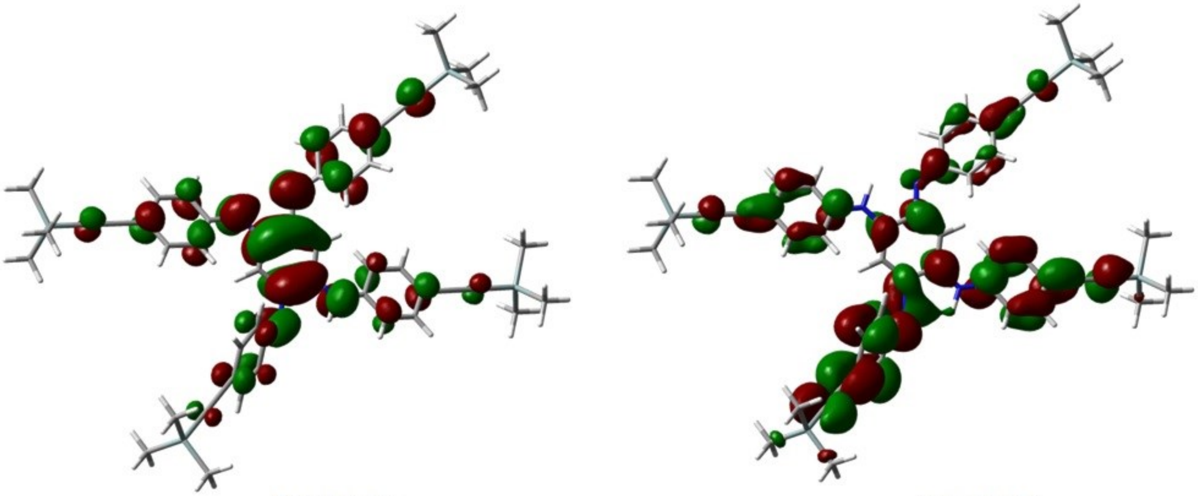

HSOMO LSOMO

Figure S3. Triplet optimized structure of **TAI**.

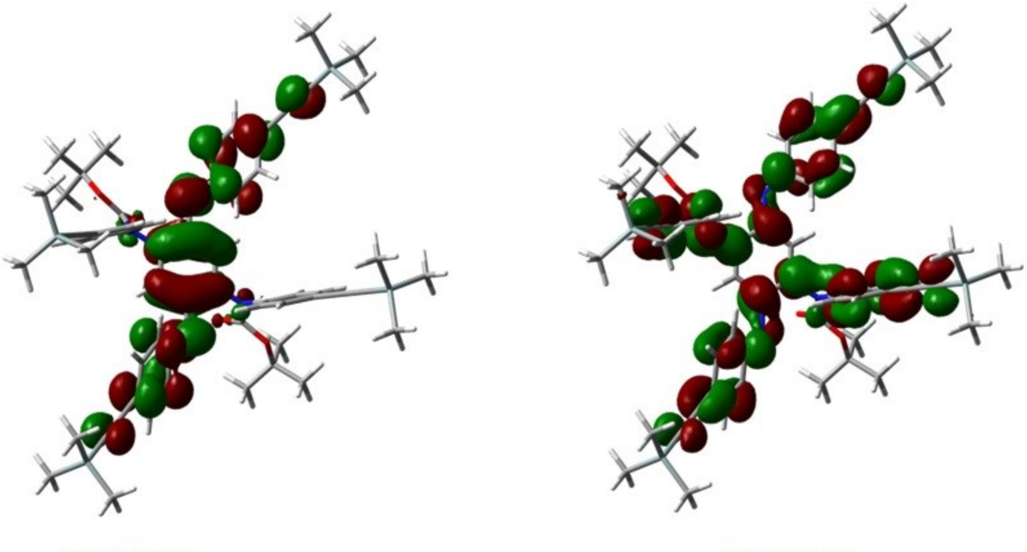

HSOMO LSOMO

Figure S4. Triplet optimized structure of **TAI-Boc**.

TDDFT Electronic Transition Table

Table S1. Calculated position of the pure electronic transitions, oscillator strength (f) and major contributions to the transitions for the first 100 transitions of **TAI.**

λ(nm)	f	Major contributions (%)	λ(nm)	f	Major contributions (%)
606.9	0.1676	H→L (94%)	242.2	0	H-22→L (38%), H-9→L+2 (35%), H-9→L+4 (15%)
541.5	0.9885	H-1→L (92%)	241.7	0.0001	H-23→L (51%), H-10→L+2 (19%)
457.4	0.0624	H-2→L (93%)	240.7	0.003	H-4→L+4 (22%), H→L+9 (33%)
424.3	0.155	H-4→L (88%)	240.4	0.007	H-2→L+6 (18%), H-2→L+7 (41%), H-1→L+7 (12%)
413.9	0.048	H-3→L (93%)	239.7	0.0076	H-21→L (17%), H-4→L+4 (28%), H→L+13 (26%)
347.7	0.4418	H-14→L (11%), H-5→L (75%)	239.0	0.0256	H-21→L (12%), H-4→L+4 (19%), H-1→L+9 (13%), H→L+9 (21%), H→L+13 (10%)
336.3	0.0037	H-6→L (93%)	238.4	0.0042	H-25→L (12%), H-21→L (29%), H-8→L+3 (11%)
334.7	0.0567	H-7→L (82%)	238.1	0.0108	H-25→L (17%), H-2→L+5 (13%), H-2→L+6 (23%)
326.3	0.0341	H-14→L (53%), H→L+2 (16%)	237.7	0.0025	H-25→L (28%), H-21→L (27%)
325.7	0.0277	H-11→L (64%), H-8→L (20%)	237.7	0.0011	H-22→L (59%), H-9→L+2 (21%)
324.6	0.007	H→L+1 (82%)	237.3	0.0034	H-23→L (35%), H-10→L+2 (15%)
324.3	0.0118	H-12→L (86%)	236.2	0.0061	H-2→L+5 (52%), H-2→L+6 (19%)
321.3	0.1879	H→L+2 (59%)	235.9	0	H-24→L (99%)
318.8	0.0047	H-10→L (81%)	235.2	0.0046	H-3→L+4 (76%)
318.0	0.0128	H-9→L (84%)	234.9	0.0058	H-10→L+2 (16%), H→L+12 (23%)
315.9	0.0166	H-11→L (18%), H-8→L (71%)	234.7	0.0182	H-1→L+9 (32%), H-1→L+11 (17%)
315.6	0.0917	H-15→L (65%)	234.3	0.0024	H-6→L+2 (10%), H-4→L+8 (27%), H-2→L+8 (23%)
313.8	0.205	H-1→L+1 (74%), H→L+3 (10%)	232.9	0.0129	H-5→L+2 (11%), H-1→L+9 (21%),

					H-1→L+11 (31%)
311.4	0.5601	H-1→L+1 (12%), H-1→L+2 (15%), H→L+3 (52%)	232.2	0.0202	H-5→L+2 (57%)
306.1	0.0008	H-13→L (92%)	231.8	0.0071	H-5→L+1 (84%)
298.1	0.1317	H-1→L+2 (72%)	231.5	0.0037	H-26→L (59%)
295.9	0.1257	H-1→L+3 (97%)	230.7	0.0324	H-5→L+3 (73%)
290.3	0.0966	H→L+4 (90%)	229.4	0.001	H-27→L (73%)
283.5	0.3778	H-16→L (67%), H-1→L+4 (15%)	228.8	0.0068	H-4→L+5 (73%)
279.6	0.0254	H→L+6 (76%)	226.3	0.0017	H-4→L+8 (38%), H-2→L+8 (56%)
276.9	0.0703	H-2→L+1 (84%)	224.4	0.0182	H-4→L+6 (47%), H-2→L+6 (13%), H→L+14 (12%)
273.5	0.0049	H-2→L+2 (11%), H-1→L+4 (10%), H→L+7 (61%)	223.3	0.0004	H-6→L+1 (96%)
272.4	0.0186	H-2→L+2 (25%), H-1→L+4 (40%), H→L+7 (19%)	223.0	0.0215	H-28→L (10%), H-4→L+6 (14%), H→L+14 (50%)
271.1	0.0912	H→L+5 (69%)	222.4	0.0011	H-3→L+10 (85%)
269.3	0.2986	H-2→L+2 (36%), H-1→L+4 (11%), H→L+5 (10%)	221.6	0.0002	H-28→L (19%), H-7→L+1 (67%)
266.8	0.1043	H-4→L+1 (52%), H-3→L+1 (13%), H-2→L+1 (10%)	221.4	0.0003	H-28→L (46%), H-7→L+1 (25%)
265.9	0.0251	H-1→L+5 (10%), H-1→L+8 (53%), H→L+8 (17%)	219.7	0.0152	H-7→L+2 (11%), H-4→L+7 (63%)
265.4	0.1115	H-4→L+1 (11%), H-2→L+3 (76%)	219.3	0.0022	H-14→L+2 (11%), H-4→L+7 (13%), H-3→L+6 (12%), H-3→L+7 (52%)
263.3	0.0216	H-1→L+5 (61%), H→L+8 (19%)	218.8	0.008	H-14→L+2 (27%), H-3→L+7 (10%), H→L+10 (34%)
263.0	0.2729	H-17→L (41%), H-3→L+1 (26%)	218.8	0.0026	H-14→L+2 (14%), H→L+10 (60%)
261.8	0.2767	H-17→L (28%), H-3→L+1 (27%), H→L+8 (22%)	218.6	0.0013	H-3→L+8 (87%)
261.4	0.0906	H-3→L+1 (13%), H-1→L+8 (17%), H→L+8 (38%)	217.5	0.0103	H-15→L+2 (13%), H-9→L+1 (46%)
258.0	0.1556	H-4→L+2 (71%)	217.4	0.011	H-15→L+2 (10%), H-9→L+1 (52%)
256.3	0.0113	H-1→L+6 (64%), H-1→L+7 (16%)	217.1	0.0069	H-11→L+2 (24%), H-8→L+2 (10%), H-3→L+6 (29%),

					H-3→L+7 (10%)
255.1	0.006	H-1→L+6 (23%), H-1→L+7 (55%)	217.0	0.0014	H-11→L+2 (20%), H-3→L+6 (17%), H-3→L+7 (11%)
254.8	0.0117	H-3→L+2 (76%)	216.7	0.0051	H-12→L+2 (23%), H-11→L+2 (11%), H→L+11 (31%)
252.9	0.0014	H-19→L (18%), H-13→L+1 (11%), H-12→L+1 (25%), H-3→L+2 (12%), H-3→L+5 (13%)	216.6	0.0014	H-12→L+2 (55%), H→L+11 (27%)
252.5	0.0103	H-19→L (28%), H-13→L+1 (46%)	216.4	0.0006	H-11→L+1 (26%), H-8→L+1 (27%), H-5→L+4 (13%)
252.1	0.0139	H-19→L (16%), H-13→L+1 (30%), H-3→L+5 (21%)	216.2	0.0037	H-11→L+1 (16%), H-8→L+1 (18%), H-5→L+4 (20%)
251.2	0.0452	H-18→L (62%), H-4→L+3 (16%)	215.6	0.0019	H-7→L+3 (61%), H-6→L+3 (21%)
251.0	0.0131	H-4→L+3 (20%), H-2→L+4 (68%)	215.5	0.0028	H-10→L+1 (82%)
249.4	0.0095	H-18→L (17%), H-4→L+3 (46%), H-2→L+4 (16%), H→L+9 (10%)	215.3	0.0048	H-7→L+3 (16%), H-6→L+2 (12%), H-1→L+14 (23%)
246.1	0.0017	H-3→L+3 (85%)	215.0	0.0007	H-7→L+3 (10%), H-6→L+3 (67%)
243.7	0.0012	H-21→L (10%), H-8→L+3 (55%), H→L+13 (10%)	214.7	0.0023	H-11→L+1 (38%), H-8→L+1 (40%)
242.5	0.0017	H-20→L (72%)	214.5	0.0154	H-2→L+9 (50%)

Table S2. Calculated position of the pure electronic transitions, oscillator strength (f) and major contributions to the transitions for the first 100 transitions of **TAI-Boc.**

λ(nm)	f	Major contributions (%)	λ(nm)	f	Major contributions (%)
562.7	0.8645	H→L (88%)	250.3	0.0027	H-27→L (16%), H-11→L+1 (45%), H-11→L+2 (21%)
527.5	0.0035	H-1→L (97%)	250.3	0.0003	H-28→L (97%)
508.4	0.1276	H-2→L (89%)	249.3	0.0483	H-3→L+4 (46%), H-3→L+5 (23%)
492.6	0.0208	H-3→L (92%)	248.8	0.0016	H-26→L (48%), H-6→L+2 (25%)
367.1	0.058	H-5→L (69%)	248.6	0.0022	H-27→L (77%), H-11→L+1 (10%)
360.6	0.1433	H-7→L (11%),	248.1	0.0001	H-29→L (99%)

		H-5→L (12%), H-4→L (56%)			
355.9	0.053	H-10→L (12%), H-7→L (62%)	243.2	0.0027	H→L+8 (89%)
352.5	0.0062	H-10→L (38%), H-9→L (36%)	242.4	0.0025	H→L+7 (14%), H→L+9 (75%)
351.6	0.1411	H-14→L (14%), H-9→L (27%), H-8→L (23%), H-7→L (14%)	242.0	0.0026	H-32→L (11%), H-31→L (25%), H-30→L (46%)
347.8	0.0068	H-10→L (30%), H-9→L (17%), H-8→L (38%)	240.9	0.0024	H-3→L+10 (17%), H→L+10 (56%)
346.6	0.0058	H-8→L (15%), H-6→L (52%)	240.2	0.0007	H-13→L+1 (12%), H-13→L+3 (75%)
344.8	0.0389	H-16→L (17%), H-6→L (38%)	240.1	0.0074	H-31→L (44%), H-30→L (39%)
337.4	0.0278	H-18→L (11%), H-17→L (29%), H-15→L (51%)	238.2	0.0705	H-5→L+1 (21%), H-4→L+1 (28%)
335.2	0.0432	H-18→L (15%), H-17→L (11%), H-16→L (26%), H-15→L (20%)	237.3	0.0014	H-32→L (57%), H-31→L (11%), H-1→L+6 (14%)
330.2	0.004	H-16→L (10%), H-12→L (83%)	237.1	0.0039	H-32→L (17%), H-1→L+6 (50%)
328.8	0.0108	H-18→L (40%), H-16→L (28%), H-12→L (10%)	234.8	0.0009	H-3→L+6 (12%), H-2→L+6 (42%), H-1→L+6 (17%)
325.6	0.0045	H-11→L (85%)	234.6	0.0005	H-12→L+1 (18%), H-12→L+2 (23%), H-12→L+4 (40%)
319.7	0.4991	H-17→L (23%), H-14→L (38%), H-4→L (12%)	234.4	0.0037	H-3→L+6 (21%), H-3→L+7 (10%), H-2→L+7 (21%), H→L+7 (16%)
318.9	0.0001	H-13→L (93%)	232.8	0.0047	H-33→L (11%), H-1→L+7 (56%)
303.4	0.0117	H-19→L (13%), H→L+1 (71%)	231.8	0.0422	H-33→L (39%), H-4→L+1 (10%), H-2→L+6 (11%)
299.8	0.0071	H-21→L (11%), H-19→L (60%), H→L+1 (20%)	231.2	0.0051	H-3→L+6 (19%), H-2→L+6 (25%)
294.7	0.0192	H→L+2 (83%)	230.8	0.0059	H-33→L (22%), H-4→L+1 (17%), H-4→L+2 (28%)
289.8	0.0802	H→L+3 (89%)	229.5	0.0266	H-10→L+3 (11%), H-4→L+2 (14%), H-4→L+3 (20%)
286.6	0.4548	H-1→L+1 (73%)	228.5	0.0005	H-3→L+7 (31%), H-2→L+7 (44%)
283.2	0.0298	H-21→L (30%), H-20→L (45%), H-19→L (17%)	227.5	0.0005	H-3→L+8 (34%), H-2→L+9 (11%), H-1→L+8 (43%)
281.8	0.1338	H-21→L (40%), H-20→L (40%)	226.9	0.002	H-3→L+9 (20%), H-2→L+8 (15%), H-1→L+9 (47%)
279.9	0.2326	H-2→L+1 (31%),	226.4	0.0091	H-34→L (12%), H-5→L+1

		H-1→L+2 (41%)			(18%), H-5→L+2 (22%)
278.3	0.169	H-2→L+1 (39%), H-1→L+2 (32%)	226.0	0.0026	H-34→L (80%)
276.3	0.1466	H-2→L+2 (77%)	225.5	0.0079	H-4→L+1 (18%), H-4→L+2 (17%)
275.1	0.014	H→L+5 (78%)	225.2	0.0019	H-35→L (88%)
274.2	0.126	H-3→L+1 (68%)	224.3	0.0001	H-3→L+8 (26%), H-3→L+9 (23%), H-2→L+9 (28%)
272.4	0.2477	H-1→L+2 (11%), H-1→L+3 (48%)	224.1	0.0009	H-3→L+8 (24%), H-3→L+9 (22%), H-2→L+8 (26%)
270.7	0.3234	H-3→L+2 (77%)	223.4	0.0032	H-10→L+1 (16%), H-7→L+1 (41%)
267.8	0.246	H-2→L+3 (34%), H→L+4 (39%)	223.1	0.0074	H-14→L+1 (10%), H-14→L+2 (11%), H-8→L+2 (11%)
267.2	0.0672	H-22→L (24%), H-2→L+3 (24%), H→L+4 (17%)	222.6	0.0072	H-9→L+1 (22%), H-7→L+1 (21%)
265.8	0.04	H-22→L (52%), H-3→L+3 (17%)	222.5	0.0036	H-9→L+1 (27%), H-7→L+2 (11%)
263.9	0.0433	H-23→L (64%), H-3→L+3 (14%)	222.0	0.0043	H-9→L+1 (10%), H-4→L+3 (13%), H→L+13 (15%)
263.7	0.0319	H-23→L (13%), H-3→L+3 (53%)	222.0	0.0003	H-3→L+13 (13%), H→L+13 (27%)
261.6	0.0767	H-1→L+5 (21%), H→L+6 (33%)	221.6	0.0088	H-16→L+1 (17%), H-2→L+12 (20%), H-1→L+12 (11%)
261.3	0.0069	H-25→L (10%), H-24→L (54%)	221.4	0.0015	H-16→L+1 (10%), H-2→L+12 (25%), H-1→L+12 (13%)
260.2	0.0249	H-2→L+5 (10%), H-1→L+4 (13%), H-1→L+5 (19%), H→L+6 (18%)	221.3	0.0008	H-6→L+1 (49%), H-6→L+2 (18%)
258.6	0.0392	H-2→L+5 (29%), H-1→L+5 (10%)	221.1	0.0001	H-16→L+1 (10%), H-8→L+2 (18%), H-6→L+1 (17%)
256.6	0.0221	H→L+7 (26%)	220.0	0.0017	H-10→L+2 (23%), H-7→L+2 (21%)
255.3	0.025	H-25→L (18%), H-1→L+4 (14%), H→L+7 (16%)	219.0	0.0091	H→L+11 (46%)
255.0	0.0519	H-2→L+5 (13%), H-1→L+4 (52%)	218.8	0.0019	H-15→L+1 (24%), H-15→L+3 (28%), H-7→L+3 (20%)
253.8	0.0003	H-26→L (50%), H-6→L+2 (24%)	218.0	0.0009	H-7→L+2 (10%), H-7→L+3 (15%)
253.2	0.0161	H-1→L+8 (19%)	217.2	0.0137	H-14→L+1 (23%), H-4→L+5 (14%)
253.1	0.0395	H-2→L+4 (48%), H-1→L+5 (17%)	216.5	0.0546	H-9→L+2 (22%), H-9→L+3 (18%)
252.4	0.0237	H-2→L+4 (26%), H-2→L+5 (17%)	216.3	0.0339	H-4→L+4 (15%)
250.9	0.0152	H-3→L+4 (27%), H-3→L+5 (49%)	216.2	0.03	H-9→L+3 (11%), H-7→L+2 (13%), H-7→L+3 (13%), H-4→L+4 (10%)

Table S3. The calculated phosphorescence wavelength for compound **TAI-Boc.**

Calculated Phosphorescence Emission	
S_0 total energy (a.u.)	-4007.592
T_1 total energy (a.u.)	-4007.573
S_0-T_1 energy gap (a.u.)	0.0190
phosphorescence position (eV)	0.517
phosphorescence position (nm)	2398.1

a.u. = atomic units in Hartrees.

Table S4. The S_0-T_1 bond, angle and dihedral angle differences (**Δ Bond**, **Δ Angle** and **Δ Dihedral angle**, respectively) for both singlet and triplet optimized geometries of **TAI**. **NA, NB** and **NC** are adjacent atoms to the examined atom **X**, where the bond length was determined between **NA** and **X**. The angles were determined between **NA, NB** and **X** while the dihedral angles were determined between **NA, NB, NC** and **X**. (See Chart 1 for the atoms numbering in **TAI**).

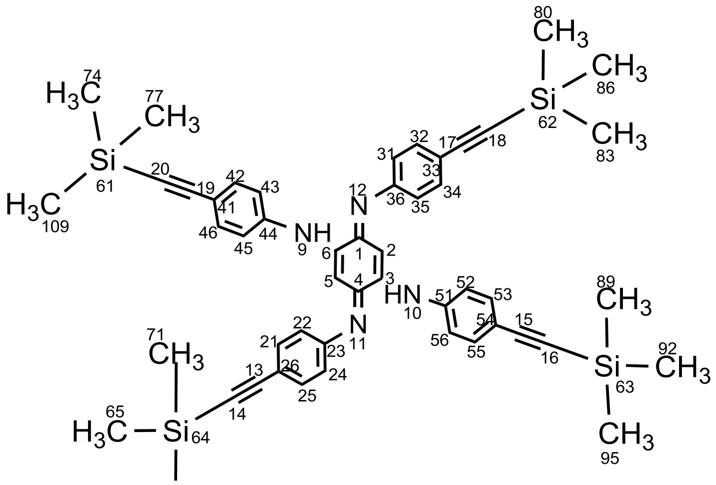

Chart 1. The numbering atoms of **TAI.**

Atom	**Adjacent atoms**					
X	**NA**	**NB**	**NC**	**Δ Bond**	**Δ Angle**	**Δ Dihedral angle**
C1						
C2	1			0.016		
C3	2	1		-0.020		
C4	3	2	1	0.058		
C5	4	3	2	0.043	-0.945	
C6	5	4	3	-0.031	1.505	-2.542
H7	2	1	6	0.005	-1.378	-3.280
H8	5	4	3	0.000	-0.308	-2.520
N9	6	5	4	-0.001	0.971	0.215
N10	3	2	1	-0.006	-0.331	4.027
N11	4	3	2	-0.084	2.263	0.004
N12	1	2	3	-0.041	-0.993	0.714
C13	11	4	3	0.032	-3.480	2.482
C14	13	11	4	-0.001	0.488	-1.095
C15	10	3	2	0.021	**9.627**	**24.745**
C16	15	10	3	0.001	**-8.006**	-18.178
C17	12	1	2	0.009	**-8.528**	**35.121**
C18	17	12	1	0.001	-7.813	**-34.864**
C19	9	6	5	-0.004	2.986	-12.168
C20	19	9	6	0.002	-3.112	10.220
C21	13	11	4	0.014	1.393	**28.567**
C22	21	13	11	0.016	-7.546	**-50.551**
C23	11	4	3	0.050	0.065	12.907
C24	23	11	4	-0.023	-0.523	1.973
C25	24	23	11	0.012	5.853	**31.402**
C26	21	13	11	-0.003	-0.067	**-22.316**
H27	21	13	11	0.002	-0.313	-8.906
H28	22	21	13	0.003	**28.531**	-5.483
H29	24	23	11	0.001	0.719	-7.491
H30	25	24	23	0.002	-0.305	-7.168
C31	12	1	2	0.008	1.003	6.640
C32	31	12	1	0.004	-0.349	0.543
C33	32	31	12	-0.001	-5.111	**20.843**
C34	33	32	31	-0.001	-0.067	**23.730**
C35	34	33	32	0.006	-0.138	3.087
C36	12	1	2	0.022	0.263	0.411
H37	31	12	1	0.001	-0.248	-1.065
H38	32	31	12	0.001	1.671	-12.947

H39	34	33	32	0.001	0.184	**-20.212**
H40	35	34	33	0.001	-0.014	-3.786
C41	19	9	6	0.003	0.221	0.787
C42	41	19	9	0.002	0.301	0.289
C43	42	41	19	0.000	4.110	**58.764**
C44	9	6	5	0.004	-1.204	**62.471**
C45	44	9	6	-0.001	-0.059	-4.233
C46	45	44	9	0.005	1.007	**20.070**
H47	42	41	19	0.002	1.784	-15.798
H48	43	42	41	0.003	-0.195	-4.902
H49	45	44	9	0.001	-0.041	3.097
H50	46	45	44	0.003	-0.251	-0.628
C51	10	3	2	0.045	0.559	1.940
C52	51	10	3	-0.010	-0.309	-1.499
C53	52	51	10	0.008	**-9.678**	**31.236**
C54	53	52	51	0.001	-2.443	**88.503**
C55	54	53	52	0.001	-0.237	-4.528
C56	55	54	53	0.003	-0.924	-0.237
H57	52	51	10	0.004	0.861	1.189
H58	53	52	51	0.002	-0.418	0.445
H59	55	54	53	0.001	-0.961	2.794
H60	56	55	54	0.001	0.522	-0.859
Si61	20	19	9	0.002	-0.106	0.149
Si62	18	17	12	0.003	0.348	-0.280
Si63	16	15	10	0.006	-4.929	**-128.580**
Si64	14	13	11	-0.004	-1.183	**-153.907**
C65	64	14	13	0.003	-5.334	**-149.207**
H66	65	64	14	0.000	-3.574	**-166.319**
H67	65	64	14	0.001	0.389	**99.910**
C68	64	14	13	0.004	0.214	-0.489
H69	68	64	14	0.001	-0.100	0.361
H70	68	64	14	0.001	-0.019	**-100.469**
C71	64	14	13	0.002	-0.076	-3.131
H72	71	64	14	0.001	0.104	2.875
H73	71	64	14	0.001	0.998	19.061
C74	61	20	19	0.003	-0.173	-0.433
H75	74	61	20	0.002	0.141	0.399
H76	74	61	20	0.001	-0.866	**-81.884**
C77	61	20	19	0.004	-0.067	0.773
H78	77	61	20	0.001	-0.117	-1.095
H79	77	61	20	0.002	-0.073	**64.206**

C80	62	18	17	0.000	-0.114	-2.228
H81	80	62	18	0.000	0.176	2.448
H82	80	62	18	0.001	0.052	**64.992**
C83	62	18	17	0.002	0.010	2.005
H84	83	62	18	0.003	-0.016	-2.086
H85	83	62	18	0.002	0.052	**54.829**
C86	62	18	17	0.001	0.183	3.522
H87	86	62	18	0.001	-0.038	-3.350
H88	86	62	18	0.001	-0.276	**-142.927**
C89	63	16	15	-0.001	-0.002	-0.391
H90	89	63	16	0.002	0.082	0.384
H91	89	63	16	0.000	0.887	**151.419**
C92	63	16	15	0.002	0.186	0.954
H93	92	63	16	0.001	0.181	-0.839
H94	92	63	16	0.000	-0.544	**-42.646**
C95	63	16	15	0.003	-0.083	-1.993
H96	95	63	16	0.001	0.133	1.877
H97	95	63	16	0.001	-1.347	**-78.413**
H98	68	64	14	0.001	0.056	1.323
H99	71	64	14	0.002	-0.146	-1.426
H100	65	64	14	0.000	0.277	-3.078
H101	77	61	20	0.001	0.169	-0.288
H102	74	61	20	0.001	0.216	0.315
H103	83	62	18	0.003	-0.104	-2.196
H104	80	62	18	0.001	0.218	-0.707
H105	86	62	18	0.002	-0.194	-3.555
H106	89	63	16	0.001	-0.004	-1.329
H107	95	63	16	0.001	0.020	-0.122
H108	92	63	16	0.001	-0.385	-0.923
C109	61	20	19	0.000	0.130	-1.415
H110	109	61	20	0.001	0.065	-2.027
H111	109	61	20	0.001	0.857	**55.290**
H112	109	61	20	0.001	-0.004	0.578
H113	10	3	2	0.010	-0.002	-0.475
H114	9	6	5	0.002	-0.107	0.087

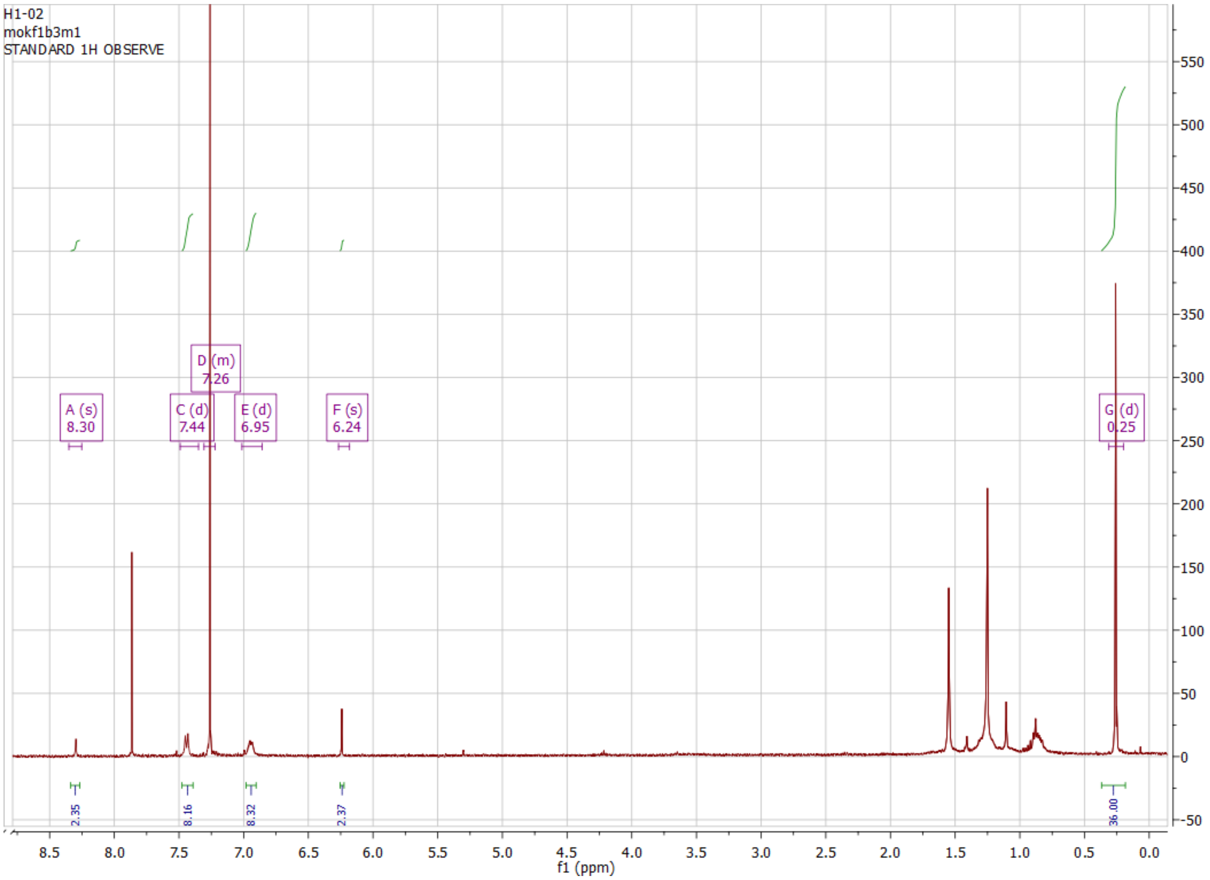

Figure S5. ^{1}H NMR spectrum of **TAI** in $CDCl_3$**.**

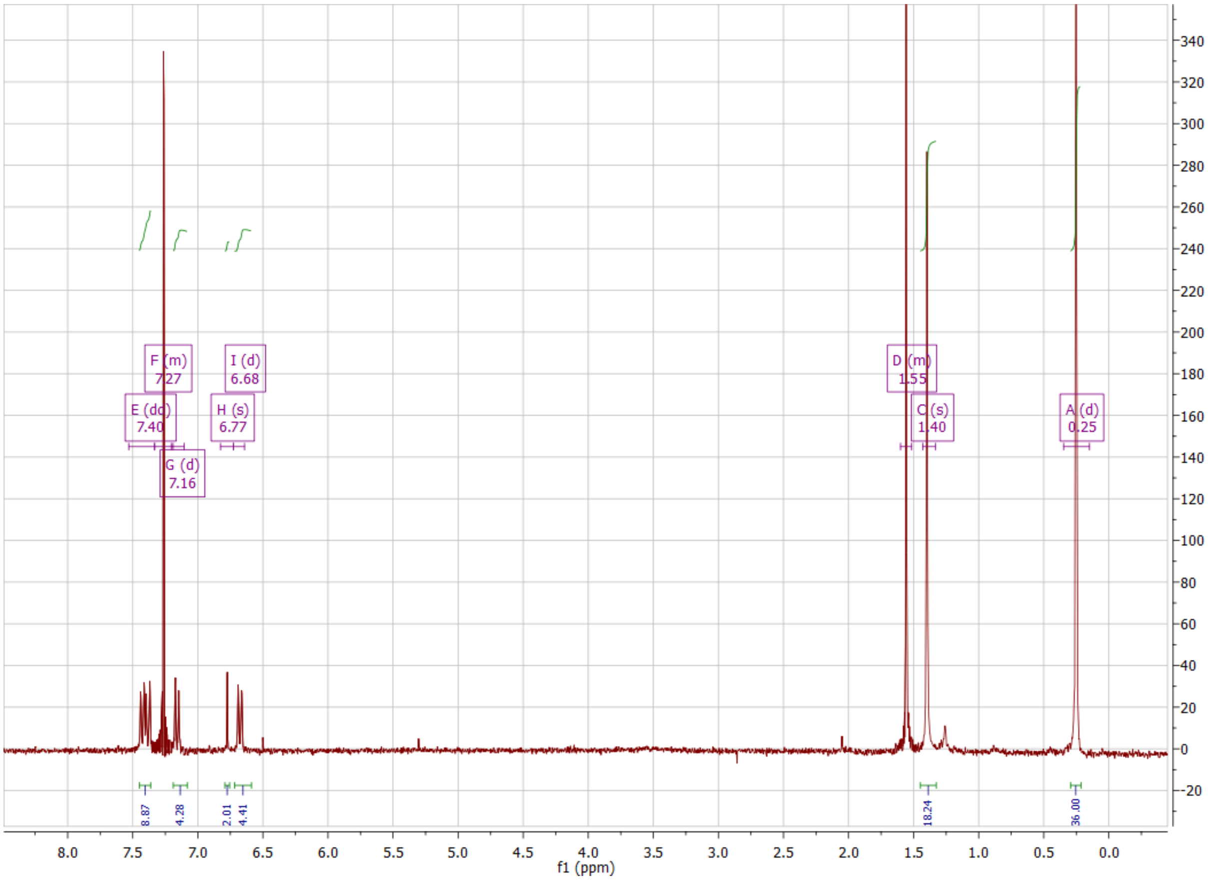

Figure S6. ^{1}H NMR spectrum of **TAI-Boc** in $CDCl_3$**.**

Figure S7. ^{1}H NMR spectrum of **TAI-Boc-H** in CDCl$_3$**.**

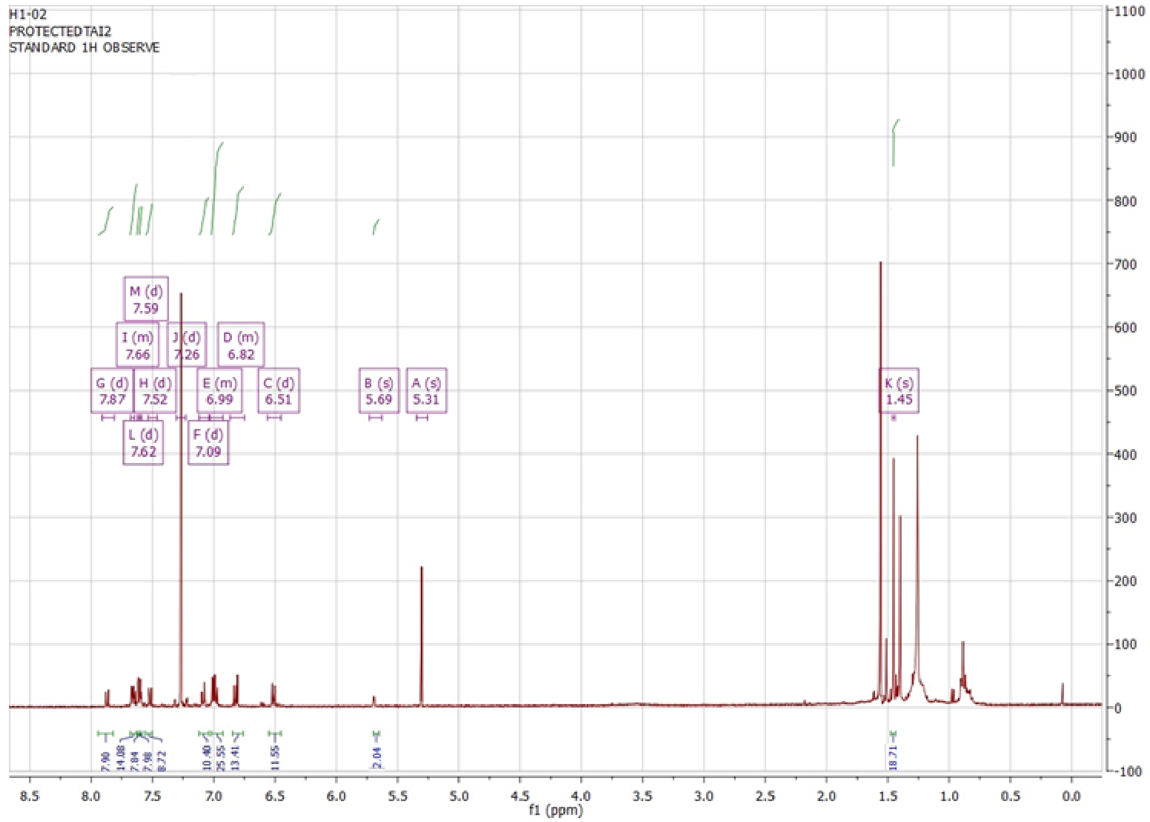

Figure S8. ^{1}H NMR spectrum of **TAA** in $CDCl_3$.

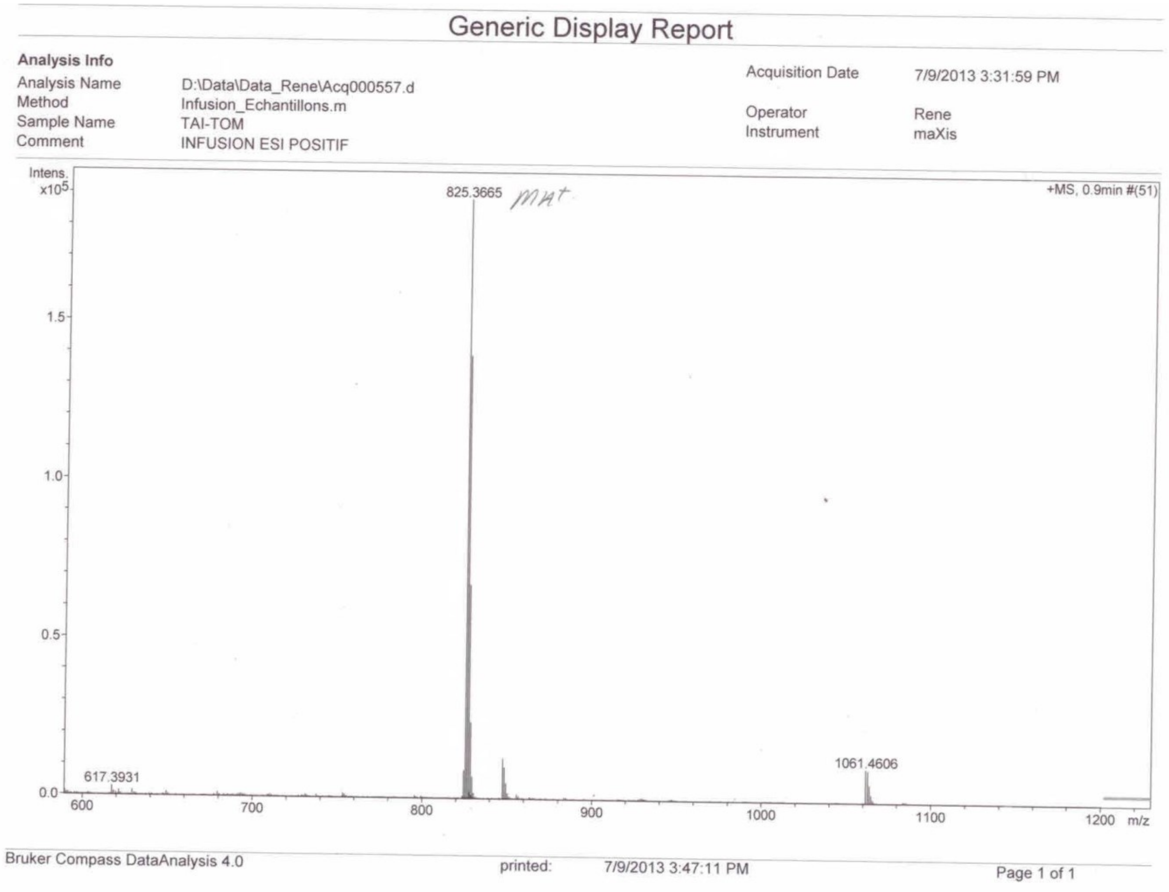

Generic Display Report

Analysis Info

Analysis Name D:\Data\Data_Rene\Acq000557.d
Method Infusion_Echantillons.m
Sample Name TAI-TOM
Comment INFUSION ESI POSITIF

Acquisition Date 7/9/2013 3:31:59 PM
Operator Rene
Instrument maXis

Bruker Compass DataAnalysis 4.0
printed: 7/9/2013 3:47:11 PM
Page 1 of 1

Figure S9. Mass spectrum of compound **TAI**.

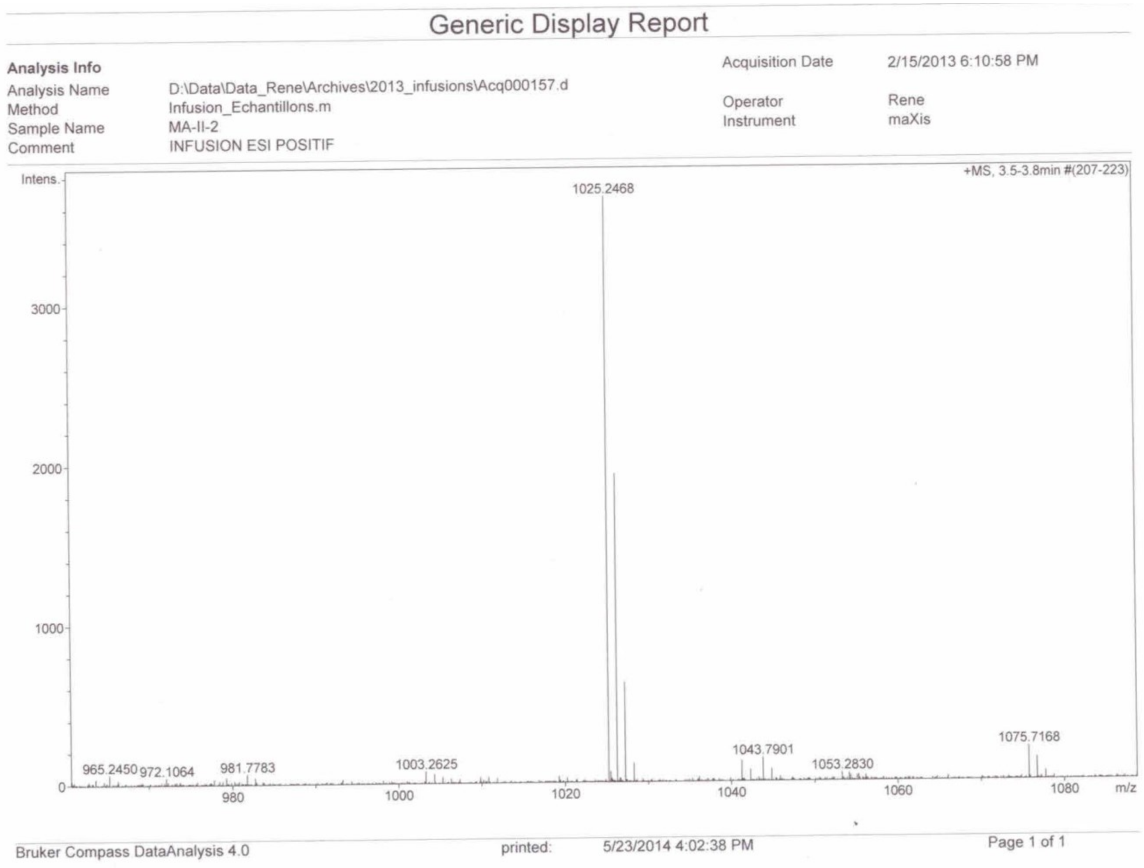

Generic Display Report

Analysis Info

Analysis Name D:\Data\Data_Rene\Archives\2013_infusions\Acq000157.d
Method Infusion_Echantillons.m
Sample Name MA-II-2
Comment INFUSION ESI POSITIF

Acquisition Date 2/15/2013 6:10:58 PM
Operator Rene
Instrument maXis

Bruker Compass DataAnalysis 4.0 printed: 5/23/2014 4:02:38 PM Page 1 of 1

Figure S10. Mass spectrum of compound **TAI-Boc**.

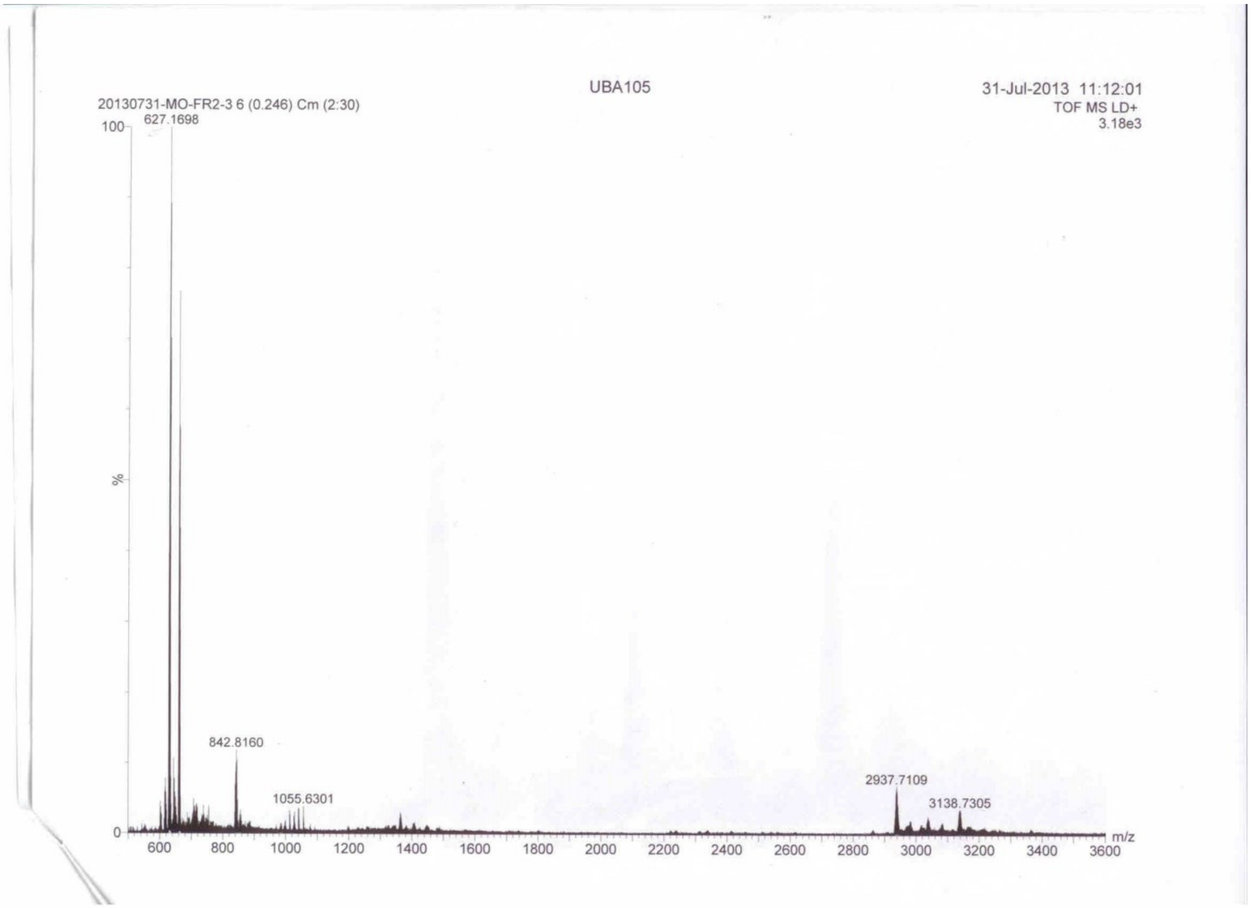

Figure S11. Mass spectrum of compound **TAA**.

References

[1] M. J. Frisch et al. Gaussian, Inc., Wallingford CT, (2004).

[2] P. Hohenberg and W. Kohn, *Phys. Rev.,* (1964); **136**, B864–871.

[3] P. Hohenberg and W. Kohn., *J. Phys. Rev.,(* 1965), **140**, A1133–1138.

[4] R.G. Parr and W. Yang, Density-functional theory of atoms and molecules, Oxford Univ. Press: Oxford, (1989).

[5] D. R. Salahub and M. C. Zerner, The Challenge of d and f Electrons, Amer. Chem. Soc. Washington, D.C. (1989).

[6] R. Bauernschmitt and X. Ahlrichs, *Chem. Phys. Lett*., (1996), **256**, 454–464.

[7] M. E. Casida, C. Jamorski, K. C. Casida and D. R Salahub, *J. Chem. Phys*., (1998), **108**, 4439–4449.

[8] R. E. Stratmann, G. E. Scuseria and M. J. Frisch, *J. Chem. Phys*., (1998), **109**, 8218–8224.

[9] C. Lee, W. Yang and R. G. Parr, *Phys. Rev. B*, (1988), **37**, 785–789.

[10] B. Miehlich, A. Savin, H. Stoll and H, *Preuss. Chem. Phys. Lett.*, (1989), **157**, 200–206.

[11] A. D. Becke, *J. Chem. Phys*., (1993), **98**, 5648–5652.

[12] R. Ditchfield, W. J. Hehre, and J. A. Pople, *J. Chem. Phys.*, (1971), **54**, 724-728.

[13] W. J. Hehre, R. Ditchfield, and J. A. Pople, *J. Chem. Phys.*, (1972), **56**, 2257-2261.

[14] P. C. Hariharan and J. A. Pople, *Mol. Phys.,* (1974), **27**, 209-214.

[15] M. S. Gordon, *Chem. Phys. Lett.,* (1980), **76**, 163-168.

[16] P. C. Hariharan and J. A. Pople, *Theo. Chim. Acta*, (1973), **28**, 213-222.

[17] J.-P. Blaudeau, M. P. McGrath, L. A. Curtiss, and L. Radom, *J. Chem. Phys.*, (1997), **107**, 5016-5021.

[18] M. M. Francl, W. J. Pietro, W. J. Hehre, J. S. Binkley, D. J. DeFrees, J. A. Pople, and M. S. Gordon, *J. Chem. Phys.*, 1982, **77**, 3654-3665.

[19] N.M. O'Boyle, A.L.Tenderholt and K.M. Langner., *J. Comp. Chem.*, 2008, **29**, 839-845.

General Discussion

Motivated by our interest in Harvey's research group in organic and organometallic oligomers and polymers with potential photonic applications, this thesis focused on the photophysical properties of some promising models. During the course of this study, a photophysical study of many examples of these oligomers and polymers led to more understanding of the energy transfer processes which occur within these systems and factors that control and affect these transfers.

The first examples of these compounds are the **[Ir]** oligomers and polymers linked by a **[Pt]** bridge (**[Ir]**$_3$ and **[Ir]**$_n$, Chart 1)[25] (**[Ir]**= bis(phenylpyridinato)(bipyridine)iridium(III), **[Pt]** = *trans*-C≡CPt(PBu$_3$)$_2$(C≡C)$_2$) which showed a triplet energy transfer from the terminal iridiums to the central Ir subunit. The replacement of one of the iridium subunit with a zinc(II) tetraphenylporphyrin chromophore, [**ZnTPP], ([Ir]-Pt-[ZnTPP],** Chart 4) revealed the absence of emission quenching or decrease in the phosphorescence liftime, τ_{p}, of the **[Ir]** lumophore. This result indicated the absence of any electronic communication in the T$_1$ excited state and hence that, no T$_1$**[Ir]**→S$_1$/T$_1$**[ZnTTP]** energy transfer occurs.[11] The unexpected complete shut off of the T$_1$ process upon a small structural change was explained by the absence of MO overlaps of the donor and acceptor, so no efficient double electron exchange is likely to occur.

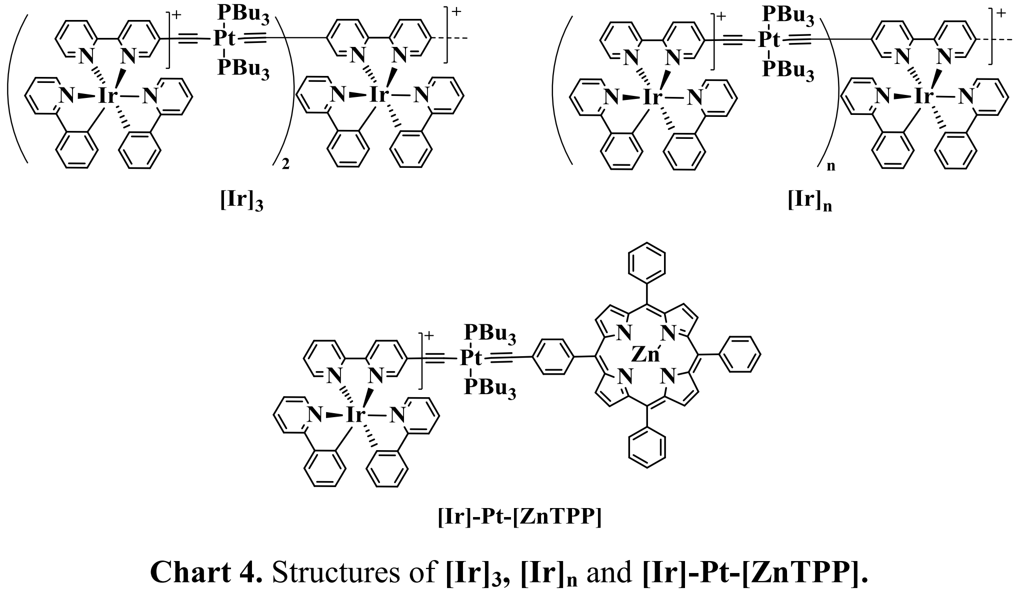

[Ir]$_3$

[Ir]$_n$

[Ir]-Pt-[ZnTPP]

Chart 4. Structures of **[Ir]**$_3$**,** **[Ir]**$_n$ and **[Ir]-Pt-[ZnTPP].**

The double electron transfer process, Dexter energy transfer, to occur efficiently needs the overlap of emission spectra of donor and absorption spectra of acceptor (i.e. the J-integral), as well as the need of the overlap of wavefunctions which implies that the excited donor and ground-state acceptor should be close enough so the electrons exchange could occur. The rate constant of exchange energy transfer is given by k_{Dexter}=KJexp(-2r_{DA}/L) where K is an experimental factor, r_{DA} is the center-to-center distance between the donor and acceptor, and L is the sum of van der Waals radius (r_{vdW}) of both chromophores and J is the spectral overlap integral. The r_{DA} obtained from the optimized geometries (DFT; B3LYP), between the **[Ir]** and **[ZnTPP]** species, of **[Ir]-Pt-[ZnTPP]** dyad was found to be 21.97 Å compared to 16.81 Å in **[Ir]$_2$** (Chart 5), as a model compound for **[Ir]$_3$** and **[Ir]$_n$**. The 5.16 Å difference seems to bring the two chromophores, **[Ir]** and **[ZnTPP],** far enough from each other to hinder the electrons exchange and leads to the complete absence of communication between them. However, other comounds in the literature[26-27] showed the absence of the triplet → singlet/triplet energy transfer for a small r_{DA} values. This led to the deduction that Dexter formulation appears as an approximation.

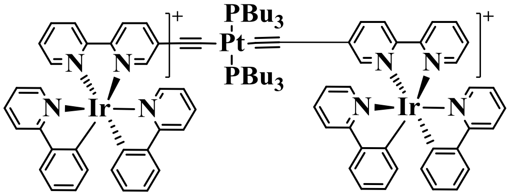

[Ir]$_2$

Chart 5. The structure of **[Ir]$_2$.**

The prospective work related to this project is to

1) replace the **[ZnTPP]** with other chromophores (i.e. BODIPY) to see the effect of different center-to-center distances, r_{DA}, between the two chromophores and the J-intergral.

2) synthesize the dyad **[Ir]-Pt-*meso*[ZnTPP]** where the acetylene group attaches directly to the porphyrin ring in the *meso* position, (Chart 6) to render the compound planar.

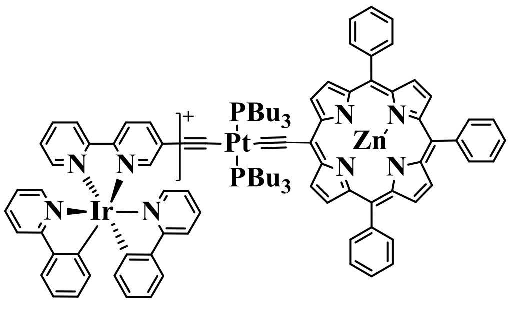

[Ir] -Pt-*meso*[ZnTPP]

Chart 6. The structure of the proposed compound.

Several sets of bisporphyrin dyads were reported in this thesis. The first dyad of this type, (**[Zn-Fb],** Chart 4), composed of a zinc(II)porphyrin (donor) and a free base porphyrin (acceptor) held together by β, β-N,N-carbene-Pd-β, β-N,N-carbene bridge, **[PdI2]**. This dyad showed a slow S_1 energy transfer despite the favorable structural parameters (expected electronic communication by π-conjugation, relatively short center-to-center distances, non-nil κ^2 (i.e. orientation factor of the transition moments). In the second dyad, (**[Fb-Zn],** Chart 7), the zinc(II)porphyrin and its corresponding free base linked by β,β-linked *trans*-Pd(NH)$_2$(C=O)$_2$, **[PdNO]**. The dyad **[Fb-Zn]** exhibited the fastest rate of singlet energy transfer (k_{ET} = 1.5 x 10^{12} s^{-1}) of the metallo-bridged bisporphyrin dyad categorie, as well as those which are linked by a carbon-based linker.

The slow and ultrafast S_1 energy transfers in both dyads **[Zn-Fb]** and **[Fb-Zn]** were rationalized by:

1) The lack of large MO overlaps and presence of a significant frontier MO coupling between the frontier MOs of the donor and acceptor units in **[Zn-Fb]** and **[Fb-Zn]** respectively.

2) The electronic shielding induced by the presence of **[PdI$_2$]** bridge in **[Zn-Fb]** prevented the two chromophores to fully interact via their transition dipoles while in dyad **[Fb-Zn]** (mainly because of the large electron clouds of the iodide ligands), the Pd(II) in **[PdNO]** had non-nil atomic contribution to the π-systems permitting Dexter mechanism to operate efficiently.

3) The absence of an electric field screening effect in **[Fb-Zn],** because no atoms, nor groups are placed between the donor and the acceptor, promotes the ultrafast energy transfer to occur.

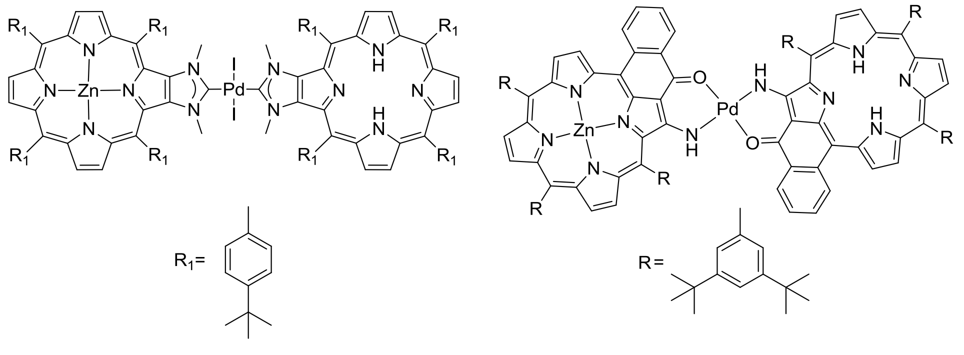

(1) **(2)**

Chart 7. structures of **[Zn-Fb]**(left) and **[Fb-Zn]**(right).

The previous results led to the conclusion that Dexter and Föster parameters are not enough to account for the energy transfer in some compounds and hence, those two mechanisms appear as an approximation. In fact, the structure on the left of Chart 4 will be modified by replacing the PdI_2 group by $[Au(I)](PF_6)$ and by $[Au(III)I_2](PF_6)$. These new systems will demonstrate beyond any doubts that the iodide slows down the rate of energy transfer. Furthermore, the I ligand can also be relaplaced by Br and Cl as well (i.e. $[Au(III)X_2]$ (PF_6); X = Cl, Br, I). Having a series of variable electronic clouds, one can try to correlate the rates vs the nature of the halide ligand. The synthesis will be performed by the Strasbourg and Montpellier groups (Romain Ruppert and Sebastien Richeter), and the photophysical work will be performed by the Sherbrooke team.

In Chapter 5, according to the promising results of charge transfer that was found in **P1** and **P2** as well as these of **TAI** and **TAI-Boc** (Chart 8), synthesis of the polymers **P3** and **P4** will be needed as a future work, which implies incorporating four metallo-porphyrins to the **TAI** and **TAI-Boc** bakbone, towards more understanding of the photosystem II process which occurs in the photosynthetic process. It is interesting to note that in this list, the incorporation of a methyl group is made. This may change the nature of the charge transfer interaction mentioned above, but on a synthetic point of view, this can also ease the synthesis of the target compounds and polymers. The NH groups are prone to react in acidbase fashion, as well as redox, whereas Boc is supposed to act as a protecting group. Because of the failure, we are not so sure this group was innocent. Was there a redox process occurring at the same time with the residual water in the solution? This still need to be elucidated.

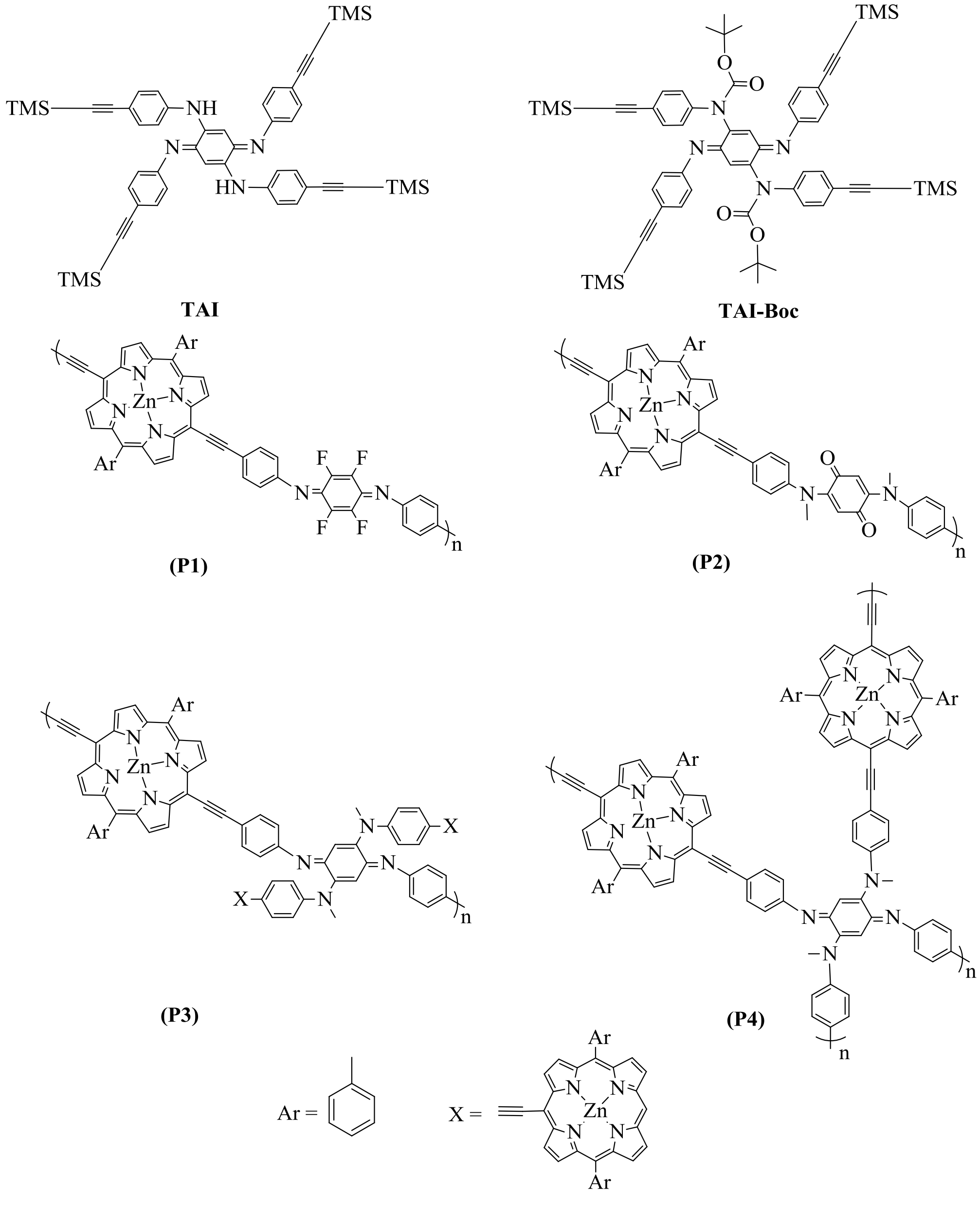

Chart 8. Structures of **TAI, TAI-Boc, P1, P2, P3, P4.**

Conclusion

The research works reported in this master thesis addresses the energy and charge transfers in several oligomers and polymers, and different factors affecting these transfers. It was inspired by the photosynthesis in the biological systems and plants towards improving the energy conversion process in the man-made devices such as solar cells.

In Chapter 2, we were able to develop a new dyad, **[Ir]-[Pt]-[ZnTPP]** (**[ZnTPP]** = (tetraphenylporphyrin)zinc(II), **[Ir]** = bis(phenylpyridinato)(bipyridine)iridium(III), **[Pt]** = trans-C≡CPt(PBu3)$_2$-C≡C), which showed the complete absence of T_1**[Ir]**→S_1/T_1**[ZnTTP]** energy transfer, unlike many similar reported dyads incorporating **[Ir]-[Pt]** chromophores (i.e. **[Ir]-Pt-[Ir]-Pt-[Ir])** which showed a triplet energy transfer from the terminal to the central iridiums). The main reason assigned to that unexpected behavior of the **[Ir]-[Pt]-[ZnTPP]** is the absence of the molecular orbitals overlap between the HSOMO(donor*) and HSOMO(acceptor), and LSOMO(acceptor) and LSOMO(donor*) and then inefficient double electron transfer is likely to occur. These results led to the conclusion that the Dexter formulation, $k_{Dexter} = KJ\exp(-2r_{DA}/L)$, appears as an approximation.

Chapter 3 reported a new dyad built upon a zinc(II)porphyrin and the corresponding free base, which acts as singlet energy donor and acceptor respectively, linked by a bridging β, β-N,N-carbene-Pd-β, β-N,N-carbene, **[PdI$_2$]**. A slow S_1 energy transfer was obseved which is significantly slow when compared to other similar dyads and to calculated values based on the Förster theory. The slow transfer was assigned to both, the weak MO overlaps between the frontier MOs of the donor and acceptor, as well as the electronic shielding induced by the presence of **[PdI$_2$]** preventing the two chromophores to fully interact via their transition dipoles. Replacing the **[PdI$_2$]** bridge by β,β-linked *trans*-Pd(NH)$_2$(C=O)$_2$, **[PdNO]**, between the zinc(II)porphyrin and the corresponding free base, as shown in chapter 4, secured the electronic communication between the two chromophores and led to an ultrafast singlet energy transfer which was rationalized by the strong MO couplings of the donor and acceptor and the very weak atomic contribution of the Pd(II) atom to this MOs.

The first three chapters showed results varied between the complete absence and efficient energy transfer. There are two main factors affected that transfer, first is the molecular orbitals, MOs, overlap of the donor and acceptor and secondly is the nature of the bridge that links the two chromophore and its contribution to the frontier MOs of the of the system.

Chapter 5 presented several bioinspired oligomers and polymers that exhibited a charge transfer and showed the effect of the **Boc** group, *tert*-butyloxycarbonyl, as an electron withdrawing group to shift the charge transfer band maximum more red.

In orveral, this thesis showed that there are a large number of parameters that influence the rate for energy transfers. Two of them were clearly stressed in this work: MO couplings and electronic screening. The next step is to build a data bank to generalize these phenomena and sensistive parameters. The second topic of this thesis was essentially preliminary work towards the design of low band gap polymers. In this respect, members of Harvey's laboratory have recently succeeded at bringing the low energy CT absorption and fluorescence bands completely in the near-IR region. We now need a larger data bank of such new polymers to fing the best one for bulk-heterojunction solar cells.

References

[1] International Energy outlook 2009, DOE/EIA-0484,(2013).

[2] O. Morton, *Nature*, (2006), **443**, 7107, 19-22.

[3] D. O. Hall, and K. K. Rao, (1999), Photosynthesis. (6th ed) Cambridge University Press.

[4] N. A. Campbell, G. M. Lawrence, B. R. Jane, (1999). Biology: Concepts and Connections, 3rd Ed. Benjamin/Cummings Publ. Co., Inc. Menlo Park, CA. (plus earlier editions).

[5] G. D. Scholes and G. R. Fleming, *Adv. Chem. Phys*., (2006), **132**, 57-129.

[6] E. D.Sternberg, D. Dolphin and C. Bruckner, *Tetrahedron,(*1998), **54**, 4151-4202.

[7] C. A. Mirkin and M. A. Ratner, *Annu. Rev. Phys.Chem.,(*1992), **43**, 719-754.

[8] F. Remacle, S. Speiser and R. D. Levine, *J. Phys.Chem.*, *(*2001), **105**, 5589-5591.

[9] R. K. Lammi, A. Ambroise, T. Balasubramanian, R. W. Wagner, D. F. Bocian, D. Holten and J. S. Lindsey, *J. Am. Chem. Soc*., (2000), **122**, 7579-7591.

[10] P. G. Van Patten , A. P. Shreve, J. S. Lindsey and R. J. Donohoe, *J. Phys. Chem. B,* (1998), **102**, 4209-4216.

[11] A. M. Soliman, M. Abdelhameed, E. Zysman-Colman* and P. D. Harvey*, *Chem. comm.*, (2013), **49**, 5544-5546.

[12] S. Lamare, S. M. Aly, D. Fortin and P. D. Harvey*, *Chem. comm.*, (2011), **47**, 10942–10944.

[13] P. D. Harvey, C. Stern, C. P. Gros, and R. Guilard, *J. Inorg. Biochem.*, (2008), **102**, 395-405.

[14] R. A. Marcus, *Pure Appl. Chem.*, (1997), **69**, 13-30.

[15] R. A. Marcus, *Annu. Rev. Phys. Chem.*, (1964), **15**, 155-196.

[16] R. A. Marcus, *Angew. Chem.*, (1993), **105**, 1161-1172.

[17] R. A. Marcus, *J. Chem. Phys.*, (1956), **24**, 966-978.

[18] R. A. Marcus, *J. Chem. Phys.*, (1965), **43**, 679-701.

[19] L. D. Landau, *Phys. Z. SSR*, (1932), **2**, 46-49.

[20] J. R. Miller, J. V. Beitz, And R. K. Huddleston, *J. Am. Chem. Soc.*, (1984), **106**, 5057-5086.

[21] R.A. Marcus, *Pure Appl. Chem.,*(1997), **69**, 13-30.

[22] B. Valeur, Molecular Fluorescence: Principles and Applications, Wiley-VCH, Weinheim, Germany, (2002), chapter 3, P 35.

[23] J. Michl, V. Bonacic-Koutechy, Electronic Aspects of Organic Photochemistry, Wiley Interscience, New York, (1990), chapter 2.

[24] G. Porter, Flash Photolysis and some of Its Applications, Nobel Lecture, (1967).

[25] A. M. Soliman, D. Fortin, E. Zysman-Colman, P. D. Harvey, *Chem. Comm.*, (2012), **48**, 6271-6273.

[26] S. Faure, C. Stern, E. Espinosa, R. Guilard, and P. D. Harvey, *Chem. Eur. J.*, (2005)**,** **11**, 3469-3481.

[27] (a) B. Ventura, A. Barbieri, A. Degli Esposti, J. B. Seneclauze, and R. Ziessel, *Inorg. Chem.,* (2012), **51**, 2832. (b) J. Osio Barcina, N. Herrero-Garcia, F. Cucinotta, L. De Cola, P. Contreras-Carballada, R. M. Williams, and A. Guerrero-Martinez, *Chem. Eur. J.,* (2010), **16**, 6033-6040. (c) F. Nastasi, F. Puntoriero, S. Campagna, S. Schergna, S. M. Maggini, F. Cardinali, B. Delavaux-Nicot, J.-F. Nierengarten, *ChemComm,* (2007), 3556-3558. (d) V. L. Whittle and J. A. G. Williams., *Dalton Trans.*, (2009), 3929-3940.